

WAKE TRANSITIONS AND INTERACTIONS BEHIND WALL-MOUNTED PRISMS

BY

SHUBHAM GOSWAMI

A THESIS SUBMITTED IN PARTIAL FULFILMENT OF THE REQUIREMENTS FOR THE DEGREE OF

DOCTOR OF PHILOSOPHY

DEPARTMENT OF MECHANICAL ENGINEERING

UNIVERSITY OF ALBERTA

© SHUBHAM GOSWAMI, 2025

ABSTRACT

This dissertation identifies and characterizes the wake evolution, transitions, and interactions, as well as evaluates the influence of geometrical and dynamic parameters on the wake of wall-mounted prisms. The wake of wall-mounted prisms is highly three-dimensional, where topology is partly dictated by the prism geometry, such as changing aspect-ratio (height-to-width). However, the influence of depth-ratio (length-to-width) has not been well characterized. Numerical simulations, based on direct techniques and Large Eddy Simulations, were utilized to explore a wide range of parameters, including aspect-ratio of $0.25 - 1.5$ and depth-ratios of $0.016 - 4$ at Reynolds numbers of $5 \times 10^1 - 1 \times 10^4$. The minimum depth-ratio considered here accounts for the special case of a wall-mounted thin prism, similar to a flat plate. First, a comprehensive classification of wake topology is presented as a multivariate function of depth-ratio and Reynolds number. Evolution in the mean and instantaneous wake topologies is first discussed at low Reynolds numbers ($Re = 5 \times 10^1 - 5 \times 10^2$), which establishes that there is a unique asymmetric wake system formed behind wall-mounted prisms with sufficiently small depth-ratios due to alternating shear-layer peel-off on either side of the body. This study also reveals the formation of asymmetric hairpin-like vortices and the origins of wake asymmetry, offering fresh insights into their dynamics. Further, interactions between secondary vortex structures and leading-edge shear-layer are quantified. This dissertation, thereafter, uniquely identifies the role of depth-ratio in the interactions between Kelvin-Helmholtz instability and hairpin-like vortices at moderate Reynolds numbers ($Re = 1 \times 10^3 - 1 \times 10^4$). Understanding these interactions provides critical insights into wake dynamics with increasing Reynolds numbers. Finally, the study breaks new ground by identifying and quantifying the mechanism of interactions between leading-edge shear layers and free-end vortices at moderate Reynolds numbers, which lead to increased wake irregularity. Thus, the role of geometrical parameters in dictating the wake topology and evolution are defined, which provides a comprehensive understanding of the wake dynamics behind wall-mounted prisms.

PREFACE

This dissertation is the original work of Shubham Goswami, completed under the supervision of Dr. Arman Hemmati. The results from Chapters 4, 5 and 6 are published in *Journal of Fluid Mechanics*, *International Journal of Heat and Fluid Flow* and *Physics of Fluids*, respectively, and their citations are:

1. Goswami, S., & Hemmati, A. (2022). Mechanisms of wake asymmetry and secondary structures behind low aspect-ratio wall-mounted prisms. *Journal of Fluid Mechanics*, 950, A31.
2. Goswami, S., & Hemmati, A. (2023). Mean wake evolution behind low aspect-ratio wall-mounted finite prisms. *International Journal of Heat and Fluid Flow*, 104, 109237.
3. Goswami, S., & Hemmati, A. (2024). Impact of depth-ratio on shear-layer dynamics and wake interactions around wall-mounted prisms. *Physics of Fluids*, 36(11):115–149.

Results from Chapter 7 are accepted for publication in *Journal of Fluid Mechanics* and the citation reads:

4. Goswami, S., & Hemmati, A. (2024). Influence of depth-ratio on turbulence transition in the wake of wall-mounted prisms. *Journal of Fluid Mechanics*.

And, results from Chapter 8 are currently under review by *Journal of Fluid Mechanics* with the following citation:

5. Goswami, S., & Hemmati, A. (2025). Destabilization of leading-edge shear-layer behind wall-mounted long prisms. *Journal of Fluid Mechanics*.

*To Pappa, for always supporting and inspiring me,
To Mummy, for your never-ending love and motivation,
To Om, for always inspiring me with a can-do attitude,
And to My Riddhi...
no words can describe how grateful I am for your love.*

“Not all those who wander are lost”

-J.R.R. Tolkien

ACKNOWLEDGEMENTS

Firstly, I convey my deepest appreciation and graduate to my supervisor, Dr. Arman Hemmati, for your excellent guidance, support and patience. You believed in me and guided me to rise above the ordinary and achieve the extraordinary. Thank you for your tutelage, encouragement, and advice. I am grateful for your mentorship and for the opportunities you have provided me to grow and develop as a researcher. I am also grateful for the time you have spent reading my work, providing feedback, and helping me to improve my writing. I am truly fortunate to have had you as my supervisor.

I am most grateful to Dr. Suyash Verma and Dr. Muhammad Saif Ullah Khalid, who provided me with much needed guidance in understanding OpenFOAM, CFD, data-driven modelling and much more. Your friendship, support, and encouragement have been invaluable to me. I truly appreciate your patience in teaching me and supporting me. I would have been lost without you both.

Further, I thank all my colleagues at the University of Alberta, Dr. Ahmet Gungor, Mr. Benjamin Freeman, Mr. Shahab Ahmadizade, Mr. Stanley John, and Dr. Zaib Un Nisa, with whom I have had the pleasure of working with. I am grateful for the support, encouragement, and camaraderie that you have provided me. I am also grateful for the many discussions we have had, which have helped me to grow as a researcher. I am truly fortunate to have had all of you as my colleagues. My deepest appreciation also goes to my friends with whom I shared office space, and time during various departmental seminars, and extra-curricular activities.

Finally, I would like to extend my gratitude to the Natural Sciences and Engineering Research Council of Canada (NSERC) and Alberta Innovates for their support during my research. And to Digital Research Alliance of Canada for providing me with the resources to carry out my research.

To all of you, I am forever grateful.

Contents

Abstract	ii
Preface	iii
Acknowledgements	v
List of Tables	x
List of Figures	xi
List of Abbreviations, Symbols, and Nomenclature	xxiv
1 INTRODUCTION	1
1.1 Overview	1
1.2 Motivations and Objectives	6
1.3 Novelty	10
1.4 Structure of the thesis	11
2 BACKGROUND	14
2.1 Flow around bluff bodies	15
2.2 Wake of wall-mounted rectangular prisms	17
2.2.1 Mean wake topology	22
2.2.2 Unsteady wake topology	25
2.2.3 Wake features and instabilities	28
2.3 Wake of suspended bluff bodies	31
2.3.1 Wake of suspended prisms	32

2.3.2	Wake behind flat plates	34
2.3.3	Wake of circular cylinders	35
2.4	Approaches to Flow Studies	36
2.4.1	Experimental Studies	37
2.4.2	Numerical Simulations	39
2.4.3	OpenFOAM	40
3	METHODOLOGY	44
3.1	Problem Description	45
3.2	Governing Equations and Discretization	48
3.2.1	Direct Numerical Simulations	48
3.2.2	Large Eddy Simulations	49
3.2.3	Discretization Schemes	50
3.3	Boundary Conditions	51
3.3.1	Inlet Boundary Condition	51
3.3.2	Outlet Boundary Conditions	52
3.3.3	Wall Boundary Conditions	52
3.3.4	Symmetry/Periodic Boundary Conditions	53
3.4	Boundary Layer Thickness	54
3.5	Statistical analysis and time-averaging	57
3.6	Verification Studies	60
3.7	Validation Studies	69
3.8	Assessment of Wake Dynamics	71
3.8.1	Assessing the strength of vortex	72
3.8.2	Dynamic Mode Decomposition (DMD)	73
4	WAKE ASYMMETRY AND SECONDARY STRUCTURES BEHIND WALL-MOUNTED PRISMS	75

4.1	Results and Discussion	76
4.1.1	Wake Classification	78
4.1.2	Instantaneous wake characteristics	83
4.1.3	Time-averaged wake characteristics	88
4.1.4	Upwash and downwash motion	90
4.1.5	Flow periodicity and spanwise coherence	94
4.1.6	Mechanism of asymmetric shedding	102
4.2	Summary	111
5	MEAN WAKE EVOLUTION BEHIND WALL-MOUNTED PRISMS	113
5.1	Results and Discussion	114
5.1.1	Time-averaged wake characteristics	117
5.1.2	Effects of downwash and upwash flows	122
5.2	Summary	132
6	IMPACT OF DEPTH-RATIO ON SHEAR-LAYER DYNAMICS AND WAKE INTERACTIONS	134
6.1	Results and Discussion	135
6.1.1	Mean Flow Characteristics	138
6.1.2	Flow periodicity and Instantaneous Flow Characteristics	141
6.1.3	Wall Pressure Distribution	147
6.1.4	Origins of fluctuating wall pressure	149
6.2	Summary	154
7	INFLUENCE OF DEPTH-RATIO ON TURBULENCE TRANSITION	156
7.1	Results and Discussion	157
7.1.1	Unsteady Shear-Layer Motion	162
7.1.2	Flow Periodicity	163
7.1.3	Leading-edge Shear-layer Interactions	165

7.1.4	Observations across the parameter space	169
7.2	Summary	172
8	DESTABILIZATION OF LEADING-EDGE SHEAR-LAYER	174
8.1	Results and Discussion	175
8.1.1	Mean flow characteristics	178
8.1.2	Onset of Kelvin-Helmholtz Instability	180
8.1.3	Flow processes with typical frequencies	185
8.1.4	Mechanism of destabilization of leading-edge shear-layer	188
8.1.5	High Reynolds number flow	199
8.2	Summary	199
9	CONCLUSIONS	201
10	FUTURE WORK	205
Bibliography		207

List of Tables

3.1	Grid sensitivity analysis results for wall mounted thin prism case ($DR = 0.016$). . .	61
3.2	Domain and grid sensitivity analysis results for wall mounted prism with $DR = 4$ at $Re = 2.5 \times 10^3$. The relative error is calculated with respect to Domain 2 and Grid 4, respectively.	65

List of Figures

1.1	Schematics of large aspect-ratio (Left) and large depth-ratio (Right) prisms.	4
2.1	Quadrupole (Left) and Dipole (Right) wake topologies in the wake of wall-mounted prisms, presented using streamwise vorticity distribution above and below the critical aspect-ratio.	23
2.2	Case structure in OpenFOAM	42
3.1	Schematics of computational domain (Not to scale) for (a) $DR = 0.016$ and (b) $DR = 4$	45
3.2	Spatial grid distribution for the wall mounted prism of (a) $DR = 0.016$ and (b) $DR = 4$, presented in (a, b) Side view at $z/d = 0$ and (c, d) Top view at $y/d = 0.5$. .	47
3.3	Schematics of multi-block grid setup for wall-mounted prism with $DR = 4$	47
3.4	(a) Distribution of the time-averaged and root-mean-square of streamwise velocity, i.e. \bar{u} and u' , normalized by free-stream velocity (U_b), at $Re = 2.5 \times 10^2$. Measurements were performed in the absence of the prism. Dashed line shows the boundary-layer thickness (δ/d). (b) Boundary layer profile prior to reaching the prism compared with the Blasius boundary layer profile.	55

3.5 (a) Distribution of the time-averaged and root-mean-square of the streamwise velocity (\bar{u} and u') at the location of the leading-edge of the prism at $Re = 2.5 \times 10^3$; and (b) Distribution of the time-averaged streamwise velocity (\bar{u}) at the location of the leading-edge of the prism at $Re = 1 \times 10^3, 2.5 \times 10^3$, and 5×10^3 . Measurements were performed in absence of the prism. Dashed line shows the boundary layer thickness (δ/d).	56
3.6 Complete time-history and moving cumulative average of (a, c) streamwise (u) and (b, d) normal velocity (v) in the wake of the prism with $AR = 1$ and $DR = 4$ at $Re = 2.5 \times 10^3$	59
3.7 Effect of grid size on mean velocities at $x/d = 3$ and $y/d = 0.5$, for prism of $DR = 0.016$ at Reynolds number of 2.5×10^2 . Shown are profiles of (a) \bar{U} and (b) \bar{V}	62
3.8 Effect of grid size on wake turbulence characteristics at $x/d = 3$ and $y/d = 0.5$, for prism of $DR = 0.016$ at Reynolds number of 2.5×10^2 . Shown are profiles of (a) k/U_b^2 and (b) $\bar{u}'u'/U_b^2$	62
3.9 Contours of the ratio of grid-size to Kolmogorov length scale (Δ/η) at $y/d = 0.5$ for the case of wall mounted thin prism ($DR = 0.016$) at Reynolds number of 2.5×10^2	63
3.10 Effect of (a, b) Domain and (c, d) Grid sizes on mean and turbulent wake characteristics. Shown are (a, c) \bar{u} and (b, d) $\bar{u}'u'$	66
3.11 Contours of (a, b) instantaneous and (c, d) time-averaged (mean) distributions of the ratio of grid size to Kolmogorov length scale (Δ/η) in the (a, c) symmetry plane ($z/d = 0$) and (b, d) x-z plane ($y/d = 0.5$) for the case of $DR = 4$ at $Re = 2.5 \times 10^3$	67
3.12 Contours of ratio between time-step (Δt) and the Kolmogorov time scale (τ_η) for the instantaneous flow field in the (a) symmetry plane ($z/d = 0$) and (b) x-z plane ($y/d = 0.5$) for the case of $DR = 4$ at $Re = 2.5 \times 10^3$	67

3.13 Histogram of the (a) ratio of grid size to Kolmogorov length scale (Δ/η) and (b) ratio of time-step size to the Kolmogorov time scale (τ_η) for the case of $DR = 4$ at $Re = 2.5 \times 10^3$. Histogram is presented for the instantaneous flow field in the entire computational domain.	68
3.14 Time-averaged (a) streamwise and (b) spanwise velocity distributions at $Re = 2.5 \times 10^2$, behind a rectangular prism with $AR = 4$ compared with DNS result of Zhang et al. (2017) and Saha (2013).	70
3.15 Comparison of (a) mean axial velocity (\bar{u}) and (b) root-mean-squared velocity (u'_{rms}) profiles obtained from LES with the experimental results of Saeedi et al. (2014).	71
4.1 Classification of the wake topology in terms of Reynolds number and depth-ratio. .	78
4.2 Instantaneous vortex structures of $DR = 0.016$ prism identified using $Q^* = 6 \times 10^{-6}$ and overlaid with mean streamwise velocity (\bar{u}/U_b), at (a) $Re = 1.5 \times 10^2$; (b) $Re = 2 \times 10^2$; (c) $Re = 2.5 \times 10^2$; and (d) $Re = 5 \times 10^2$. All figures are shown in three-dimensional view.	79
4.3 Contours of instantaneous streamwise vorticity ($\bar{\omega}_x^*$) structures (solid blue lines: positive values, dashed red lines: negative values) for $DR = 0.016$ at (a-c) $Re = 2.5 \times 10^2$ and (d-f) $Re = 5 \times 10^2$. The line contour cutoff levels for $\bar{\omega}_x^*$ are ± 0.12 and the contour interval is 0.001. The contours are shown at $x/d = 0, 1$ and 2. . . .	81
4.4 Instantaneous vortex structures for (a) $DR = 1$ and (b) $DR = 1.5$ prisms at Reynolds number of 5×10^2 , identified using $Q^* = 6 \times 10^{-6}$ and overlaid with mean streamwise velocity (\bar{u}/U_b). All figures are shown in three-dimensional view.	82
4.5 Trends of drag coefficient (C_d) with varying depth-ratios and Reynolds numbers. .	82

4.6 Instantaneous vortex structures identified using Q -criterion and overlaid with mean streamwise velocity (\bar{u}/U_b), for (a) $DR = 0.016$; (b) $DR = 0.1$; (c) $DR = 0.3$; (d) $DR = 1$; (e) $DR = 2$ and (f) $DR = 4$, at Reynolds number of 2.5×10^2 . The threshold of $Q^* = 6 \times 10^{-6}$ is used for $DR = 0.016, 0.1, 1 - 4$, while $Q^* = 1 \times 10^{-6}$ is used for $DR = 0.3$ to avoid distorted contours. All figures are shown in three-dimensional view.	84
4.7 Instantaneous vortex structures identified using $Q^* = 6 \times 10^{-6}$ for (a) $DR = 0.016$ and (b) $DR = 0.1$, at Reynolds number of 2.5×10^2 . Figures are presented from top view.	86
4.8 Time-averaged vortex structures identified using $Q^* = 1 \times 10^{-6}$, colored with $\overline{\omega}_x^*$ for (a) $DR = 0.016$; (b) $DR = 0.1$; (c) $DR = 0.3$; (d) $DR = 1$; (e) $DR = 2$ and (f) $DR = 4$. The iso-surface for $\overline{\omega}_x^*$ is shown for each case on the top-right corner.	89
4.9 Contours of time-averaged axial vorticity ($\overline{\omega}_x^*$) structures (solid blue lines: positive values, dashed red lines: negative values) for (a-c) $DR = 0.016$; (d-f) $DR = 0.1$; (g-i) $DR = 0.3$ and (j-l) $DR = 1$. The line contour cutoff levels for $\overline{\omega}_x^*$ are ± 3 and the contour interval is 0.06. The contours are shown at $x/d = 2, 5$ and 10.	91
4.10 The $\overline{\omega}_z^*$ contours overlapped with the time-averaged streamlines for (a) $DR = 0.016$; (b) $DR = 0.1$; (c) $DR = 0.3$; (d) $DR = 1$; (e) $DR = 2$ and (f) $DR = 4$. Plots are shown at $y/d = 0$	92
4.11 Location of the maximum Reynolds shear stress, $Y_M(-\overline{u'v'})$, and $Z_M(\overline{ u'w' })$, normalized by the prism width (d), downstream of the wall mounted prism, at (a) $z/d = 0$ and (b) $y/d = 0.5$ plane.	94
4.12 The power spectral density function, E_u , of the streamwise streamwise velocity (u) at $x/d = 2.5$, $y/d = 0.5$ and $z/d = 0.5$, for (a) $DR = 0.016$ and (b) $DR = 0.1$ prisms at Reynolds number of 2.5×10^2	95

4.13 The normalized autocorrelation function, ρ_τ , of the streamwise velocity at $x/d = 2.5$ and $y/d = 0.05, 0.5$ and 0.95 , for (a) $DR = 0.016$ and (b) $DR = 0.1$. Note that $\tau^* = \tau f_{sh}$ is the number of vortex shedding periods, where f_{sh} is the vortex shedding frequency corresponding to St_{sh} .	97
4.14 Spectral coherence, $Coh_{u_1u_2}$, between streamwise velocity u_1 and u_2 for $DR = 0.016$, at $x/d = 2.5$ and $z/d = 0.5$. u_1 was measured at $y/d = 0.008$, and u_2 was measured at $y/d = 0.05, 0.5$ and 0.95 .	99
4.15 The variation of instantaneous streamwise velocity components, u_1 and u_2 , at locations $(2.5, 0.95, \pm 0.4)$ as shown in the schematic plot, for $DR = 0.016$ prism. t^* is the convective time, given as $t^* = tU_b/d$.	101
4.16 Instantaneous vortex structures identified using $Q^* = 6 \times 10^{-6}$ and overlaid with streamwise vorticity ($\bar{\omega}_x^*$), surrounded by the line contours of $\bar{\omega}_x^*$ (solid blue lines: positive values, dashed red lines: negative values) for $DR = 0.016$ prism at Reynolds number of 2.5×10^2 . The line contour cutoff levels for $\bar{\omega}_x^*$ are ± 0.12 and the contour interval is 0.001. Contours are shown at $x/d = 0 - 2.5$ at intervals of 0.5.	103
4.17 Circulation (Γ), normalized by bulk velocity (U_b) and prism width (d), computed for Top and side surface shear-layers of (a) $DR = 0.016$ and (b) $DR = 0.1$ prisms at Reynolds number of 2.5×10^2 . t^* is the arbitrary range of convective time, given as $t^* = tU_b/d$.	104
4.18 Time marching, line contours of $\bar{\omega}_x^*$ (solid blue lines: positive values, dashed red lines: negative values) plotted at $x/d = 2$ for $DR = 0.016$ at Reynolds number of 2.5×10^2 . The line contour cutoff levels for $\bar{\omega}_x^*$ are ± 0.12 and the contour interval is 0.001. Contours are shown at (a) $t_1 = t_o$; (b) $t_2 \approx t_o + \frac{1}{5}\tau^*$; (c) $t_3 \approx t_o + \frac{2}{5}\tau^*$; (d) $t_4 \approx t_o + \frac{3}{5}\tau^*$; (e) $t_5 \approx t_o + \frac{4}{5}\tau^*$ and (f) $t_6 \approx t_o + \tau^*$. τ^* is the time scale based on $\tau^* = d/(U_b St)$.	106

4.19 (a,b) Reconstructed vortex structures identified using Q -criterion and overlaid with instantaneous streamwise vorticity and (c,d) Reconstructed streamwise vorticity structures. Structures are reconstructed using the addition of (a,c) mean with DMD Mode 1 (St_{sh}); (b,d) mean with DMD Mode 1 (St_{sh}) and Mode 2 ($St_{sh}/2$).	108
4.20 Instantaneous vortex structures of prisms with (a) $DR = 0.6$ at $Re = 4 \times 10^2$; and (b) $DR = 1$ at $Re = 5 \times 10^2$, identified using $Q^* = 6 \times 10^{-6}$ and overlaid with $\bar{\omega}_x^*$. All figures are shown in three-dimensional view.	110
4.21 Instantaneous vortex structures identified using $Q^* = 6 \times 10^{-6}$ and overlaid with streamwise vorticity ($\bar{\omega}_x^*$), surrounded by the line contours of $\bar{\omega}_x^*$ (solid blue lines: positive values, dashed red lines: negative values) for $DR = 0.1$ prism at Reynolds number of 2.5×10^2 . The line contour cutoff levels for $\bar{\omega}_x^*$ are ± 0.12 and the contour interval is 0.001. Contours are shown at $x/d = 0, 1, 1.5, 2$ and 2.5	111
5.1 Classification of the mean wake topology in terms of Reynolds number and depth-ratio for prism with aspect-ratio of 1. Note: the vertical axis is non-linear, representing depth-ratios between 0.016–4.	114
5.2 Line contours of $\bar{\omega}_x d/U_b$ (solid blue lines: positive values, dashed red lines: negative values) showing (a) Dipole-type, (b) Multipole, and (c) Quadrupole-type cross-sectional wake topology. All cases are for prism with Aspect-ratio of 1. Contours are shown at $x/d = 5$	115
5.3 Time-averaged (mean) wake structures identified using $\lambda_2 = -0.0001$ colored with $\bar{\omega}_x d/U_b$. Shown are (a) $DR = 1$ at $Re = 2.5 \times 10^2$, (b) $DR = 1$ at $Re = 3 \times 10^2$, and (c) $DR = 1$ at $Re = 3.5 \times 10^2$. Line contours of $\bar{\omega}_x d/U_b$ are also drawn on the yz -planes at $x/d = 5$ and 8 , resembling the streamwise wake topology identified in Figure 5.2.	118

5.4 Time-averaged (mean) wake structures identified using $\lambda_2 = -0.0001$ colored with $\bar{\omega}_x d / U_b$. Shown are (a) $DR = 2$ at $Re = 3 \times 10^2$, (b) $DR = 3$ at $Re = 4.5 \times 10^2$, and (c) $DR = 0.016$ at $Re = 2.5 \times 10^2$. Line contours of $\bar{\omega}_x d / U_b$ are also drawn on the yz -planes at $x/d = 5$ and 8 , resembling the streamwise wake topology identified in Figure 5.2.	119
5.5 Line contours of $\bar{\omega}_x d / U_b$ (solid blue lines: positive values, dashed red lines: negative values) showing evolution of primary tip vortex (TV_1), secondary tip vortex (TV_2), and upper vortex (UV), in (a-d) Dipole-type ($DR = 1$ at $Re = 2.5 \times 10^2$), (e-h) Multipole ($DR = 1$ at $Re = 3 \times 10^2$), and (i-l) Quadrupole-type ($DR = 1$ at $Re = 3.5 \times 10^2$) wake topology. All cases are for prism with Aspect-ratio of 1.	120
5.6 Variation in Circulation ($\bar{\Gamma} / U_b d$) of primary tip vortex (TV_1) and upper vortex (UV). Shown are Dipole ($DR = 1$ at $Re = 2.5 \times 10^2$), Multipole ($DR = 1$ at $Re = 3 \times 10^2$), and Quadrupole ($DR = 1$ at $Re = 3.5 \times 10^2$).	122
5.7 Contours of time-averaged normal velocity (\bar{v} / U_b) with wake topology identified using line contours of $\bar{\omega}_x d / U_b$ on top-right. Shown are (a) $DR = 1$ at $Re = 2.5 \times 10^2$, (b) $DR = 1$ at $Re = 3 \times 10^2$, and (c) $DR = 1$ at $Re = 3.5 \times 10^2$. Contours are shown at $z/d = 0$	123
5.8 The location of saddle point (\bar{Y}_s / d) as a function of Re and DR for prisms with Aspect-ratio of 1. Note: the vertical axis is non-linear, representing depth-ratios between 0.016–4.	124
5.9 Spanwise variation of time-averaged (mean) axial (\bar{u} / U_b) and normal velocity (\bar{v} / U_b) for different wake topologies. Shown are Dipole ($DR = 1$ at $Re = 2.5 \times 10^2$), Multipole ($DR = 1$ at $Re = 3 \times 10^2$), and Quadrupole ($DR = 1$ at $Re = 3.5 \times 10^2$).	125

5.10 Streamwise variation of maximum shear stress ($\overline{-u'v'}$), normalized by free-stream velocity (U_b). Shown are Dipole ($DR = 1$ at $Re = 2.5 \times 10^2$), Multipole ($DR = 1$ at $Re = 3 \times 10^2$), and Quadrupole ($DR = 1$ at $Re = 3.5 \times 10^2$).	126
5.11 Streamwise variation of axial ($\overline{u'u'}$) shear stress ($\overline{u'v'}$) normalized by free-stream velocity (U_b). Shown are Dipole ($DR = 1$ at $Re = 2.5 \times 10^2$), Multipole ($DR = 1$ at $Re = 3 \times 10^2$), and Quadrupole ($DR = 1$ at $Re = 3.5 \times 10^2$) wakes.	127
5.12 Streamwise variation of axial ($\overline{u'u'}$) shear stress ($\overline{u'v'}$) normalized by free-stream velocity (U_b). Shown are Dipole ($DR = 1$ at $Re = 4 \times 10^2$), Multipole ($DR = 1.5$ at $Re = 4 \times 10^2$), and Quadrupole ($DR = 2$ at $Re = 4 \times 10^2$) wakes.	128
5.13 Line contours of $\overline{\omega_x}d/U_b$ (solid blue lines: positive values, dashed red lines: negative values) showing evolution from Quadrupole to Dipole wake, at $x/d = 5$, with increasing depth-ratio at Reynolds number of 2.5×10^2	128
5.14 Time-averaged streamlines, overlaid by contours of $\overline{C_p}$, at spanwise plane of (a,b) $y/d = 0.5$ and (c, d) $y/d = 0.95$ for (a,c) Dipole and (b,d) Quadrupole-type wakes, along with mean velocity vectors in the top-right corner. Shown are (a,c) $DR = 1$ at $Re = 2.5 \times 10^2$, and (b,d) $DR = 1$ at $Re = 3.5 \times 10^2$	129
5.15 Time-averaged streamlines, overlaid by contours of $\overline{C_p}$ at normal plane of $z/d = 0$ for (a) Dipole and (b) Quadrupole-type wakes. The bold black line shows the mean velocity streamline of $\overline{u}/U_b = 0$. Shown are (a) $DR = 1$ at $Re = 2.5 \times 10^2$, and (b) $DR = 1$ at $Re = 3.5 \times 10^2$	130
5.16 Streamwise axial velocity gradient ($\partial u / \partial x$) normalized by prism width (d) and free-stream velocity (U_b). Shown are Dipole ($DR = 1$ at $Re = 2.5 \times 10^2$), Multipole ($DR = 1$ at $Re = 3 \times 10^2$), and Quadrupole ($DR = 1$ at $Re = 3.5 \times 10^2$) wakes. Profiles are shown at $x/d = 5$	131
6.1 Instantaneous flow realizations identified using $Q^* = 10$ and overlaid with contours of streamwise velocity (u) for (a) $DR = 1$ and (b) $DR = 4$ at $Re = 2.5 \times 10^3$	136

6.2	Contours of mean axial velocity (\bar{u}/U_b) overlaid with mean streamlines for (a,c) $DR = 1$ and (b,d) $DR = 4$ at (a,b) $z/d = 0$ and (c,d) $y/d = 0.5$. Dotted axis indicates the line of symmetry. Dotted streamlines show negative streamwise velocity regions.	139
6.3	Contours of turbulence kinetic energy (k/U_b^2) for (a,c) $DR = 1$ and (b,d) $DR = 4$ at (a,b) $z/d = 0$ and (c,d) $y/d = 0.5$. Dotted axis indicates the line of symmetry. ‘ \times ’ marker shows the location of maximum turbulence kinetic energy.	140
6.4	Premultiplied power spectral density of streamwise (E_u), Normal (E_v), and Span- wise velocity (E_w) fluctuations at at $(x/d, y/d, z/d) = (0.5, 1.3, 0)$ for (a) $DR = 1$ and (b) $DR = 4$	142
6.5	Instantaneous span-wise vorticity field for (a,b) $DR = 1$ and (c,d) $DR = 4$ at $z/d =$ 0. The time increment, $t^* = d/U_b f_{kh}$, where f_{kh} is the frequency of KHI rollers. . .	143
6.6	Instantaneous axial velocity profiles (u/U_b) at $z/d = 0$ for (a) $DR = 1$ and (b) $DR = 4$. Dotted red lines show the trajectory of shear-layer.	145
6.7	Axial pressure gradient profiles ($\partial p/\partial x$) at $z/d = 0$ for (a) $DR = 1$ and (b) $DR = 4$.	146
6.8	Distribution of (a) coefficient of pressure ($\overline{C_p}$) and (b) root-mean-square of pressure fluctuations (p'_{rms}) on the prism top ($z/d = 0$) and side ($y/d = 0.5$) surfaces with depth-ratio of $DR = 1$ and $DR = 4$ at $Re = 2.5 \times 10^3$. Solid line represents top surface and dashed line represents side surface of the prism. Dotted line shows the mean reattachment point (\bar{x}_R) on $DR = 4$ prism.	148
6.9	Contours of root-mean-square of turbulence-mean-shear interaction (TMI) for (a,c) $DR = 1$ and (b,d) $DR = 4$ at (a,b) $z/d = 0$ and (c,d) $y/d = 0.5$. Dotted axis indicates the line of symmetry. ‘ \times ’ marks the location of maximum TMI.	150
6.10	Contours of root-mean-square of turbulence-turbulence interaction for (a,c) $DR =$ 1 and (b,d) $DR = 4$ at (a,b) $z/d = 0$ and (c,d) $y/d = 0.5$. Dotted axis indicates the line of symmetry.	151
6.11	Cross spectral density of pressure fluctuations (p') for (a) $DR = 1$ and (b) $DR = 4$, at locations marked in the contour of ω_z^* on left.	152

6.12 Instantaneous flow realizations identified using $Q^* = 10$ and overlaid with contours of streamwise velocity (u) at (a) $DR = 2$ and (b) 4 at $Re = 1 \times 10^3$; and (c) $DR = 1.5$ and (d) 3.5 at $Re = 1.5 \times 10^3$	154
7.1 (a,b) Mean streamwise velocity (\bar{u}) and (c,d) turbulent kinetic energy (k) contours overlaid with mean velocity streamlines at $z/d = 0$ for (a, c) $DR = 1$ and (b, d) $DR = 4$ prisms.	157
7.2 Instantaneous vortex structures overlaid with axial velocity (u) contours for (a) $DR = 1$ and (b) $DR = 4$ prisms identified using Q -criterion ($Q^* = 1$). Lateral view of the instantaneous vortex structures for (c) $DR = 1$ and (d) $DR = 4$ prisms. . .	159
7.3 Distribution of maximum turbulent kinetic energy (k_{\max}) along the mid-span ($z/d = 0$) of both prisms at $Re = 2.5 \times 10^3$	160
7.4 Contours of span-wise vorticity, ω_z^* , for (a) $DR = 1$ and (b) $DR = 4$, superimposed with instantaneous streamlines and the isopleth of $\bar{u} = 0$ (bold, green line) at $z/d = 0.161$	
7.5 Axial wall-pressure gradient ($\partial p_w / \partial x$) along the mid-span ($z/d = 0$) of both prisms at $Re = 2.5 \times 10^3$	162
7.6 Space-time plot of the instantaneous wall shear-stress (τ_w) along the top surface of the prism with $DR = 4$ at $z/d = 0$. $\tau_w > 0$ (White) represents the region of forward flow, while $\tau_w < 0$ (Gray) represents the region of reverse flow.	164
7.7 Pre-multiplied power spectral density of streamwise (E_u), normal (E_v) and spanwise (E_w) velocity fluctuations near the leading-edge at $(0.5, 1.3, 0)$ for (a) $DR = 1$ and (b) $DR = 4$	165
7.8 Profiles of maximum values of root-mean-squared (a) turbulence-mean-shear interaction (TMI_{\max}) and (b) turbulence-turbulence interaction (TTI_{\max}) terms of the Poisson's equation for $DR = 1$ and 4 prisms at $z/d = 0$ (Blue) and $y/d = 0.5$ (red). The axial distances are normalized using prism length (l). \bigcirc represents $DR = 1$; \square represents $DR = 4$	166

7.9	Magnitude mode bi-spectrum for $DR = 4$, using $N_{fft} = 2^{10}$, in the sum and difference regions.	168
7.10	BMD interaction map for $DR = 4$ prism, showing the interactions between (a) Kelvin-Helmholtz instability and mean flow and (b) Kelvin-Helmholtz instability and large-scale vortex shedding.	168
7.11	Instantaneous vortex structures overlaid with axial velocity (u) contours for (a, c) $DR = 1.5$ and (b, d) 3.5 at (a, b) $Re = 1.5 \times 10^3$, (c, d) $Re = 4 \times 10^3$ identified using Q -criterion ($Q^* = 1$).	170
7.12	Instantaneous vortex structures overlaid with axial velocity (u) contours for prisms with $AR = 1.5$ and (a) $DR = 1.5$ and (b) 3.5 at $Re = 2.5 \times 10^3$ identified using Q -criterion ($Q^* = 1$).	171
7.13	Axial wall-pressure gradient along the mid-span ($z/d = 0$) of prisms with (a) $AR = 1.5$ at $Re = 2.5 \times 10^3$, and (b) $AR = 1$ at $Re = 4 \times 10^3$	171
8.1	Instantaneous vortex structures overlaid with axial velocity (u) contours for (a, c) $DR = 1$ and (b, d) $DR = 4$ prisms with (a, b) $AR = 1$ and (c, d) $AR = 1.5$ at Reynolds number of 2.5×10^3 , identified using Q -criterion ($Q^* = 1$).	175
8.2	Instantaneous vortex structures overlaid with axial velocity (u) contours for (a, c) $DR = 1$ and (b, d) $DR = 4$ prisms at (a, b) $Re = 5 \times 10^3$ and (c, d) $Re = 1 \times 10^4$, identified using Q -criterion ($Q^* = 1$).	177
8.3	(a,b) Mean streamwise velocity (\bar{u}) contours overlaid with mean velocity streamlines; and (c,d) contours of root-mean-squared streamwise fluctuations (u'_{rms}) overlaid with streamline of $\bar{u} = 0$. Contours presented for (a,c) $DR = 1$ and (b,d) $DR = 4$ prisms at $Re = 2.5 \times 10^3$ at spanwise plane of $z/d = 0$	178
8.4	Profiles of root-mean-squared of the normal velocity fluctuations (v'_{rms}) at different streamwise locations shown in Figures 8.3c and 8.3d for (red) $DR = 1$ and (blue) $DR = 4$ prisms at $Re = 2.5 \times 10^3$. Solid lines show profiles for $AR = 1$ prisms, while the \times markers indicate the profiles for $AR = 1.5$ prisms.	179

8.5 Mean shear (τ) at leading-edge of (a) $DR = 1$ and (b) $DR = 4$ prisms with $AR = 1$ at $Re = 2.5 \times 10^3$. Contours are overlaid with streamline of $\bar{u} = 0$ (green) and critical streamlines (black).	180
8.6 Iso-surfaces of streamwise vorticity, $\omega_x^* = \pm 5$, at (a,b) $Re = 2.5 \times 10^3$ and (c,d) $Re = 1 \times 10^4$ for (a,c) $DR = 1$ and (b,d) $DR = 4$ prisms.	181
8.7 Contours of span-wise vorticity, ω_z^* , for (a) $DR = 1$ and (b) $DR = 4$ at Reynolds number of 2.5×10^3 , superimposed with instantaneous streamlines and the isopleth of $\bar{u} = 0$ (bold, green line) at $z/d = 0$	182
8.8 Downstream trajectory of maximum turbulence kinetic energy (k_{\max}) along the prism mid-span ($z/d =$) for (a) $DR = 1$ and (b) $DR = 4$ prisms. Leading-edge of the prisms (shown in grey) is located at $x/d = 0$	184
8.9 Integrated turbulence kinetic energy along the prism mid-span ($z/d =$) for (a) $DR = 1$ and (b) $DR = 4$ prisms. Axial length is normalized by the prism length (l).	185
8.10 Pre-multiplied power spectral density of streamwise (E_u) velocity fluctuations near the leading-edge at $(0.5, 1.3, 0)$ for (a) $DR = 1$ and (b) $DR = 4$	186
8.11 Contours of the real part of DMD mode for streamwise component, corresponding to (a,c) shear-layer and (b,d) Kelvin-Helmholtz instability for (a,b) $DR = 1$ and (c,d) $DR = 4$ prism at $Re = 2.5 \times 10^3$	187
8.12 Contours of spanwise vorticity (ω_z^*) overlapped with critical streamline representing Recirculating region, at $Re = 2.5 \times 10^3$ for $DR = 4$ prism.	189
8.13 Trends of (a) pressure and (b) root-mean-squared velocity fluctuations (u'_{rms} , v'_{rms} , w'_{rms}) along the recirculating region for $DR = 4$ prism at $Re = 2.5 \times 10^3$. γ' represents the normalized curvilinear coordinate length.	190
8.14 Trends of (a) turbulence-mean-shear interaction (TMI) and (b) turbulence-turbulence interaction (TTI) along the recirculating region. γ' represents the normalized curvilinear coordinate length.	191

8.15 Trends of (a) turbulence kinetic energy production (P_k), (b) turbulent dissipation (ε_k) and (c) convection (C_k) along the recirculating region. γ' represents the normalized curvilinear coordinate length. Quantities are normalized by the free-stream velocity and prism width.	193
8.16 (a) Pre-multiplied power spectral density of streamwise velocity fluctuations (E_u) in SR, at $(x, y, z) = (0.5d, 1.05d, 0)$, and (b) probability density function of mean streamwise velocity (\bar{u}) along the secondary recirculation region.	195
8.17 (a) Streamwise velocity fluctuation (u') showing feedback near SR region; and (b) Contours of the real part of DMD mode for streamwise component corresponding to feedback frequency (St_{fb}), for $DR = 4$ prism at $Re = 2.5 \times 10^3$	195
8.18 Contours of spanwise vorticity (ω_z^*) overlapped with critical streamline representing the path following free shear-layer, at $Re = 2.5 \times 10^3$ for $DR = 4$ prism.	196
8.19 Trends of (a) pressure and (b) root-mean-squared velocity fluctuations (u'_{rms} , v'_{rms} , w'_{rms}) along the path following free shear-layer for $DR = 4$ prism at $Re = 2.5 \times 10^3$. γ' represents the normalized curvilinear coordinate length.	196
8.20 Trends of (a) turbulence-mean-shear interaction (TMI) and (b) turbulence-turbulence interaction (TTI) along the path following free shear-layer. γ' represents the normalized curvilinear coordinate length.	197
8.21 Trends of (a) turbulence kinetic energy production (P_k), (b) turbulent dissipation (ε_k) and (c) convection (C_k) along the recirculating region for (\square) $Re = 5 \times 10^3$ and (\circ) 1×10^4 . γ' represents the normalized curvilinear coordinate length. P_k and C_k are normalized by the free-stream velocity and prism width.	198
8.22 Probability density function of mean streamwise velocity (\bar{u}) along the secondary recirculation region for (a) $Re = 5 \times 10^3$ and (b) 1×10^4 . Dashed line represents the mean streamwise velocity.	198

LIST OF ABBREVIATIONS, SYMBOLS, AND NOMENCLATURE

Latin Symbols

AR	Aspect-ratio
DR	Depth-ratio
l	Prism length
d	Prism width
h	Prism height
L	Domain length
L_u	Domain upstream length
L_d	Domain downstream length
W	Domain width
H	Domain height
Re	Reynolds number
k	turbulence kinetic energy
U_b	free-stream or bulk velocity
t	time
u	Cartesian streamwise velocity component
v	Cartesian normal velocity component
w	Cartesian spanwise velocity component
p	pressure
p_∞	free-stream pressure
x_i	Cartesian coordinate spatial identifier
u_i	Cartesian velocity component identifier
C_d	Coefficient of Drag

C_l	Coefficient of Lift
C_p	Coefficient of Pressure
F_d	Drag force
F_l	Lift/normal force
F_s	Side force
f	frequency
St	Strouhal Number
St_{kh}	Strouhal Number for Kelvin-Helmholtz Instability
St_{sh}	Strouhal Number for large-scale vortex shedding
c_s	Sub-grid scale coefficient
n	Normal vector
x, y, z	Coordinates of Cartesian frame
A	Mapping coefficient/Surface-area
y_{\max}^+	Maximum non-dimensional wall-distance
N_{total}	Total number of elements
Q	Vortex-identification criterion

Greek Symbols

δ_o	Boundary layer thickness
Δ	Grid size
Δt	Time-step
$\Delta x, \Delta y, \Delta z$	Grid size in x, y, and z direction
ε	Turbulent kinetic energy dissipation rate
ω	Turbulence specific dissipation rate
τ	Stress tensor

τ_w	Wall Shear Stress
η	Kolmogorov length scale
ρ	density
μ	dynamic viscosity
ν	kinematic viscosity
Γ	Circulation
λ_2	Vortex-identification criterion
σ_i	Standard deviation

Other Symbols

∇	Gradient operator
$\overline{\square}$	Mean (time-averaged)
∂	Partial derivative
$\square \cdot \square$	Dot product
\approx	Approximately
$[]^T$	Transpose
$O[]$	Order of
$()_{rms}$	Root-mean-squared value
$()'$	Flutuating quantity

Abbreviations

2D	Two-Dimensional
3D	Three-Dimensional
CFD	Computational Fluid Dynamics

FVM	Finite Volume Method
DNS	Direct Numerical Simulation
LES	Large Eddy Simulation
DES	Detached Eddy Simulation
RANS	Reynolds Averaged Navier Stokes
SST	Shear Stress Transport
PIV	Particle Image Velocimetry
LDA	Laser Doppler Anemometry
CFL	Courant-Friedrichs-Levy Number
SIMPLE	Semi-Implicit Method for Pressure Linked Equations
PISO	Pressure Implicit with Splitting of Operators
PIMPLE	Combination of PISO and SIMPLE

Chapter 1

INTRODUCTION

This dissertation numerically investigates the flow physics and fundamental wake dynamics behind finite, wall-mounted prisms with different depth-ratios (or streamwise-length) at low to moderate Reynolds numbers. Particularly, this work looks at vortex interaction mechanisms, and wake evolution, due to both geometrical and flow dynamics. It aims to expand the fundamental understanding of wake transition and interaction mechanisms, and flow instabilities associated with free-end effects in wall-mounted prisms. The inherently unsteady nature of interactions in the wake of prisms favors high fidelity numerical simulations, which provide deeper insight into velocity and pressure fields over a wide spatial domain. As such, this dissertation utilizes Computational Fluid Dynamics (CFD) as a tool to investigate the complex wake dynamics behind finite prisms.

1.1 Overview

Since development of the boundary layer theory by Ludwig Prandtl in 1904 (Schlichting and Gersten, 2016), there has been extensive research in the field of separated flows to characterize (Bradshaw and Wong, 1972; Kim et al., 1980; Balachandar, 1990), model (Launder and Spalding, 1983; Johnson and King, 1985; Wilcox et al., 1998; Menter et al., 2003) and scale (Roache, 1982; Zagarola and Smits, 1998) various dynamic behaviors. The phenomenon of

flow separation is commonly encountered in both internal (Simpson, 1989) and external flows (Von Kármán, 1963; Hemmati et al., 2018a). It is a subject of particular relevance to numerous practical engineering applications such as aerodynamics of aircraft wings (Ravindran, 1999; Gursul et al., 2014) and turbines (Lin et al., 1991; Corten, 2001), flow around buildings (Paterson and Apelt, 1989; Baskaran and Kashef, 1996), flow over vehicles (Dominy, 1992; Hucho and Sovran, 1993; Katz, 2006; Choi et al., 2014), underwater locomotion (Verma and Hemmati, 2020), pipe flows (Shah et al., 2012; Yamagata et al., 2014; Dutta et al., 2016; Goswami and Hemmati, 2021a,b) and channel flows (Kim et al., 2001). Particularly, these applications demand better understanding of pressure losses, added turbulence, heat and mass transfer, and reduced rates of erosion and corrosion.

Dynamics of flow separation due to abrupt changes in surface conditions, such as the presence of an obstacle, is particularly important in studies related to the flow over prisms. Turbulent flow around wall-mounted prisms, or step change in the flow, represents a class of perturbed or non-equilibrium flow, the behavior of which is typically complex (Smits et al., 1979; Wang et al., 2006; Wang and Zhou, 2009; Smits et al., 2019a). Abrupt surface variations, especially in the presence of a prism, creates a contraction in the flow, which leads to an overshoot in flow characteristics, such as the formation of larger pressure gradients and higher Reynolds shear stresses, in the vicinity of the prism. It also results in the formation and interactions of various flow structures in the wake. Moreover, the flow past wall-mounted prisms constitutes a classic problem in fluid mechanics. Contrary to aerodynamic bodies at low angles of attack, sharp-edged bodies such as prisms and flat plates have an extended flow region of velocity deficit behind them referred to as the *wake* (Von Kármán, 1963). The topology or organization of the wake is dictated by both the transient and time-averaged (mean) nature of the vortex formations and their interactions. The wake of wall-mounted prisms is typically complex and highly three-dimensional due to various end-effects, including the free-end and junction flows (Wang and Zhou, 2009). The flow response to wall-mounted obstacles have thus motivated extended research in the field of separated flow, such as flow over prisms (Martinuzzi and Tropea, 1993; Hussein and Martinuzzi,

1996; Wang et al., 2014; Wang and Lam, 2019a), and internal flow around surface-attached prism (Smits et al., 1979; Durst and Wang, 1989; Yamagata et al., 2014; Smits et al., 2019a).

Turbulent shear flows, such as those encountered in the wake of prisms, are characterized by the presence of spatially coherent, temporally evolving vortical motions called coherent structures. These are responsible for the transport of momentum and energy in the flow (Jeong and Hussain, 1995). As such, wake flows have been described and investigated in terms of coherent vortical structures since the pioneering work of Von Karman (1911), Fage and Johansen (1927), and Roshko (1961). Since then, a great deal of work has been done in the field of identifying coherent structures (Jeong and Hussain, 1995), and qualitatively understanding them in shear flows (Hussain, 1983, 1986). However, due to inherent subjectivity in the identification of these structures, quantitative analysis and dynamical characterization of coherent structures in turbulent flows remain a challenging task. Such wakes are characterized by the presence of large-scale coherent structures (Roshko, 1961). Interactions between coherent structures are of particular interest in the study of wakes, as they play a crucial role in determining the flow characteristics and forces acting on the body. To this end, there have been many studies to understand the flow past circular cylinders (Roshko, 1961; Williamson, 1988; Okamoto and Sunabashiri, 1992; Williamson, 1996), rectangular prisms (Okajima, 1982; Lyn et al., 1995; Wang and Zhou, 2009), flat disks (Marshall and Stanton, 1931; Berger et al., 1990; Cannon et al., 1993; Zhong et al., 2011), and wall-mounted prisms (Sakamoto and Arie, 1983; Okamoto and Sunabashiri, 1992; Martinuzzi and Tropea, 1993; Martinuzzi and Havel, 2000; Wang and Zhou, 2009).

Coherent vortical structures in the wake of prisms are significantly affected by flow parameters, such as Reynolds number (Hwang and Yang, 2004; Zhang et al., 2017) and boundary layer thickness (Hosseini et al., 2013; El Hassan et al., 2015), and geometrical parameters, including aspect-ratio (height-to-width) (Wang et al., 2006; Wang and Zhou, 2009; Saha, 2013), incident (yaw) angle (Zargar et al., 2021a), cross-sectional shape (Kindree et al., 2018), and depth-ratio (length-to-width) (Rastan et al., 2021; Zargar et al., 2022b). Many studies have

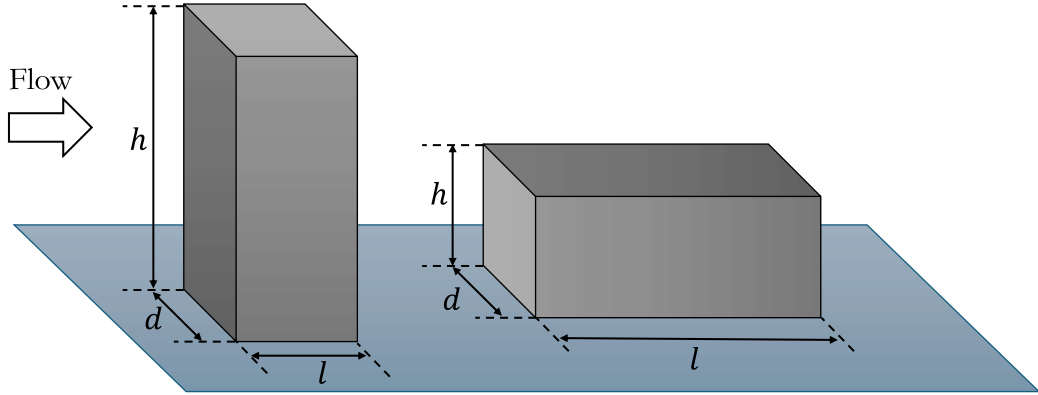


Figure 1.1: Schematics of large aspect-ratio (Left) and large depth-ratio (Right) prisms.

focused on the implications of aspect-ratio and Reynolds number in characterizing large-scale vortical structures in the wake of wall-mounted finite prisms. Contrary to square prisms or circular cylinders with large aspect-ratio, there have not been many studies exploring how depth-ratio (length-to-width) of prisms dictate their wake behavior. In brief, increasing the depth-ratio has resulted in changes of global flow features, such as lowering Strouhal number (St_{sh}) and mean drag coefficient ($\overline{C_d}$) (Mashhadi et al., 2021). The wake dynamics of large depth-ratio prisms differed from that of finite wall-mounted square prisms due to flow separation-reattachment on surfaces of the prism influencing the downstream wake (Wang and Zhou, 2009). Joubert et al. (2015) investigated the wake of a wall-mounted finite prism with aspect-ratio of 5 and depth-ratio of 2.63 at Reynolds number of 7.6×10^4 . Their results indicated that the flow reattaches on the prism top surface, and not on the sides, resulting in Kármán-type vortex shedding. Wang and Lam (2019b) observed similar results experimentally, and further reported that the prism depth-ratio did not influence its wake dynamics at high Reynolds number, as long as flow reattachment did not occur on the prism side surfaces. Evolution of coherent vortex structures with varying aspect-ratio confirmed the importance of geometrical parameters in defining the wake topology (Wang and Zhou, 2009; Saha, 2013; Joubert et al., 2015; Rastan et al., 2017). As such, further investigations are needed to understand the influence of geometry on the wake dynamics behind wall-mounted prisms.

This dissertation focuses on evaluating the influence of flow and geometric parameters on wake mechanisms and vortex development behind wall-mounted prisms. Building on the foundational work of Zargar et al. (2022b), which provided critical insights into wake dynamics and vortex interactions for specific geometric configurations at low Reynolds number, this research expands the scope to systematically investigate the effects of depth-ratio on the wake development, evolution and interactions at low and moderate Reynolds numbers. In particular, this study explores how such geometric variations influence vortex dynamics, wake structures, and their interactions in the wake of finite prisms over a broader range of depth-ratios. Furthermore, the corresponding dependence of depth-ratio on the aforementioned critical parameters, including its role in modulating wake mechanisms and vortex development, remains relatively unexplored, making this an important contribution to the field. Here, depth-ratio is defined as the ratio of streamwise length (l) of the prism to its width (d), given by $DR = l/d$. Aspect-ratio is defined as the ratio of height (h) to width (d) of the prism, given by $AR = h/d$. Schematics of a prism with large aspect-ratio and a large depth-ratio is shown in Figure 1.1. Depth-ratio in this study is varied from 1 to 4, and a finite aspect-ratio range is considered between 0.25 and 1.5. A range of Reynolds numbers between 5×10^1 and 1×10^4 are considered for this dissertation. This range corresponds to low and moderate Reynolds number regime, which is associated with the onset of complex flow phenomena for wall-mounted long prisms (Zargar et al., 2022b), including transition to turbulence in the wake which significantly influences the wake dynamics and aerodynamic forces. Reynolds numbers between $5 \times 10^1 - 1.5 \times 10^3$ are considered as low Reynolds number regime (Rastan et al., 2017; Zargar et al., 2021b, 2022b), and Reynolds numbers between $1.5 \times 10^3 - 1 \times 10^4$ are considered as moderate Reynolds number regime (Sattari et al., 2012; Hosseini et al., 2013; Zargar et al., 2022b). This distinction is made based on the flow characteristics and the onset of turbulence in the wake of wall-mounted prisms (Martinuzzi, 2008; Hemmati et al., 2016; Zargar et al., 2022b). Understanding these phenomena is crucial for applications involving wall-mounted prisms, as they can significantly influence the wake dynamics and, consequently, the aerodynamic forces.

and structural response (Martinuzzi, 2008; Hemmati et al., 2016; Zargar et al., 2022b). As such it is important to investigate and characterize the wake of wall-mounted prisms in this regime.

Wake of wall-mounted finite prisms is dominated by end-effects, especially an induced downward-directed local velocity field, referred to as downwash flow (Sumner et al., 2017), which makes the wake highly three-dimensional. Free-end downwash flow is induced by the tip vortex, generated due to shear-layer separation at the free end of the prism. Vortex shedding behind wall-mounted prisms is strongly dictated by the downwash flow and the interactions between the tip vortex and the shear-layer roll-up at the leading edge of the prism (Saha, 2013; Rastan et al., 2017). The intensity of interaction engenders the formation of large-scale coherent structures, such as hairpin-like vortices, which play a crucial role in momentum transfer and mixing processes in the wake (Wang and Zhou, 2009; Tenaud et al., 2016). As such, the fundamental study of the influence of downwash flow and mixing in the wake of wall-mounted prisms is crucial for engineering applications related to wind-loading in buildings (Sousa et al., 2018) and pollutant dispersion from chimney stacks (Jiang and Yoshie, 2020). This dissertation also studies a special case of flow past wall-mounted thin prism, which represents a case of very small depth-ratio prism. Computationally, the flow past thin prism is investigated by using the streamwise length of the smallest grid as the thickness of the plate. As such, a single grid point across the plate length fixes the flow separation at the leading-edge of the prism without possibility of flow reattachment on the surfaces. This results in a flow topology that is significantly different from that of a finite, long prism (Chan et al., 2022).

1.2 Motivations and Objectives

Understanding the flow dynamics around wall-mounted prisms has been central to research investigations in the past (Taneda, 1952; Schofield and Logan, 1990; Martinuzzi and Havel, 2000; Farhadi and Rahnama, 2006; Wang and Zhou, 2009; Saha, 2013; Wang and Lam, 2019b; Yin et al., 2020). Considerable effort has been made to understand various flow phenomena in this

field, including flow separation (Dimaczek et al., 1989; Jovic and Driver, 1995), separation bubbles (Kiya and Sasaki, 1983; Mollicone et al., 2017), reattachment of separated shear layers (Bradshaw and Wong, 1972; Kim et al., 1980), and flow recovery (Smits et al., 1979; Simpson, 1989). Additionally, extensive literature exists on the effects of aspect-ratio (Sakamoto and Arie, 1983; Saha et al., 2000; Wang et al., 2006; Wang and Zhou, 2009; Saha, 2013) and Reynolds number (Zhou et al., 2002; Yauwenas et al., 2019; Wang and Lam, 2019b) in characterizing the large-scale vortical structures behind wall-mounted prisms. Previous studies on the evolution of vortex structures with varying aspect-ratios underscore the significance of geometrical parameters in defining wake topology. However, while extensive research has been conducted on aspect-ratio, there is a notable gap in comprehensive studies addressing the influence of depth-ratio on wake mechanisms and vortex development behind wall-mounted prisms. *The primary aim of this thesis is to identify and characterize the mechanisms of flow transitions and vortex interactions, towards better understanding the wake evolution and dynamics.* To achieve this, the following objectives are set:

(A) **First objective of this dissertation is to classify the mean and instantaneous wake topology as a multivariate function of depth-ratio and Reynolds number.** The large-scale vortical structures in the wake of wall-mounted prisms are influenced by multiple critical parameters (Yauwenas et al., 2019). For example, studies have demonstrated that time-averaged (mean) wake topology of wall-mounted prisms transitions from quadrupole to dipole with increasing Reynolds number (Zhang et al., 2017). Moreover, both aspect-ratio and depth-ratio significantly influence the instantaneous wake topology (Wang and Zhou, 2009; Rastan et al., 2021). Aspect-ratio also affects the onset of unsteady wake features, leading to symmetric hairpin-like vortex shedding at low Reynolds numbers (Saha, 2013) and antisymmetric or irregular unsteady shedding at moderate to high Reynolds numbers (Zhang et al., 2017; Rastan et al., 2021; Zargar et al., 2022b). These findings highlight the multivariate impact of aspect-ratio and Reynolds number on characterizing wake dynamics behind wall-mounted prisms. Recent numerical studies by Mashhadi et al. (2021) confirmed this multivariate influence on vortex

evolution in infinite-span prisms with varying depth-ratios. They emphasized the role of shear-layer separation in shaping downstream wake topology, which is affected by variations in both depth-ratio and Reynolds number. Thus, classifying the mean and instantaneous wake topology as a multivariate function of depth-ratio and Reynolds number is essential for understanding the wake dynamics behind wall-mounted prisms.

(B) Second objective of this thesis is to identify and characterize the mechanisms of interaction between secondary vortex structures and leading-edge shear-layer roll-up at low-to-moderate Reynolds numbers. Wake features are another critical aspect of the flow around wall-mounted prisms. These features include secondary vortex structures that appear alongside coherent structures, such as arch-type, Kármán-type, or hairpin-like vortex shedding. Interactions between these secondary vortex structures and the shear layer at the leading edge of the prism are particularly significant for understanding prism wakes, as they influence downstream wake topology. Thus, identifying and characterizing the mechanisms of interaction between secondary vortex structures and leading-edge shear-layer roll-up at low-to-moderate Reynolds numbers is essential for understanding the wake dynamics behind wall-mounted prisms. Specifically, unsteady wake features characterized by symmetric shedding of hairpin-like vortices behind small aspect-ratio prisms (e.g., cubes) manifest at relatively low Reynolds numbers (Diaz-Daniel et al., 2017b). However, varying the depth-ratio can delay or accelerate the onset of unsteady and irregular wake features at low Reynolds numbers.

(C) Third objective of this thesis is to characterize the role of depth-ratio in driving interactions between Kelvin-Helmholtz instability and hairpin-like vortices at low-to-moderate Reynolds numbers. The formation and evolution of Kelvin-Helmholtz instability (KHI) and its interactions with hairpin-like vortices around wall-mounted prisms remain poorly understood. KHI rollers originate from the leading-edge shear layer and are characterized by high-frequency signatures (St_{kh}). These rollers significantly influence the pressure distribution on the prism surfaces and contribute to the formation of downstream wake

structures, such as hairpin-like vortices (Tenaud et al., 2016). These hairpin-like structures are recognized as large-scale coherent structures that play a crucial role in momentum transfer and mixing processes, exhibiting comparatively low-frequency signatures (St_{sh}). Moreover, characteristics of the interactions between Kelvin-Helmholtz instability and hairpin-like vortices vary depending on the length of the prism (depth-ratio, DR, in the present study). In this context, Reynolds number is critical in determining the intensity of these interactions. Lander et al. (2018) proposed a scaling relationship ($St_{kh}/St_{sh} = 0.18 \times Re^{0.6}$) that equates the frequency of Kelvin-Helmholtz instability to that of hairpin-like vortices. More recently, Kumahor and Tachie (2023) demonstrated that these interactions are strongly influenced by the streamwise length (or depth-ratio) of the infinite-span prism. These findings underscore the significance of geometric factors in shaping the interactions between Kelvin-Helmholtz instability and hairpin-like vortices. Thus, understanding the mechanisms of interactions between KHI and large-scale vortex shedding at low-to-moderate Reynolds numbers forms a critical aspect of this study.

(D) Fourth objective of this thesis is to identify the mechanism of destabilization of the leading-edge shear-layer at moderate Reynolds numbers. Influence of depth-ratio on global unsteadiness and interactions between KHI and large-scale vortex shedding have been reported for infinite-span suspended prisms (Zhang et al., 2023). However, these interactions significantly differ compared to the case of wall-mounted prisms, mainly due to the infinite-span nature of the prisms, where the wake is bounded by free-end effects (Wang and Zhou, 2009). Thus, in the context of wall-mounted prisms, interactions between KHI and large-scale vortex shedding, influenced by depth-ratio and free-end effects, have not been quantified in the past literature. Specifically, this study investigates the possibility of enhanced momentum transport with increasing depth-ratio as a precursor to wake transition. Further, this study aims to identify and characterize the mechanism of shear-layer destabilization, which leads to enhanced wake irregularity at moderate Reynolds numbers. The implications of shear-layer flapping-like motion are explored for long prism, and the mechanism of interactions are evaluated.

1.3 Novelty

Novelty of this study is multifold and belongs to the field of wake dynamics and vortex interactions behind wall-mounted prisms. They are summarized below:

1. **Influence of Depth-ratio on wake topology:** The influence of depth-ratio on wake topology of wall-mounted prisms has not been comprehensively studied in the past literature. This study is the first to classify the mean and instantaneous wake topology as a multivariate function of depth-ratio and Reynolds number. *Identification and characterization of the transition in the mean and instantaneous wake topology and the associated mechanism for wall-mounted bluff bodies as a multivariate function constitutes a novel contribution.*
2. **Secondary vortex interactions:** Interactions between secondary vortex structures and leading-edge shear-layer vortex shedding at low-to-moderate Reynolds numbers have not been studied in the past literature. This study is the first to identify and characterize the mechanisms of interaction between secondary vortex structures and leading-edge shear-layer at low-to-moderate Reynolds numbers. Further, *the role of secondary vortex structures in the formation of asymmetric hairpin-like vortices, as well as identification of the origins of wake asymmetry at low Reynolds numbers, is a novel contribution to the field of bluff-body wake.*
3. **Kelvin-Helmholtz instability interactions:** Interactions between Kelvin-Helmholtz instability and hairpin-like vortices around wall-mounted prisms have not been studied in the past literature. This study is the first to characterize the role of depth-ratio in the interactions between Kelvin-Helmholtz instability and hairpin-like vortices at low-to-moderate Reynolds numbers. *Understanding the wake transition mechanism, and vortex interactions influenced by end-effects at a moderate Reynolds number constitutes a major contribution to the field of unsteady wakes.*
4. **Free-end vortex interactions:** The mechanism of interactions between leading-edge shear-layer and free-end vortex at moderate Reynolds numbers, which results in enhanced wake irregularity, has not been quantified in the past literature. *This study is the first to identify the*

mechanism of interactions between leading-edge shear-layer and free-end vortex at moderate Reynolds numbers, which results in enhanced wake irregularity.

1.4 Structure of the thesis

This dissertation begins with a comprehensive review of the literature in Chapter 2. The background review covers fundamental concepts of bluff body wake, including flow separation, reattachment, and vortex shedding, as well as the influence of geometrical and flow parameters on the wake dynamics of wall-mounted prisms and cylinders. The review also discusses the state-of-the-art numerical and experimental studies on wake of prisms, focusing on the influence of aspect-ratio and Reynolds number. The review highlights the gaps in the literature and motivates the need for a detailed study on the influence of depth-ratio on wake dynamics behind wall-mounted prisms. This is followed by a detailed description of the numerical simulation setup, including the computational domain, boundary conditions, and numerical methods used in this study, in Chapter 3. Verification and validation analysis of the numerical simulations are also included, which provides sufficient confidence in the numerical setup used for assessing the complex wake dynamics of wall-mounted prisms with varying depth-ratios.

Chapter 4 describes the wake of wall-mounted prisms with small aspect-ratio and changing depth-ratios at low Reynolds numbers ($5 \times 10^1 - 5 \times 10^2$). The mechanism of asymmetric shedding patterns is evaluated in this chapter, in order to identify the origins of wake asymmetry. Furthermore, the role of secondary vortex structures in the formation of asymmetric hairpin-like vortices is established here. Further, Chapter 5 characterizes the time-averaged (mean) wake of wall-mounted prisms using the same parameter space as Chapter 4. The transitions in mean wake topology are evaluated as a multivariate function of Reynolds number and depth-ratio. Moreover, it identifies and characterizes the transition in the mean wake topology and the associated mechanism for wall-mounted prisms as a multivariate function of depth-ratio and Reynolds number. Collectively, Chapters 4 and 5 provide a comprehensive understanding of the wake

dynamics behind wall-mounted prisms with varying depth-ratios at low Reynolds numbers and address Objectives A and B of this thesis highlighted in Section 1.2.

Chapter 6 evaluates the influence of moderate range of Reynolds number ($1 \times 10^3 - 2.5 \times 10^3$) on the wake dynamics behind wall-mounted prisms. This chapter focuses on the formation and evolution of Kelvin-Helmholtz instability and its interactions with coherent wake structures, such as hairpin-like vortices. Additionally, it explores how the depth-ratio influences surface pressure distribution and the origin of pressure fluctuations, expanding the analysis into a regime where turbulence transition plays a pivotal role in shaping the flow dynamics. This chapter addresses the Objective C of this thesis highlighted in Section 1.2.

Chapter 7 presents a numerical study of the turbulence transition in the wake of wall-mounted prisms at moderate Reynolds numbers ($1 \times 10^3 - 5 \times 10^3$). While earlier chapters demonstrated the influence of depth-ratio on wake dynamics at lower Reynolds numbers, this chapter extends that investigation into moderate Reynolds numbers, introducing the added complexity of turbulence transition and intensified vortex interactions. This chapter further investigates the mechanism of interactions between leading-edge shear-layer and free-end vortex at moderate Reynolds numbers, which results in enhanced wake irregularity. The implications of shear-layer flapping-like motion are explored for long prism, and the mechanism of interactions are evaluated. Further, Chapter 8 investigates the mechanisms driving the destabilization of leading-edge shear layer in the wake of wall-mounted long prisms, focusing on flow topology and onset of Kelvin-Helmholtz instability. The focus of this chapter is on the onset of Kelvin-Helmholtz instability, which amplifies flow irregularity and modulates spanwise vortex structures, contributing to the destabilization process. Moreover, the mechanism of upstream energy transfer from the secondary recirculation region to the leading-edge shear layer is studied to address the influence of depth-ratio on vortex interactions at moderate Reynolds numbers. Collectively, Chapters 7 and 8 provide a comprehensive understanding of the mechanisms of interactions between leading-edge shear-layer and free-end vortices at moderate Reynolds numbers, and address Objectives C and D of this thesis highlighted in Section 1.2.

Chapter 9 summarizes the key findings of this dissertation and provides a comprehensive discussion on the influence of depth-ratio on wake dynamics behind wall-mounted prisms. The chapter also highlights the contributions of this study to the field of prism wake. Finally, Chapter 10 outlines potential future research directions and opportunities for further investigation in the field of prism wakes.

Chapter 2

BACKGROUND

Separated flow is a fundamental phenomenon in fluid dynamics that occurs when the flow around a body or surface detaches due to adverse pressure gradients or changes in geometry (Schlichting and Gersten, 2016). The separation of flow is particularly common in flows around bluff bodies such as circular cylinders, rectangular prisms, and flat plates, where the streamlined flow cannot maintain attachment to the surface, resulting in large-scale wake formation behind the body (Derakhshandeh and Alam, 2019). These wake regions are characterized by flow deceleration and increased vorticity, leading to fluctuating flow patterns and the formation of large-scale vortices. As the flow separates, it creates a low-pressure recirculation zone behind the body, and in many cases, this recirculation is accompanied by alternating vortex shedding, known as von Kármán vortex street (Von Kármán, 1963). The interaction of these vortices is a major source of turbulence in wakes, contributing to energy dissipation, mixing, and generation of unsteady forces on the body.

Turbulence plays a crucial role in both the development and evolution of separated flows and wakes. When flow separates from the surface, it becomes highly unstable. This leads to the breakdown of an orderly laminar flow to an irregular and unsteady flow (Pope, 2001). In the wake region, turbulence is dominated by large-scale coherent structures, which are responsible for much of the momentum transfer, mixing, and energy dissipation (More et al., 2015). Irregular

vortex shedding from the sides of prisms, for example, is a key feature of turbulent wake dynamics, and it significantly influences the pressure distribution and forces. Further, the formation of separated flow regions marks the onset of complex flow structures and unsteady flow behavior, directly influencing drag, lift, and the production of turbulence.

Since wakes are an amalgamation of such complexities, flow past prisms constitutes a classic problem in fluid mechanics. Thus, it has been studied extensively over the past century. This chapter provides a comprehensive literature review on bluff body wakes, focusing on the flow past prisms, flat plates, and circular cylinders. The chapter is divided into three main sections: Section 2.1 provides an overview of the flow around bluff bodies, discussing the wake topology and key features of wakes. This is followed by a detailed discussion of the wake behind wall-mounted prisms in Section 2.2, which includes a review of the mean and instantaneous wake topology, such as vortex shedding and flow transition. This is followed by a brief review of the wake behind suspended prisms and cylinders in Section 2.3, focusing on differences between wall-mounted and suspended prisms. This is followed by a brief discussion of the wake behind flat plates in Section 2.3.2, which represent a special case of a very thin prism. Section 2.3.3 provides an overview of the wake behind circular cylinders, focusing on the flow topology and key features of such wakes. Section 2.4 discusses approaches and tools for studying prism wakes, including experimental and numerical techniques, and provides an overview of OpenFOAM, which is a numerical tool utilized in this thesis to study the wake of prisms.

2.1 Flow around bluff bodies

Placing an object in an incoming flow creates a region of disturbed flow behind it. Extent of this disturbance is strongly influenced by the shape of the object and flow conditions. For example, a streamlined body with a small incidence angle, such as an airfoil or wing, generates a relatively small wake region. In contrast, bluff bodies, like circular cylinders or rectangular prisms, produce larger regions of disturbed flow characterized by complex and unsteady structures. At the leading-

edge of a sharp-edged bluff body, such as a prism, the flow slows down and forms a boundary layer along its surfaces. This boundary layer eventually separates due to adverse pressure gradients or geometric changes, resulting in free shear layers and what is referred to as the *wake* (Zdravkovich, 1997).

Formation of large-scale coherent (organized) structures depends on the state of the flow, i.e., laminar, transitional, or turbulent. In laminar flows, the wake is characterized by regular and ordered structures, while turbulent wakes are irregular and unsteady. Transition from laminar to turbulent flow is a complex process that depends on Reynolds number, geometrical properties of the body, and flow dynamics. Further, transition may occur in three key regions: the wake, shear-layers bordering the wake, and boundary layers on the body (Schlichting and Gersten, 2016). Transition to turbulence depends on Reynolds number. However, other parameters such as shape of the body and free-end effects (in case of finite bluff bodies) also affect the flow transition (Zdravkovich, 1997). The wake transition occurs at low Reynolds numbers, in order of a few hundreds (Williamson, 1996), and thus for most practical applications, the flow around bluff bodies is turbulent. In case of sharp edged prisms, transition to turbulence in shear layers occurs rapidly due to the flow separation at leading edges, and the wake becomes fully turbulent (Martinuzzi, 2008). Large-scale coherent structures account for a significant portion of the overall turbulent kinetic energy budget (Pope, 2001). These structures are coherent, meaning they are organized, continuous regions of spatially correlated fluid motion. Further, this definition implies that coherent structures are recurring, periodically or quasi-periodically, and their scales are larger than the inertial sub-range (Kolmogorov micro scales). Energy transfer from large to small (Kolmogorov) scales follows a cascade (Wilcox et al., 1998).

Two key features of prism wakes are flow separation at the leading-edges and the formation of large-scale coherent structures. Organization of large-scale coherent structures behind the bluff body is referred to as *wake topology*. This topology depends on shape of the body and the flow conditions. For example, wake of circular cylinder is characterized by the formation of von Kármán vortex street, which consists of alternating vortices shed from either sides of the

cylinder (Von Kármán, 1963). In contrast, wake of wall-mounted prisms are characterized by complex interactions of free-end and junction vortices, which are responsible for the momentum transfer and energy dissipation in the wake region (Wang et al., 2006). The wake topology is significant because it directly influences drag, lift, and unsteady forces acting on the body. Further it is used to classify different types of bluff bodies, based on their flow characteristics.

Another important feature of the flow past bluff bodies is the formation of recirculation region or “dead zones” behind it. In these recirculation regions, the flow moves in the reverse direction relative to the free-stream, and it is characterized by low velocity and high vorticity (Moreau, 2013). The formation of recirculation regions is important because it directly influences drag and lift acting on the body. For example, drag is directly proportional to the size of the recirculation region, and it is inversely proportional to the velocity of the flow in the recirculation region (Zdravkovich, 1997). Further, large *pressure drag* is due to the formation of recirculation regions and the induced pressure difference between the front (high pressure) and rear (low pressure) parts of the body.

2.2 Wake of wall-mounted rectangular prisms

The wake of wall-mounted finite rectangular prisms is dominated by end effects, especially an induced downwash flow (Sumner et al., 2017). Thus, the wake three-dimensionality becomes more profound compared to those of infinite span (Mashhadi et al., 2021) and two-dimensional prisms (Park et al., 2013). Moreover, they retain quasi periodic vortex shedding for small aspect-ratio prisms and pyramids (Sakamoto and Arie, 1983; Martinuzzi and Tropea, 1993; Martinuzzi and AbuOmar, 2003; Martinuzzi, 2008). The wake features for a wall-mounted finite prism can be divided into three components: free-end downwash, wall-body junction upwash, and free shear flow (Wang and Zhou, 2009). These end effects result in flow complexities and vortex shedding patterns. Free-end downwash flow is induced by tip vortices generated due to the shear layer separation at the free-end, while wall-body junction upwash flow is induced by the generation

of counter-rotating base vortices at the wall-body junction (Wang et al., 2006). Induced upwash and downwash effects entrain the flow into mid-span of the prism, resulting in the generation of mid-span coherent structures. Thus, the wake becomes highly three-dimensional. Further, wall-body junction induces a shear-layer roll-up in front of the body, which results in the formation of a horseshoe vortex at the base that is generally associated with downward flow (Simpson, 2001). Vortical structures in the wake of such bodies are significantly affected by flow parameters, such as Reynolds number (Hwang and Yang, 2004; Zhang et al., 2017), boundary layer thickness (Hosseini et al., 2013; El Hassan et al., 2015), and geometrical parameters, including aspect-ratio (height-to-width) (Wang et al., 2006; Wang and Zhou, 2009; Saha, 2013), incident (yaw) angle (Zargar et al., 2021a), cross-sectional shape (Kindree et al., 2018), and depth-ratio (length-to-width) (Rastan et al., 2021; Zargar et al., 2022b).

Abundance of literature exists that focus on the effects of aspect-ratio (Sakamoto and Arie, 1983; Saha et al., 2000; Wang et al., 2006; Wang and Zhou, 2009; Saha, 2013; McClean and Sumner, 2014) and Reynolds number (Zhou et al., 2002; Yauwenas et al., 2019; Wang and Lam, 2019b) on characterizing large scale vortical structures behind wall-mounted finite prisms. Several studies on wall-mounted, finite prisms have established that changing Reynolds number does not alter the presence of main features of the wake topology, such as a horseshoe vortex, tip and base vortices, and mid-span vortex shedding (Saha et al., 2000; Krajnović and Davidson, 2005; Zhang et al., 2017), while they do alter the wake dynamics associated with such structures. To this effect, Saha et al. (2000) numerically showed that the wake of a wall-mounted finite prism at Reynolds number of 1×10^2 has negligible change compared to the wake (coherent topological components) of a two-dimensional prism at $Re = 2.14 \times 10^4$ (Lyn et al., 1995) and $Re = 1.4 \times 10^5$ (Cantwell and Coles, 1983).

Vortex shedding is suppressed at lower Reynolds numbers or smaller prism aspect-ratios. For example Zargar et al. (2021b) reported this suppression at Reynolds number of 2.5×10^2 for aspect-ratio of 1.2, which corroborated with the results of Saha (2013) for a prism with aspect-ratio of 2 at Reynolds number of 2.5×10^2 . Further, mid-span coherent structures, as well

as the cross-sectional wake topology, vary with changes in the prism aspect-ratio. Experimental study of the flow past finite circular and square wall-mounted prisms by Sakamoto and Arie (1983) in a turbulent boundary layer revealed two types of wake structures for aspect-ratios of 1 to 8. These structures were the Kármán-type and arch-type structures, which were strongly influenced by the aspect-ratio. To this effect, the arch-type structures only appeared at aspect-ratio below 2. This hints at a threshold in aspect-ratio, below which the downwash flow in the near wake region suppressed the periodic and asymmetric Kármán type vortex shedding. This process was restored for aspect-ratios above this threshold. Evolution of the vortex shedding by decreasing aspect-ratio confirmed that geometrical parameters are critical in defining the wake topology. Later, Wang and Zhou (2009) modified the earlier model of Wang et al. (2006), revealing the presence of a single arch-type structure in the near-wake region. They argued that the spanwise base and tip vortices are inherently connected to form an arch-type structure. Further, Wang and Zhou (2009) reported that arch-type structures may shed into the wake in the form of hairpin-like vortices. These structures were unique to large aspect-ratios. However, in case of small aspect-ratio prisms (e.g., a cube), Hwang and Yang (2004), Yakhot et al. (2006), and Diaz-Daniel et al. (2017b) reported only hairpin-like vortices in the wake, which are usually formed at a particular range of Reynolds numbers ($Re > 5 \times 10^2$). The formation of hairpin-like structures were attributed to destabilization of the shear-layer that had separated from the top leading edge of the prism. Despite these efforts, there has not been a comprehensive study of the cylinder depth-ratio on wake mechanisms and vortex development.

Contrary to square or circular prisms with a large aspect-ratio, there have not been many studies on how the prism depth-ratio influences the wake. Majority of the research efforts in this area have focused on infinite span prisms or flat plates, which is a special case of a very thin infinite-span prism (Narasimhamurthy and Andersson, 2009; Ying et al., 2012; Ranjan and Dewan, 2016; Hemmati et al., 2018b). Variations in depth-ratio resulted in changes in the global aerodynamic features, such as the mean drag coefficient ($\overline{C_d}$) and shedding frequency (St_{sh}) (Mashhadi et al., 2021). Increasing the prism depth-ratio led to a lower St_{sh} and $\overline{C_d}$. The wake dynamics of large

depth-ratio prisms differs from that of finite square prism due to the flow reattachment-separation on the prism free-surfaces that influence the wake (Wang and Zhou, 2009). Below, we look at a handful of studies focused on the effect of depth-ratio on the wake of rectangular prisms.

One of the first prominent studies on effects of depth-ratio was performed by Zargar et al. (2021b), numerically analyzing the wake of small aspect-ratio prisms (~ 1.2). They reported a steady wake between Reynolds numbers of 5×10^1 and 2.5×10^2 across a range of depth-ratios between 0.83 and 3. Further, Zargar et al. (2021b) observed dominant downwash flow with increasing depth-ratio, which resulted in dipole-type mean wake topology for large depth-ratio prisms. Rastan et al. (2021) performed a similar investigation, numerically and experimentally, on a prism with aspect-ratio 7 and varying depth-ratios (1 – 4) at Reynolds number of 1.2×10^4 . Their results indicated that the flow reattachment on top surfaces occurs earlier than side surfaces ($DR \geq 3$). Further, increasing depth-ratio suppressed the spanwise Kármán-type vortex shedding and reduced the interaction of spanwise vortex structures with the downwash flow. Rastan et al. (2021) further noted that increasing depth-ratio led to a transition in the mean wake topology from dipole-type to no-pole type wakes, indicating weakened downwash flow that increases with depth-ratio. The differences observed in the wake evolution due to depth-ratio between Rastan et al. (2021) and Zargar et al. (2021b) stems from the high aspect-ratio of the former study, where the upwash flow remains prominent (Wang and Zhou, 2009).

An essential aspect of the flow around rectangular prisms is the separation-reattachment phenomenon. Flow separation-reattachment influenced by the depth-ratio by changing the flow reattachment process on the top and side surfaces of the prism (Rastan et al., 2021). Flow reattachment is attributed to the downwash flow due to the tip vortex, which suppresses the separation of the shear layer on the top surface. This downwash flow is more pronounced for prisms with larger depth-ratios, leading to flow reattachment on the top surface. Joubert et al. (2015) analyzed the wake of a wall-mounted finite prism with depth-ratio of 2.63 and aspect-ratio 5 at Reynolds number of 7.6×10^4 . Their results revealed that after the initial flow separation, the shear layer reattachment only occurred for the top surface and not for the side surfaces. Wang and

Lam (2019b) observed similar results, and reported that depth-ratio does not influence the mean wake structures as long as the flow separation and reattachment does not occur on the side surfaces. Moreover, sharp-edged flow separation generates turbulence due to the adverse pressure gradient at the leading-edge. Recovery of pressure persists till the flow reattachment, which enhances unsteady fluctuations in this region (Awasthi et al., 2014). As such, reattachment of the flow significantly influences the flow dynamics, specifically the pressure distribution on prism surfaces. Small and large scale vortices, especially hairpin-like vortices formed in the reattachment region, influences large pressure fluctuations near the prism (Saathoff and Melbourne, 1997). Rastan et al. (2021) observed similar pressure effects in the wake due to the downwash flow induced by the tip vortex, which is a critical factor influencing pressure fluctuations and the base pressure along the prism length. Since pressure fluctuation correlates with velocity fluctuations via Poisson's equation, investigating pressure fluctuations can offer novel insights into flow dynamics around wall-mounted prisms, particularly highlighting interactions among different flow structures. Furthermore, pressure fluctuations can be associated with interactions between Kelvin-Helmholtz and hairpin-like vortices, which are influenced by the prism depth-ratio.

Large-scale vortical structures in the wake of wall-mounted prisms are affected by more than one critical parameter (Yauwenas et al., 2019). Zhang et al. (2017) reported that the mean wake topology changes from quadrupole to dipole wake with increasing Reynolds number from 5×10^1 to 1×10^3 for a wall-mounted square prism with aspect-ratio 4. Zhang et al. (2017) observed that increasing the Reynolds number enhanced unsteady wake features, resulting in symmetric hairpin-like vortex shedding at $Re = 1.5 \times 10^2 - 2.5 \times 10^2$ and antisymmetric shedding at $Re = 5 \times 10^2 - 1 \times 10^3$. Rastan et al. (2017) observed similar results for a prism with aspect-ratio of 7, where unsteady wake features were initiated at lower ranges of Reynolds number. For the case of small aspect-ratio prism (i.e. a cube), Diaz-Daniel et al. (2017b) reported the initiation of unsteady wake at Reynolds number of 5×10^2 . These results indicate a multivariate influence of both aspect-ratio and Reynolds number in characterizing the wake dynamics of wall-mounted

prisms. Recent numerical study of Mashhadi et al. (2021) confirmed such multivariate influence on the vortex evolution for infinite-span prisms with changing depth-ratios. Mashhadi et al. (2021) further scrutinized the role of shear-layer separation in dictating the downstream wake topology, which results from varying depth-ratio and Reynolds number.

2.2.1 Mean wake topology

Topology of three-dimensional separation patterns in the wake of wall-mounted prisms can be characterized through the surface shear-stress distribution. The basis of analyzing wall shear-stress topology was first given by Lighthill (1963), who showed that the shear-stress distribution on surfaces are orthogonal to vorticity, and thus provide a direct measure of the orientation of vorticity in the wake. Further, wall shear-stress distribution can identify the point of flow separation and reattachment on the body. As such, examining the wall shear-stress reveals critical points such as nodes, foci and saddles, which are associated with the presence of vortices in the wake (Zargar et al., 2021b). This is based on the critical point theory (Perry and Fairlie, 1975), providing a framework to understand the wake topology. Thus, there are studies that have proposed different vortex skeleton models of the mean wake of prisms (Martinuzzi and Tropea, 1993; Zargar et al., 2022b). In brief, the mean wake topology of wall-mounted prisms consist of various streamwise vortices, e.g., tip, base and mid-span vortices, and shear-layer roll-up in front of the prism due to wall-body junction effects, forming the horseshoe vortex (Simpson, 1989).

Complexity of the flow around wall-mounted prisms stems from the influence of '*junction*' and '*free-end*' flows (Wang and Zhou, 2009). Junction flow refers to the formation of base vortices from the wall-body junction due to the interaction of the boundary-layer with the body, while free-end flow refers to the formation of tip vortices from the prism free-end due to adverse-pressure gradients. These typical tip and base vortices appear in time-averaged (mean) flow topology as counter-rotating streamwise vortex pairs. Moreover, tip vortex induces a downwash flow and base vortex induces an upwash flow, as showed in Figure 2.1. This entrains the flow into the mid-span of the prism, resulting in the formation of mid-span coherent

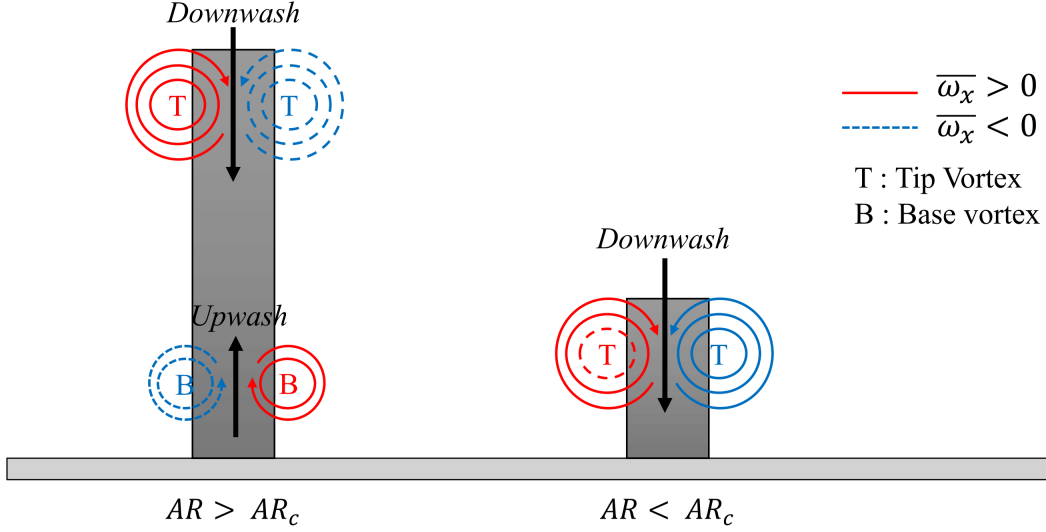


Figure 2.1: Quadrupole (Left) and Dipole (Right) wake topologies in the wake of wall-mounted prisms, presented using streamwise vorticity distribution above and below the critical aspect-ratio.

structures. Based on the number of streamwise vortex pairs appearing in the wake, past studies have classified the mean-wake topology into *Dipole*, *Quadrupole*, *Multipole* and *No-Pole* wakes (Zhang et al., 2017). Dipole type wake consists of a tip vortex pair, while Quadrupole-type wake has both counter-rotating tip and base vortices. Further, past literature scrutinized that the evolution in mean-wake topology is affected by both flow dynamics, i.e., Reynolds number and boundary-layer thickness, and geometrical features, i.e., aspect-ratio (height-to-width), depth-ratio (length-to-width) and cross-sectional shape of the body (Porteous et al., 2014; Derakhshandeh and Alam, 2019). While there are studies that have identified the evolution in mean wake topology based on a single parameter, the multivariate evolution of the wake has not been explored thoroughly.

The evolution of mean wake topology behind a wall-mounted prism has been mainly studied in the literature in terms of changing aspect-ratio (Sumner et al., 2004; Sumner and Heseltine, 2008; Yauwenas et al., 2019) and Reynolds numbers (Zhang et al., 2017; Rastan et al., 2017; Diaz-Daniel et al., 2017b). Sumner et al. (2004) experimentally studied the mean wake of a wall-mounted circular prism with changing aspect-ratios between 3 and 9. They observed that the mean-wake topology changes from Dipole-type at aspect-ratio of 3 to Quadrupole-type at aspect-

ratio of 5. This study was further complemented by Sumner and Heseltine (2008), who reported that the tip vortex dominated the wake of small aspect-ratio prisms. It was also observed that increasing aspect-ratio reduces the strength of the tip vortex, while increasing that of the base vortex. Yauwenas et al. (2019) reported similar distinction with increasing aspect-ratio for sharp-edged prisms. Furthermore, Hosseini et al. (2013) and Yauwenas et al. (2019) examined the role of both aspect-ratio and boundary-layer thickness in determining Dipole/Quadrupole wakes and noted discrepancies compared to Wang and Zhou (2009) and Bourgeois et al. (2011). Wang and Zhou (2009) observed the evolution from Dipole to Quadrupole wakes at aspect-ratio of 5, contrary to Yauwenas et al. (2019) who reported them at 6 – 10. Since both studies had a similar Reynolds number and boundary layer thickness, there may be other factors affecting the wake evolution. This hints at the need to characterize the mean wake topology for small aspect-ratio prisms, considering that there remains a notable gap concerning how changing depth-ratios (normalized length) impacts the wake.

For a particular aspect-ratio, the mean wake topology was determined based on changing Reynolds number. Zhang et al. (2017) numerically studied the wake of wall-mounted square prism of aspect-ratio 4 with varying Reynolds numbers ($5 \times 10^1 - 1 \times 10^3$). Zhang et al. (2017) noted an evolution from Quadrupole-type wake at $Re = 5 \times 10^1 - 1 \times 10^2$ to a Dipole-type wake at $Re = 5 \times 10^2 - 1 \times 10^3$. They further reported *six-vortex-type* Multipole wake as an Intermediate topology at $Re = 1.5 \times 10^2 - 2.5 \times 10^2$. Rastan et al. (2017) numerically reported similar observations for a prism with aspect-ratio 7, further noting the Dipole type wake appearing at lower Reynolds number of 8.5×10^1 . Such early evolution in case of Rastan et al. (2017) was attributed to stronger tip vortex with increasing aspect-ratio at low Reynolds numbers. In case of small aspect-ratio prisms, such as a cube, Diaz-Daniel et al. (2017b) reported the dominant effects of tip vortex in determining downstream wake characteristics. In case of a small aspect-ratio prism, a strong downwash flow (induced by the tip vortex) resulted in a Dipole-type wake. Changing the depth-ratio (length) of the prism had a significant effect on the free-end vortices (Rastan et al., 2021; Zargar et al., 2022a). Rastan et al. (2021) recently showed that for a

prism with aspect-ratio 7, increasing the depth-ratios in the range of 1 – 4 led to the suppression of tip vortex and a no-pole type wake. For small aspect-ratio prisms, Zargar et al. (2021b) showed that increasing the depth-ratio from 0.016 to 1 led to an enhanced downwash flow. Further, a Quadrupole type wake at depth-ratio of 0.016 changed to Dipole-type wake at depth-ratio of 1. For larger depth-ratios (~ 4), Dipole-type wake prolonged until $Re \simeq 6.25 \times 10^2$ (Zargar et al., 2022b). Based on these findings, one can hypothesize that the tip vortex, and its induced downwash flow, play an important role in determining the mean wake topology, especially for small aspect-ratio prisms.

2.2.2 Unsteady wake topology

The three-dimensional wake behind wall-mounted prisms is mainly attributed to the entrainment of flow into the prism mid-span by the induced upwash and downwash flows (Wang and Zhou, 2009). As such, mid-span coherent structures are responsible for the formation of large-scale vortices and alternating vortex shedding in the wake region, and are influenced by the prism aspect-ratio and depth-ratio. Sakamoto and Arie (1983) discussed the influence of increasing aspect-ratio between 1 and 8 on the coherent and mean wake features behind wall-mounted circular cylinders and square prisms. Kármán-type or hairpin-like structures in the wake were strongly influenced by the prism aspect-ratio. For example, hairpin-like structures only appeared at aspect-ratios below 2. Thus, a threshold aspect-ratio exists, below which the intense downwash flow suppresses the asymmetric, periodic Kármán-type vortex shedding. From the limited studies on large depth-ratio prisms, it is evident that depth-ratio affects the unsteady wake topology. Joubert et al. (2015) studies the wake of a wall-mounted finite prism with an aspect-ratio of 5 and a depth-ratio of 2.63 at Reynolds number of 7.6×10^4 . The flow reattached on the top surface of the prism, but not on the sides, leading to Kármán-type vortex shedding. Similarly, Wang and Lam (2019b) experimentally observed similar results and concluded that depth-ratio did not significantly affect the overall wake dynamics at high Reynolds numbers, if the flow does not reattach on the prism side surfaces.

Depth-ratio also affects the onset of unsteady wake evolution. For example, numerical study of Zargar et al. (2021b) revealed that the wake of a low aspect-ratio ($AR = 1.2$) prism remains steady at Reynolds numbers of 5×10^1 to 2.5×10^2 for both small and large depth-ratios (i.e., 0.83 – 3). Zargar et al. (2022b) further demonstrated that increasing Reynolds number above 7.5×10^2 for a large depth-ratio prism ($DR = 5$) leads to an irregular (unstable) unsteady regime, resembling a transitional state. Irregular shedding resulted in flow reattachment and subsequent detachment from the prism surfaces. Rastan et al. (2021) reported similar observations at Reynolds number of 1.2×10^4 . These results showed that increasing the prism depth-ratio lead to diminished vortex shedding, which was attributed to the suppressed interactions between the separating shear-layer and the wake. This suppression was linked to strengthening of the downwash flow.

Quasi-periodic vortex shedding behind wall-mounted prisms is a common feature for small aspect-ratio prisms (Sakamoto and Arie, 1983; Martinuzzi and Tropea, 1993; Martinuzzi and AbuOmar, 2003; Martinuzzi, 2008). Previous studies, such as by Sakamoto and Arie (1983) and Hosseini et al. (2013), have shown the effect of aspect-ratio and boundary-layer thickness on the quasi-periodic vortex shedding. The boundary-layer thickness changes momentum of the approaching flow and affects the intensity and size of the base vortex structures (horseshoe and junction vortices), which in turn modifies the interactions with shed vortices from the prism top and side surfaces (Bourgeois et al., 2011). Moreover, previous studies have similarly described the wake of wall-mounted prisms as symmetric and/or anti-symmetric under the influence of a very thin boundary-layer. For instance, Okamoto and Sunabashiri (1992) noted the possibility of symmetric shedding at high Reynolds numbers and very thin boundary layer. In such an arrangement, two symmetric vortices would form in the prism base region, shed simultaneously and travel downstream together. However, no direct evidence of symmetric shedding have been found at high Reynolds numbers (Sattari et al., 2012).

Sattari et al. (2012) and Bourgeois et al. (2011) reported the existence of full-loop and half-loop vortex structures in the wake wall-mounted square prisms with increasing aspect-ratios. Specifically, instantaneous wake topology for aspect-ratio of 4 were presented in the form of half

loops, whereas full-loop structures were observed for aspect-ratio of 8. These structures were attributed to the interactions between tip and base vortices, and flow reattachment on the prism surfaces. Vortex structures were also influenced by the boundary-layer thickness, which affected the strength of base vortices and the interactions with tip vortices. Briefly, half-loop structures were identified by an arch-type vortex consisting of a principal vortex core and a streamwise connector strand as described by Bourgeois et al. (2011). Full-loop structures were previously attributed to the interactions of tip and base vortices, which resulted in the formation of a single large-scale vortex in the wake (Wang and Zhou, 2009).

It is well-documented that separated shear-layers have the capacity to reattach over the side and top surfaces of the prism at elevated Reynolds numbers ($Re > 1 \times 10^3$), provided there is a significant increase in depth-ratio (Rastan et al., 2021). The entailed enhancement of the downwash flow suppresses the wake unsteadiness in long prisms (Rastan et al., 2021). Meanwhile, aspect-ratio plays a role in intensifying the upwash flow and contributing to the overall wake unsteadiness (Saha, 2013). Thus, enhancement of the unsteadiness, or onset of an irregular unsteady flow topology in the wake of wall-mounted prisms, can be achieved by either increasing the prism aspect-ratio or reducing its depth-ratio. This heightened wake unsteadiness suggests that abrupt changes in geometry may be associated with the transition to turbulence.

The separation-reattachment phenomenon is an essential aspect of the flow around rectangular prisms. Influenced by the depth-ratio, it is characterized by the reattachment of the flow on the top and side surfaces of the prism (Rastan et al., 2021). Flow reattachment is attributed to the downwash flow generated by the tip vortex, which suppresses separation of the shear layer on the top surface. This downwash flow is more pronounced for prisms with larger depth-ratios, leading to flow reattachment on the top surface. Moreover, sharp-edged flow separation generates unsteady fluctuations as part of the adverse pressure gradient generated at the leading-edge. Recovery of pressure persists till the flow reattachment, which enhances unsteady fluctuations in this region (Awasthi et al., 2014). As such, reattachment of the flow significantly influences the flow dynamics, specifically the pressure distribution on prism surfaces. Small and large scale

vortices, especially hairpin-like vortices formed in the reattachment region, influence large pressure fluctuations near the prism (Saathoff and Melbourne, 1997). Rastan et al. (2021) observed similar pressure effects in the wake due to the downwash flow induced by the tip vortex, which is a critical factor influencing pressure fluctuations and base pressure along the prism length. Since pressure fluctuation correlates with velocity fluctuations via Poisson's equation, investigating pressure fluctuations can offer novel insights into flow dynamics around wall-mounted prisms, particularly highlighting interactions among different flow structures.

2.2.3 Wake features and instabilities

Wake features and instabilities become an important aspect of the flow around wall-mounted prisms. These features include secondary vortex structures appearing in the wake alongside the coherent structures, such as the arch-type, Kármán-type, or hairpin-like vortex shedding. Diaz-Daniel et al. (2017b) observed secondary vortex structures in the wake of wall mounted prisms at $Re \geq 6 \times 10^2$, placed symmetrically alongside the primary vortex structures. They attributed such structures to secondary interactions by the vortical motion of horseshoe vortex legs. Further, three-dimensional turbulent effects, at higher Reynolds number, cause stronger interactions between vortices. This results in higher number of secondary structures that lose streamwise coherence in close vicinity of the prism. Khan et al. (2020a) numerically studied the laminar vortex shedding regime of flow around a suspended cube to examine the three-dimensional vortex shedding mechanism and understand temporal evolution of the wake. They observed hairpin-like shedding, which appeared asymmetric in normal streamwise plane and symmetric in the orthogonal streamwise plane. They also observed secondary structures forming between two shedding hairpins. Secondary structures formed limbs, protruded from the first hairpin-like structure, which connected the two primary hairpins. Khan et al. (2020b) noted similar wake structures at moderate Reynolds numbers.

In case of flow around wall-mounted finite prisms, no clear consensus was identified in the terminology of secondary vortex structures and their interactions. Zhang et al. (2017) identified

formation of a secondary tip vortex from top surface of the prism leading edge, referred to as *tornado-like* tip vortices due to their spiraling rotations. These observations were consistent with the findings of Rastan et al. (2021), who reported that secondary tip vortices vanished in the vicinity of the prism. Both these studies discussed secondary vortex structures in terms of time-averaged streamwise vortices observed in the wake. Insights into the interactions of secondary vortex structures with the shedding coherent structures remains unexplored in literature.

Near-wake low- or high-frequency instability processes are other important aspect of the wake of low aspect-ratio wall mounted prisms (Morton et al., 2018; Kindree et al., 2018). They are harmonics of the dominant shedding frequency in the near-wake. The analysis of such complex flow field and inherent wake instabilities in the past literature focused mainly on Floquet analysis (Williamson, 1988; Barkley and Henderson, 1996) and model reduction methods (Akhtar et al., 2009; Rowley et al., 2009; Schmid, 2010; Khalid et al., 2020). In post-processing, model reduction methods such as Proper Orthogonal Decomposition, or POD (Morton et al., 2018; Kindree et al., 2018), and Dynamic Mode Decomposition, or DMD (Rowley et al., 2009; Schmid, 2010), are useful techniques to investigate complex flow phenomenon. Moreover, discrete Fourier transform based methods like Fourier Averaged Navier-Stokes (FANS) (Freeman et al., 2024) provide a framework to obtain direct insights into the dynamics of complex coherent wake interactions. Using POD, Morton et al. (2018) established that the near-wake of a wall-mounted finite circular prism consists of a vortex shedding instability centered at the shedding Strouhal number (St_{sh}) as well as low-frequency signatures centered at $St_{sh}/2$ and $St_{sh}/4$. They further observed that such low-frequency signatures are independent of Reynolds number, defined based on d over the range of $3 \times 10^2 - 1.18 \times 10^4$, but dependent on the boundary layer state, and hence Reynolds number based on boundary layer thickness. Morton et al. (2018) further proposed that such low-frequency instabilities are only observed in circular cross-section prisms with aspect-ratios smaller than 4. Further, Kindree et al. (2018) expanded on this study by investigating the low-frequency periodicity of both circular and square cross section prisms of

aspect-ratio 4 positioned inside a thin laminar boundary layer. This study reported the low-frequency instability in sharp-edged prisms, *i.e.*— square cross-section. Hence, reducing the aspect-ratio of wall-mounted prisms highly influences the wake structure by means of the free-end instabilities. To this end, it is important to explore how the larger depth-ratio of a prism can impact its free-end instabilities, and thus the wake topology and dynamics.

An important free shear-layer instability, most commonly encountered in the flow around prisms, is Kelvin-Helmholtz instability. Studies on infinite-span rectangular prisms show that flow separates at the leading edge and forms a separated shear-layer at Reynolds number above 1.5×10^2 , which rolls up into a train of small-scale vortices (Moore et al., 2019a). These result in Kelvin-Helmholtz Instability (KHI) of the shear layer and they are characterized by high-frequency signatures (St_{kh}). Kelvin-Helmholtz instability significantly impacts pressure distribution on the prism surfaces and contributes to the formation of downstream structures, such as hairpin-like vortices (Tenaud et al., 2016). These hairpin-like structures are considered large-scale coherent structures and play a crucial role in the momentum transfer and mixing processes. Moreover, these hairpin-like vortices manifest at comparatively low frequency (St_{sh}). Depending on the length of the prism (DR in the present study), interactions between Kelvin-Helmholtz and hairpin-like vortices exhibit different characteristics. In this realm, Reynolds number plays a critical role in determining the intensity of these interactions, such that Lander et al. (2018) (Lander et al., 2018) proposed a scaling ($St_{kh}/St_{sh} = 0.18 \times Re^{0.6}$) that equate the frequency of Kelvin-Helmholtz instability to that of hairpin-like vortices. Later, (Kumahor and Tachie, 2023) showed that these interactions strongly depend on the streamwise length of the infinite-span prism. These findings emphasize the importance of geometry in shaping the interactions between Kelvin-Helmholtz and hairpin-like vortices.

Influence of depth-ratio on global unsteadiness and interactions between Kelvin-Helmholtz instability (KHI) and large-scale vortex shedding have been reported for infinite-span suspended prisms (Zhang et al., 2023). However, these interactions significantly differ compared to the case of wall-mounted prisms, mainly due to the infinite-span nature of the prisms, where the wake is

bounded by free-end effects (Wang and Zhou, 2009). Thus, in the context of wall-mounted prisms, interactions between KHI and large-scale vortex shedding, influenced by depth-ratio and free-end effects, have not been quantified in the past literature.

2.3 Wake of suspended bluff bodies

Suspended prisms are fully immersed in the flow without contact with any walls or surfaces contrary to wall-mounted prisms. This allows the flow to develop symmetrically around the entire body, both above and below, without the interference of boundary layer effects from a nearby surface. The flow over such suspended bodies are separated into two categories based on the cross-section shape (Derakhshandeh and Alam, 2019): (i) shapes of continuous and finite curvature such as circular or elliptical cylinders, and (ii) sharp edged structures of infinite curvature such as square or rectangular prisms. These differences are primarily based on the nature of boundary-layer separation. For instance, in case of circular and elliptical cylinders, the flow smoothly separates from the surface, leading to the formation of symmetric vortices and the well-known von Kármán vortex street (Taneda, 1952). Smooth curvature results in a more gradual boundary layer separation, which contributes to less severe pressure gradients and more organized vortex shedding. For sharp-edged prisms, the flow separates abruptly at the edges, creating stronger vortices and more intense turbulence in the wake (Wang and Lam, 2019a). Sharp edges induce higher pressure drag due to abrupt boundary layer separation, resulting in a more irregular and incoherent wake structure with significant vortex shedding and flow fluctuations.

Flow behavior in both wall-mounted and suspended prisms is heavily influenced by the Reynolds number, with low Reynolds number flows tending to remain laminar and attached for a longer distance before separating, while higher Reynolds number flows exhibit turbulent separation and wake patterns dominated by vortex shedding (Williamson, 1988). These differences in flow separation and wake formation significantly affect the drag, lift, and pressure

distribution around the bluff body. In subsequent sections, the wake dynamics of suspended bodies, such as sharp-edged prisms, flat plates and circular cylinders, are discussed.

2.3.1 Wake of suspended prisms

Sharp-edged, blunt bluff bodies, such as prisms, in addition to the large wake region typical of bluff bodies, experience an interesting phenomenon of flow recirculation (Sohankar, 2008). This implies reattachment of the separated shear-layer onto surfaces of the prism. This behavior of separating and reattaching flows have attracted attention in the field of fluid dynamics (Williamson, 1988; Sohankar, 2008; Cimarelli et al., 2018; Mashhadi et al., 2021). One of the main features of these flows is the combined presence of small scales, owing to the occurrence of turbulent motions and large scales associated with coherent vortex shedding behind prisms. Moreover, these flows differ from the wake of wall-mounted prisms due to the overarching influence of free-end effects in the latter.

Various regimes of the flow over square cylinder were briefly presented by Bai and Alam (2018). They reported that the flow remained steady till $Re = 5 \times 10^1$, characterized by two symmetric vortices appearing in the wake and the flow separating at the trailing edges. At low Reynolds numbers, the laminar regime of square cylinder was further characterized by increasing length of recirculation region and reducing drag coefficient with increasing Re . At Reynolds numbers of $5 \times 10^1 < Re < 1.6 \times 10^2$, the flow becomes unsteady with laminar two-dimensional vortex shedding. The trailing edged flow separation further continues till $Re = 1.2 \times 10^2$, after which the flow separated from the leading-edges. Specifically at this boundary ($Re \approx 1.2 \times 10^2$) there is a drop in length of recirculation region as well as drag coefficient, mainly attributed to the leading-edge flow separation and adverse pressure gradient effects on the wake. Further, as noted by Williamson (1996) and Robichaux et al. (1999), within the range of $1.6 \times 10^2 < Re < 2.2 \times 10^2$, dominance of *Mode A* and *Mode B* instabilities cause the transition from two to three dimensional fluctuations in the wake, with the drag coefficient reaching a minima while recirculation length remains invariant. This range of Reynolds numbers, where the

regime of two-dimensional vortex shedding transitions to three-dimensional vortex shedding, is of particular interest in the study of flow around sharp-edged prisms. From there on, the transition to fully turbulent shear-layer beyond the trailing edge is observed at $2.2 \times 10^2 < Re < 1 \times 10^3$. This regime is characterized by the presence of large-scale vortices in the wake, which are attributed to the interactions between separated shear-layers and free-end vortices (Williamson, 1988). Moreover, at $Re > 1 \times 10^3$, the transition to turbulence within the shear-layer occurs closer to the leading-edge of the prism, leading to an intermittent reattachment of the shear-layer on the prism surfaces (Lander et al., 2018). In this high Reynolds number turbulent regime, the drag coefficient and recirculation lengths increase.

Flow around sharp-edged prisms with varying aspect-ratios (length-to-height) and Reynolds numbers is characterized by Mashhadi et al. (2021), whose study of rectangular prisms focused on low Reynolds numbers between 3×10^1 and 2×10^2 . They observed the changes in wake stability by changing aspect-ratio, such that elongated bodies (rectangular cross-sections) exhibited steady and two-dimensional wakes. Moreover, the critical Reynolds number associated with the onset of vortex shedding increased with aspect-ratio. Further, increasing aspect-ratio resulted in higher probability of the separated flow to reattach onto side surfaces of the prism. Moreover, at higher Reynolds numbers ($Re = 2 \times 10^2$), increasing aspect-ratio made the three-dimensional unsteady flow transition into two-dimensional unsteady regime (Mashhadi et al., 2021).

Influence of leading-edge flow separation was studied by Moore et al. (2019a), who experimentally investigated the flow around rectangular prisms at Reynolds numbers between 1×10^4 and 1×10^5 . At such high Reynolds numbers, sharp leading-edge of the prism induces flow separation regardless of the adverse pressure gradient. Moore et al. (2019a) further noted that with sufficiently long prism lengths, the separated leading-edge shear-layer, initially laminar, soon undergoes transition to turbulence and reattach onto the prism side surfaces. Further, the transition to turbulence in the shear-layer is accompanied by a train of co-rotating vortices forming from the leading-edge separation, which are characterized by their high-frequency signatures in the frequency spectra. These co-rotating train of vortices and the related phenomena

of Kelvin-Helmholtz instability are, thus, of significant interest in the study of flow around sharp-edged prisms.

2.3.2 Wake behind flat plates

Wall-mounted thin flat plate is a special case of prisms with changing depth-ratio. The fixed leading-edge flow separation with no reattachment on the side surfaces of the flat plate makes it an interesting case to study the wake dynamics. Previously, such cases have been investigated in terms of flow over fences (Chan et al., 2022). Experimentally, the flow around suspended flat plates have been studied by Fage and Johansen (1927) and Wu et al. (2005) using sharp-edged flat plates. Numerically, however, investigating the flow around flat plates becomes complicated owing to the sharp leading-edge flow separation and the absence of reattachment on the side surfaces. To address these challenges numerically, a thin flat plate is generated of the streamwise length of a single grid point (Najjar and Balachandar, 1998; Narasimhamurthy and Andersson, 2009; Hemmati et al., 2016).

Wake dynamics of such bodies are complex and highly three-dimensional. Further, the vortex shedding processes and wake structures differed between low and high Reynolds number flows. At low Re , a laminar regime was observed and led to symmetric vortex shedding (Najjar and Balachandar, 1998). Moreover, the shedding process at low Re was attributed to transition-in-wake phenomena as a result of laminar instabilities in the flow (Zdravkovich, 1997). At high Re , transition in shear-layer was observed, mainly associated with the formation of dominant vortices shedding from the shear-layers. Thus, as Reynolds number increased for the flow around thin flat plates, flow instabilities magnified with the formation and interactions of small-scale eddies and three-dimensional effects, leading to highly incoherent wake structures (Wu et al., 2005). In simple terms, the flow around flat plates were highly influenced by Reynolds numbers.

Three-dimensional wake of normal infinite-span thin flat plate was first numerically investigated by Najjar and Vanka (1995). This study investigated three-dimensional effects of vortex structures in the wake, such as the formation and breakdown of ribs and rollers. Spanwise,

large-scale vortex structures that shed from the plate edges are referred to as vortex rollers, while smaller-scale, secondary streamwise structures connecting the rollers are referred to as ribs (Williamson, 1996). Moreover, vortex roll-up behind the flat plate was prolonged downstream, enabling a prolonged spanwise vortex shedding (Zdravkovich, 2003). As such, the wake of infinite-span thin flat plate was highly incoherent and asymmetric compared to two-dimensional flat plates. Finite aspect-ratio thin flat plate showed different topologies compared to infinite-span flat plate (Hemmati et al., 2015). Suppression of secondary spanwise instabilities in case of finite flat plates, as well as indication of a single dominant shedding frequency, indicated that the two shear-layer from either sides of the plate rolled-up simultaneously into a single large-scale vortex structure. The dominant shedding structures in this case resembled a hairpin-like vortex (Hemmati et al., 2016). Moreover, a shear-layer peel-off mechanism was observed, which significantly increased the shedding frequency and reduced the length of recirculation region compared to infinite-span flat plates (Hemmati et al., 2016).

2.3.3 Wake of circular cylinders

Flow over circular cylinders differ from that of sharp-edged prisms due to the continuous curvature of its surface. Flow separates from the circular surfaces due to shear-layer detachment caused by the adverse pressure gradient around them (Norberg, 2001). Moreover, flow around circular cylinders is divided into several regimes based on Reynolds number. At low Reynolds numbers ($\leq 3 \times 10^5$), flow separates symmetrically on both sides, resulting in a von Kármán vortex street, i.e. a periodic and alternating vortex shedding. This range of Reynolds numbers is referred to as sub-critical regime, where it experiences high drag coefficients ($\sim 1 - 1.2$). At higher Reynolds numbers, especially in the supercritical regime ($Re > 3 \times 10^5$), boundary layer transition to turbulence can cause flow reattachment downstream, reducing drag significantly in the “drag crisis” phenomenon (Singh and Mittal, 2005). Once the drag crisis occurs and the boundary layer transitions to turbulence, the drag coefficient drops significantly, to as low as $0.3 - 0.5$, depending on the flow conditions and surface roughness. Wake of circular cylinders

depend entirely on Reynolds numbers (Roshko, 1993; Williamson, 1996). The aspect-ratio (length-to-diameter ratio) has a limited effect on the overall flow structure, as the primary wake features are dominated by the circular cross-section. The flow behavior remains relatively consistent along the length of the cylinder unless its aspect-ratio is extremely small, leading to end effects (Sakamoto and Arie, 1983).

Shear-layer transition to turbulence and generation of instabilities occurs beyond the supercritical Reynolds number regime. At higher Reynolds numbers, the turbulence transition point in the shear-layer moves upstream, resulting in a turbulent wake (Bloor, 1964; Wei and Smith, 1986). Two dimensional shear-layer vortices eventually transition to three-dimensional turbulent structures with increase in Reynolds number due to the influence of three-dimensional small-scale fluctuations (Wei and Smith, 1986). Shear-layer instability in this case is the same as Kelvin-Helmholtz instability (Bloor, 1964). Kelvin-Helmholtz instability driven vortices interact with the primary von Kármán vortices and aid the entrainment of fluid into the formation region. Similar to sharp-edged prisms, interactions between the shear-layer vortices and primary vortices are interesting to study.

2.4 Approaches to Flow Studies

There has been a variety of approaches over the past decades to study wake structures formed around wall-mounted prisms. Experimental methods have historically provided direct observations and measurements of flow behavior (Williamson, 1996), while numerical simulations (Wilcox et al., 1998) have enabled detailed investigation of the flow dynamics over a wide range of conditions. More recently, data-driven approaches (Mendez et al., 2023), leveraging advances in machine learning and data analytics, have gained momentum in analyzing and predicting flow fields with unprecedented accuracy and efficiency. Each of these approaches offers distinct advantages and presents its own set of challenges. Experimental methods allow for real-world validation of theoretical models but are often limited by instrumentation and scale

effects. Numerical simulations, on the other hand, provide high-resolution data and predictive capabilities, though they can be computationally expensive. This section provides an overview of these approaches, specifically focusing on numerical analysis using OpenFOAM.

2.4.1 Experimental Studies

Experimental methods have played a foundational role in advancing our understanding of wakes. Early experimental studies were essential in observing complex flow phenomena, such as vortex shedding, boundary layer separation, and the development of turbulent wakes (Castro and Robins, 1977; Hussain, 1986; Sumner et al., 2004; Miau et al., 2004). Techniques like wind tunnel testing, water channel experiments, and flow visualization have provided valuable insights into the physical behavior of fluids interacting with bluff bodies. One of the primary advantages of experimental approaches is the ability to directly measure flow quantities, such as velocity fields, pressure distributions, and forces acting on the body. Laser Doppler Velocimetry (LDV) and Particle Image Velocimetry (PIV) have become critical tools for capturing velocity profiles and turbulence characteristics in wakes. These methods allow for detailed investigation of flow structures, including vortex formation and shedding.

Castro and Robins (1977) investigated the flow around a wall-mounted cube using wind tunnel experiments and examined two types of incoming flow over the cube, namely an irrotational uniform flow and turbulent shear flow. They observed that size of the recirculation region behind the cube reduced with increasing Reynolds number, using the turbulent inflow conditions. Hunt et al. (1978) further performed water channel experiments to study the vortical structures behind wall-mounted obstacles to identify mean and instantaneous wake topologies behind typical wall-mounted obstacles, e.g., sharp-edged and smooth cylinders. Experimental studies have also enabled sensitivity studies on Reynolds number and aspect-ratio. For example, wind-tunnel experiments of Park and Lee (2000) quantified a direct correlation between cylinder aspect-ratio and vortex-shedding characteristics behind wall-mounted circular cylinders. They observed that aspect-ratio significantly influenced the vortex shedding frequency and wake

dynamics, such that the peak in turbulence intensity moved further downstream in the wake with decreasing aspect-ratio. High-Reynolds-number experiments have demonstrated the critical role of flow separation points and their influence on drag, lift, and the formation of coherent structures in the wake (Wang et al., 2006; Wang and Zhou, 2009; Wang and Lam, 2019a; Moore et al., 2019a).

The range of Reynolds numbers studied in experiments has been crucial in understanding the transition from laminar to turbulent flow regimes. For example, Okajima (1982) studied a wide range of Reynolds numbers between 7×10^1 and 2×10^4 using water channel and wind tunnel experiments. They observed that within a special range of Reynolds numbers and aspect-ratios, flow patterns abruptly changed, accompanied by discontinuities in Strouhal number. Further, PIV measurements of Bourgeois et al. (2011) and Sattari et al. (2012) revealed the formation of large-scale structures and quasi-periodic vortex shedding behind wall-mounted prisms with aspect-ratio of 4. They further reported the existence of full-loop and half-loop vortex structures in the wake of wall-mounted square prisms with increasing aspect-ratios. These studies have provided valuable insights into the flow dynamics and wake characteristics of bluff bodies, highlighting the importance of experimental methods in understanding complex flow phenomena.

Experimental studies are often limited by cost, scale, and accessibility. Williamson (1996) discussed how performing a comprehensive set of experiments over a wide range of Reynolds numbers and geometries would require substantial resources, making it impractical for academic research. Further, Scarano and Riethmuller (2000) and Scarano and Poelma (2009) found that PIV was unable to resolve the smallest turbulent scales in very-high Reynolds-number flows around bluff bodies, which affected their ability to fully capture three-dimensional unsteady structures in the wake. Despite these challenges, experimental studies remain indispensable in fluid dynamics, especially for validating numerical models and providing insights into phenomena that are difficult to capture computationally. The limitations of experiments are often mitigated by combining them with numerical simulations and data-driven approaches, creating a more comprehensive understanding of the flow.

2.4.2 Numerical Simulations

Numerical simulations, particularly Computational Fluid Dynamics (CFD), have become essential tools for investigating fluid flow around bluff bodies, offering a high degree of control over flow conditions and the ability to explore a wide range of Reynolds numbers. These simulations provide detailed insights into the flow fields, including the intricate structures in the wake and boundary layer regions that are difficult to capture experimentally. CFD studies of wakes have leveraged various numerical methods, such as Direct Numerical Simulation or DNS (Hemmati et al., 2018b; Zargar et al., 2022b; Rastan et al., 2017), Large Eddy Simulation or LES (Hemmati et al., 2018b; Saeedi and Wang, 2015; Rastan et al., 2021), and Reynolds-Averaged Navier-Stokes or RANS models (Uffinger et al., 2013; Tominaga, 2015; Hassan et al., 2022), to predict flow separation, reattachment, vortex shedding, and wake characteristics. Moreover, CFD simulations have been performed over a wide range of Reynolds numbers and geometries to explore the influence of these parameters on flow dynamics.

Extensive computational requirements for detailed numerical simulations, such as DNS, intuitively limit the range of Reynolds numbers at reasonable cost. DNS solves full Navier-Stokes equations without any modeling, resolving all scales of turbulence down to the smallest (Kolmogorov) scales. For example, Mittal and Balachandar (1995) conducted DNS of flow past a square cylinder at a Reynolds number of 3×10^2 , providing detailed analysis of vortex shedding patterns and flow reattachment. This approach provides a complete picture of the flow, including the intricate details of turbulence, making it an invaluable tool for fundamental research. DNS is highly effective at low Reynolds numbers, $Re \leq 5 \times 10^3$ (Saha et al., 2000; Yakhot et al., 2006; Sohankar, 2008; Saha, 2013), where computational resources can handle the full resolution required to capture turbulent structures.

At higher Reynolds numbers, where fully turbulent flows are dominant, LES and RANS models are commonly used due to their lower computational cost compared to DNS. LES and RANS models enable simulations at higher Reynolds numbers in the order of $O(10^4 - 10^6)$. LES captures large, energy-containing eddies and models smaller scales, making it particularly effective for

flows where vortex dynamics and wake structures are critical (Saeedi and Wang, 2015). RANS on the other hand models the entire turbulent flow field, providing a time-averaged solution that is computationally less expensive than LES. For example, Uffinger et al. (2013) used RANS to study the flow around a wall-mounted square cylinder at Reynolds numbers ranging from 1×10^4 to 1×10^5 , providing insights into the flow separation and reattachment behavior. Another example is the work of Rodi (1997), which compared the flow around wall-mounted cube at Reynolds numbers between 2.2×10^4 and 4×10^4 . Moreover, a well validated numerical model, such as LES, can provide detailed insights into the flow dynamics, including formation of coherent structures, evolution of vortices, and interactions between shear-layers and the wake (da Silva et al., 2020, 2024). In this dissertation, numerical simulations are employed to study the flow around wall-mounted prisms, specifically utilizing LES and DNS methods to capture complex wake features and vortex interactions. The results from these simulations are validated against experimental data and other high-fidelity numerical simulations to ensure the accuracy and reliability of the computational approach.

2.4.3 OpenFOAM

LES and DNS results were obtained using Open Field Operation and Manipulation (OpenFOAM), which was initially developed by Jasak (1996) at Imperial College London, with further advancements by Weller et al. (1998). It is an open-source CFD framework based on the finite volume method, capable of handling polyhedral meshes. OpenFOAM provides a suite of *C++* libraries and tools designed to simulate complex fluid flow phenomena, including turbulence, combustion, magnetohydrodynamics, and chemical reactions, among others. Additionally, it includes pre- and post-processing applications for mesh generation, field manipulation, decomposition, and data sampling. This dissertation utilized the ESI version of OpenFOAM (v2012 and v2312) for all simulations.

OpenFOAM applications are organized into two primary categories: *solvers* and *utilities*. Solvers perform the core calculations required to solve flow equations, while utilities offer a wide range of pre- and post-processing capabilities.

A key strength of OpenFOAM is its extensibility. Built using *C++* and object-oriented programming principles, the source code is freely available as open-source, allowing users to modify and extend its functionalities. This object-oriented design makes the implementation of equations and solvers more intuitive. For example, the fluid flow momentum equation,

$$\frac{\partial \rho \mathbf{u}}{\partial t} + \nabla \cdot \varphi \mathbf{u} - \nabla \cdot \mu \nabla \mathbf{u} = -\nabla p, \quad (2.1)$$

is represented by the code as,

```
solve
(
    fvm::ddt(rho, U)
    + fvm::div(phi, U)
    - fvm::laplacian(mu, U)
    ==
    - fvc::grad(p)
)
```

One of the disadvantages of OpenFOAM is a lack of Graphics User Interface (GUI). It works using a structure of input files for each case, as shown in Figure 2.2. Here, the case is divided in to three directories:

- “0” is a time directory containing initial and boundary conditions required for the simulation, along with individual files containing the data for particular fields such as velocity (“U”), pressure (“p”), etc.

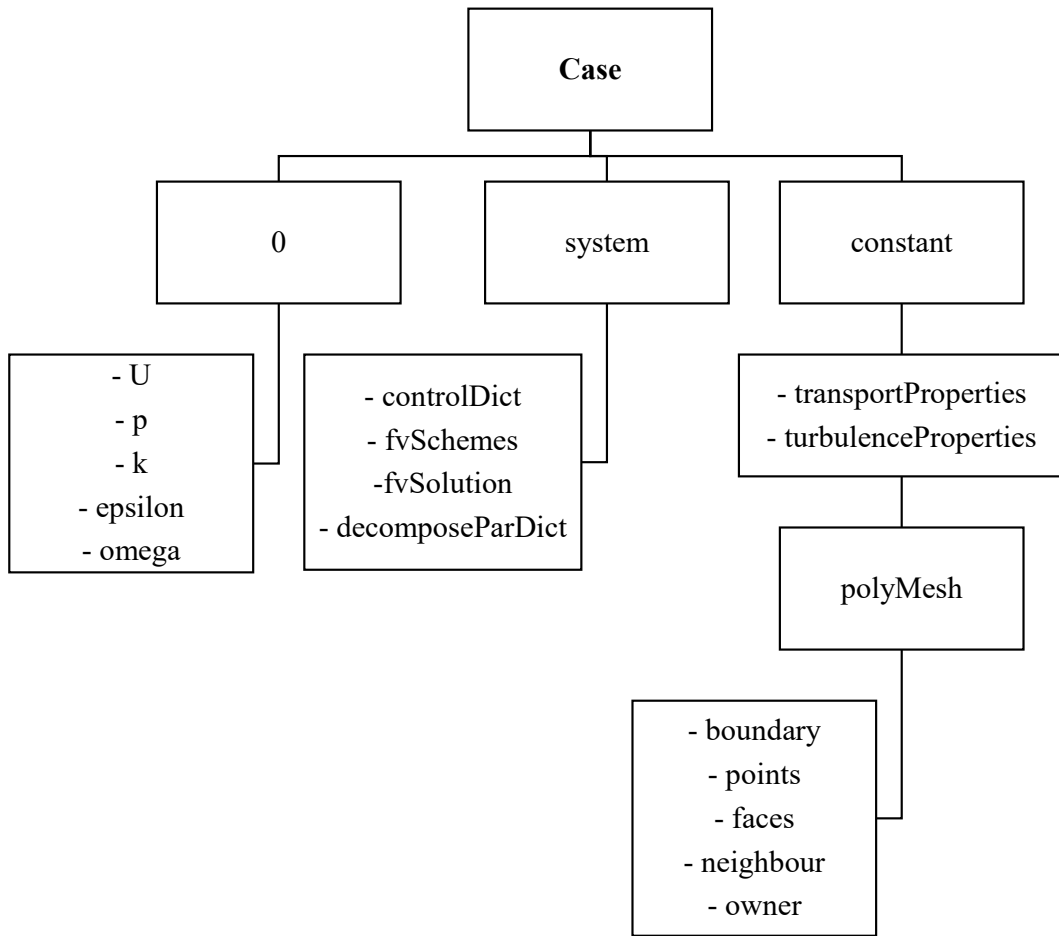


Figure 2.2: Case structure in OpenFOAM

- “system” directory contains the setting parameter files associated with the solution procedure. It should have at least 3 files: “controlDict”, where the simulation control parameters are defined including start/end time and time step; “fvSchemes”, where the discretization schemes are set; “fvSolution”, where the algorithm and solver tolerances are set.
- “constant” directory contains the files describing the fluid properties and specifying turbulence modelling. It also contains the full description of the domain mesh in a sub-directory named “polyMesh”.

Once the file structure in OpenFOAM is understood, the next critical component to explore is its extensive library of solvers and utilities. OpenFOAM offers a wide range of pre-built solvers

tailored for different types of flow problems, such as incompressible flows, compressible flows, multiphase flows, turbulent flows, and heat transfer. These solvers are accessible via the command line and are highly customizable, allowing users to modify them to suit specific requirements of their simulation. Solver *simpleFoam* is commonly used for steady-state, incompressible flow simulations, while *pimpleFoam* and *pisoFoam* are used for transient simulations involving large time steps. Similarly, *icoFoam* and *potentialFoam* are used for low Reynolds number laminar flow or potential flow problems, respectively. Transient solvers *pimpleFoam* and *pisoFoam* are utilized for unsteady flow simulations in this thesis. These solvers are based on the pressure-velocity coupling algorithm, which is essential for capturing complex wake dynamics and vortex shedding. Moreover, modular structure of OpenFOAM enables the addition of custom solvers or modification of existing ones, which is one of its key strengths in academic and research environments.

Chapter 3

METHODOLOGY[‡]

This dissertation employs numerical simulations to study the wake of wall-mounted prisms. This chapter presents the methodology of simulating the flow in this study. First, the problem description provides details on case selection, construction of domain and spatial discretization in Section 3.1. The governing equations and discretization schemes are discussed in Section 3.2. A discussion of the boundary conditions in setting up the numerical simulations is provided in Section 3.3. The boundary layer thickness measurement and its implications on the flow are discussed in Section 3.4 followed by statistical analysis and time-averaging in Section 3.5. Verification and validation studies are presented in Sections 3.6 and 3.7, respectively. This is followed by a brief discussion of different quantitative and qualitative methods used in assessment of wake dynamics in Section 3.8.

[‡]The content of this chapter has been published in whole or part, in *Journal of Fluid Mechanics* (Goswami and Hemmati, 2022), *International Journal of Heat and Fluid Flow* (Goswami and Hemmati, 2023), and *Physics of Fluids* (Goswami and Hemmati, 2024) under citations:

“Goswami, S., & Hemmati, A. (2022). Mechanisms of wake asymmetry and secondary structures behind low aspect-ratio wall-mounted prisms. *Journal of Fluid Mechanics*, 950, A31”.

“Goswami, S., & Hemmati, A. (2023). Mean wake evolution behind low aspect-ratio wall-mounted finite prisms. *International Journal of Heat and Fluid Flow*, 104, 109237”.

“Goswami, S., & Hemmati, A. (2023). Impact of depth-ratio on shear-layer dynamics and wake interactions around wall-mounted prisms. *Physics of Fluids*, 36(11):115–149”

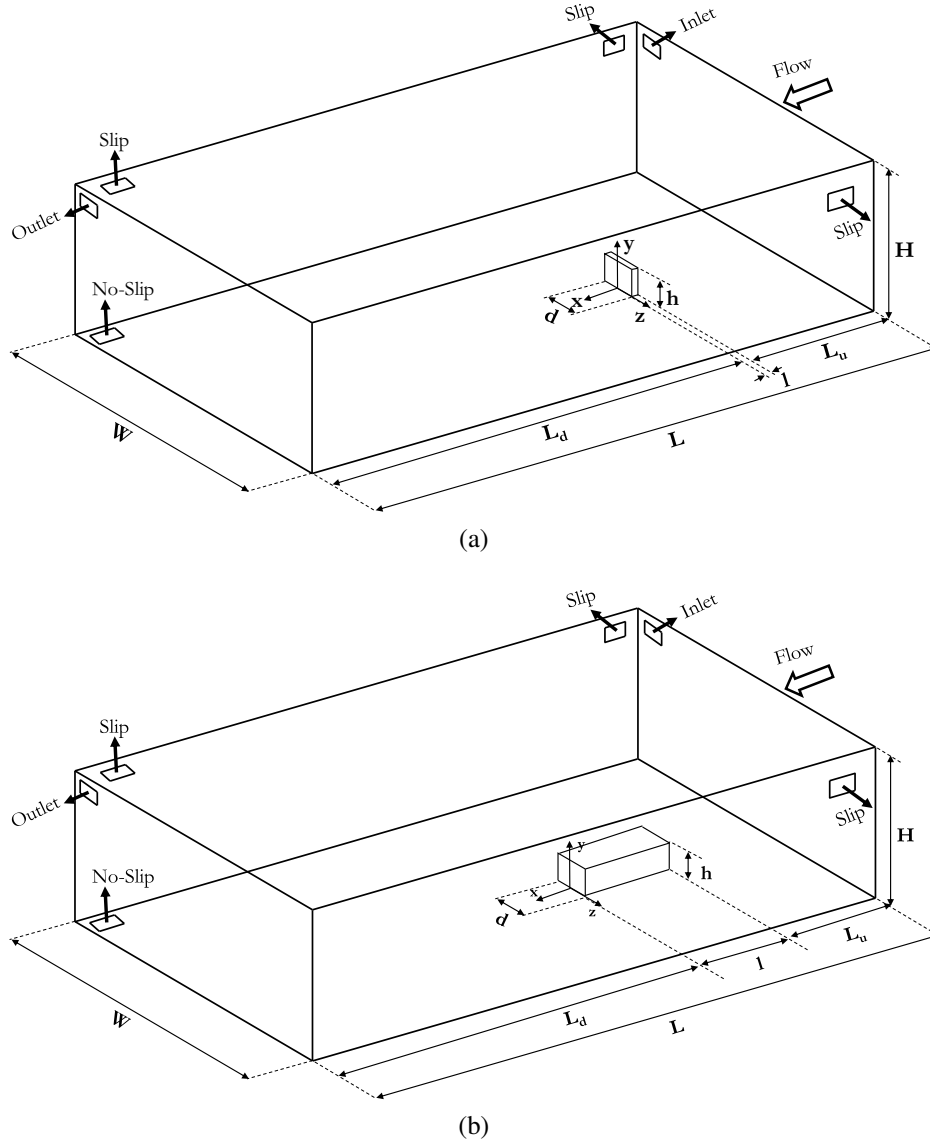


Figure 3.1: Schematics of computational domain (Not to scale) for (a) $DR = 0.016$ and (b) $DR = 4$.

3.1 Problem Description

Flow over wall-mounted prisms of different aspect-ratios and depth-ratios is investigated numerically using OpenFOAM. Both flow and geometrical parameters were selected following the experimental study of Wang and Zhou (2009) and numerical setup of Saeedi et al. (2014). Schematics of the computational domain, containing the wall-mounted prism and the definition of the coordinate system, is presented in Figure 3.1. Streamwise (x), spanwise (z) and normal (y) dimensions of the prism were presented in terms of length (l), width (d) and height (h). Here, a

rectangular prism with aspect-ratios of $AR = h/d = 0.25 - 1.5$ were mounted on the base (ground) of the domain. Multiple cases of varying depth-ratios ($DR = l/d$) were considered between $0.016 - 4$. The study of $DR = 0.016$ represents the special case of a wall-mounted very thin prism, the wake of which have been partly characterized in literature in terms of flow over fences (Chan et al., 2022). Computational domain with dimensions $L_u = 10d, L_d = 20d, H = 6d$, and $W = 12d$ was considered for all simulations. This numerical setup was designed following the detailed sensitivity studies on the computational domain size presented later in Section 3.6. Choice of depth-ratio and aspect-ratio were based on the design of electronics chips (Rastan et al., 2017) and flow manipulators employed in biomedical applications (Jia et al., 2021).

Reynolds number was defined based on the prism width (d) and free-stream velocity (U_b), i.e., $Re = U_b d / \nu$, where ν is the kinematic viscosity of the fluid. Multiple simulations were completed over the range of Reynolds numbers (Re) between 5×10^1 and 1×10^4 using direct methods of solving the Navier-Stokes equations for $Re \leq 1.5 \times 10^3$ and Large Eddy Simulation for $Re > 1.5 \times 10^3$. In past studies (Zhang et al., 2017; Rastan et al., 2021), numerical analysis using DNS, LES, and RANS have covered Reynolds numbers between 5×10^1 and 1×10^3 . While a handful of studies looked at Reynolds numbers between $10^3 - 10^4$, they were all case specific and provide limited understanding of the complex, multivariate wake dynamics. Since the onset of unsteady wake and turbulent effects in the wake of prisms occur at Reynolds numbers between 10^3 and 10^4 (Wang and Zhou, 2009; Rastan et al., 2021; Zargar et al., 2022b), the present study aimed to bridge the gap in the literature by providing a comprehensive analysis of the wake dynamics over a wide range of Reynolds numbers.

A non-homogeneous, multi-block grid, consisting of $7.32 \times 10^6 - 4 \times 10^7$ hexahedral elements, depending on depth-ratio and Reynolds numbers, was developed for the simulations. As an example, the grid distribution for the smallest depth-ratio ($DR = 0.016$) and the largest depth-ratio ($DR = 4$) prisms are demonstrated in Figure 3.2. Grid setup mimicked previous numerical studies of Saha (2013) and Zargar et al. (2021a), where the finer grid was placed close to the prism and the wall, while maintaining a low grid expansion ratio below 3% throughout the

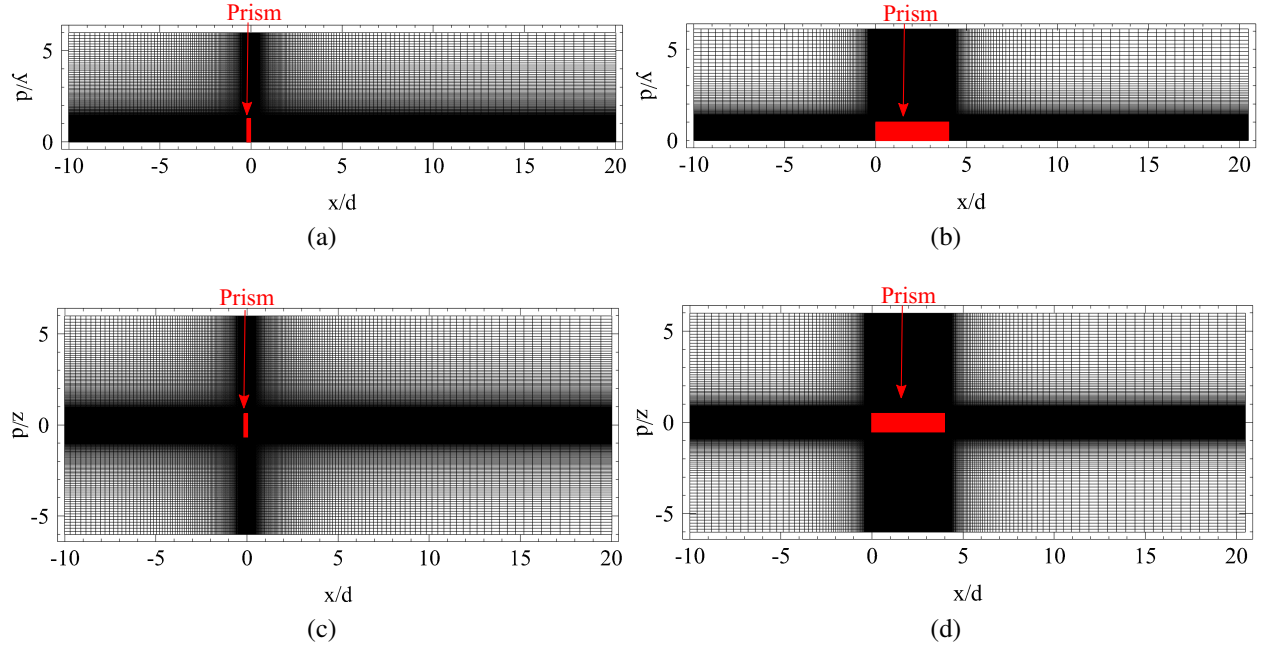


Figure 3.2: Spatial grid distribution for the wall mounted prism of (a) $DR = 0.016$ and (b) $DR = 4$, presented in (a, b) Side view at $z/d = 0$ and (c, d) Top view at $y/d = 0.5$.

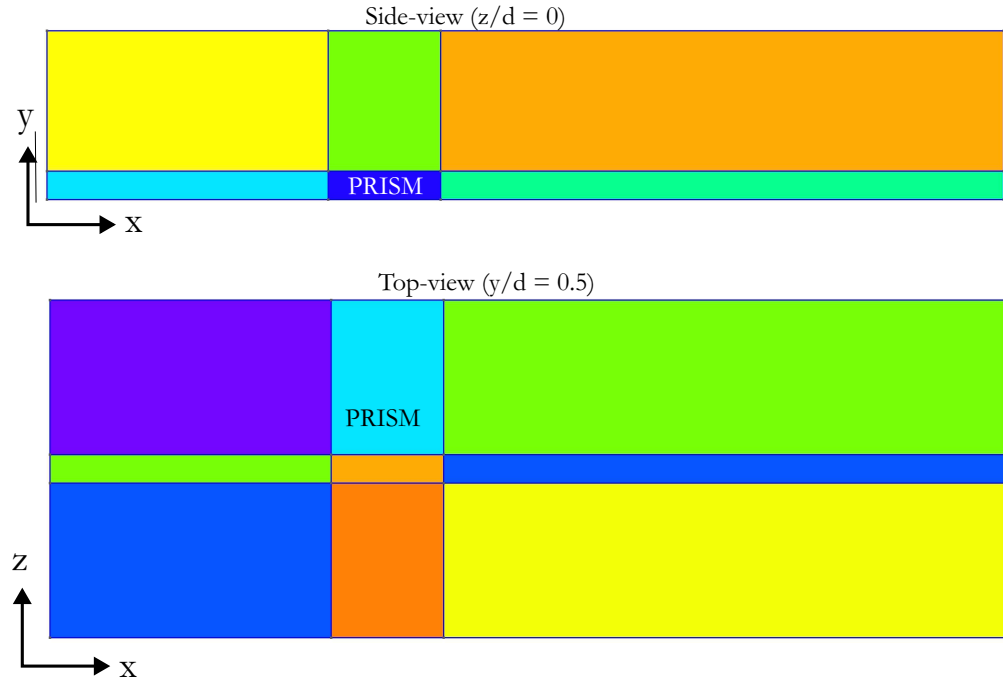


Figure 3.3: Schematics of multi-block grid setup for wall-mounted prism with $DR = 4$.

domain. This enabled accurate simulation of anisotropic small-scale flow structures in the vicinity of the prism, as well as downstream wake structures. The grid was refined in the vicinity of the

prism to capture the boundary layer and shear layer development, accurately. Grid refinement in the wake region further enabled capturing the evolution of wake structures, vortex shedding, and their interaction with the shear layer. Refinement in the spanwise direction provided the necessary resolution to capture spanwise vortices and their interaction with the shear layer. Multi-block meshing strategy helped generate a smoother mesh and non-homogeneous element placement, allowing user defined adjustment of the number of elements per specific area. Schematics of multi-block grid is shown in Figure 3.3. This was particularly useful in the present study as it allowed for a more accurate representation of flow around the prism, especially in regions of interest, such as the leading-edge shear layer and downstream vortex shedding.

3.2 Governing Equations and Discretization

DNS was employed for $Re \leq 1.5 \times 10^3$, while LES was used for $Re > 1.5 \times 10^3$. The governing equations were discretized using the finite volume method and were solved using OpenFOAM. Further details on the governing equations and discretization schemes are provided below.

3.2.1 Direct Numerical Simulations

Three-dimensional (3D) incompressible continuity and Navier-Stokes momentum (Eq.3.1 and Eq.3.2) equations were directly solved using OpenFOAM for $Re \leq 1.5 \times 10^3$:

$$\frac{\partial u_i}{\partial x_i} = 0 \quad (3.1)$$

$$\frac{\partial u_i}{\partial t} + u_j \frac{\partial (u_i)}{\partial x_j} = -\frac{1}{\rho} \left(\frac{\partial p}{\partial x_i} \right) + \nu \frac{\partial^2 u_i}{\partial x_j x_j}. \quad (3.2)$$

Here, u_i is the velocity component, p is pressure, ρ is density, and ν is kinematic viscosity. All flow parameters were normalized using the free-stream velocity, U_b , and the prism width, d . Discretized equations were solved using *pimpleFoam*, which enabled better numerical stability (Holzmann, 2016). PIMPLE algorithm is the combination of pressure implicit with splitting operator (PISO)

and semi-implicit method for pressure linked equations (SIMPLE) algorithms (Holzmann, 2016). *pimpleFoam* solver was utilized in PISO mode by specifying single outer-correction iteration and three pressure correction loops to couple pressure and velocity equations.

3.2.2 Large Eddy Simulations

LES was employed for $Re > 1.5 \times 10^3$, which utilizes sub-grid scale (SGS) models through spatial filtering of the Navier-Stokes equations to distinguish between large and small scale structures in the flow. Sub-grid scale models assume that capturing the exact feature of dissipative eddies is not critical if large scale turbulence is correctly resolved (Reif and Durbin, 2011). Thus in LES, large scale eddies defined by the grid-size (Δ) are solved directly, while small scale eddies are modeled based on an Eddy viscosity model. In this dissertation, Dynamic Smagorinsky Model was utilized to model the sub-grid scale eddies (Reif and Durbin, 2011).

Large-scale components were calculated using filtered incompressible, three-dimensional continuity and Navier-Stokes equations, given by:

$$\frac{\partial \tilde{u}_i}{\partial x_i} = 0 \quad (3.3)$$

$$\frac{\partial \tilde{u}_i}{\partial t} + \tilde{u}_j \frac{\partial (\tilde{u}_i)}{\partial x_j} = -\frac{1}{\rho} \left(\frac{\partial \tilde{p}}{\partial x_i} \right) + \nu \frac{\partial^2 \tilde{u}_i}{\partial x_j \partial x_j} - \frac{\partial \tau_{ij}^{SGS}}{\partial x_j}, \quad (3.4)$$

where,

$$\tau_{ij}^{SGS} = \widetilde{u_i u_j} - \tilde{u}_i \tilde{u}_j = \nu_{SGS} \left(\frac{\partial \tilde{u}_j}{\partial x_i} + \frac{\partial \tilde{u}_i}{\partial x_j} \right) = c_s^2 m_{ij} \quad (3.5)$$

is the sub-grid scale (Leonard) stress tensor, which is modeled (Reif and Durbin, 2011). Here, ν_{SGS} is the sub-grid scale viscosity and c_s is the sub-grid scale coefficient defined as (Lilly, 1992):

$$c_s^2 = \frac{L_{ij}^a M_{ij}}{M_{ij} M_{ij}}, \quad (3.6)$$

where

$$M_{ij} = \left(m_{ij}^{test} - \widehat{m}_{ij}^{SGS} \right). \quad (3.7)$$

Here, m_{ij}^{test} is the test-grid and \widehat{m}_{ij}^{SGS} denotes the grid level stress tensors. The resolved quantities at the grid level are denoted using an overbar, while quantities filtered at the test-grid level for the dynamic processure are denoted using a tilde. In order to perform the dynamic modeling procedure, filter size ratio between the grid and test-grid levels is set to 2. Smagorinsky-lilly model (Lilly, 1992) minimizes the error in the system of equations using the least square method. The sub-grid scale coefficient, c_s^2 , varied significantly over space and time. In order to avoid numerical instabilities, the value of c_s was restricted to positive values,

$$c_s = \max(c_s, 0). \quad (3.8)$$

Dynamic Smagorinsky model was implemented in OpenFOAM using the *LESModel* library, which is a part of the *pisoFoam* solver, a transient solver for incompressible flows incorporating the Pressure Implicit with Splitting Operator (PISO) algorithm.

3.2.3 Discretization Schemes

The diffusive and convective terms of the governing equations were discretized, spatially and temporally, using second-order accurate numerical schemes. A second-order implicit backward Euler scheme was utilized for temporal discretization. The discretized equations were then solved using *pimpleFoam* and *pisoFoam* solvers. A Preconditioned bi-conjugate gradient (PBiCGStab) iterative solver was utilized to solve both, pressure and pressure-velocity coupled equations. The diagonal incomplete-Cholesky (DIC) preconditioner was used for pressure equation and diagonal incomplete-LU preconditioner method was used in pressure-velocity coupled equation. The absolute error tolerance criteria for pressure and velocity was set at 10^{-6} . Time-marching simulations were performed with an adjusted temporal grid to maintain a maximum Courant number below 0.8 to ensure numerical stability.

3.3 Boundary Conditions

Appropriate prescription of boundary conditions is crucial for accurate simulation of the flow. Different types of boundary conditions were utilized in this research. These are discussed below.

3.3.1 Inlet Boundary Condition

Influence of the inlet boundary conditions on the accuracy of flow statistics and wake dynamics has been studied both experimentally (Castillo and Johansson, 2002; Slessor et al., 1998) and numerically (Saeedi and Wang, 2015; Boersma et al., 1998) across various flow configurations. However, this topic remains an open question in the field of numerical simulations of turbulent flow, particularly for turbulent wakes (Saeedi et al., 2014; Saeedi and Wang, 2015). Prescribing accurate inflow boundary conditions at the inlet of a computational domain presents a significant challenge in DNS and LES studies. Since the exact time-dependent flow conditions at the inlet are often unknown, boundary conditions must be applied to ensure a statistically realistic representation of actual turbulent flow.

Several approaches have been developed to generate realistic inflow conditions for DNS and LES (Tabor and Baba-Ahmadi, 2010). These include imposing synthesized turbulence at the inlet boundary, also known as stochastic reconstruction from one-point statistics, and a deterministic approach based on solving the Navier-Stokes equations at the inlet. Both methods aim to provide inflow conditions that are statistically consistent with the flow. However, both these methods have notable limitations. A major drawback is that generated fluctuation field is not derived from the physical flow characteristics and does not satisfy the governing equations of flow, which can introduce additional errors.

In this thesis, the focus was to understand the wake of wall-mounted prisms under inherent boundary layer conditions that naturally form over a flat plate (ground). To this end, a fixed uniform velocity profile was prescribed at the inlet boundary enabling the flow to evolve naturally over the

prism. The uniform velocity profile was set to the free-stream velocity (U_b) and was directed along the streamwise direction.

3.3.2 Outlet Boundary Conditions

When the outlet boundary is placed sufficiently far from any sources of perturbation within the flow domain, it can be assumed that the flow has reached a fully developed state by the time it reaches the outlet. For turbulent flow over wall-mounted obstacles, flow instabilities, separated boundary layers, and vortex shedding should have significantly decayed before reaching the outlet boundary. In such cases, a zero-gradient boundary condition (also known as the Neumann boundary condition) can be applied. This condition sets the derivative of flow properties perpendicular to the outlet boundary to zero, i.e.,

$$\frac{\partial \psi}{\partial n} = 0, \quad (3.9)$$

where, ψ is the flow property and n is the normal vector to the outlet boundary. This boundary condition was applied to the velocity components and pressure at the outlet boundary. Neumann-type boundary conditions were applied instead of convective outflow conditions since the outflow boundary was placed sufficiently far from the physical region of interest. Further, Neumann conditions minimized reflections and boundary-induced disturbances.

3.3.3 Wall Boundary Conditions

Wall boundary condition was one of the fundamental boundary conditions frequently encountered in simulations of wall-bounded flows. Specific wall boundary conditions are applied to the prism surface and the ground surface, as discussed below.

No-Slip Wall

No-slip boundary condition is often applied to walls of the computational domain (Ferziger et al., 2002). This condition implies that the immediate layer of fluid adjacent to the surface accelerates with the same tangential velocity as the surface (Ferziger et al., 2002). The no-slip boundary condition assumes that there is no tangential component of relative velocity at the surface. This condition was applied to the prism surface and the ground surface in numerical simulations within this dissertation. No-slip boundary condition was implemented in OpenFOAM using the *fixedValue* function, which set the velocity components to zero at the wall.

Slip Wall

This boundary condition describes free-surface flow conditions such as open channels or boundaries. Thus, in cases such as free-surface water channel, the interface boundary between water and surrounding air can be described by slip boundary condition. In that case, the velocity component perpendicular to the boundary is set to zero to maintain the impermeability condition while for other velocity components, the normal gradient are set to zero:

$$\frac{\partial u_i}{\partial n} = 0, \quad (3.10)$$

where, n is the normal vector to the slip boundary. In this study, slip boundary condition was implemented in OpenFOAM using the *slip* function, which set the normal gradient of the velocity components to zero at the wall.

3.3.4 Symmetry/Periodic Boundary Conditions

If the flow is homogeneous in a specific direction, turbulence statistics are invariant in that direction. For example, turbulent plane channel flow is homogeneous in spanwise and streamwise directions. In such cases, if the domain is large enough to account for the largest turbulent structures and eddies, the flow can be assumed to be periodic in the spanwise direction. Similarly,

if the flow is symmetric about a plane, flow statistics are invariant about that plane. In the present research, domain boundaries were designed to be sufficiently far from the wall-mounted prism and as such the flow was assumed to be periodic in the spanwise direction. Periodic boundary condition for any typical flow quantity (ψ) is given by

$$\psi(x, y, z) = \psi(x, y, z + W), \quad (3.11)$$

where W is the spanwise width of the computational domain. In OpenFOAM, periodic boundary condition was implemented using the *cyclic* function, which sets velocity components at the periodic boundary to be equal to their corresponding values at the opposite periodic boundary.

3.4 Boundary Layer Thickness

Boundary layer refers to the thin layer of fluid that forms near a surface at a different velocity. This formation is attributed to friction between the surface and the fluid, which creates a region of large velocity-gradient, known as boundary layer (Schlichting and Gersten, 2016). The distance from the surface, where the fluid velocity increases from zero to 99% of the free-stream velocity, is referred to as the boundary layer thickness. Calculation of the boundary layer thickness depends on whether the flow is laminar or turbulent. Consider the flow over a flat plate. In a laminar boundary layer, the flow is smooth and steady with lower friction. Thus, its thickness can be calculated using the Blasius solution (Blasius, 1950):

$$\delta \approx 5x/\sqrt{Re_x}, \quad (3.12)$$

where, x is the distance from the leading edge of the plate and Re_x is the Reynolds number based on x and δ is the boundary layer thickness. In turbulent flows, characterized by surface roughness, randomness, and higher intensity, the boundary layer thickness is typically estimated using the following approximation (Blasius, 1950):

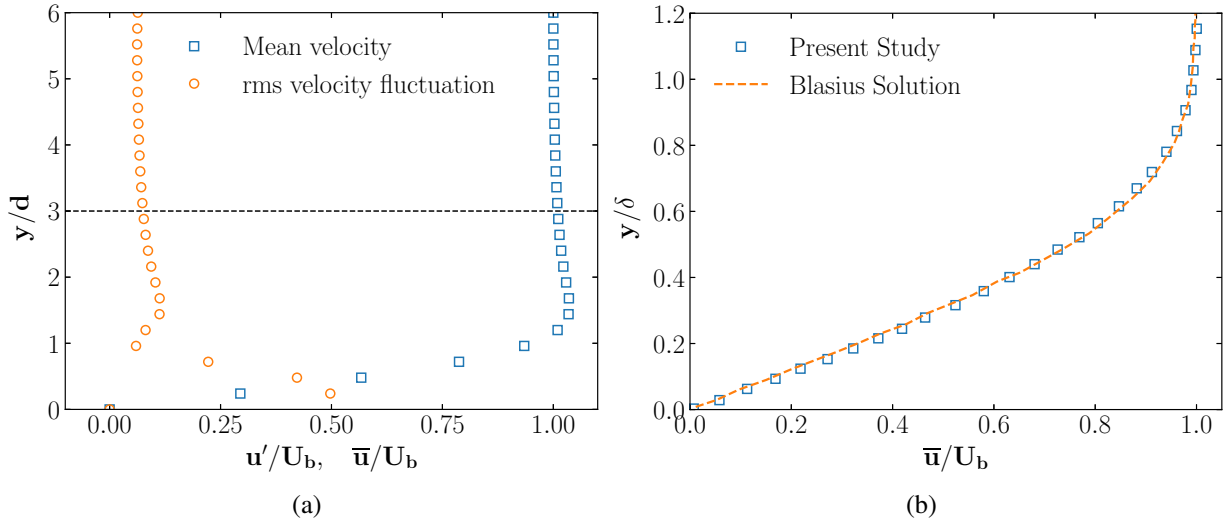


Figure 3.4: (a) Distribution of the time-averaged and root-mean-square of streamwise velocity, i.e. \bar{u} and \bar{u}' , normalized by free-stream velocity (U_b), at $Re = 2.5 \times 10^2$. Measurements were performed in the absence of the prism. Dashed line shows the boundary-layer thickness (δ/d). (b) Boundary layer profile prior to reaching the prism compared with the Blasius boundary layer profile.

$$\delta \approx 0.37x/Re_x^{1/5}, \quad (3.13)$$

Boundary layer thickness was calculated for different Reynolds number cases, and their variation with Reynolds number, as well as their implications on the flow field, are discussed in subsequent sections.

Low Reynolds number flow

Figure 3.4 presents distributions of time-averaged streamwise velocity (\bar{u}) and root-mean-square of streamwise velocity (\bar{u}') normalized by free-stream velocity (U_b) in the case of a free-flow with no prism. Dashed lines shows the boundary layer thickness (δ), which is $\delta/d \approx 3$ for $Re = 2.5 \times 10^2$. The boundary layer thickness varied between 2.65 and 3.95 with lowering Reynolds number from 5×10^2 to 5×10^1 . It is important to note that a laminar boundary layer is expected at low Reynolds numbers analyzed in this dissertation (Saha, 2013; Zargar et al., 2021b). Since the boundary layer was laminar, and its thickness changed with Reynolds number,

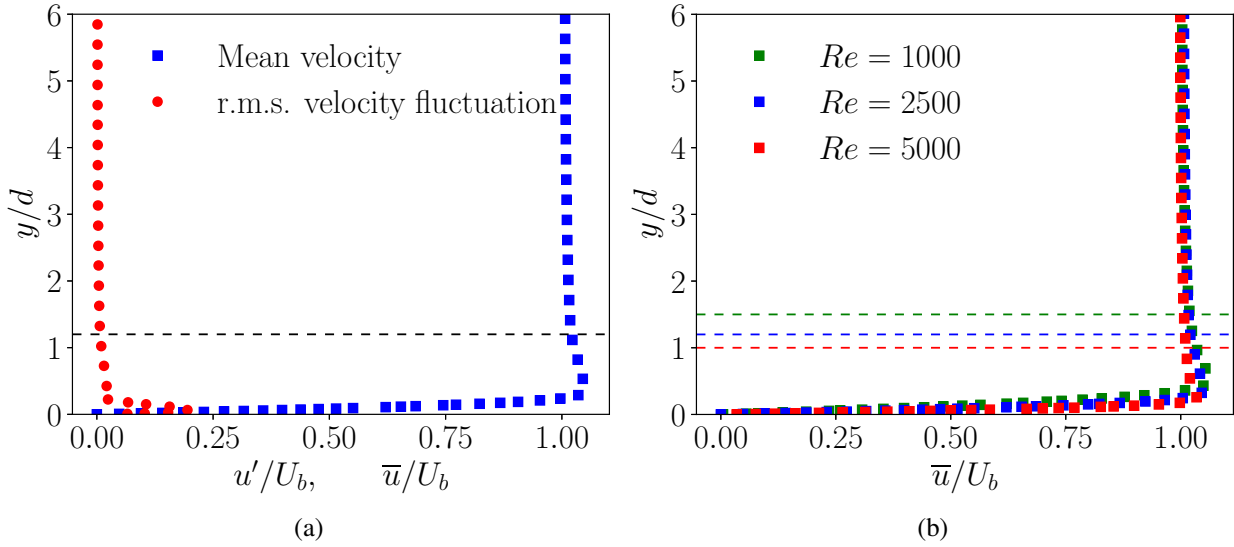


Figure 3.5: (a) Distribution of the time-averaged and root-mean-square of the streamwise velocity (\bar{u} and u') at the location of the leading-edge of the prism at $Re = 2.5 \times 10^3$; and (b) Distribution of the time-averaged streamwise velocity (\bar{u}) at the location of the leading-edge of the prism at $Re = 1 \times 10^3, 2.5 \times 10^3$, and 5×10^3 . Measurements were performed in absence of the prism. Dashed line shows the boundary layer thickness (δ/d).

implications of boundary-layer thickness and dynamics on the wake topology were incorporated in the analysis. Moreover, Smits et al. (2019b) and Goswami and Hemmati (2020) have had scrutinized how immersing the prism inside the boundary layer affect flow dynamics compared to partially immersed case. Given the aspect-ratios considered for this research ($AR = h/d = 0.25 - 1.5$), prisms were always fully immersed in the boundary layer. Boundary layer thickness may have a pronounced effect on the flow dynamics around the prism, such that increasing the boundary-layer thickness enhances upwash flow, significantly Wang et al. (2006). Finally, Figure 3.4b presents a comparison of the boundary layer profile with that of a theoretical Blasius solution with a high-order polynomial fitting (9th order).

Moderate Reynolds number flow

At moderate Reynolds numbers (definition provided in Chapter 1), the boundary layer thickness is expected to be thinner compared to low Reynolds numbers. δ varied between $1.5d$ and d for $Re = 1 \times 10^3$ and 5×10^3 , respectively, when simulating the flow without placing the prism in the

domain. The boundary layer thickness at $Re = 2.5 \times 10^3$ was $\delta/d \approx 1.2$ as shown in Figure 3.5a. Since the boundary layer thickness changes with Reynolds number (see Figure 3.5b), implications of boundary layer thickness and dynamics on the wake topology has been naturally incorporated in the current analysis. As noted by Behera and Saha (2019), implications of boundary layer thickness on the wake are negligible considering a small ($\sim 10\%$) variation in δ . In the current study, the change in δ is $\sim 8\%$, while the variations in Reynolds number is $\sim 100\%$ and that for the depth-ratio is $\sim 99\%$. Thick boundary-layer ($\delta/h \geq 1$, fully submerged body) considered in this study imply that the oncoming flow over the prism length plays a significant role in dictating the wake characteristics through variations in the strength of separated vortex sheets over the prism length (Bourgeois et al., 2011).

Further, a local maximum in the streamwise mean velocity profile close to the wall was noted in Figure 3.5a due to the presence of an unbounded boundary layer. These are typically exterior boundary layers forming along ground surfaces. Defining characteristic of this type of flow is that the velocity profile goes through a peak or a local maxima near the viscous boundary layer edge and then slowly asymptotes to the free stream velocity (U_b) (Swanson and Langer, 2016). Such boundary layers are typical of numerical studies with open-channel flow configurations and some very large gap interior flows in channels and pipes. An example of this type of boundary layer flow is near-wall air flow over a wing in flight (Swanson and Langer, 2016).

3.5 Statistical analysis and time-averaging

Turbulent phenomena are reproducible only in a statistical sense (Reif and Durbin, 2011). Therefore, various averaged quantities are used to describe turbulent flows, providing physical insights and a robust understanding of the mechanisms that govern flow structures and their evolution. In the context of statistically stationary turbulence, where mean quantities are invariant under any time translation, all mean values are derived through time-averaging. Consequently,

statistical analysis of the flow is essential for understanding flow dynamics. To analyze unsteady simulation results in this thesis, both instantaneous and time-averaged quantities were examined.

Turbulent flow fields in this thesis were statistically converged, meaning their statistical quantities did not depend on time translation. However, time windows for conducting the time-averaging must be carefully adjusted to ensure that statistical data are accurately representing physical flow behavior. A key issue in selecting the averaging time window was determining when to start collecting flow statistics, which should not be influenced by the initial conditions. It was crucial to ensure that the flow was fully developed and had reached a statistically converged state before beginning the data collection. To this end, unphysical initial conditions were excluded prior to statistical analysis.

Evolution of the flow from initial state to a fully-developed state is considered here, for example, using LES results of the case with $AR = 1$ and $DR = 4$ at $Re = 2.5 \times 10^3$. Boundary conditions of this simulation followed those described in Section 3.3. The flow was initialized with a uniform velocity profile at the inlet and a zero-gradient condition at the outlet. The prism was placed at the center of the domain, and the flow was allowed to evolve for a sufficient number of vortex shedding cycles to ensure its statistical convergence. Sufficient duration of the time window over which the averaging is performed is another important factor for conducting the time-averaging. Depending on the flow configuration, duration of the time window can be characterized based on different time-scales. For the flow around a prism, duration of one vortex shedding cycle was considered as a proper time-scale. Typically, window for conducting time-averaging must be long enough such that time-averaged results do not change by increasing the duration, which is an indication of converged time-averaged statistics.

In the present thesis, all simulations continued for 150 vortex shedding cycles. This number was chosen based on preliminary results presented in Figure 3.6, which shows the complete time-history and moving cumulative average of streamwise (u) and normal velocity (v) near the leading-edge and in the wake of the prism. Figure 3.6 demonstrates that the mean (time-averaged) quantities are statistically converged after approximately 50 shedding cycles and remained stable

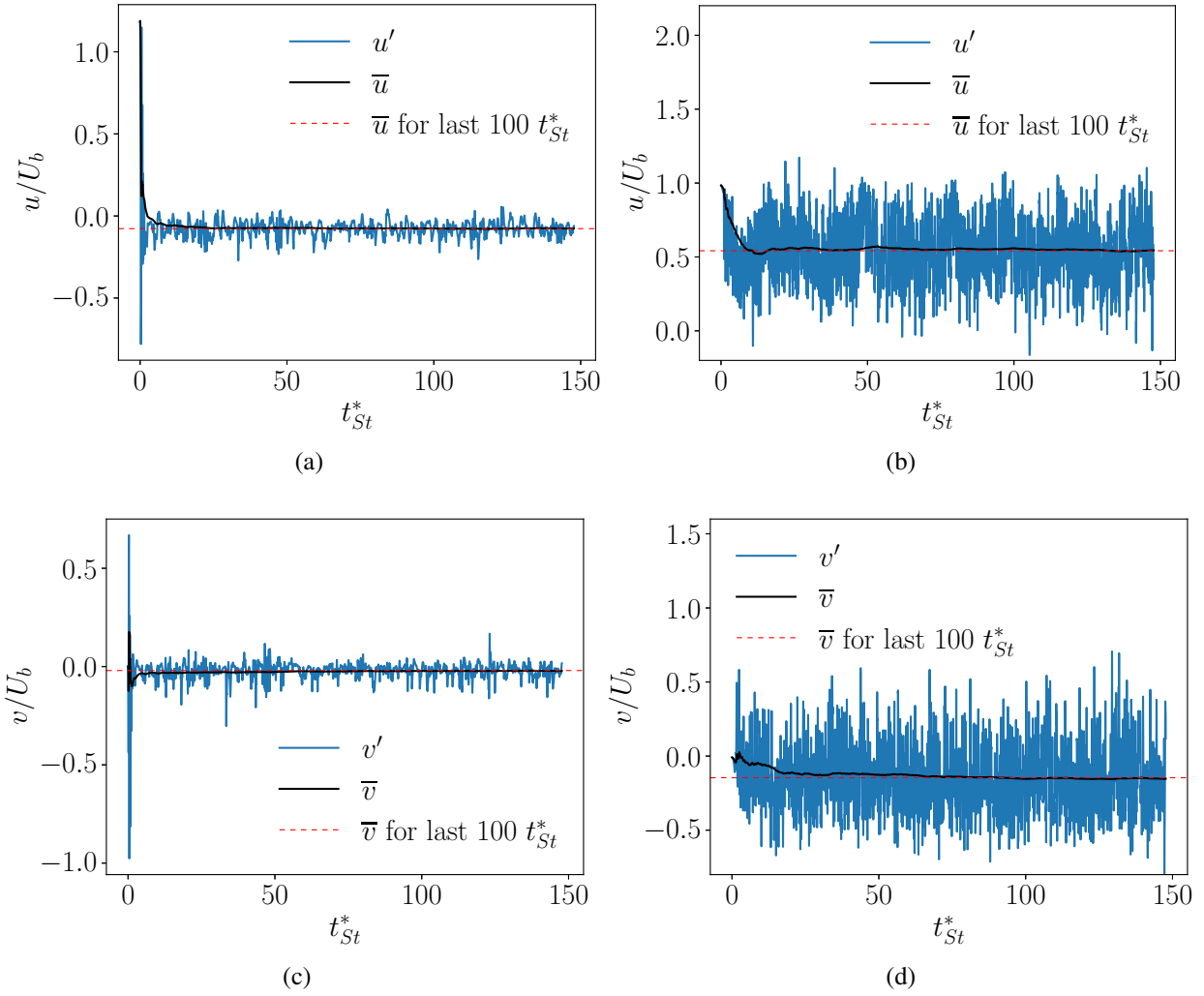


Figure 3.6: Complete time-history and moving cumulative average of (a, c) streamwise (u) and (b, d) normal velocity (v) in the wake of the prism with $AR = 1$ and $DR = 4$ at $Re = 2.5 \times 10^3$.

for the remainder of the simulation time. Further, the final 50 shedding cycles showed no significant differences in the mean drag coefficient, indicating that the flow is statistically converged. This time-history provided a clear indication that the flow had reached steady state conditions after 50 vortex shedding cycles, and the last 100 cycles were sufficient to obtain reliable time-averaged quantities. The same time-averaging procedure was applied to all simulations in this thesis.

3.6 Verification Studies

Verification studies ensured that numerical simulations were accurate and reliable. Numerical setup is verified by evaluating the sensitivity of results to domain size, spatial grid resolution, and temporal grid resolution (Hemmati et al., 2018b). Sections below discuss verification studies in this dissertation.

Low Reynolds number flow

The case of wall-mounted thin flat plate ($DR = 0.016$) at Reynolds number of 2.5×10^2 was considered for domain and grid sensitivity since it provided the most complex unsteady wake dynamics compared to other cases at low Reynolds numbers. All verification and validations simulations were completed by directly solving the Navier-Stokes equations using *pimpleFoam* solver in OpenFOAM. Quantitative assessment of the sensitivity results involved the mean and turbulent flow quantities, as well as the integral (global) flow variables. The mean axial (\bar{u}/U_b) and normal (\bar{v}/U_b) velocities, along with Reynolds stresses, and turbulence kinetic energy trends were studied at multiple axial locations downstream of the body. The integral (global) flow variables compared here were Strouhal number, defined by

$$St_{sh} = f_{sh}d/U_b, \quad (3.14)$$

and mean drag coefficient, defined by

$$\overline{C_d} = \frac{\overline{F_d}}{0.5\rho U_b^2 dh}. \quad (3.15)$$

Here f_{sh} is the vortex shedding frequency and $\overline{F_d}$ is the mean drag force acting on the body.

Sensitivity of simulation results to domain size was evaluated using three domains: Domain 1 ($30d \times 5d \times 10d$), Domain 2 ($30d \times 6d \times 12d$), and Domain 3 ($35d \times 6d \times 12d$). These domains were designed such that they are larger than those in previous studies involving the wake of wall-mounted prisms (Saha, 2013; Saeedi et al., 2014; Rastan et al., 2021). Further, Sohankar et al.

Table 3.1: Grid sensitivity analysis results for wall mounted thin prism case ($DR = 0.016$).

Study	N_{total}	Domain Size	St_{sh}	$ \Delta St_{sh}\% $	\bar{C}_d	$ \Delta \bar{C}_d\% $
Domain 1	6.59×10^6	$30d \times 5d \times 10d$	0.1894	—	1.12255	—
Domain 2	7.32×10^6	$30d \times 6d \times 12d$	0.1875	1	1.0919	2.75
Domain 3	7.58×10^6	$35d \times 6d \times 12d$	0.1876	0.05	1.0918	0.01
Grid 1	8.07×10^5	$30d \times 6d \times 12d$	0.1570	—	1.0835	—
Grid 2	2.49×10^6	$30d \times 6d \times 12d$	0.1804	12.97	1.0940	0.96
Grid 3	7.32×10^6	$30d \times 6d \times 12d$	0.1875	3.78	1.0919	0.21
Time 1	7.32×10^6	$30d \times 6d \times 12d$	0.1875	—	1.0919	—

(1998) and Saha (2013) defined a criterion for design of domains based on blockage ratio (β) and domain height (H):

$$\beta = (d \times h) / (W \times H) \leq 0.05 \quad \& \quad H \geq h + 5d.$$

This ensured that there are negligible effects on the global flow quantities. Here, the blockage ratio and domain height were 0.01 and $6d$, respectively. Table 3.1 compares Strouhal number and time-averaged (mean) drag coefficient obtained from three domain sizes, which indicates less than 1% deviation between Domain 2 and Domain 3. Thus, Domain 2 was selected for the final simulations.

Quality of the spatial grid was evaluated using three successively refined grids with 8.07×10^5 , 2.49×10^6 and 7.32×10^6 elements. The grid resolution was identical to previous wake studies (Narasimhamurthy and Andersson, 2009; Hemmati et al., 2018b; Rastan et al., 2021; Zargar et al., 2021a). Comparison of the global flow variables in Table 3.1 indicates a good agreement between Grid 2 and Grid 3. The maximum deviation in Strouhal number and mean drag coefficient between Grid 2 and Grid 3 was $\sim 4\%$ and $\sim 0.5\%$, respectively. Since the variations are less than 5%, based on the recommendations of Saha (2013) and Zargar et al. (2021b), Grid 3 was sufficient to capture global wake features. Finally, assessment of time-step sensitivity was evaluated using two time steps: Grid 3 ($\Delta t^* = \Delta t U_b/d = 0.0065$) and Time 1 ($\Delta t^* = 0.00325$). The results in

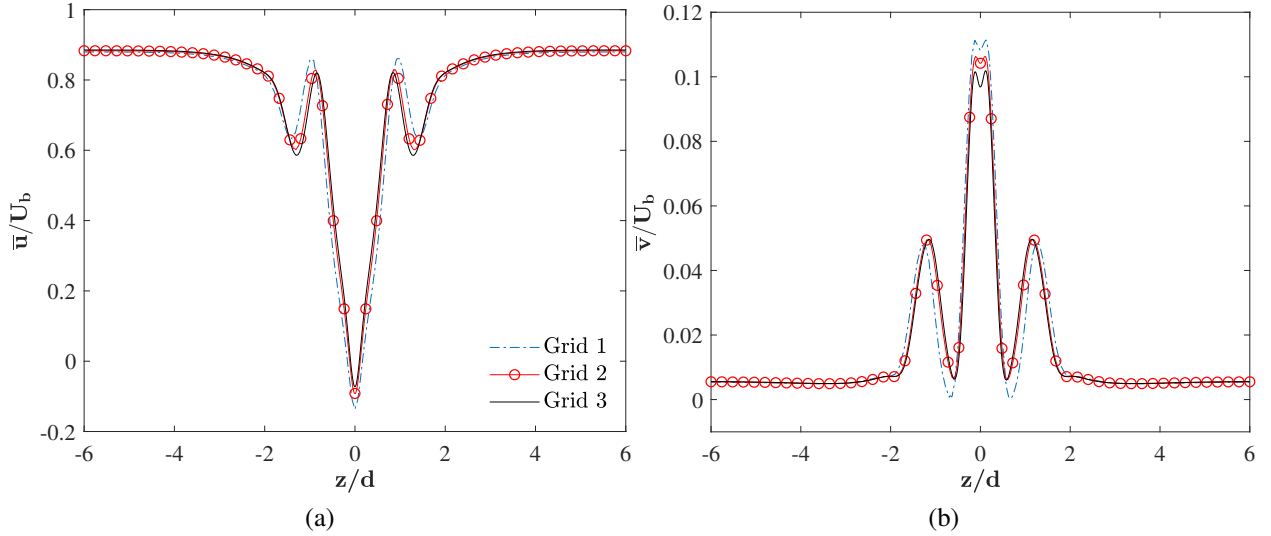


Figure 3.7: Effect of grid size on mean velocities at $x/d = 3$ and $y/d = 0.5$, for prism of $DR = 0.016$ at Reynolds number of 2.5×10^2 . Shown are profiles of (a) \bar{U} and (b) \bar{V} .

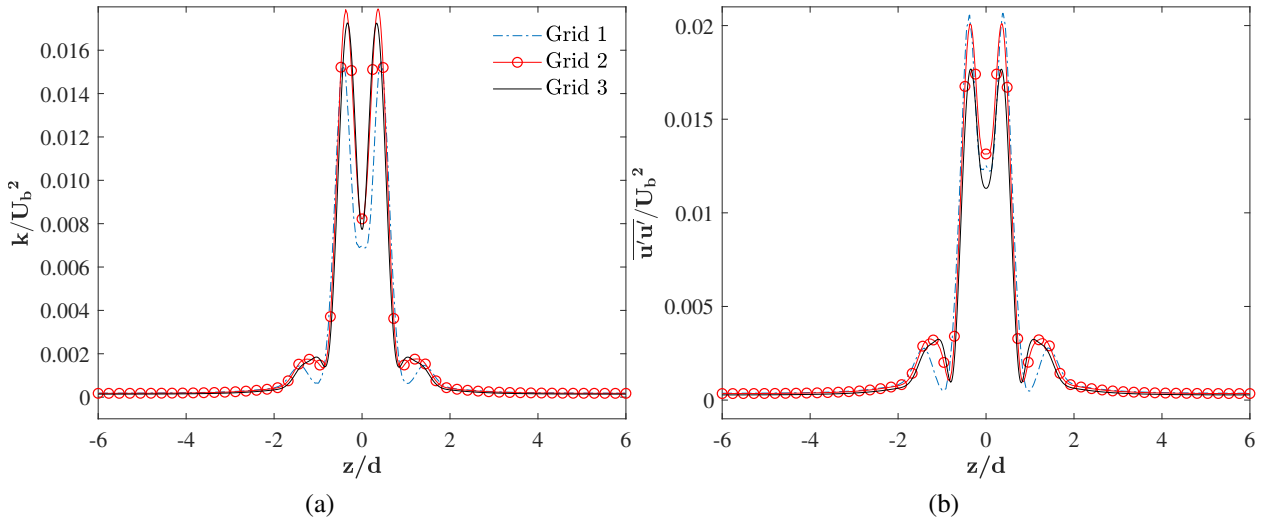


Figure 3.8: Effect of grid size on wake turbulence characteristics at $x/d = 3$ and $y/d = 0.5$, for prism of $DR = 0.016$ at Reynolds number of 2.5×10^2 . Shown are profiles of (a) k/U_b^2 and (b) $\bar{u}'\bar{u}''/U_b^2$.

Table 3.1 show that the Strouhal number and mean drag coefficient were consistent between Grid 3 and Time 1. Since the variations were negligible, temporal resolution of Grid 3 was selected for the final simulations at Reynolds numbers between 5×10^1 and 5×10^2 .

The grid sensitivity analysis was expanded by tracing the effects of grid resolution on mean velocities, Reynolds normal stress ($\bar{u}'\bar{u}''$), and turbulence kinetic energy defined as

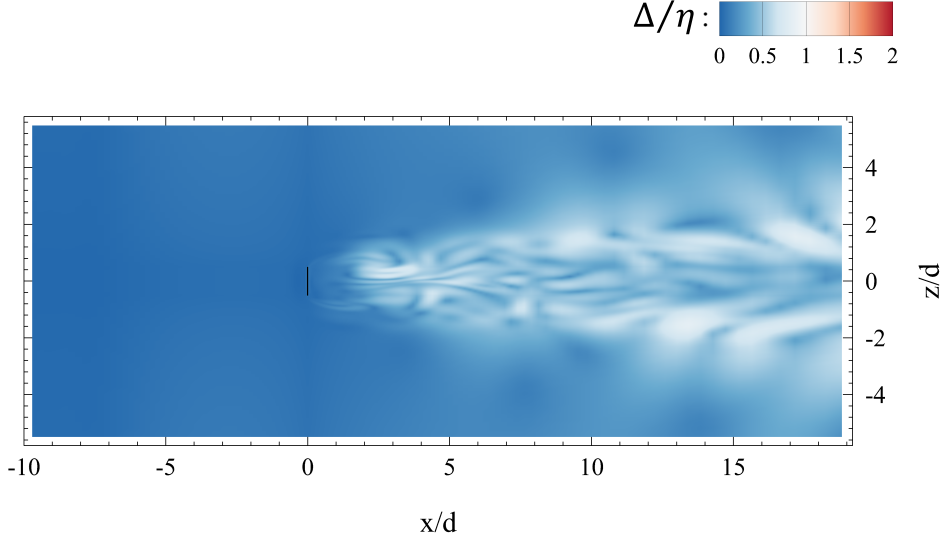


Figure 3.9: Contours of the ratio of grid-size to Kolmogorov length scale (Δ/η) at $y/d = 0.5$ for the case of wall mounted thin prism ($DR = 0.016$) at Reynolds number of 2.5×10^2 .

$$k = \frac{1}{2}(\overline{u'u'} + \overline{v'v'} + \overline{w'w'}). \quad (3.16)$$

While grid sensitivity was performed at two streamwise locations (i.e. $x/d = 3$ and 5), only the results at $x/d = 3$ are shown in Figures 3.7 and 3.8 for brevity. The mean streamwise and normal velocity profiles are compared in Figure 3.7, where the difference between Grid 2 and Grid 3 was not substantial inside the base region ($\sim 5\%$). However a slight discrepancy, corresponding to a maximum of $\sim 11\%$, was noted in normal velocity. Figure 3.8 compares the profiles of Reynolds normal stress ($\overline{u'u'}$), which was the largest stress in the near-wake region, and turbulence kinetic energy (k). The results were consistent with those of mean flow, meaning that the turbulent field was not sensitive to spatial grid size for Grid 2 and Grid 3. Although Grid 2 was sufficient for accurately solving the flow, Grid 3 was utilized to ensure the grid resolution was sufficient for capturing all small- and large-scale flow features.

Further examination of the spatial resolution was complemented by investigating the ratio of grid size to Kolmogorov length scales (Δ/η). Accuracy of the simulation results requires the smallest resolved scales to be of the same order of magnitude as the Kolmogorov length scale (Moin and Mahesh, 1998; Kawamura et al., 2007; Narasimhamurthy and Andersson, 2009;

Saeedi et al., 2014; Hemmati et al., 2018b; Rastan et al., 2021). The grid size was estimated using

$$\Delta = (\Delta x \times \Delta y \times \Delta z)^{1/3}$$

following the recommendations of Yakhot et al. (2006). Kolmogorov length scale was estimated using

$$\eta = (v^3/\epsilon)^{1/4},$$

where ϵ is the viscous dissipation rate defined by

$$\epsilon = 2\nu\overline{S_{ij}S_{ij}},$$

and S_{ij} was the strain-rate tensor (Pope, 2001). Contours of Δ/η are studied to ensure adequacy of downstream grid quality. Past studies on bluff body wakes recommend $\Delta/\eta \leq 4$ until $8d$ downstream of the body (Narasimhamurthy and Andersson, 2009; Hemmati et al., 2016), while numerical studies of Yakhot et al. (2006) and Saeedi et al. (2014) on wall-mounted prisms recommend an optimum criterion of $2 \leq \Delta/\eta \leq 5$ for the critical wake region. Contour of Δ/η in Figure 3.9 reveals that Δ/η increases with x/d such that the maximum Δ/η is 0.1 at $x/d = 1$ and marginally increases to ≈ 0.8 at $x/d = 5$. Further downstream, the maximum ratio remains below 1 until $x/d = 20$. My grid resolution (Figure 3.9) follows these criteria stringently in the critical regions of the flow such that Δ/η does not exceed 1 for the entire domain. This confirms the adequacy of the numerical results.

Moderate Reynolds number flow

Since Large Eddy Simulations were utilized at moderate Reynolds numbers, it became essential to verify the numerical setup. For this purpose, the case of a wall-mounted long prism ($DR = 4$) at Reynolds number of 2.5×10^3 was selected. LES results were verified by evaluating the sensitivity of results to domain size and grid resolution. The domain development criteria followed those

Table 3.2: Domain and grid sensitivity analysis results for wall mounted prism with $DR = 4$ at $Re = 2.5 \times 10^3$. The relative error is calculated with respect to Domain 2 and Grid 4, respectively.

Study	N_{total}	Domain Size	y_{max}^+	\bar{C}_d	$ \Delta \bar{C}_d\% $	\bar{C}_l	$ \Delta \bar{C}_l\% $
Domain 1	17.3×10^6	$30d \times 5d \times 10d$	0.8	1.102	5.60	0.921	5.14
Domain 2	19.6×10^6	$30d \times 6d \times 12d$	0.8	1.041	—	0.875	—
Domain 3	20.9×10^6	$35d \times 6d \times 12d$	0.8	1.043	0.19	0.876	0.10
Grid 1	5.1×10^6	$30d \times 6d \times 12d$	3.1	1.100	5.51	0.914	5.33
Grid 2	15.1×10^6	$30d \times 6d \times 12d$	1.55	1.061	2.36	0.899	3.55
Grid 3	19.6×10^6	$30d \times 6d \times 12d$	0.8	1.041	0.38	0.875	0.90
Grid 4	25.2×10^6	$30d \times 6d \times 12d$	0.44	1.037	—	0.868	—
Time 1	25.2×10^6	$30d \times 6d \times 12d$	0.44	1.037	—	0.868	—

discussed earlier in this section. Moreover, based on the practices of Sohankar et al. (1998) and Saha (2013), blockage ratio (β) and Domain height (H) were set as 0.01 and $6d$, respectively, following the criterions of

$$\beta = (d \times h) / (W \times H) \leq 0.05 \quad \& \quad H \geq h + 5d,$$

to ensure negligible effects of domain on global flow features.

Grid sensitivity was assessed using four successively refined grids with 5.1×10^6 , 15.1×10^6 , 19.6×10^6 , and 25.2×10^6 elements. Sensitivity of the domain size and grid distribution on global flow features, e.g., mean drag (\bar{C}_d) and lift coefficients (\bar{C}_l), were evaluated. The results in Table 3.2 indicates that Domain 2 ($30d \times 6d \times 12d$) is sufficient. Relative errors in \bar{C}_d and \bar{C}_l between Grid 3 and Grid 4 were below 1%, indicating grid convergence for Grid 3 as presented in Table 3.2. As such, Domain 2 and Grid 3 were selected for further analysis.

Sensitivity analysis were expanded to the mean and turbulent flow characteristics simulated using LES. The results are presented in Figure 3.10. Comparing profiles of \bar{u} and $\overline{u'u'}$, a close agreement is noted between Domain 2 and Domain 3, at $x/d = 1$ downstream of the prism for all domain sizes. The influence of blockage is further apparent in Domain 1, where the centerline velocity is significantly higher compared to other domains. Based on these results, it was confirmed

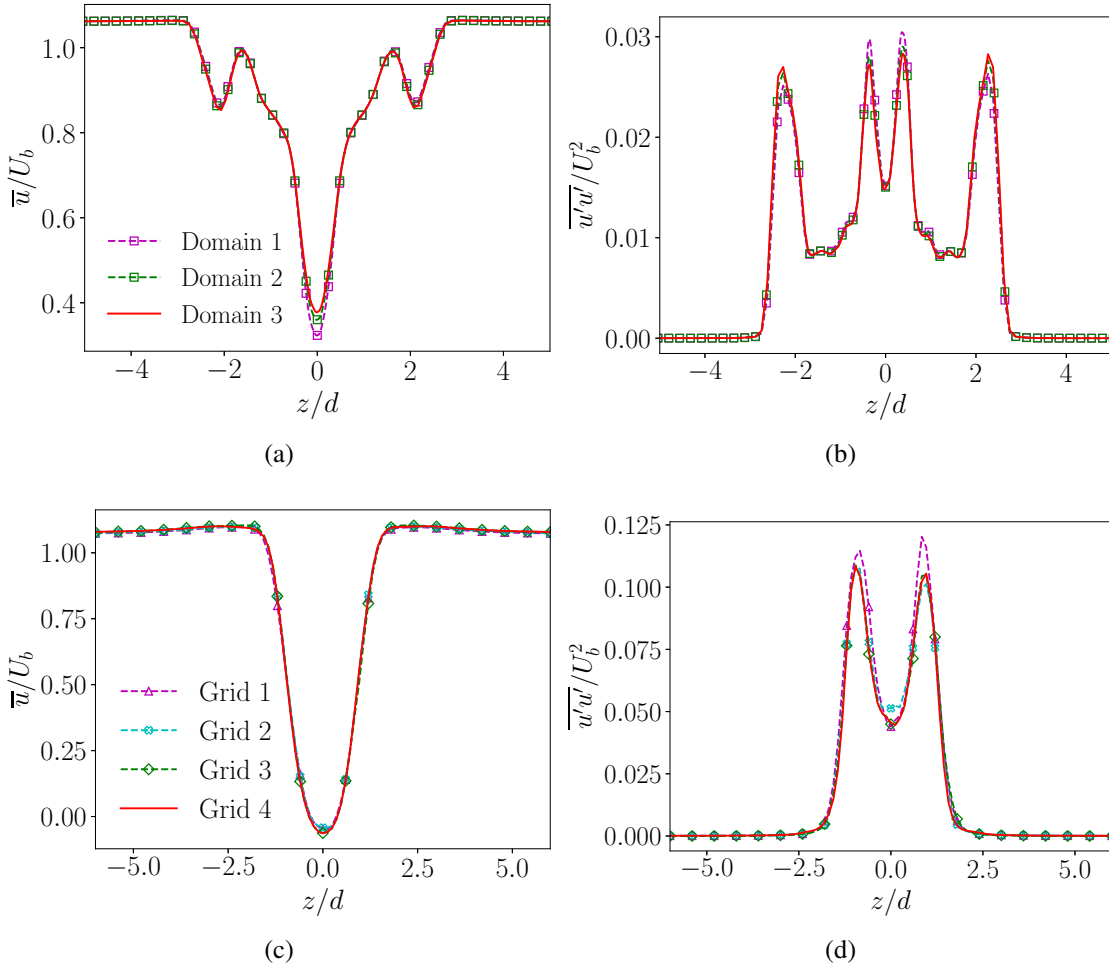


Figure 3.10: Effect of (a, b) Domain and (c, d) Grid sizes on mean and turbulent wake characteristics. Shown are (a, c) \bar{u} and (b, d) $\overline{u'u'}$.

that Domain 2 was sufficient to capture wake characteristics. Similarly, the grid sensitivity analysis revealed that Grid 3 was sufficient to capture the wake characteristics with negligible influence of further grid refinement. The results in Figure 3.10c and 3.10d indicate an excellent agreement between Grid 3 and Grid 4 with a maximum of 1% deviation. The results of the grid and domain sensitivity analysis confirm that selected domain and grid sizes are sufficient to capture the wake characteristics at moderate Reynolds numbers. Finally, a temporal grid sensitivity analysis was performed using two time steps: Grid 4 ($\Delta t^* = 0.001$) and Time 1 ($\Delta t^* = 0.0005$). The results in Table 3.2 show that Strouhal number and mean drag coefficient were consistent between Grid 4

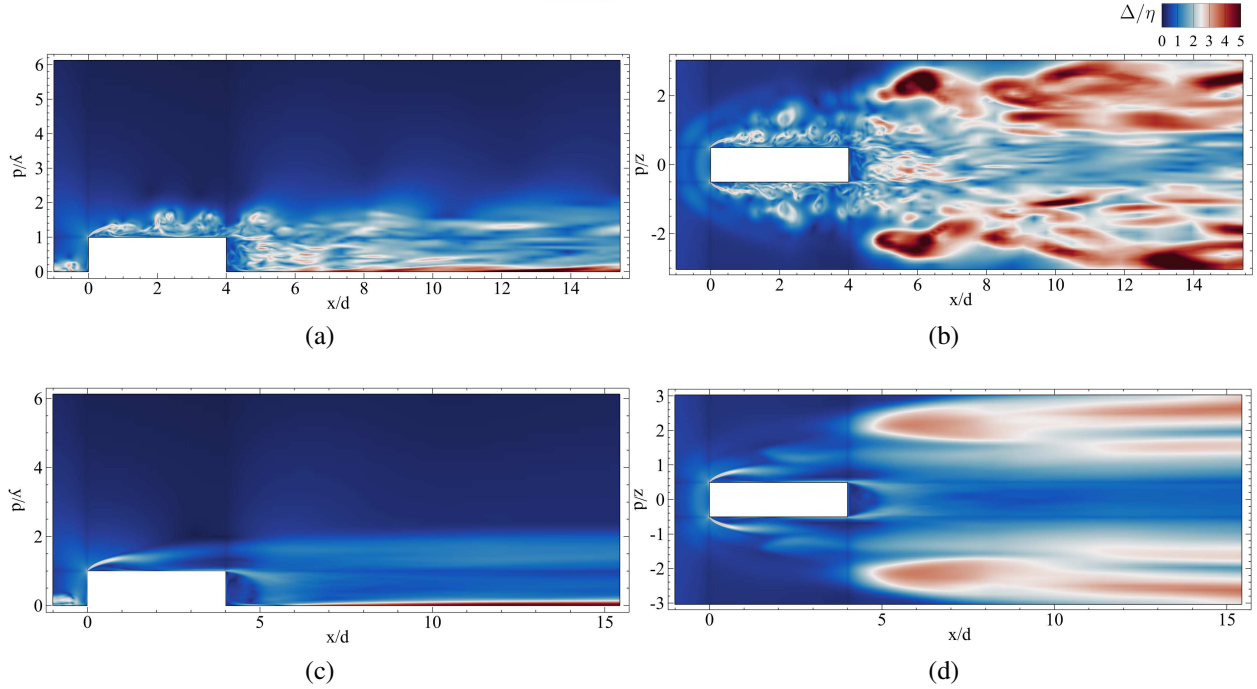


Figure 3.11: Contours of (a, b) instantaneous and (c, d) time-averaged (mean) distributions of the ratio of grid size to Kolmogorov length scale (Δ/η) in the (a, c) symmetry plane ($z/d = 0$) and (b, d) x-z plane ($y/d = 0.5$) for the case of $DR = 4$ at $Re = 2.5 \times 10^3$.

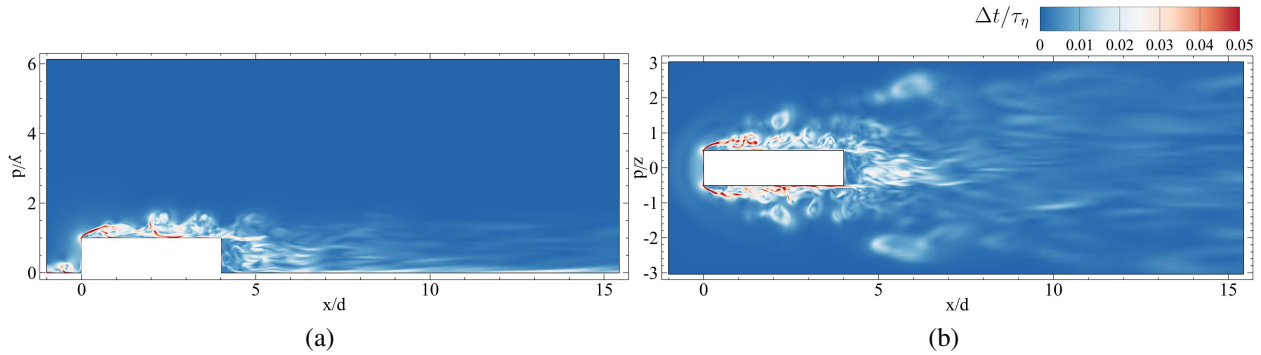


Figure 3.12: Contours of ratio between time-step (Δt) and the Kolmogorov time scale (τ_η) for the instantaneous flow field in the (a) symmetry plane ($z/d = 0$) and (b) x-z plane ($y/d = 0.5$) for the case of $DR = 4$ at $Re = 2.5 \times 10^3$.

and Time 1. Negligible variations were noted, indicating that the temporal resolution of Grid 4 was sufficient for simulations at Reynolds numbers between 1×10^3 and 5×10^3 .

The analyses in this thesis demands accurate resolution of the smallest resolvable flow features, such as the leading-edge shear-layer and KHI. To this end, grid size should be

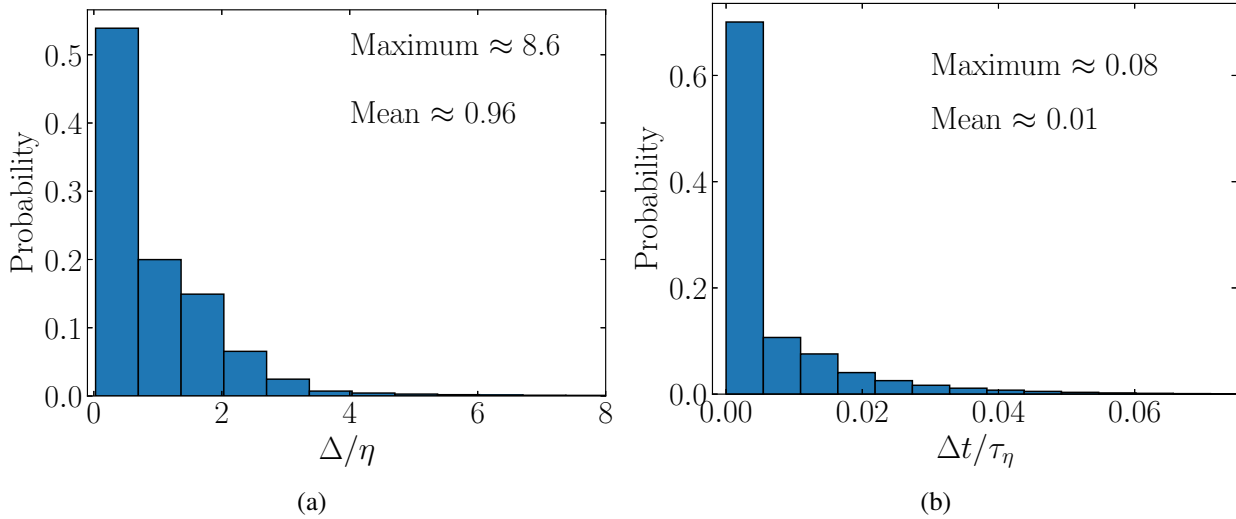


Figure 3.13: Histogram of the (a) ratio of grid size to Kolmogorov length scale (Δ/η) and (b) ratio of time-step size to the Kolmogorov time scale (τ_η) for the case of $DR = 4$ at $Re = 2.5 \times 10^3$. Histogram is presented for the instantaneous flow field in the entire computational domain.

comparable to Kolmogorov length scale (Moin and Mahesh, 1998). Therefore, ratio of grid size (Δ) to Kolmogorov length scale (η) was analyzed for further verification. Contours of Δ/η in Figure 3.11 show that both instantaneous and time-average (mean) values of Δ/η fall within the required range of 5 – 10 discussed earlier. Particularly, Δ/η is smaller than 5 in the mean, while it is greater than 5 in the unsteady flow. Maximum value of Δ/η is ≈ 8.6 at $x/d = 15$, with Δ/η between 1 and 3 in the immediate vicinity of the prism. Probability density histogram of Δ/η for the entire computational domain is presented in Figure 3.13a. Results further confirms that the majority of the flow was resolved with $\Delta/\eta < 5$. Further, the maximum values of Δ/η is 8.6, well within the range of 5 – 10 (Yakhot et al., 2006; Saeedi et al., 2014; Celik et al., 2009; Rastan et al., 2021). The mean value of Δ/η is ≈ 0.96 , which fits well within the ratio suggested by Cimarelli et al. (2018), indicating that the grid resolution was sufficient to capture the transitional mechanisms and shear-layer instabilities of the leading-edge shear-layer. Together, the results of Δ/η indicated that resolution of Grid 3 was sufficient to capture critical flow features behind the wall-mounted prism at moderate Reynolds numbers.

Closeness between the smallest resolved time-scales and Kolmogorov time-scale (τ_η) determines the accuracy in resolving the fluctuations in turbulent flow (Moin and Mahesh, 1998; Li et al., 2020). As such, the ratio between time step size (Δt) and Kolmogorov time-scale, given as $\tau_\eta = (v/\epsilon)^{1/2}$, is evaluated to confirm the validity of the numerical setup. This analysis complemented the temporal grid sensitivity study discussed earlier. Li et al. (2020) had suggested that the mean time ratio ($\Delta t/\tau_\eta$) should be less than 0.0205 for finely resolved time-scale corresponding to ≈ 50 eddy-turnover times. Moreover, Duong et al. (2024) suggested the ratio remain in the range of $0.02 \leq \Delta t/\tau_\eta \leq 0.05$ near the leading-edge and side shear layers. Contours of $\Delta t/\tau_\eta$ are presented in Figure 3.12 and the Probability density of $\Delta t/\tau_\eta$ in the entire computational domain is presented in Figure 3.13b. Results in Figure 3.13b show that the maximum and mean values of $\Delta t/\tau_\eta$ are 0.08 and 0.01, respectively, indicating that the time-step size was well within the range suggested by Li et al. (2020). Further, majority ($\sim 95\%$) of the computational domain had $\Delta t/\tau_\eta < 0.02$, while only $\sim 0.5\%$ area confined to the leading-edge of the prism showed $0.02 \leq \Delta t/\tau_\eta \leq 0.06$. As shown in Figure 3.12, $\Delta t/\tau_\eta \approx 0.05$ in the immediate vicinity of the prism, with average $\Delta t/\tau_\eta \approx 0.01$ in the wake region. $\Delta t/\tau_\eta$ distribution, following the criterion of Li et al. (2020) and Duong et al. (2024), confirmed that temporal grid resolution was sufficient to capture the small-scale turbulent fluctuation in this dissertation.

3.7 Validation Studies

Verification studies presented in the previous section provided an accurate and optimized numerical setup to evaluate the wake dynamics of wall-mounted prisms at low and moderate Reynolds numbers. Validation was performed to ensure that this numerical setup accurately captured the wake dynamics around wall-mounted prisms.

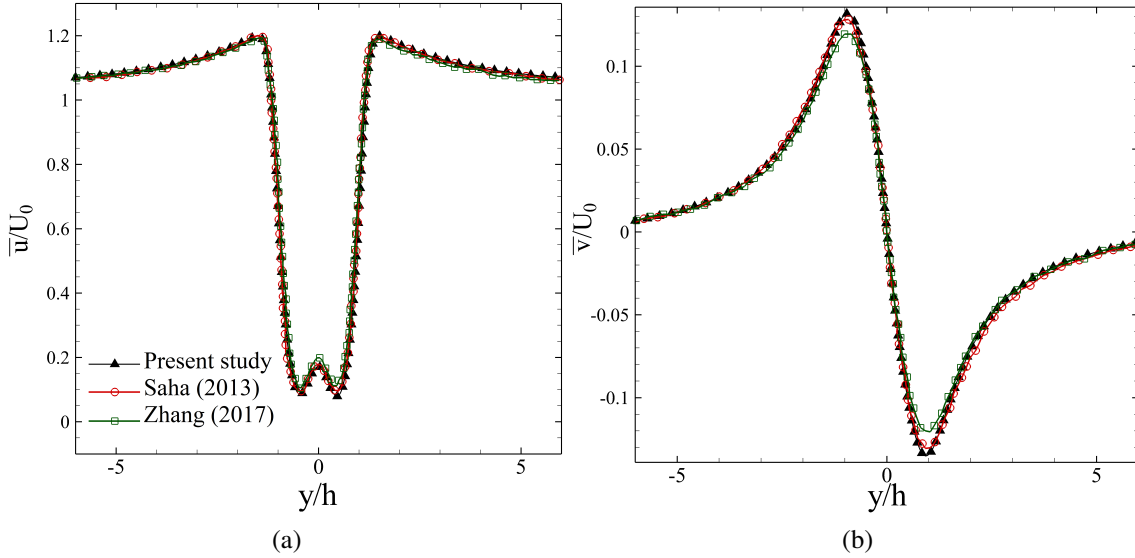


Figure 3.14: Time-averaged (a) streamwise and (b) spanwise velocity distributions at $Re = 2.5 \times 10^2$, behind a rectangular prism with $AR = 4$ compared with DNS result of Zhang et al. (2017) and Saha (2013).

Low Reynolds number flow

There have been several attempts to validate numerical results from OpenFOAM in literature (Robertson et al., 2015; Verma and Hemmati, 2020; Goswami and Hemmati, 2020; Ren et al., 2022). The current numerical set-up at low Reynolds numbers were compared with validated numerical studies of Saha (2013) and Zhang et al. (2017). This is due to limited experimental analysis at low Reynolds number range and varying depth-ratios. Since there are no comprehensive studies, to the best of my knowledge, on the wake of prisms with varying depth-ratios at low Reynolds numbers ($Re \leq 10^3$), Figure 3.14 presents a comparison with well established DNS results in literature for validation of the numerical setup. Figure 3.14 compares time-averaged streamwise and spanwise velocity distributions behind a rectangular prism with aspect-ratio 4 at Reynolds number of $Re = 2.5 \times 10^2$, which was studied by Zhang et al. (2017) and Saha (2013) using DNS. Profiles in Figure 3.14 collapse well, showing only small discrepancies in the streamwise velocity deficit. These results confirm that the numerical setup accurately captures the wake dynamics of wall-mounted prisms at low Reynolds numbers.

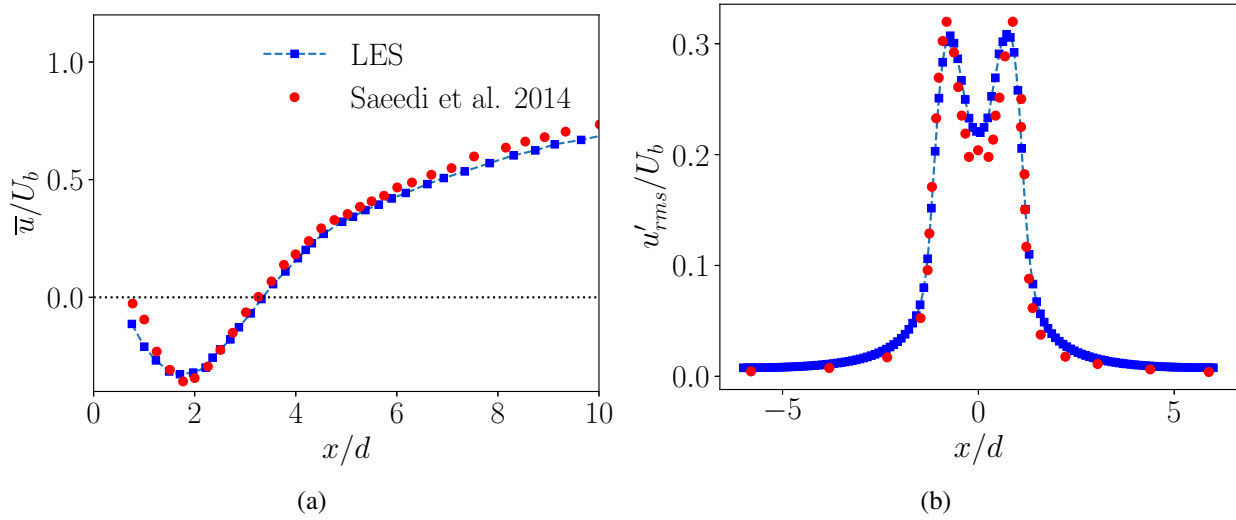


Figure 3.15: Comparison of (a) mean axial velocity (\bar{u}) and (b) root-mean-squared velocity (u'_{rms}) profiles obtained from LES with the experimental results of Saeedi et al. (2014).

Moderate Reynolds number flow

Lack of experimental data for the specific case of a prism with $DR = 4$, $Re = 2.5 \times 10^3$, demanded an alternative validation approach that mimicked the setup of Saeedi et al. (2014) for the case of $AR = 4$ prism at $Re = 1.2 \times 10^5$ using LES. LES grid resolution and computational setup mirrored that presented in this dissertation. Mean axial velocity profiles from LES agreed well with Saeedi et al. (2014), such that less than 5% deviation (Figure 3.15a) was noted between experiments and numerical simulations. Figure 3.15b further shows satisfactory agreement between LES and experimental results in capturing the root-mean-squared velocity profiles. Further, the trends at the peak and into the wake were well reproduced by numerical simulations. This outcome validated the LES numerical setup.

3.8 Assessment of Wake Dynamics

The main objective of this dissertation requires qualitative and quantitative assessment of a complex wake flow. Qualitative methods include visualizing wake features using two- or three-dimensional iso-contours of Q -criterion (Jeong and Hussain, 1995). Quantitative methods

include characterizing the wake using vortex circulation (Godoy-Diana et al., 2009), transport of mean shear-layers (Smits et al., 2019b), and recovery of momentum (More et al., 2015). Further data-driven quantitative assessment of coherent structures is performed using Dynamic Mode Decomposition (DMD) (Schmid, 2010) and Bi-Spectral Mode Decomposition (Schmidt, 2020).

3.8.1 Assessing the strength of vortex

Distribution of axial vorticity (ω_x^*) and spanwise vorticity (ω_z^*) provides deeper insight into the cross-sectional wake topology and axial wake features. Past wake studies have utilized circulation (Γ) to assess the strength and size of vortices in the wake (Godoy-Diana et al., 2009; Verma and Hemmati, 2021; Zargar et al., 2022b). Mathematically, circulation (Γ) is calculated using the line-integral of velocity along a closed curve encompassing the vortex, or by area-integral of vorticity (Godoy-Diana et al., 2009), given as:

$$\Gamma = \iint_A (\nabla \times u) \cdot dA, \quad (3.17)$$

where A is the surface area bounding the vortex. Godoy-Diana et al. (2009) has shown the discrepancy in line-integral based methods, involving spurious contribution of opposite signed vortices in the integral. Thus, the area-integral based method is used in this thesis, which uses a rectangular integration window constructed over the the contour plot of vorticity surrounding the vortex. Center of the window denotes the location of maximum or minimum vorticity for anti-clockwise or clockwise rotating structures, respectively. A Gaussian-fit centered at the location of minimum or maximum vorticity corresponds to $e^{-(x_i/\sigma_i)}$, where σ_i denotes the standard deviation of vorticity. Size of the vortex is quantified as $2\sigma_i$, and circulation (Γ) is calculated by area-integral over a rectangular window within $2\sigma_i$.

3.8.2 Dynamic Mode Decomposition (DMD)

Physical mechanisms underlying the flow relies on spatio-temporal characterization of coherent structures in the wake, especially for a complex system, i.e., flow around a wall-mounted prism (Schmid, 2010). This thesis utilizes DMD to investigate complex flow behavior around a wall-mounted prism, which enables identifying spatial structures with characteristic frequencies associated with them. Thus, it provides a spatio-temporal characterization of the wake. The general description of the flow is given by a time series:

$$x_t = Ax_{t-1} + r, \quad (3.18)$$

where x_t denotes the snapshot vector in time, t , and A is the linear mapping coefficient vector. Snapshots are assumed to be related via the linear mapping coefficient (A):

$$X_2 = \{x_2, x_3, \dots, x_t\} \approx A\{x_1, x_2, \dots, x_{t-1}\} = AX_1. \quad (3.19)$$

Thus, temporal dynamics of the flow can now be analyzed using eigenvalue analysis. DMD uses *Koopman* algorithm to approximate the coefficient matrix (Schmid, 2010), based on which Singular Value Decomposition (SVD) is performed on the matrix (X_1):

$$X_1 = USV^T, \quad (3.20)$$

where U and V are the left and right singular vectors, and S is the diagonal matrix composed of the singular values. This is followed by computing the Koopman matrix using truncated SVD:

$$\tilde{A} = U_r^T X_2 V_r S_r^{-1}. \quad (3.21)$$

Finally, computation of the eigenvalue decomposition of the Koopman matrix is performed by

$$\tilde{A} = Q\Phi Q^T, \quad (3.22)$$

where \mathbf{Q} consists of eigenvectors and Φ consists of eigenvalues. Dynamic modes, or DMD modes, are eigenvectors. Thus, DMD analysis enables segregating the induced effects of each frequency on the overall wake by reconstructing the wake using these modes.

In this study, a total of 310 three-dimensional, high-fidelity numerical simulations were conducted to investigate the wake dynamics and vortex interactions behind wall-mounted prisms. These simulations were performed using OpenFOAM CFD toolbox. The simulations varied across a range of depth-ratios, aspect-ratios and Reynolds numbers, providing a comprehensive dataset to analyze and understand the wake dynamics of wall-mounted bluff bodies. The results of these simulations are presented in the following chapters.

Chapter 4

WAKE ASYMMETRY AND SECONDARY STRUCTURES BEHIND WALL-MOUNTED PRISMS[‡]

Depth-ratio (length-to-width) of wall-mounted prisms with small aspect-ratio (height-to-width) is a critical parameter influencing instantaneous wake dynamics and downstream wake topology. Among the limited studies addressing depth-ratio effects (see Section 2.2), the emphasis has primarily been on wake topology and force characteristics. Detailed analyses of near-wake instabilities, both low- and high-frequency processes (Morton et al., 2018; Kindree et al., 2018), are notably absent. These instabilities are fundamental to understanding wake dynamics, particularly the transition from steady to unsteady wake regimes (Section 2.2). Furthermore, they lead to the formation of secondary vortex structures alongside coherent structures such as arch-type, Kármán-type, or hairpin-like vortex shedding (Diaz-Daniel et al., 2017a). For wall-mounted finite prisms, there is no clear consensus on the terminology or interactions of secondary vortex structures. Previous studies, summarized in Section 2.2, have described these

[‡]The content of this chapter has been published in *Journal of Fluid Mechanics* under the citation (Goswami and Hemmati, 2022): “Goswami, S., & Hemmati, A. (2022). Mechanisms of wake asymmetry and secondary structures behind low aspect-ratio wall-mounted prisms. *Journal of Fluid Mechanics*, 950, A31”.

structures in terms of time-averaged streamwise vortices observed in the wake. However, the interaction between secondary vortex structures and shedding coherent structures remains largely unexplored.

This chapter investigates the wake of wall-mounted prisms with small aspect-ratio and varying depth-ratio, focusing on wake asymmetry and secondary structures. The primary objective is to identify the mechanisms governing wake asymmetry and secondary structures, with an emphasis on transition processes across different depth-ratios and Reynolds numbers. The study examines prisms with $AR = 1$ and $DR = 0.016 - 4$ at $Re = 5 \times 10^1 - 5 \times 10^2$. These prisms are immersed in a laminar boundary layer, with the minimum depth-ratio representing a thin wall-mounted prism, analogous to a flat plate. This configuration enables the exploration of wake evolution mechanisms, including free-end effects and shear-layer dynamics, in prisms with small aspect-ratios. This chapter is structured such that the Results and Discussion are presented in Section 4.1, followed by a summary of the key findings in Section 4.2.

4.1 Results and Discussion

The classification of the wake topology as steady or unsteady is conducted across a range of Reynolds numbers and depth-ratios. Here, steady wake is defined by the absence of any fluctuations in either wake or forces, whereas unsteady wakes feature small and large wake variations and force fluctuations. A wake map is presented in Figure 4.1 for wall-mounted prisms of different depth-ratios at different Reynolds numbers. Here, the wake is classified as either steady or unsteady, which is further sub-divided into symmetric and asymmetric wakes. For clarity, symmetric wakes are defined by the symmetric orientation of the main instantaneous wake features about the mid-planar axis, such as hairpin-like structures, tip and base vortices, as well as the horseshoe vortex. Contrarily, asymmetric wakes exhibit vortical features with periodic distortions about the mid-planar axis, leading to side-way (spanwise) tilting of shed structures. This highlights a change in wake topology that closely depends on the prism depth-ratio at a

range of Reynolds numbers for a low aspect-ratio body. Particularly, results in Figure 4.1 indicate that the wake is steady for $DR = 0.016$ until $Re = 1.5 \times 10^2$, after which it becomes unsteady. The Reynolds number at which this wake transition occurs increases with increasing depth-ratio, such that the wake remains steady up to $Re = 2 \times 10^2$ for $DR = 0.1$ and $Re = 4 \times 10^2$ for $DR = 1$. In previous studies, the unsteady wake transition as a function of Reynolds number is mainly discussed with increasing aspect-ratios. Saha (2013) identified transitional flow at Reynolds number of 2.5×10^2 for $AR = 2$ prism, while Zhang et al. (2017) identified similar unsteady transition for $AR = 4$ prism at Reynolds number of 1.5×10^2 . In case of wall-mounted cube, this transition was noted at $Re = 5 \times 10^2$ (Diaz-Daniel et al., 2017b). This dissertation scrutinizes such transition as a function of Reynolds number and depth-ratios. Further classification of the unsteady wake also reveals interesting topological differences that are identified in terms of wake symmetry, or there lack of. This study only focus on identifying and characterizing the wake mechanism at Reynolds number of 250 and 500, since the wake remains coherent without three-dimensional turbulent effects that could complicate the flow at high Reynolds numbers (Saha, 2013; Zargar et al., 2021a). Moreover, this Reynolds number exhibits both categories of unsteady wake, the mechanisms associated with which are important in development of the wake topology. However, discussions on changing wake topology with Reynolds number and depth-ratio form the basis of a future study.

The instantaneous wakes are characterized starting with the lowest depth-ratio ($DR = 0.016$) at $Re = 2.5 \times 10^2$. There exists a wake unsteady transition with increasing depth-ratio at this Reynolds number. The wake is unsteady for $DR \leq 0.1$ and it transitions to a steady wake for $DR = 0.3 - 4$. Moreover, the wake of the very thin prism exhibits unique features at $Re = 2.5 \times 10^2$, leading to asymmetric characteristics. These were not observed at lower Reynolds numbers or for larger depth-ratios. The characterization of these wake features are initially discussed in the next section, followed by analyzing the mechanisms associated with the wake development for low depth-ratio prisms, i.e., $DR \leq 0.1$, and characterizing secondary structures in the wake in latter sections.

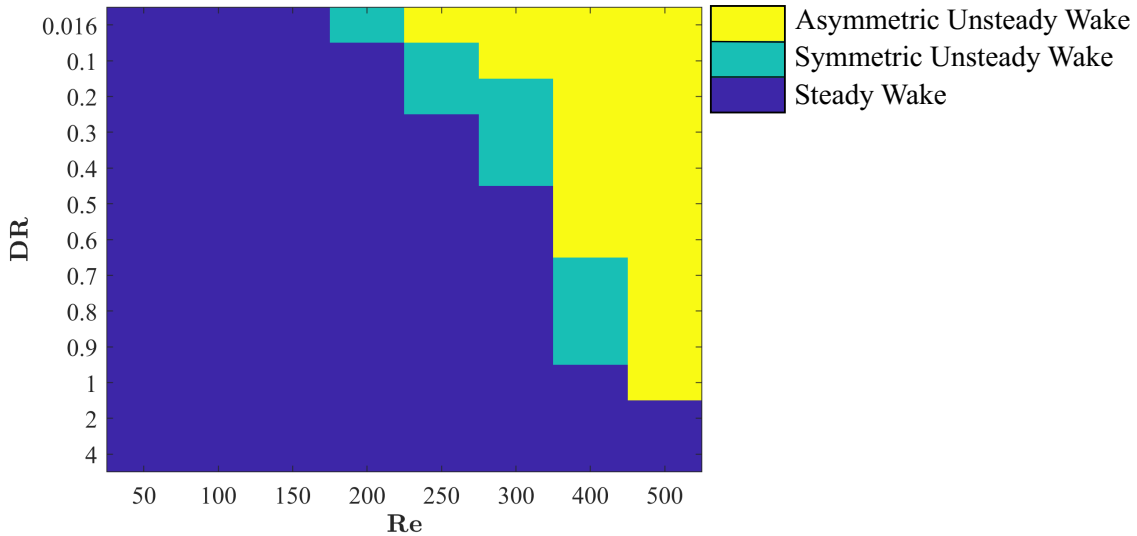


Figure 4.1: Classification of the wake topology in terms of Reynolds number and depth-ratio.

4.1.1 Wake Classification

The wake classification in Figure 4.1 identifies that Reynolds number threshold for transition to unsteady wake increases with increasing depth-ratio. It becomes clear that the wake is steady for all depth-ratios at $Re \leq 1.5 \times 10^2$. With further increase in Reynolds number to 2×10^2 , a transition to unsteady wake occurs for $DR = 0.016$, while the wake of $DR \geq 0.1$ remains steady. At $Re = 2.5 \times 10^2$, the wake transitions from unsteady to steady with changing depth-ratio. Moreover, wake of the very thin prism exhibits asymmetric characteristics, which changes to symmetric shedding, followed by a steady wake at larger depth-ratios. Although it is important to identify how wake topology changes with increasing Reynolds number and depth-ratio, and the correspondence between the two parameters, this analysis falls outside the scope of the current study. Instead, this study only focuses on identifying and characterizing the wake at $Re = 2.5 \times 10^2$, as well as the mechanism of asymmetric wake patterns that are observed at $Re \geq 2.5 \times 10^2$. To this effect, analysis of the wake of our thin prism ($DR = 0.016$) at $Re = 2.5 \times 10^2$ is first performed, which is the onset of wake asymmetry. Please note that our analyses are also valid for larger depth-ratios or Reynolds numbers, as long as the wake classification remains the same as that identified for the thin prism at the given Reynolds number.

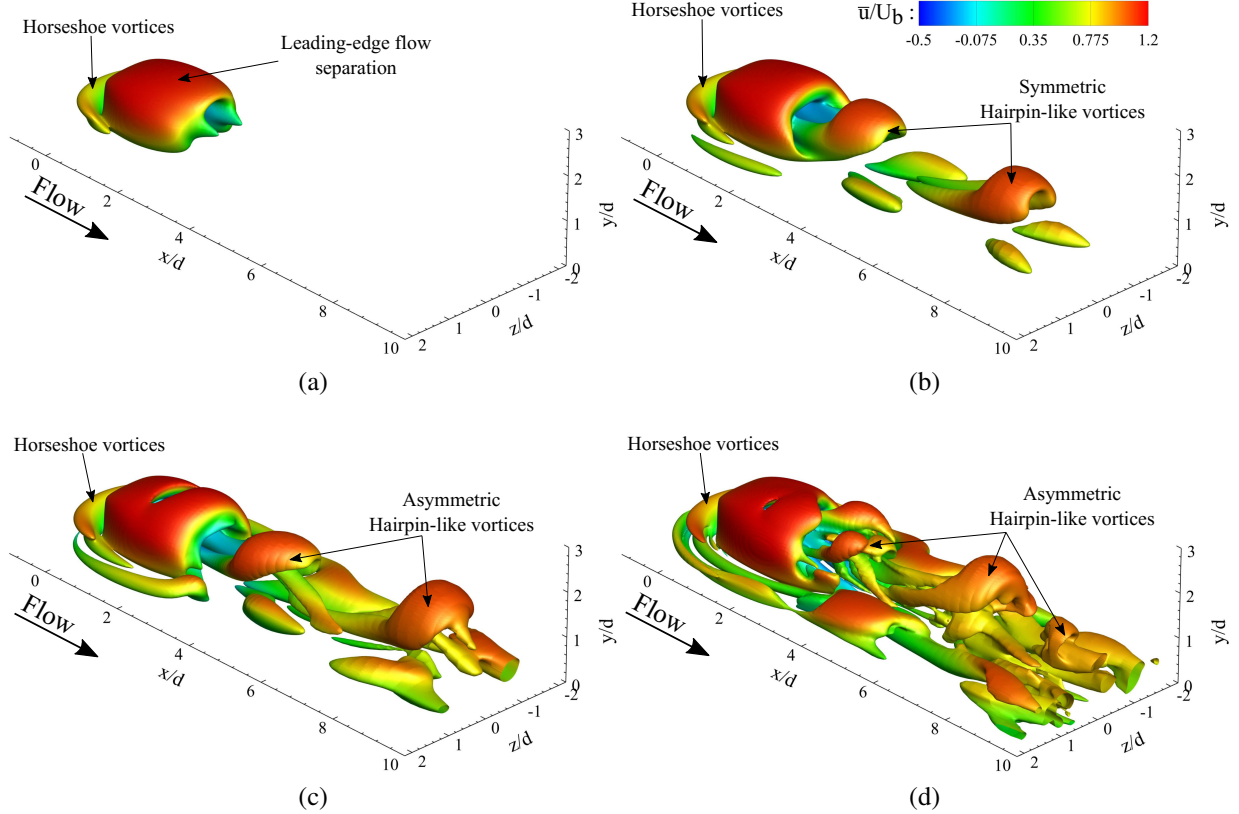


Figure 4.2: Instantaneous vortex structures of $DR = 0.016$ prism identified using $Q^* = 6 \times 10^{-6}$ and overlaid with mean streamwise velocity (\bar{u}/U_b), at (a) $Re = 1.5 \times 10^2$; (b) $Re = 2 \times 10^2$; (c) $Re = 2.5 \times 10^2$; and (d) $Re = 5 \times 10^2$. All figures are shown in three-dimensional view.

Figure 4.2 shows the wake topology behind the very thin prism ($DR = 0.016$) over the range of $Re = 1.5 \times 10^2 - 5 \times 10^2$. These results identify a clear change in wake topology with changing Reynolds number. The case of very thin prism is selected because it clearly marks the onset of unsteady wake, as well as transition from symmetric to asymmetric wake characteristics. Similar analyses can be undertaken for any other depth-ratio and Reynolds number cases, and similar observations are expected for the same wake topology (classifications based on Figure 4.1). Unsteady wake structures, their formation, evolution and interactions are investigated using the Q -criterion, as described by Hunt et al. (1988) and Jeong and Hussain (1995). Iso-surface plots overlaid with mean streamwise velocity (\bar{u}/U_b) contours in Figure 4.2 demonstrate the transition of wake features with changing Reynolds number for $DR = 0.016$. At $Re \leq 1.5 \times 10^2$, the wake remains steady, and the formation of horseshoe vortex (Simpson, 2001) and

leading-edge shear layer separation is clear. The onset of unsteady wake occurs at Reynolds number of 2×10^2 , which is characterized by formation of symmetric hairpin-like vortices. Diaz-Daniel et al. (2017b) reported similar symmetric wake structures behind a cube. They attributed the symmetric shedding to the interaction of tip vortices, formed at the upper-part of prism side surfaces, with the shear-layer created over the prism, leading to flow unsteadiness. Further increase in Reynolds number to 2.5×10^2 leads to asymmetric hairpin-like wake structures. At $Re = 5 \times 10^2$, the wake of very thin prism, although unsteady and asymmetric, cannot maintain its coherence far downstream. This could be attributed to stronger interactions between the shed structures, as a result of increased unsteadiness (Diaz-Daniel et al., 2017b; Zargar et al., 2021a). Here, the wake asymmetry is characterized by distortion of the head of the hairpin-like structure, which leads to spanwise (side-way) tilting of structures, as noted in Figure 4.2c. Identifying the wake features that are altered by the changing depth-ratios and characterizing secondary structures and their interactive mechanisms with the wake forms the basis of our analyses for the remainder of this paper.

Since the onset of asymmetric wake occurs at $Re = 2.5 \times 10^2$, this study looks at instantaneous streamwise vorticity ($\overline{\omega_x}^*$) contours for the case of very thin prism at $Re = 2.5 \times 10^2$ and 5×10^2 in Figure 4.3. These results enable us to investigate the formation, interaction and distortion of near-wake vortical structures. There are three main observations that can be discussed with respect to the results in Figure 4.3. First, the wake appears symmetric in the immediate vicinity of the prism at $x/d = 0$. Two pairs of counter-rotating tip vortices are noted here, with *primary tip vortex* forming on top part of the prism side surface, and *secondary tip vortex* forming on the prism top surface. This is consistent with the wake topology of wall mounted prisms (Rastan et al., 2021). The second observation is that near-wake structures lose streamwise coherence due to stronger interaction between shed structures and increased unsteadiness with increasing Reynolds number towards $Re = 5 \times 10^2$. As such, structures at $x/d = 1$ for $Re = 5 \times 10^2$ appear distorted compared to $Re = 2.5 \times 10^2$. The third observation relates to an influx of vorticity at $x/d = 2$, which corresponds to the formation of secondary vortex structures in the wake. These secondary structures appear

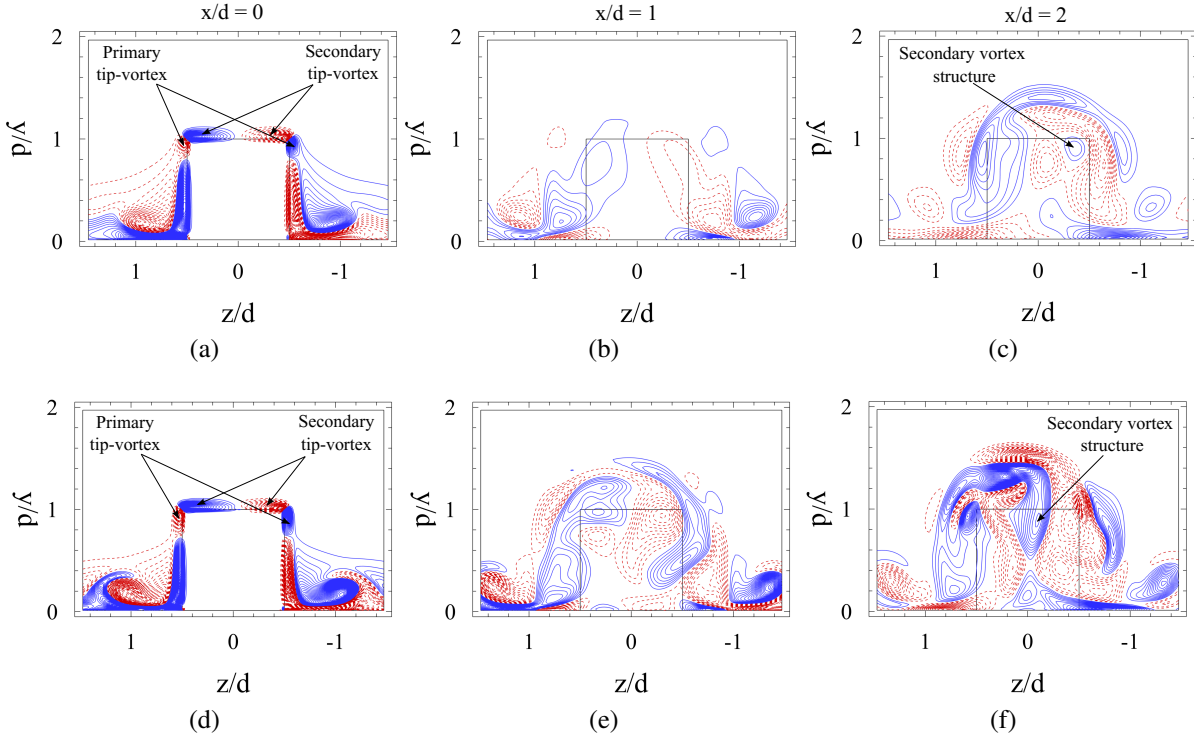


Figure 4.3: Contours of instantaneous streamwise vorticity ($\bar{\omega}_x^*$) structures (solid blue lines: positive values, dashed red lines: negative values) for $DR = 0.016$ at (a-c) $Re = 2.5 \times 10^2$ and (d-f) $Re = 5 \times 10^2$. The line contour cutoff levels for $\bar{\omega}_x^*$ are ± 0.12 and the contour interval is 0.001. The contours are shown at $x/d = 0, 1$ and 2 .

distorted at higher Reynolds numbers, compared to $Re = 2.5 \times 10^2$, possibly due to incoherent interactions with the separating shear-layers from the prism top and side surfaces (Diaz-Daniel et al., 2017b). These secondary structures also appear in case of symmetric unsteady wakes (i.e., $DR = 0.1$ at $Re = 2.5 \times 10^2$ in Figure 4.21), in which case they are placed symmetrically in the wake. Thus, this study expand on the previous investigation of the mechanism of wake asymmetry based on these observations focusing on the case of $Re = 250$, which enables characterization of wake devoid of major incoherent, transient effects.

Finally, it becomes important to scrutinize variations in flow dynamics at higher depth-ratios for the given ranges of Reynolds numbers for completeness. Figure 4.1 reveals that the unsteady asymmetric wake exists for $DR = 0.9$ at $Re = 4 \times 10^2$, while it vanishes for Reynolds number of 5×10^2 . It is evident from the iso-surface plots shown in Figure 4.4 that $DR = 1$ at Reynolds number of 5×10^2 results in asymmetric unsteady wake, which quickly becomes steady with increasing

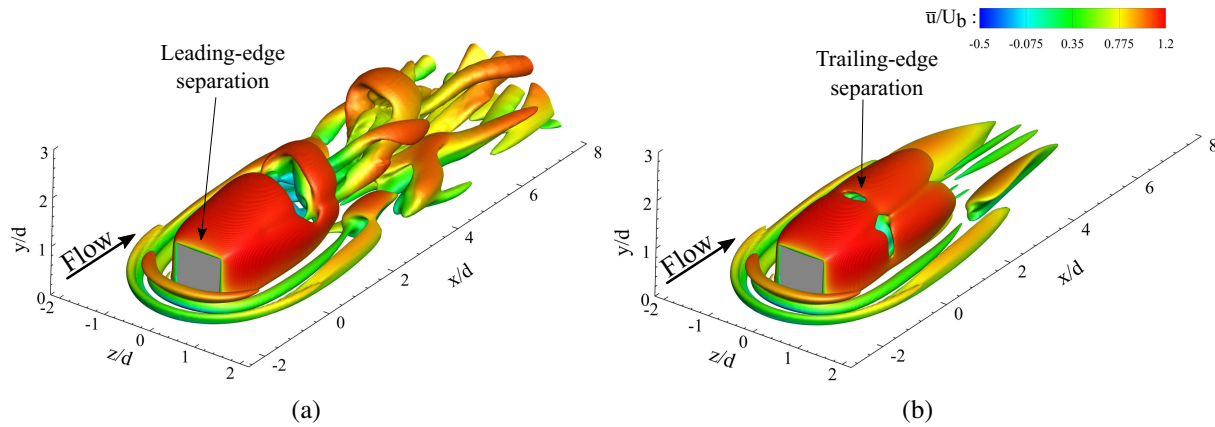


Figure 4.4: Instantaneous vortex structures for (a) $DR = 1$ and (b) $DR = 1.5$ prisms at Reynolds number of 5×10^2 , identified using $Q^* = 6 \times 10^{-6}$ and overlaid with mean streamwise velocity (\bar{u}/U_b). All figures are shown in three-dimensional view.

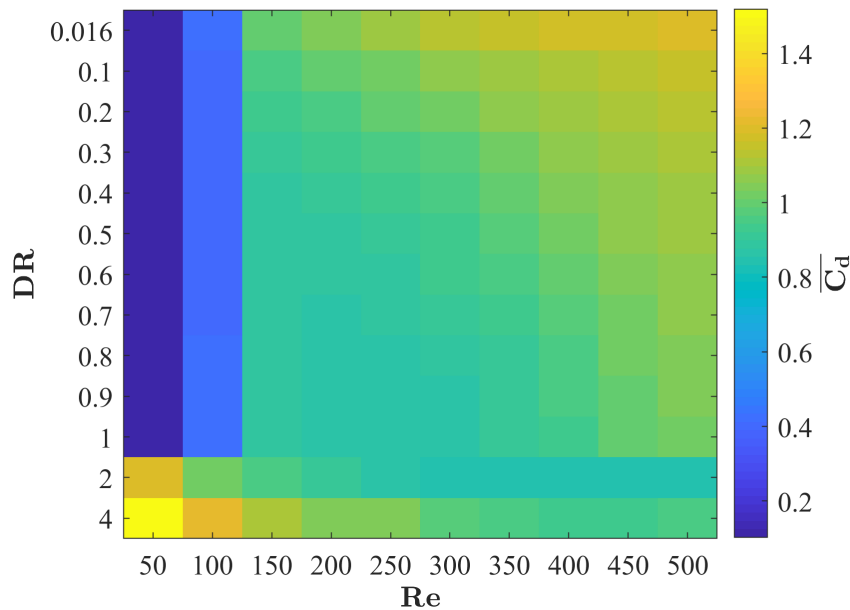


Figure 4.5: Trends of drag coefficient (C_d) with varying depth-ratios and Reynolds numbers.

depth-ratio to 1.5. Trailing edge flow separation as a result of shear-layer reattachment on the prism top and side surfaces for large depth-ratio ($DR \geq 1$) prisms lead to the suppression of unsteady flow characteristics (Zargar et al., 2021b; Rastan et al., 2021). For the present study, Figure 4.4 shows trailing-edge flow separation for the case of $DR = 1.5$ at $Re = 5 \times 10^2$, resulting in steady flow.

Figure 4.5 illustrates the variation of drag coefficient with changing depth ratio (DR) and Reynolds numbers. For $DR \leq 1$, drag coefficient increases with Reynolds number, likely due to enhanced flow separation and increased pressure drag, as inertial effects dominate. Conversely, drag coefficient decreases with Reynolds number at $DR > 1$, which is attributed to an increased recirculation length and steady flow. These findings align with the results of Zargar et al. (2021b), who observed similar trends for wall-mounted long prisms. While the present study does not establish a direct correlation between drag and wake topology, it emphasizes identifying the mechanisms governing wake transitions and vortex interactions. These interactions, particularly vortex shedding and recirculation dynamics, play a crucial role in shaping the wake behavior of wall-mounted prisms with small aspect ratios, providing insights into their aerodynamic characteristics and flow-induced forces.

4.1.2 Instantaneous wake characteristics

Wake analysis is performed by looking at the asymmetric unsteady wake formation at $Re = 2.5 \times 10^2$. Iso-surface plots are overlaid by the mean streamwise velocity (\bar{u}/U_b) contours in Figure 4.6, which demonstrate a difference in the wake with changing depth-ratio. The wake of prisms with $DR = 0.016$ and 0.1 is unsteady at $Re = 2.5 \times 10^2$, while that of $DR \geq 0.3$ is steady. This indicates an unsteady-to-steady transition of the flow with increasing depth-ratio. The two common features of the wake, for all the cases considered here, are the formation of horseshoe vortices in front of the prism, and the shear layer separation at the leading edge. The latter folds after the initial separation on top and side surfaces of the prism as the depth-ratio increases. Hereinafter, the focus of this thesis will be on the unsteady wake features, their formation mechanisms, unique characteristics, and potential sources.

The flow around a wall-mounted prism with a very small depth-ratio ($DR < 0.3$ at $Re = 2.5 \times 10^2$) experiences shear-layer separation and roll-up, leading to vortex shedding. The wake of such prisms are dominated by hairpin-like vortices that are formed along the top face of the prism. These are clearly identified in Figures 4.6a and 4.6b. This is consistent with observations of Hemmati

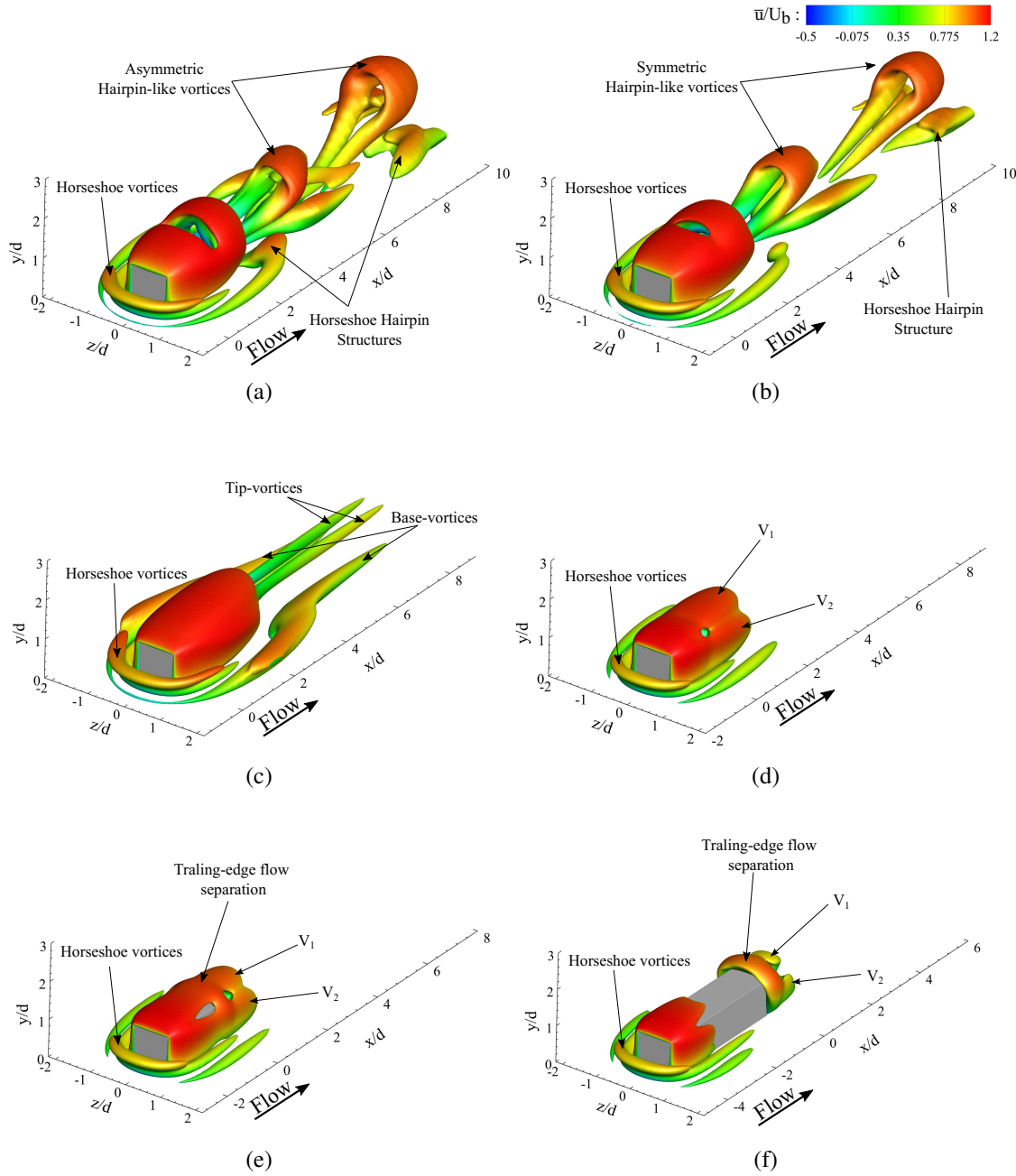


Figure 4.6: Instantaneous vortex structures identified using Q -criterion and overlaid with mean streamwise velocity (\bar{u}/U_b), for (a) $DR = 0.016$; (b) $DR = 0.1$; (c) $DR = 0.3$; (d) $DR = 1$; (e) $DR = 2$ and (f) $DR = 4$, at Reynolds number of 2.5×10^2 . The threshold of $Q^* = 6 \times 10^{-6}$ is used for $DR = 0.016, 0.1, 1 - 4$, while $Q^* = 1 \times 10^{-6}$ is used for $DR = 0.3$ to avoid distorted contours. All figures are shown in three-dimensional view.

et al. (2016), who identified the wake of a finite aspect-ratio normal thin flat plate is dominated by vortex loops that are shed on the longer edges with legs that are “peeled-off” from the side (shorter)

edges. Here, head of the hairpin-like structure moves faster downstream compared to its legs. Thus, wake structures appear elongated or distorted in the streamwise direction. This observation is consistent with the fact that head of the hairpin is closer to the free-stream, while the legs are located closer to the boundary layer on the ground. Further, shedding of hairpin-like structures changes from asymmetrically to symmetrically placed hairpins with increasing depth-ratio from 0.016 to 0.1. This hints at the implications of depth-ratio in restoring the flow symmetry (Diaz-Daniel et al., 2017b), which remains prevalent for $DR \geq 0.3$ (steady cases).

Hairpin-like structures were symmetrically placed due to the flow separation-reattachment process on the prism top surface at depth-ratio of 0.1, which is consistent with the results of Hwang and Yang (2004), Yakhot et al. (2006), and Diaz-Daniel et al. (2017b) for a cube. Here, the results thus far clearly identify that wake of a small aspect-ratio prism with a very small depth-ratio is asymmetric at $Re = 2.5 \times 10^2$, while wake symmetry is restored with reattachment of the shear layer on the body with increasing depth-ratio. In simpler terms, evidence is provided in this thesis that increasing the depth-ratio leads to the restoration of flow symmetry in small aspect-ratio prisms.

The steady wake observed for cases of $DR \geq 0.3$ in Figures 4.6c-4.6f exhibit initial flow separation on leading edge of the prism that is followed by a shear layer reattachment on top and side faces. This process suppresses the wake three-dimensionality and unsteadiness according to Zargar et al. (2021a) and Rastan et al. (2021). Two aspects of flow separation are observed in the steady wake. First, a pair of tip and base vortices are identified in Figure 4.6c ($DR = 0.3$), which are either not formed or quickly distorted for $DR > 0.3$ in Figures 4.6d-4.6f. The existence of tip vortices for $DR = 0.3$ hints at the dominance of downwash induced flow, based on the discussions of Zargar et al. (2021b), which intensifies with increasing depth-ratio. Traces of tip vortices are missing for the case of $DR > 0.3$ in Figures 4.6d-4.6f, which is attributed to folding of initial shear-layer separation on the surfaces of the prism. The second feature of the wake involves an initial shear layer separation and reattachment on top and side surfaces of the prism for $DR > 0.3$, which is followed by trailing edge separation. This leads to the shear layer roll up and the

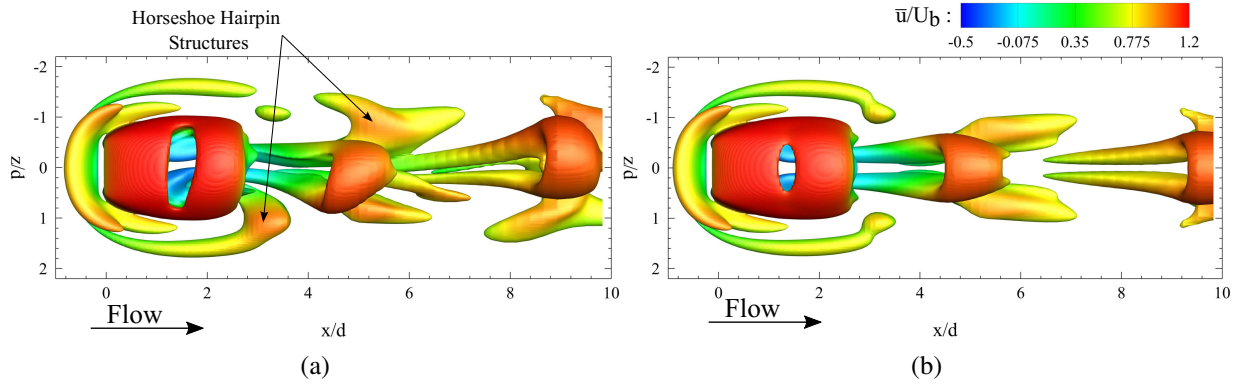


Figure 4.7: Instantaneous vortex structures identified using $Q^* = 6 \times 10^{-6}$ for (a) $DR = 0.016$ and (b) $DR = 0.1$, at Reynolds number of 2.5×10^2 . Figures are presented from top view.

formation of trailing edge vortices, identified as “ V_1'' and “ V_2'' in Figures 4.6d-4.6f on the prism top and side wakes, respectively. These trailing edge vortices entrain free-stream fluid into the wake, thus leading to intense downwash flow behind the prism. This is well aligned with previously reported observations of Zargar et al. (2021b) on the steady wake of long rectangular wall-mounted prisms.

Another important feature of the flow is the formation of a multi-part horseshoe structure at the base of the prism leading edge. For $DR < 0.3$, the legs of outer horseshoe are shed into the wake by forming hairpin-like structures. These structures are clearly identified in Figure 4.7. The formation of these hairpin-like structures has been previously reported in literature, which may be associated with vortical motions of the horseshoe vortex legs. Hwang and Yang (2004) and Diaz-Daniel et al. (2017b) reported the shedding of horseshoe vortex in the wake of a wall-mounted cube at $Re = 6 \times 10^2$. They suggested that the flow region around the horseshoe vortex is fundamentally similar to a quasi-streamwise vortex from the near-wall region of a turbulent wall-bounded flow. Hence, the hairpin structures were reasonably expected in this region, similar to those discussed by Adrian (2007). What is unique in the current study, however, is observing an asymmetric pattern for horseshoe-hairpins in Figure 4.7a (for $DR = 0.016$), while they are placed symmetrically around the prism for $DR = 0.1$. The horseshoe-hairpins for the former prism ($DR = 0.016$) are stretched as they progressed downstream, similar to the primary hairpin-like

vortices. Structures on either side of the prism appear distorted following the initial shedding close to $x/d = 3$. This coincides with their lower convective speed, which in turn leads to a small phase difference at $x/d = 9$. In case of $DR = 0.1$, however, no such phase difference exists, and the hairpins are symmetrically placed around the prism. The investigation of phase difference in the unsteady case is completed in the later part of the paper.

Expanding these studies to higher Reynolds numbers, i.e., the results in Figure 4.1, revealed that threshold depth-ratio, at which wake symmetry is restored, increases with increasing Reynolds number. This constitutes the effect of Reynolds number on wake transition mechanisms, which falls outside the scope of the current study. Nonetheless, a brief report on the transition mechanisms investigated in past literature is provided. The fundamental mechanism of wake transitions, that is the suppression of unsteadiness and restoration of wake symmetry, is a multivariate function. Wake transitions depend on flow parameters, such as Reynolds number, boundary layer thickness, and changing geometric parameters, e.g., aspect-ratio and depth-ratio. Past literature have focused on wake transition mechanisms in case of suspended cubes (Saha, 2004; Khan et al., 2020a; Meng et al., 2021) as well as wall-mounted prisms (Saha, 2013; Zhang et al., 2017; Rastan et al., 2017; Diaz-Daniel et al., 2017b). For the case of suspended cube, Hopf bifurcation (Saha, 2004; Khan et al., 2020a) results in transition to unsteady flow, mainly at Reynolds numbers of $2.5 \times 10^2 - 3 \times 10^2$. In case of wall-mounted prisms, transition is mainly investigated in terms of changing aspect-ratio (Saha, 2013) and Reynolds numbers (Zhang et al., 2017; Rastan et al., 2017; Diaz-Daniel et al., 2017b). Saha (2013) attributed the transition to unsteady flow with increasing aspect-ratio, to alternate shedding of side-edge shear-layers forming Kármán type mid-span vortices. Saha (2013) observed transition to unsteady flow at aspect-ratio of 3 and Reynolds number of 2.5×10^2 . Thereon, Zhang et al. (2017) and Rastan et al. (2017) observed transition in mean-wake topology with changing Reynolds number. Zhang et al. (2017) notably observed a *six-vortex* type cross-sectional wake topology, considered to be a transitional structure between quadrupole and dipole-type wakes, at Reynolds number of 2.5×10^2 . Finally, Diaz-Daniel et al. (2017b) attributed the transition to unsteady wake to destabilizing of leading edge shear-layers. In context of this

dissertation, suppression of unsteadiness with increasing depth-ratio is noted, leading to restoration of flow symmetry and steady wake. Further, the threshold for transition changes with Reynolds number as observed in Figure 4.1. Thus the transition mechanism here becomes a multivariate function of changing depth-ratio and Reynolds number, which is discussed more as part of a future study.

4.1.3 Time-averaged wake characteristics

While the analysis of time-averaged flow effects and influence of changing depth-ratio and Reynolds numbers remain out of scope for the present study, the characterization of time-averaged flow features becomes important to understand the flow dynamics around wall-mounted prisms. Thus, the time-averaged (mean) wake features with changing depth-ratios are characterized briefly here. Time-averaged vortex structures identified using Q -criterion and overlaid with time-averaged axial vorticity ($\bar{\omega}_x^*$) are presented in Figure 4.8, for prisms with changing depth-ratios at Reynolds number of 2.5×10^2 . A sub-plot showing iso-surfaces of streamwise axial vorticity is added on the top-right corner for each plot. Figure 4.8 shows that the time-averaged wake is symmetric for all cases, including $DR = 0.016$, in which the instantaneous unsteady wake feature asymmetric hairpin-like structures. Further, the time-averaged vortex structures for $DR < 0.3$ show *quadrupole-type* cross-sectional wake topology, composed of counter-rotating pairs of primary tip and base vortices, emanating from the tip and base of the prism, respectively. In literature, Zhang et al. (2017) and Zargar et al. (2021b) observed similar quadrupole structures at Reynolds number of 2.5×10^2 . Increasing the prism depth-ratio beyond 0.3 leads to impairment of tip vortex due to reattachment of leading edge separated flow into top and side surfaces of the prism (Rastan et al., 2021).

The iso-surfaces of vorticity, shown on the top-right corner for each plot in Figure 4.8 provides, insight into the formation of tip vortices and their dependence on depth-ratio. Two vortices forming over the top surface of the prism are primary and secondary tip vortices. Primary tip vortices form on the top part of the side surfaces, while secondary tip vortices form on the top surface of the

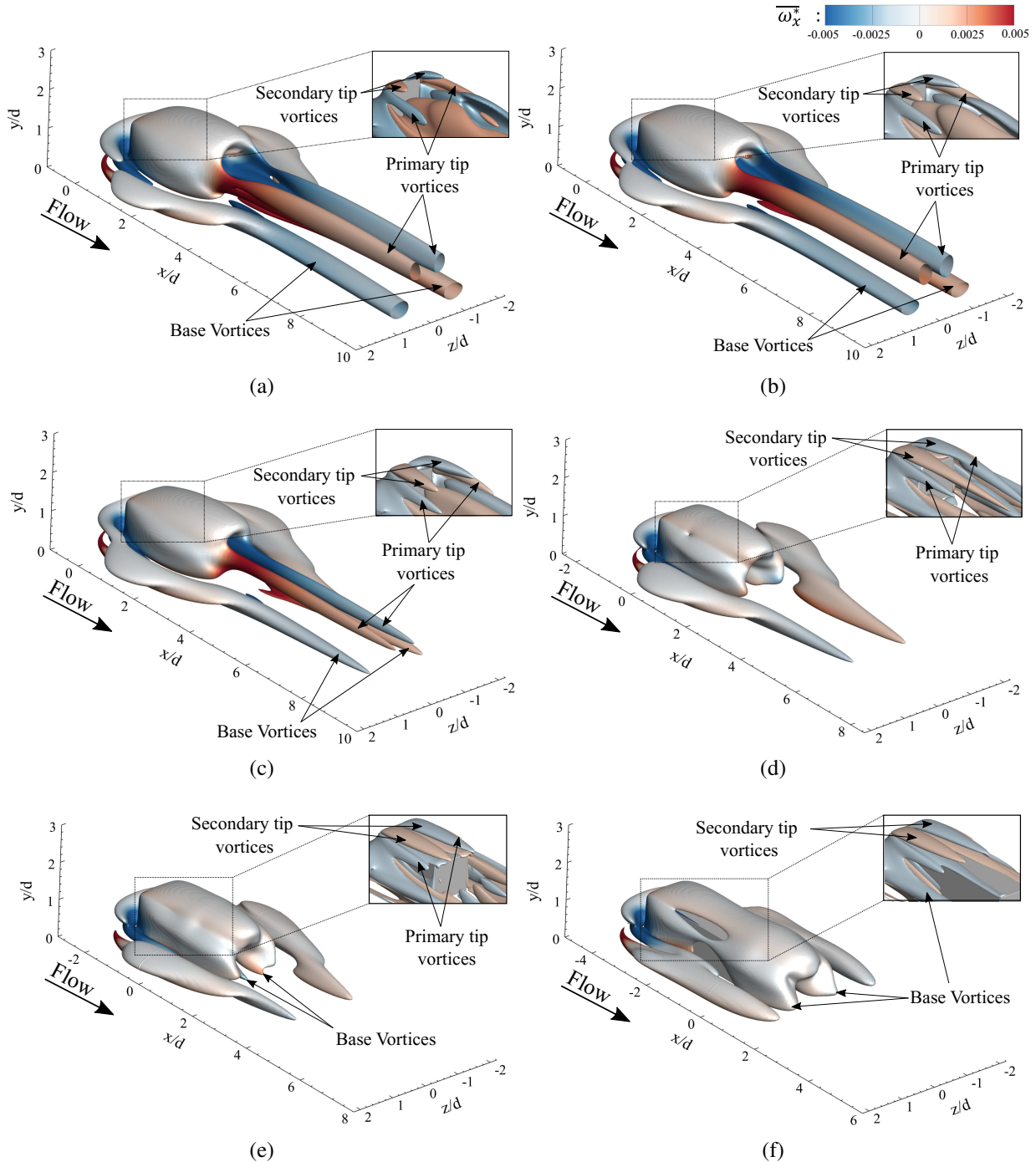


Figure 4.8: Time-averaged vortex structures identified using $Q^* = 1 \times 10^{-6}$, colored with $\overline{\omega}_x^*$ for (a) $DR = 0.016$; (b) $DR = 0.1$; (c) $DR = 0.3$; (d) $DR = 1$; (e) $DR = 2$ and (f) $DR = 4$. The iso-surface for $\overline{\omega}_x^*$ is shown for each case on the top-right corner.

prism (Rastan et al., 2021). For all cases, secondary tip vortices vanish immediately behind the

prism. In case of $DR > 0.3$, secondary tip vortices vanish due to shear-layer reattachment on the top-surface of the prism, while primary tip vortices swerve down the side surfaces.

Finally, in order to understand the evolution of time-averaged structures in near and far-wake downstream of the prism, Figure 4.9 presents profiles of time-averaged axial vorticity ($\overline{\omega}_x^*$) at $x/d = 2, 5$ and 10 . Profiles for $DR > 1$ are omitted for brevity, since their mean flow characteristics do not change compared to $DR = 1$ (Fang and Tachie, 2019; Zargar et al., 2021b). At $x/d = 2$, the profiles of $\overline{\omega}_x^*$ are similar for $DR \leq 0.3$, showing the pairs of primary and secondary tip vortices, and base vortex pairs. The horseshoe structure wrapping around the prism and extending in the wake is also apparent. The sign of vorticity for primary tip vortices are opposite to those of secondary tip vortices. The latter structures diminish beyond $x/d = 2$ and they are no longer identifiable at $x/d = 5$. Thus, secondary tip vortices only appear in the near-wake, while primary tip vortices and base vortices retain their coherence farther downstream the wake. The strength of tip and base vortices reduces with increasing depth-ratio farther downstream. Thus it becomes clear that tip and base vortices remain dominant in the very near-wake ($x/d = 2$), while they are not as dominant farther downstream at $x/d = 5 - 10$. Further, strength of the tip vortex in the far-downstream ($x/d = 10$) weakens with increasing depth-ratio up to $DR = 1$, where the tip vortex is fully distorted and the base vortex dominates the wake.

4.1.4 Upwash and downwash motion

From the past literature (Sumner et al., 2004; Wang et al., 2006; Wang and Zhou, 2009; Hosseini et al., 2013), it is well known that the free-end vortex pair or tip vortices induce downwash flow, whereas the wall-body junction vortex pair or base vortices induce an upwash flow. Sumner et al. (2004) and Hosseini et al. (2013) further elucidate that the free-end downwash dominates the wake for a dipole-type mean-wake topology. In case of a quadrupole-type wake, the strong upwash due to base vortex interacts with the downwash from the tip vortex, forming a saddle-point in the symmetry plane (Wang and Zhou, 2009). For a thicker boundary layer, Wang et al. (2006) observed that the upwash-flow is stronger resulting in the saddle-point located closer to the free-

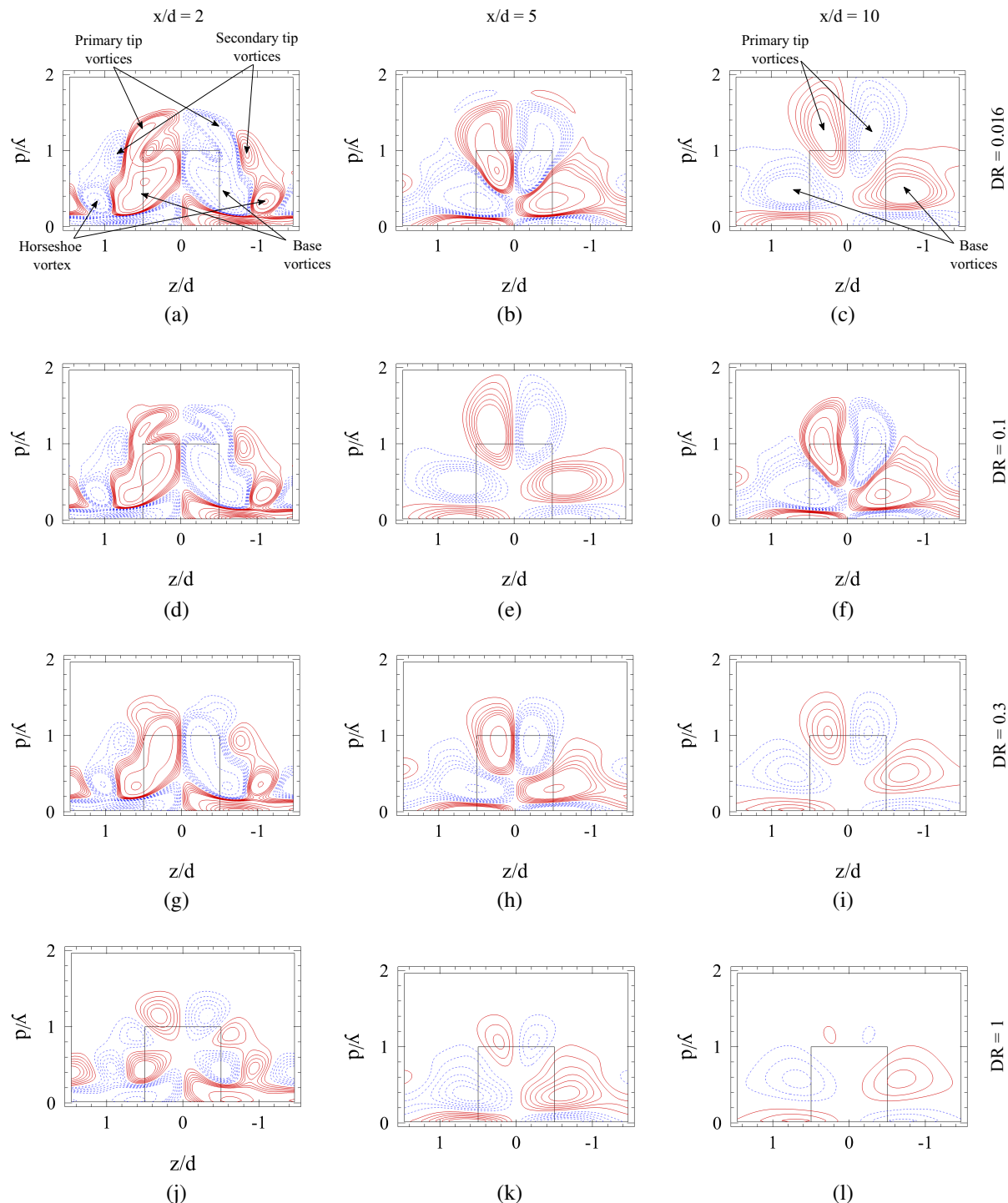


Figure 4.9: Contours of time-averaged axial vorticity ($\bar{\omega}_x^*$) structures (solid blue lines: positive values, dashed red lines: negative values) for (a-c) $DR = 0.016$; (d-f) $DR = 0.1$; (g-i) $DR = 0.3$ and (j-l) $DR = 1$. The line contour cutoff levels for $\bar{\omega}_x^*$ are ± 3 and the contour interval is 0.06. The contours are shown at $x/d = 2, 5$ and 10 .

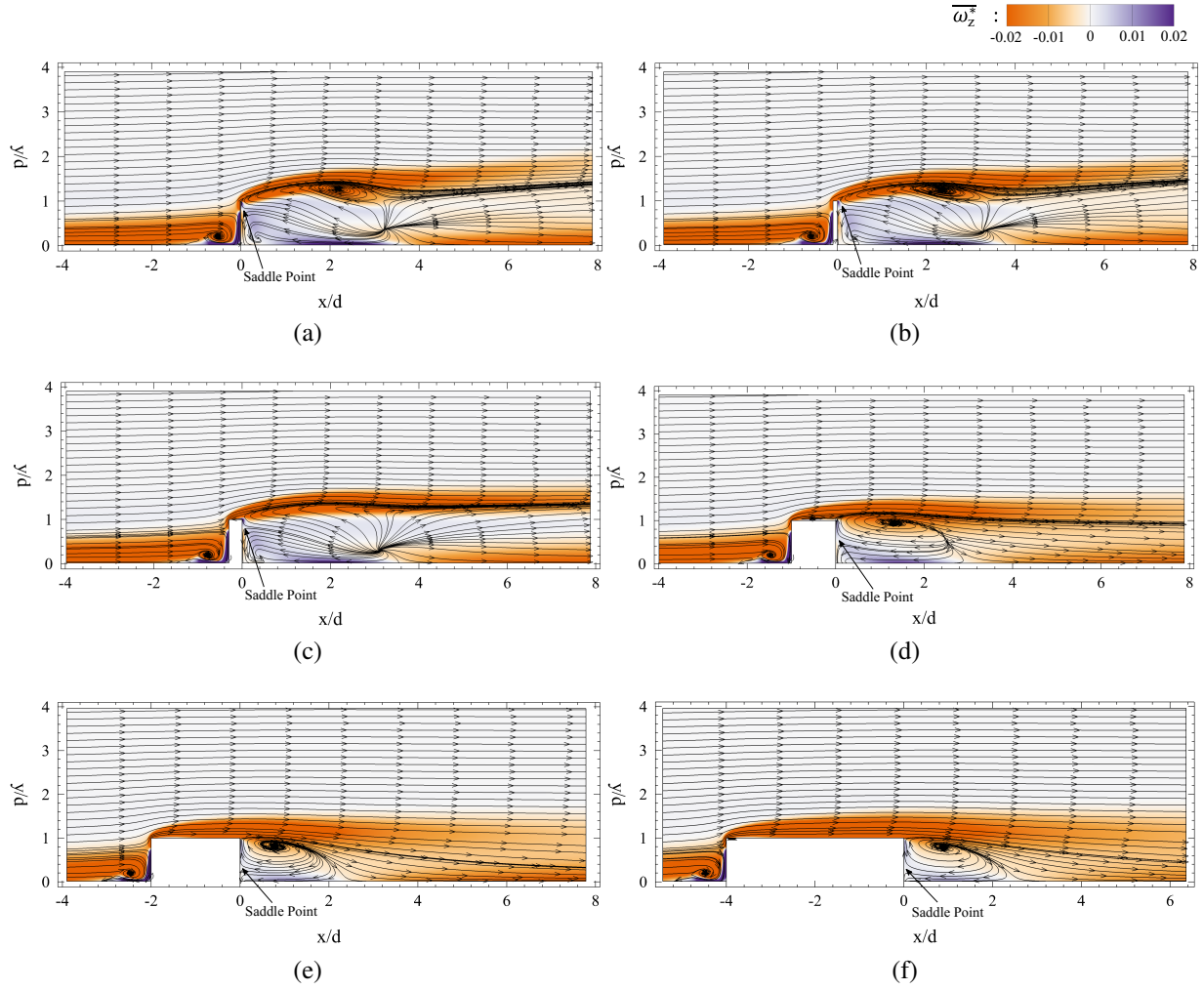


Figure 4.10: The $\bar{\omega}_z^*$ contours overlapped with the time-averaged streamlines for (a) $DR = 0.016$; (b) $DR = 0.1$; (c) $DR = 0.3$; (d) $DR = 1$; (e) $DR = 2$ and (f) $DR = 4$. Plots are shown at $y/d = 0$.

end of the prism. In the present study, it becomes important to analyze the influence of varying depth-ratio on upwash and downwash flow. To this effect, Figure 4.10 shows the contours of $\bar{\omega}_z^*$ overlapped with the time-averaged streamlines for all cases, shown at the symmetry plane. The intensity of upwash or downwash flow is clearly evident by their effect on the leading-edge shear-layer separation at prism free-end. Figure 4.10 shows the location of the saddle-point for all cases, which clearly indicates that the location of saddle-point lowers towards the wall-body junction with increasing depth-ratio. This hints at increasing strength of free-end downwash flow with larger depth-ratios(Zargar et al., 2021b).

Upwash and downwash flows have profound effects on the mean shear layer separation and elongation in the downstream wake, which in turn affects the flow periodicity (Wang et al., 2006; Wang and Zhou, 2009). Zdravkovich (2003) reported on the influence of downwash flow on the elongation of separating shear layer and widening of the near-wake. This study suggested that with increasing strength of downwash flow, the near wake widened and the shear layer elongated, resulting in prolonged spanwise vortex shedding. Wang and Zhou (2009) observed similar results for the case of increasing aspect-ratio for a finite square prism. Since the vortex shedding mechanism directly depends on the elongation of shear layer and spanwise momentum transport (Zdravkovich, 2003), this thesis quantitatively analyzes the transport and recovery of mean shear layers, under the influence of upwash and downwash flow, in Figure 4.11. Previous studies (Smits et al., 2019b; Goswami and Hemmati, 2020, 2021a) have used a similar method to investigate the recovery of a separated shear layer downstream of a sudden contraction-expansion system. Figure 4.11 shows the location of maximum Reynolds shear stress, that is $Y_M(-\overline{u'v'})$ and $Z_M(\overline{|u'w'|})$, in the wake. As the Reynolds stress reflects the stirring and mean momentum transport by fluctuating velocity component, downstream spread of $-\overline{u'v'}$ and $\overline{u'w'}$ are associated with the formation of spanwise vortices and their convection downstream (More et al., 2015). The value and trend of $\overline{u'w'}$ is also a measure of fluctuating streamwise momentum transport in the lateral direction or a degree of correlation between streamwise and cross-stream fluctuating velocities. Since $\overline{u'w'}$ is positive and negative in regions above and below the centerline, respectively, the location of maximum $\overline{|u'w'|}$ was employed for characterizing the wake.

Transport of $-\overline{u'v'}$ in Figure 4.11a sheds light on the influence of depth-ratio on the strength of upwash ($v' > 0$) and downwash ($v' < 0$) flow. For all cases, initially the stresses remain close to the height of the prism. Small depth-ratio cases ($DR = 0.016$ and 0.1) show a prolonged region of $v' > 0$ behind the prism, which entrains high-momentum fluid from the free-stream into the wake, resulting in a strong upwash flow. Thus, transport of $-\overline{u'v'}$ away from the ground, in the region of upwash flow ($4 < x/d < 10$), is clearly observed for the case of $DR \leq 0.3$. With increasing depth-ratio, a small region of upwash flow exists immediately behind the prism, while downstream wake

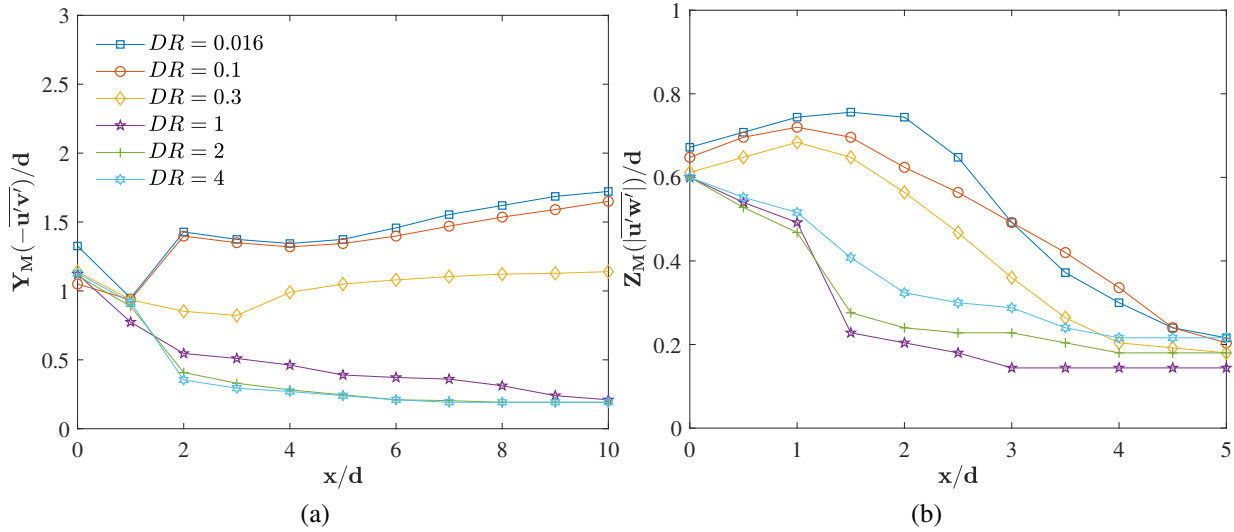


Figure 4.11: Location of the maximum Reynolds shear stress, $Y_M(-\bar{u}'\bar{v}')$, and $Z_M(|\bar{u}'\bar{w}'|)$, normalized by the prism width (d), downstream of the wall mounted prism, at (a) $z/d = 0$ and (b) $y/d = 0.5$ plane.

is mainly dominated by downwash flow. Thus, $-\bar{u}'\bar{v}'$ initially remains close to the prism height for the case of $DR > 0.3$, but it quickly recovers towards the ground farther downstream in the wake. The profiles of $\bar{u}'\bar{w}'$, in Figure 4.11b, correspond to the roll-up of shear layer from the side faces of the prism. The near wake appears widened for $DR \leq 0.3$, under the influence of strong upwash flow. Its recovery towards the core region is prolonged until $x/d \approx 5$. With increasing depth-ratio, the location of maximum shear stress is lowered towards the wake core within a short distance from the rear face of the prism, which hints at narrowing of the wake width. Thus, increasing the depth-ratio weakens the interaction between downwash flow and spanwise separating shear layers, which in-turn coincides with growing strength of upwash flow in the far-wake. The analyses that follows focus on evaluating the impact of upwash and downwash flows on periodicity in unsteady wakes.

4.1.5 Flow periodicity and spanwise coherence

Figure 4.12 presents the power spectral density (E_u) of streamwise velocity for two prisms with $DR = 0.016$ and 0.1 . Welch's averaged modified periodogram method (Welch, 1967) was utilized

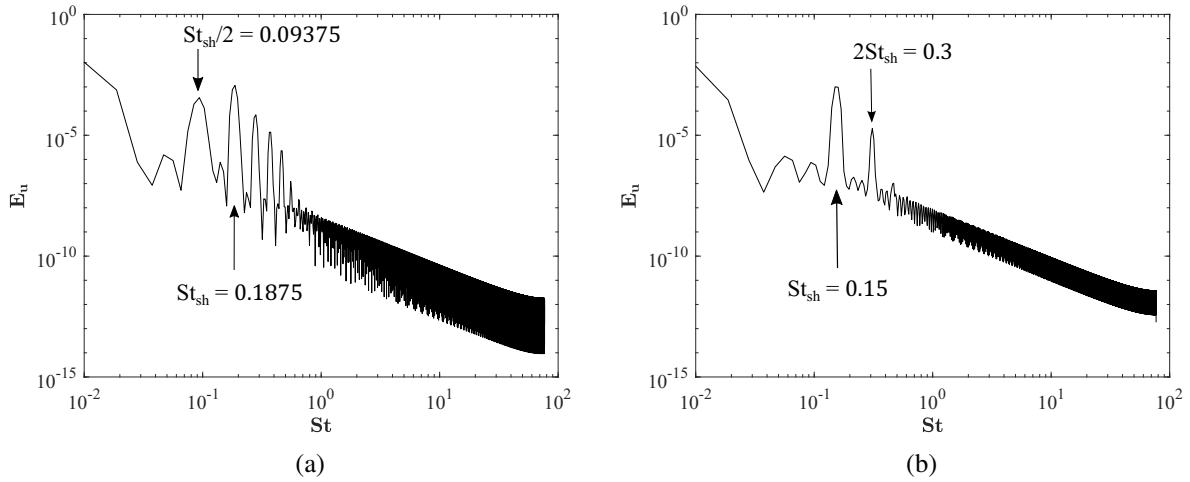


Figure 4.12: The power spectral density function, E_u , of the streamwise streamwise velocity (u) at $x/d = 2.5$, $y/d = 0.5$ and $z/d = 0.5$, for (a) $DR = 0.016$ and (b) $DR = 0.1$ prisms at Reynolds number of 2.5×10^2 .

to calculate the power spectrum, where velocity data (time-history) was split into 8 segment with 50% overlap with a Hamming window was applied on each segment. The dominant frequency for $DR = 0.016$ corresponds to $St_{sh} = 0.1875$, while it reduces to $St_{sh} = 0.15$ with increasing depth-ratio to 0.1. Visual inspection of the wake over time reveals that these dominant shedding frequencies are associated with hairpin-like structures formed by the separated shear layer at the prism leading edge. The dominant frequency noted here is higher compared to large aspect-ratio ($AR = 2 - 7$) prisms (Wang et al., 2006; Wang and Zhou, 2009; Saha, 2013; Rastan et al., 2017), in which case the range of St is $0.11 - 0.13$ at $Re = 40 - 9.6 \times 10^3$. There are, however, limited studies in literature that look at the influence of depth-ratio on vortex shedding. The recent study of Rastan et al. (2021) reported that increasing depth-ratio from 1 to 3 lowered St_{sh} . The Strouhal number noted in their work was $0.049 \sim 0.138$ for $DR = 1 - 4$ cases at $Re = 1.2 \times 10^4$ and aspect-ratio of 7, which was lower compared to the value obtained here. The reduced shedding frequencies in those studies, compared to the present case, were attributed to elongation of the vortex formation under the influence of intense downwash flow.

Hairpin-like vortex formation is a key wake feature in case of isolated bluff-bodies such as finite aspect-ratio flat-plate, isolated cubes and prisms. In case of the finite aspect-ratio flat-plate,

Hemmati et al. (2016) established that shedding occur as a result of shear-layer peel-off of side-edge vortices from the shorter side due to secondary flow induced by detachment of main vortex roller from longer side of the plate. The dominant shedding structures in this case resemble hairpin-like vortices. They observed a shedding frequency of $St_{sh} = 0.317$ for flat plate of aspect-ratio 3.2, which is significantly higher compared to the present study. The increased shedding frequency in case of Hemmati et al. (2016) is attributed to the isolated nature of the flat-plate, where shear-layers peel-off from either end of the flat-plate. Mainly, the added shear-layers contributed to the dynamics that increases the shedding frequency. Further, Hemmati et al. (2017) expanded on their previous study of normal-thin flat plates by examining the implications of aspect-ratios using cases of $AR = 1.6$ and 1.0 . The vortex shedding frequency reduces for these cases significantly, such that $St_{sh} = 0.146$ for $AR = 1$ and $St_{sh} = 0.186$ for $AR = 1.6$. In case of $AR = 1$, a second spectral harmonic peak is observed at $2St$, which they attributed to the secondary vortex shedding process observed with square plates. In the present study, the effects of horseshoe and hairpin-like vortex can be isolated by changing the ground boundary to symmetry. In that case the shedding frequency of the thin prism ($DR = 0.016$) is comparable to the results of Hemmati et al. (2017). This hints at negligible influence of the interaction between horseshoe vortex and hairpin-like vortex in wall-mounted flat-plate and prisms.

In the case of isolated cube, Saha (2004) established that the flow remains planar-symmetric and steady up to Reynolds number of 2.65×10^2 . Then, the wake transition to unsteady flow by undergoing Hopf bifurcation. The unsteady flow loses planar-symmetry, and the wake is characterized by shedding of hairpin-like vortices in the wake. Further, Khan et al. (2020a,b) and Meng et al. (2021) scrutinize the mechanism of shedding and various wake regimes for isolated cubes. They note a reduction of the shedding frequency to ≈ 0.09 at Reynolds number of 2.7×10^2 and ~ 0.13 at $Re = 4 \times 10^2$, relative to suspended thin flat-plates. The wake topology differs in the present study, where the flow is steady at similar setting, due to the reattachment of the leading-edge shear-layer on top and side surfaces of the prism, which is consistent with observations of Zargar et al. (2021b).

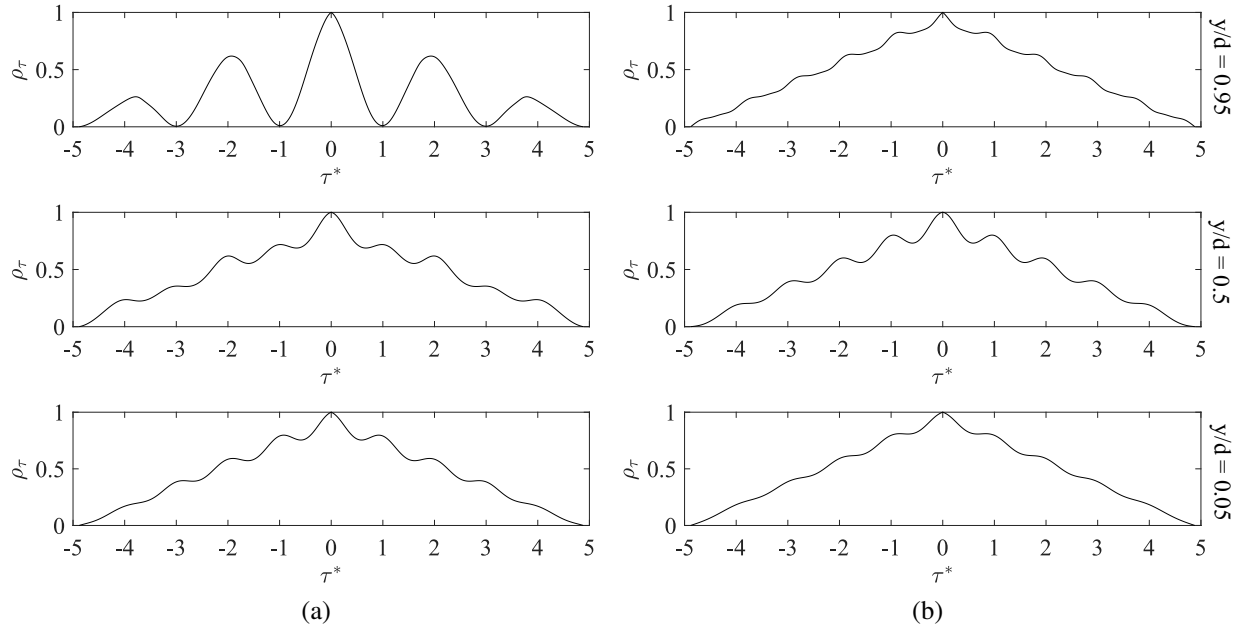


Figure 4.13: The normalized autocorrelation function, ρ_τ , of the streamwise velocity at $x/d = 2.5$ and $y/d = 0.05, 0.5$ and 0.95 , for (a) $DR = 0.016$ and (b) $DR = 0.1$. Note that $\tau^* = \tau f_{sh}$ is the number of vortex shedding periods, where f_{sh} is the vortex shedding frequency corresponding to St_{sh} .

Lowering of the shedding frequency with increasing depth-ratio continues beyond $DR=0.3$, at which point the wake becomes steady. Although this trend depends on Re , such that the threshold DR for transition to steady wake changes at higher Re , focus is retained on analyzing the wake periodicity at $Re = 2.5 \times 10^2$ to establish the mechanisms leading to such trends. The reduction in St_{sh} for the case of $DR = 0.1$ can be attributed to increasing dominance of the downwash flow, evident by the results in Figure 4.11. This follows from arguments of Zdravkovich (2003), who explained that the vortex shedding mechanism is directly dependent on elongation of the shear-layer and spanwise momentum transport under the influence of upwash-downwash flow. The shear layer elongation that was previously discussed for the case of larger DRs aligns well with lowering trend of the shedding frequency observed here and corroborated by description of Zdravkovich (2003).

The spectral analysis revealed additional flow dynamics in the wake. There are three dominant wake features identified in Figure 4.12 that can also be associated with wake structures, by

inspection: (1) St_{sh} that is associated with shedding of hairpin-like structures; (2) low-frequency signature at $St_{sh}/2$ for the case of $DR = 0.016$, which is associated with sub-harmonic of the hairpin-like vortex shedding; (3) high-frequency harmonic peaks centered at $2St_{sh}$, $3St_{sh}$ and $4St_{sh}$ for the case of $DR = 0.016$, and at $2St_{sh}$ for the case of $DR = 0.1$. Diaz-Daniel et al. (2017b) and Tiwari et al. (2019) have noted similar sub-harmonic and harmonic peaks in the wake of prisms, mainly in the near-wake region, associated with interactions of detaching shear-layers from the prism surfaces. Figures 4.12 and 4.13 provide the direct evidence of these flow features. Autocorrelation of the streamwise velocity is shown in Figure 4.13 for $DR = 0.016$ and 0.1 , where time-lag (horizontal axis) is normalized by the vortex shedding frequency, f_{sh} . Autocorrelation of a signal is defined as,

$$\rho_\tau = \frac{\langle u_t u_{t+\tau^*} \rangle}{\langle u_t^2 \rangle},$$

where the streamwise velocity signal (u_t) is correlated with itself ($u_{t+\tau^*}$) after a time delay corresponding to one vortex shedding period (τ^*). Autocorrelation analysis is carried out using the final 5 shedding cycles along the height of the prism at three locations. For the case of $DR = 0.016$, signature of the vortex shedding process is intensified close to the prism free-end, where a periodic signature is apparent corresponding to $St_{sh}/2$. At the mid-span and wall-body junction, the periodic signature corresponds to St_{sh} . In case of $DR = 0.1$, no such distinction is observed since the periodic signatures correspond to St_{sh} along the prism height.

The low frequency ($St_{sh}/2$) activity noted for $DR = 0.016$ is attributed to the region where tip vortices are present ($y/d \approx 0.95$), which is consistent with observations of Diaz-Daniel et al. (2017b). This suggests that tip vortex shedding occurs at a different frequency compared to the hairpin-like structures. Further investigation into phase lag between the shedding tip vortices on two sides may account for the asymmetry. Previously, Kindree et al. (2018) and Morton et al. (2018) reported low-frequency behavior for wall-mounted circular prisms with $AR = 4$ immersed in a thin laminar boundary layer. They proceeded to argue, based on further analysis, that

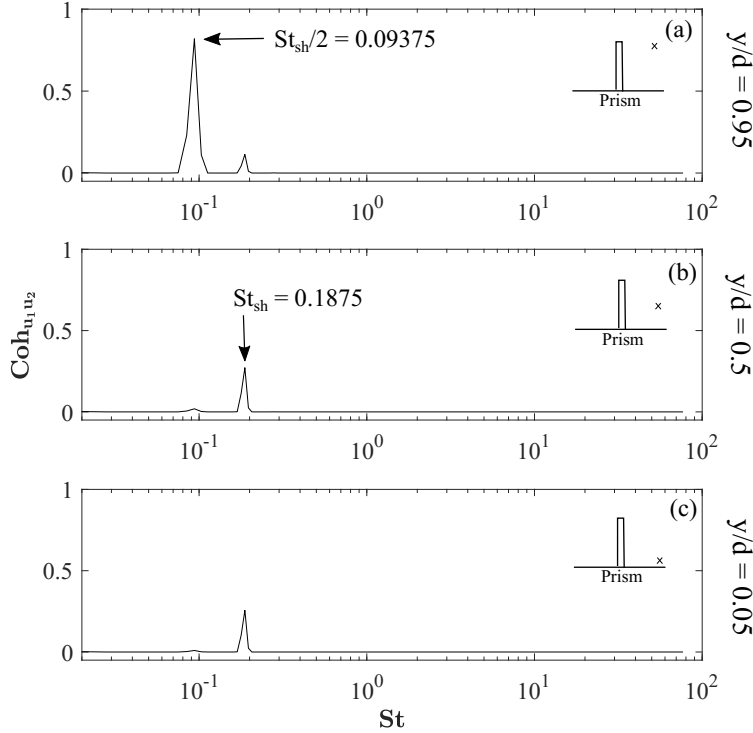


Figure 4.14: Spectral coherence, $Coh_{u_1u_2}$, between streamwise velocity u_1 and u_2 for $DR = 0.016$, at $x/d = 2.5$ and $z/d = 0.5$. u_1 was measured at $y/d = 0.008$, and u_2 was measured at $y/d = 0.05, 0.5$ and 0.95 .

low-frequency signatures are unique to circular cross-section prisms with $AR \leq 4$ that are placed in thin-laminar boundary layers, and that this process is independent from Re . Here, a similar behavior is observed for a small AR rectangular (sharp-edge) prism with sufficiently small DR that result in asymmetric features. At $Re = 2.5 \times 10^2$, this unique wake asymmetry is only apparent for the case of $DR = 0.016$, while wake symmetry is restored quickly at $DR = 0.1$. Similar wake behavior was observed for larger DRs at higher Reynolds numbers, as was previously classified in Figure 4.1. Earlier in this thesis, both quantitative and qualitative evidence hinting at the dynamics of side-edge shear layer detachment dictating the wake asymmetric behavior has been observed and discussed. Further support for this hypothesis is aimed to be provided by identifying the potential phase difference between shear layer detachment on the side edges.

To better understand near-wake dynamics associated with tip vortex low-frequency signatures, for example for the case of $DR = 0.016$, spectral coherence ($Coh_{u_1u_2}$) was employed between velocity signals along the domain span in Figure 4.14. Spectral coherence provides the degree of coherence between Fourier components of two streamwise velocity (time-history) signals, say u_1 and u_2 , such that u_1 is recorded at $y/d = 0.008$ and u_2 at $y/d = 0.05, 0.5$ and 0.95 (Wang and Zhou, 2009). Spectral coherence is defined as,

$$Coh_{u_1u_2} = \frac{Co_{u_1u_2}^2 + Q_{u_1u_2}^2}{E_{u_1}E_{u_2}},$$

where $Co_{u_1u_2}$ and $Q_{u_1u_2}$ are the co-spectrum and quadrature spectrum function of u_1 and u_2 , and E_{u_1}, E_{u_2} are the power spectral density functions of u_1 and u_2 . The signal for u_1 is measured close to the ground for reference, following the recommendation of Wang and Zhou (2009). The results in Figure 4.14 for $Coh_{u_1u_2}$ show a dominant peak at $St_{sh} = 0.1875$ along the prism span, as well as at $St_{sh}/2$ close to the prism free-end. The peak value of $Coh_{u_1u_2}$ for St_{sh} ranges from ~ 0.3 at $y/d = 0.05$ to 0.5 to ~ 0.1 at $y/d = 0.95$. This is while $Coh_{u_1u_2}$ for $St_{sh}/2$ becomes ~ 0.9 at $y/d = 0.95$. The spanwise coherence at $St_{sh} = 0.1875$ suggests a strong correlation along the prism height, which corroborates with hairpin-like structures shedding in the wake. A strong coherence corresponding to $St_{sh}/2$ is absent along the prism height near its free-end. This suggests that low-frequency signature originates from the prism free-end. Thus, low-frequency signatures observed in the wake are associated with tip vortex shedding.

Coherent vortex shedding observed in the wake of two-dimensional prisms, typically suggesting symmetric vortex shedding, correspond to no phase-lag (phase angle of zero) between laterally arranged vortices (Zhou et al., 2002). In asymmetric vortex shedding, however, there is a phase-lag between structures shed from different edges of the prism. The apparent phase difference in mid-height of the prism, comparing streamwise velocity signals along the prism span, hints at a potential phase difference between structures positioned on either edges of the prism. This accounts for the wake asymmetry observed in the shedding and convective orientation

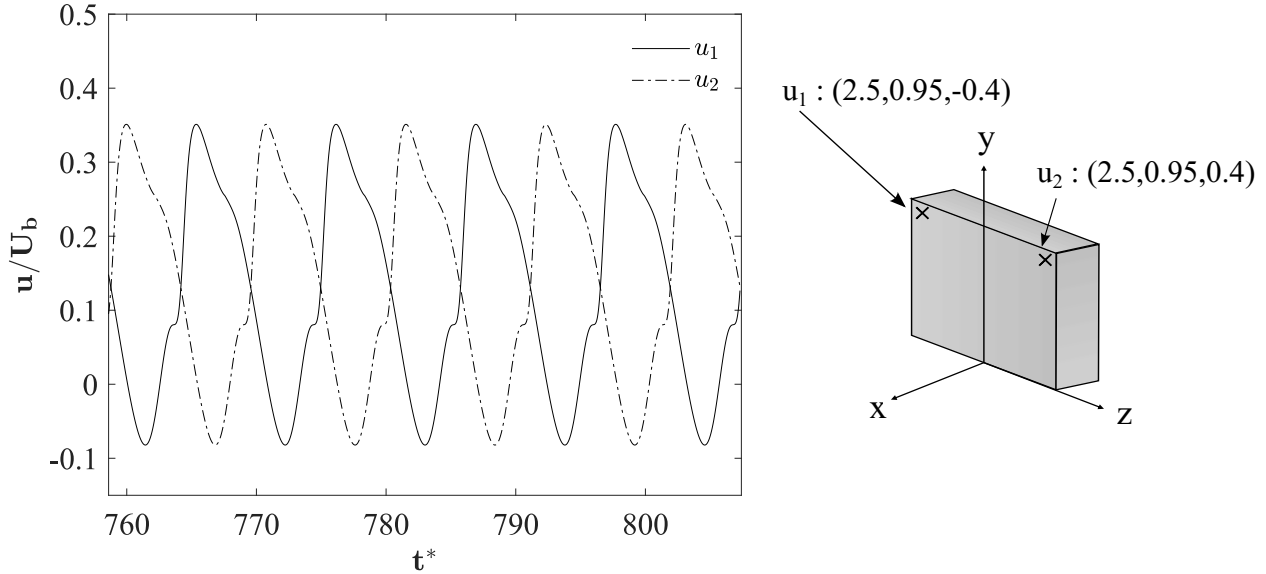


Figure 4.15: The variation of instantaneous streamwise velocity components, u_1 and u_2 , at locations $(2.5, 0.95, \pm 0.4)$ as shown in the schematic plot, for $DR = 0.016$ prism. t^* is the convective time, given as $t^* = tU_b/d$.

of hairpin-like structures. To verify the existence of a phase difference between tip vortices on two sides of the prism, instantaneous streamwise velocity variations on opposite spanwise edges of the prism are analyzed in Figure 4.15. The results are based on two instantaneous streamwise velocity signals, u_1 and u_2 , measured at opposite spanwise locations with respect to the prism middle line, that is $(2.5, 0.95, +0.4)$ and $(2.5, 0.95, -0.4)$. These spatial positions correspond to the location of low-frequency signature observed earlier for the case of $DR = 0.016$, i.e. the location of tip vortices. It becomes clear from Figure 4.15 that the two signals, u_1 and u_2 , experience a phase shift of π . At a given instant of time, the signal of u_1 leads u_2 by half a period, which corresponds to the low-frequency observed at $St_{sh}/2$. Thus, the tip vortices from either side of the prism shed alternately with a low-frequency and opposite phase. This provides us with more evidence on the mechanism of wake asymmetry associated with low depth-ratio prisms.

The implications of alternate tip vortex shedding on the hairpin-like structures in the wake are next analyzed. Interactions between the tip vortex and separating side-edge shear-layers could result in formation of secondary vortex structures, and thus contribute to shear-layer pre-mature separation, or “peel-off” following the terminology of Hemmati et al. (2016). Further, the

streamwise coherence of these secondary vortex structures is associated with the pattern of shedding of hairpin-like vortices. Hence, there is an inherent mechanism that leads to formation and shedding of hairpin-like structures in an asymmetric pattern in the wake of wall-mounted low depth-ratio prisms.

4.1.6 Mechanism of asymmetric shedding

Hwang and Yang (2004) and Yakhot et al. (2006) have previously characterized the flow around a wall-mounted cube. These studies reported a dominant hairpin-like shedding in the wake, resulting from the adverse pressure gradients formed by the abrupt boundary layer separation on the surfaces of the body. Further, Diaz-Daniel et al. (2017b) showed that such hairpin-like structures appear symmetric at low Reynolds numbers, due to the shear-layer reattachment-separation on the prism surfaces. With increasing Reynolds number, hairpin structures lose their symmetry moving downstream, which is the onset of their break down and incoherence. Moreover, Diaz-Daniel et al. (2017b) observed a low-frequency signature corresponding to tip vortices, which were absent in case of symmetric hairpin-like shedding. They hinted at potential interactions between tip vortices and the hairpin head, leading to the aforementioned dynamic wake features and vortex distortion.

A similar approach can be utilized for the current study, compared to those of Diaz-Daniel et al. (2017b), to characterize the mechanism of wake asymmetry. Thus far, it is established that for the case of $DR = 0.016$, which exhibits asymmetric wake structures, tip vortices are shed at a lower frequency and they exhibit an inherent lateral phase difference. This directly relates to the orientation and coherence of hairpin-like structures that are formed by detachment of shear layers from top and side edges of the prism. Figure 4.16 shows the instantaneous vortex structures using Q^* overlaid with contours of streamwise vorticity ($\overline{\omega}_x^*$) for $DR = 0.016$. At $x/d = 0$, both contour-line and iso-surface plots hint at the presence of symmetry in the wake, where primary and secondary tip vortices are clearly visible and are positioned symmetrically. More details on these structures have already been discussed extensively. Farther downstream, near-wake

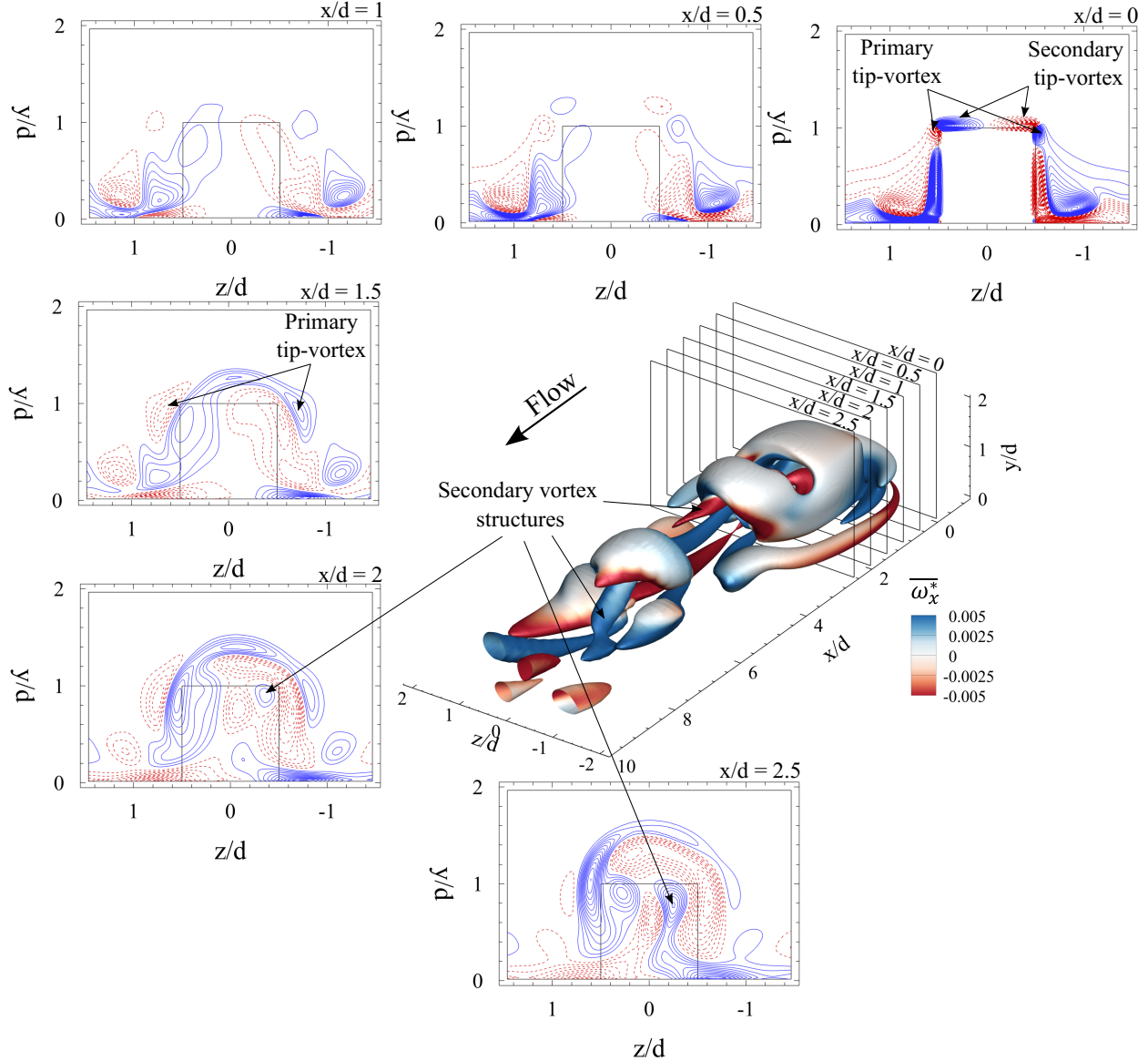


Figure 4.16: Instantaneous vortex structures identified using $Q^* = 6 \times 10^{-6}$ and overlaid with streamwise vorticity ($\overline{\omega}_x^*$), surrounded by the line contours of $\overline{\omega}_x^*$ (solid blue lines: positive values, dashed red lines: negative values) for $DR = 0.016$ prism at Reynolds number of 2.5×10^2 . The line contour cutoff levels for $\overline{\omega}_x^*$ are ± 0.12 and the contour interval is 0.001. Contours are shown at $x/d = 0 - 2.5$ at intervals of 0.5.

structures start showing signs of distortion, hinting at symmetry breaking, at $x/d = 1$. It has been already discussed how secondary tip vortices appear fully distorted at $x/d = 1$, while primary tip vortices dominate the wake (Rastan et al., 2021). Onwards from $x/d = 1.5$, primary tip vortices start interacting with the separating shear layer from top and side surfaces of the prism. At $x/d = 2$ and 2.5, there are several secondary streamwise vortex structures identified in the wake.

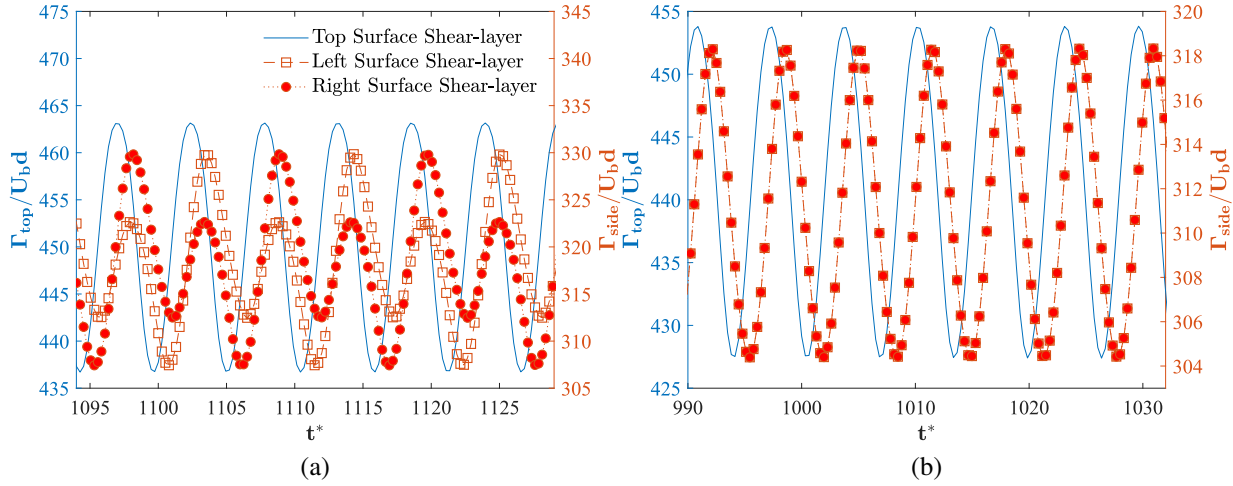


Figure 4.17: Circulation (Γ), normalized by bulk velocity (U_b) and prism width (d), computed for Top and side surface shear-layers of (a) $DR = 0.016$ and (b) $DR = 0.1$ prisms at Reynolds number of 2.5×10^2 . t^* is the arbitrary range of convective time, given as $t^* = tU_b/d$.

The sign of vorticity (direction of rotation) for secondary vortex structures is opposite to that of the corresponding shear layer (see $x/d = 2$). The influx of vorticity due to these secondary structures further facilitate their interactions with the separating shear-layer from the prism top surface, which forms the head of hairpin-like structures upon its detachment from the body (Hwang and Yang, 2004). This interaction impacts the separating hairpin-like structure on either side, causing asymmetric vortex shedding. Similar secondary vortex structures are noted downstream, the presence of which coincides with tilting of hairpin-like structure towards that respective side.

Summarizing previous discussions, key features of asymmetric wake behind small aspect-ratio wall-mounted prisms include (1) the formation of multi-part horseshoe vortex in front of the prism, (2) shedding of horseshoe legs in the wake, (3) leading edge shear-layer separation from the prism top and side surfaces, (4) the formation of secondary-vortex structures, and (5) subsequent formation of asymmetric hairpin-like structures in the wake. These key features remain common amongst the cases studied here, and shown in Figure 4.16 and 4.20.

The interactions of the tip vortex and side-edge separating shear layers, as well as the mechanism of shear-layer peel-off, are investigated next. This can establish a potential cause for

the formation of hairpin-like structures in the wake. Figure 4.17 compares the circulation (Γ) for top and side shear-layers for both asymmetric ($DR = 0.016$) and symmetric ($DR = 0.1$) hairpin shedding cases. The absolute values of circulation are compared, and normalized using bulk velocity (U_b) and prism width (d). For both depth-ratios, the strength of top-surface shear layer appears higher compared to that from either sides. Larger circulation of top shear-layer entails a roll-up from leading edge and a strong upwash flow that causes shear-layer peel-off. Further, the evidence of alternate shedding of tip vortex interacting with the side shear layer is clear from Figure 4.17. Trends of circulation computed for the dominant shear layer on one side lead those from the weaker side by a phase difference of π . This phase difference is consistent with that of tip vortex shedding from either side of the prism. Further, comparing circulation of the side shear layers at any time (t^*), it is noticed that the shear-layer on one side is stronger compared to its counterpart. As such, the side with stronger shear-layer (larger circulation) tilts the separating hairpin on that respective side. No such phase difference is observed for $DR = 0.1$, where the side surface shear-layers shed simultaneously from either side of the prism.

Analyses thus far reveal that further evaluation of the origins of secondary structures is necessary. Contour-line plots at $x/d = 2$ in Figure 4.16 suggests that the influx of vorticity (from secondary vortex structure) is consistent with the vorticity of primary tip vortex. To analyze this further at this location, temporal evolution of $\bar{\omega}_x^*$ is evaluated in Figure 4.18 within one shedding cycle. These clearly depict the formation of the head section of hairpin-like structure. Initially, a secondary vortex structure is identified at t_1 in Figure 4.18a, which tilts the separating shear-layer towards its respective side, in this case $+z$ direction. Primary-tip vortices are also identified at t_3 and t_4 in Figures 4.18c and 4.18d. Structures with a negative-sign vorticity (dashed red lines at t_4 in Figure 4.18d) interact with the shear-layers detaching from the top and side surfaces of the prism with an opposite vorticity-sign (solid blue lines at t_4 in 4.18d). This leads to an influx of opposite vorticity in the separating shear layer, the interjection of which with the shear-layer induces an inward velocity, with respect to the prism. This feature distorts the hairpin-like structure and breaks the wake symmetry.

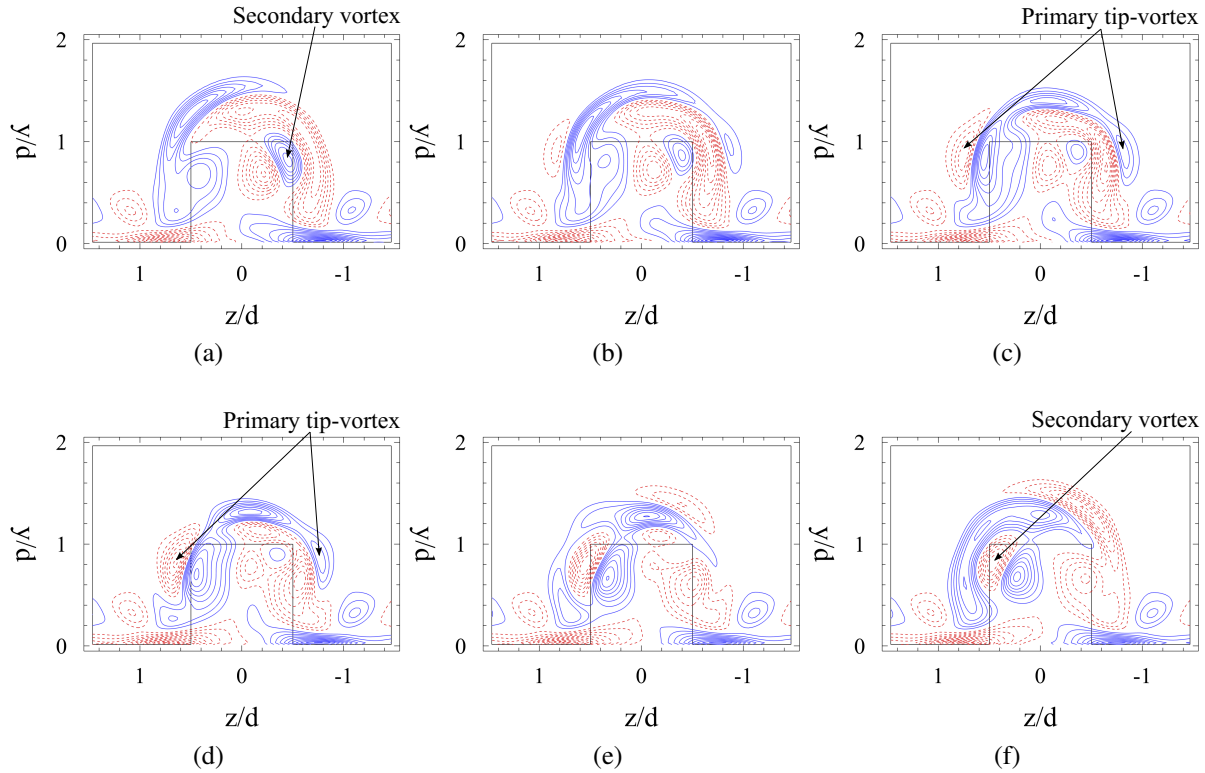


Figure 4.18: Time marching, line contours of $\bar{\omega}_x^*$ (solid blue lines: positive values, dashed red lines: negative values) plotted at $x/d = 2$ for $DR = 0.016$ at Reynolds number of 2.5×10^2 . The line contour cutoff levels for $\bar{\omega}_x^*$ are ± 0.12 and the contour interval is 0.001. Contours are shown at (a) $t_1 = t_o$; (b) $t_2 \approx t_o + \frac{1}{5}\tau^*$; (c) $t_3 \approx t_o + \frac{2}{5}\tau^*$; (d) $t_4 \approx t_o + \frac{3}{5}\tau^*$; (e) $t_5 \approx t_o + \frac{4}{5}\tau^*$ and (f) $t_6 \approx t_o + \tau^*$. τ^* is the time scale based on $\tau^* = d/(U_b St)$.

Based on their location and the vorticity-sign of secondary vortex structures in Figures 4.18a and 4.18f, it is argued that the secondary vortex structures form as a result of alternate shedding of primary tip vortices, due to excess vorticity resulting from the shear layer during the peel-off process on either side of the prism. The trends of circulation, which is the area integral of vorticity associated with the vortex, in Figure 4.17 shows the evidence of excess vorticity during shear-layer detachment from either side of very thin prism. The shear-layer on either side is stronger compared to its counterpart, resulting in excess vorticity on the respective side, that may lead to such secondary vortex structures. The excess vorticity in asymmetric wake feeds the secondary structures, which accounts for their coherence far downstream in the wake. In case of depth-ratio

0.1, the side-surface shear-layers shed simultaneously, devoid of any vorticity deficit. Thus the secondary vortex structures forming in the wake lose their coherence fairly quickly downstream.

The existence of a single coherent structure in the wake, despite different frequency signatures observed in the power spectrum (see Figure 4.12a), deserve a closer attention. On elaborating the mechanism of hairpin-like structures, Tiwari et al. (2019) attributed their formation to elongation and interactions of separating shear-layers from the prism top and side surfaces. The top and side surface shear-layers merge to form the hairpin-like structures in the wake (Khan et al., 2020a). The leading edge separation from the prism side surfaces induces vortical motions that form the tip vortices, which interact with the shear-layer formed over the cube. This interaction leads to distortion of the hairpin-like structure in the wake, and formation of secondary structures that lose their coherence downstream. The existence of secondary structures that are connected to the coherent hairpin-like structure (see Figure 4.16) accounts for the low-frequency signatures observed in the power spectrum.

Finally, DMD is utilized to explore different aspects of the wake dynamics and to confirm the origins of asymmetric hairpin-like vortices as a result of alternate shedding of primary-tip vortex at $St_{sh}/2$. DMD provides a computational framework to extract a primary low-order description of a data-set through its orthonormal modes in a temporal sense (Zheng et al., 2019; Khalid et al., 2020; Taira et al., 2020). In other words, DMD enables identification of spatial structures with characteristic frequencies associated with these structures. In the present study, since the case of $DR = 0.016$ results in sub-harmonic and harmonic peaks in the power spectrum, DMD analysis enables segregating the induced effects of each frequency on the overall wake. Here, the cases of $DR = 0.016$ and $DR = 0.1$ are considered for wake characterization using DMD analysis as a generalized example with asymmetric and symmetric wakes. DMD analysis is completed using Streaming Total Dynamic Mode Decomposition (STDMD) (Hemati et al., 2016, 2017) method implemented in OpenFOAM. The details of mathematical formulations and implementation of the algorithm is found in the work of Kiewat (2019).

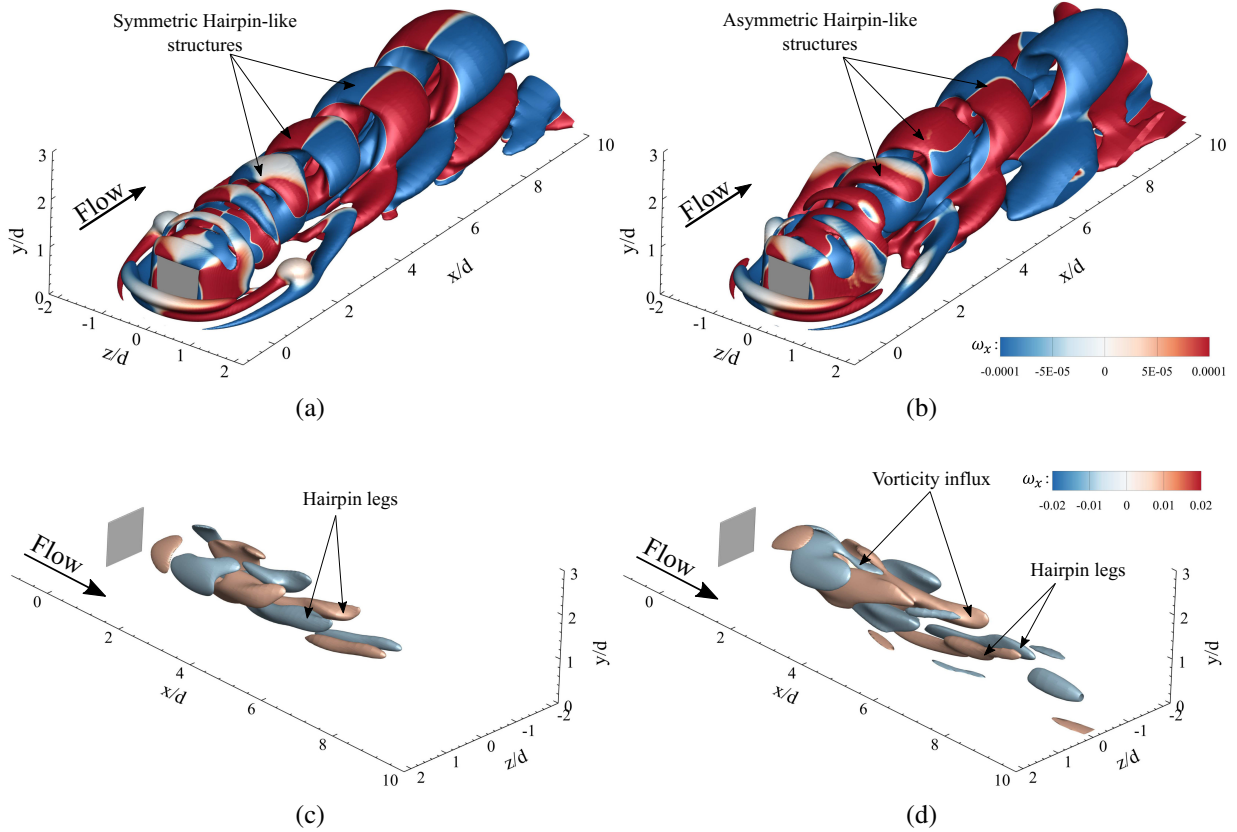


Figure 4.19: (a,b) Reconstructed vortex structures identified using Q -criterion and overlaid with instantaneous streamwise vorticity and (c,d) Reconstructed streamwise vorticity structures. Structures are reconstructed using the addition of (a,c) mean with DMD Mode 1 (St_{sh}); (b,d) mean with DMD Mode 1 (St_{sh}) and Mode 2 ($St_{sh}/2$).

The reconstructed vortex structures in Figures 4.19a and 4.19b are identified using Q -criterion iso-surfaces that are overlaid with instantaneous streamwise vorticity. Reconstruction is performed by addition of mean mode with DMD mode 1, corresponding to St_{sh} , and mode 2, corresponding to $St_{sh}/2$. In the current analysis, DMD modes 1 and 2 are the dominant modes, corresponding to $\sim 35\%$ and $\sim 31\%$ of the frequency amplitudes. This hints at the dominant influence of St_{sh} and $St_{sh}/2$ on the overall flow dynamics. From Figure 4.19a, showing the addition of mean flow to mode 1, illustrate that the dominant modes possess structures that correlate with the shedding hairpin-like structures in the wake. These shedding hairpin-like structures are symmetric, with frequency corresponding to St_{sh} . Thus it is evident from this result that the dominant frequency arises from the shedding of hairpin-like structures. Figure 4.19c,

presenting instantaneous streamwise vorticity structures obtained by addition of mean with mode 1, show the legs of hairpin-like structures forming due to anti-symmetric vorticity about the centerline. In the past literature (Kindree et al., 2018; Morton et al., 2018), the general topology of symmetric vortex shedding modes are made up of a series of counter-rotating vortices located on either side of the wake streamline. This suggests that the side-edge shear-layers shed simultaneously and result in symmetric hairpin-like structures shedding at the dominant Strouhal number (St_{sh}).

The influence of sub-harmonics ($St_{sh}/2$) on the overall flow is examined by adding mode 2 in our DMD analysis. Figure 4.19b shows the reconstructed structures by addition of mean mode with DMD mode 1 and 2, and the respective vorticity structures are shown in Figure 4.19d. With addition of mode 2 corresponding to sub-harmonic frequency, the iso-contours show asymmetry in the shed hairpin-like structures. The asymmetry arises from the influx of excess vorticity (see Figure 4.19d) to either side. Here, the excess vorticity on either side in mode 2 (Figure 4.19d) feeds into the anti-symmetric vorticity about the centerline in mode 1 (Figure 4.19c). Such influx induces an inward velocity, with respect to the prism, distorting the head of the hairpin-like structure. Thus, the origins of asymmetry can be attributed to the influx of vorticity as a result of sub-harmonic, low-frequency instability centered at $St_{sh}/2$. This observation further complements existing literature (Diaz-Daniel et al., 2017b; Morton et al., 2018; Kindree et al., 2018) by attributing the influx of vorticity to the secondary vortex-structures that interact and distort the hairpin-like shedding structures. The discussions thus here provides, for the first time, a detailed description of these structures, their physical mechanisms and their contributions to the wake asymmetry.

This observation is not limited to very thin prism at low Reynolds number. Figure 4.20 shows asymmetric wake and existence of secondary vortex structures in case of $DR = 0.6$ at Reynolds number of 4×10^2 as well as $DR = 1$ at $Re = 5 \times 10^2$. This is corroborated by the classification of wake topology in Figure 4.1. This suggests that secondary structures and the subsequent asymmetry in the wake develops at sufficiently small depth-ratios with increasing Reynolds

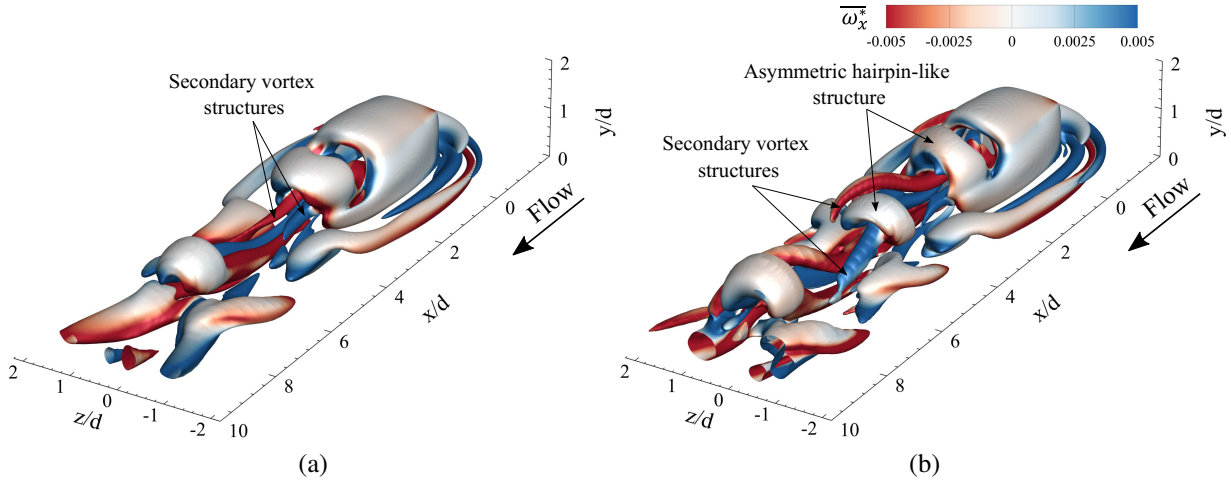


Figure 4.20: Instantaneous vortex structures of prisms with (a) $DR = 0.6$ at $Re = 4 \times 10^2$; and (b) $DR = 1$ at $Re = 5 \times 10^2$, identified using $Q^* = 6 \times 10^{-6}$ and overlaid with $\bar{\omega}_x^*$. All figures are shown in three-dimensional view.

number. The applications and effectiveness of DMD analysis at higher Reynolds number is evident from the study of Khalid et al. (2020). At higher Reynolds numbers and depth-ratios, the interactions of shedding vortex structures with detaching shear-layers results in near-wake incoherence and multiple sub-harmonic and harmonic frequencies (Diaz-Daniel et al., 2017b). The investigation of such incoherent wake using DMD analysis, though interesting, remains part of a future study. Further, higher Reynolds number leads to stronger interaction between the secondary vortex structures and separating shear layers, resulting in more disorganized distribution of wake structures downstream in Figure 4.20b. In case of symmetric shedding (see Figure 4.21), secondary vortex structures also appear symmetric and their shedding frequency corresponds to the shedding frequency of the main hairpin-like structure. As the flow progresses downstream, they lose their coherence and vanish completely. This explains the lack of these structures farther downstream the wake.

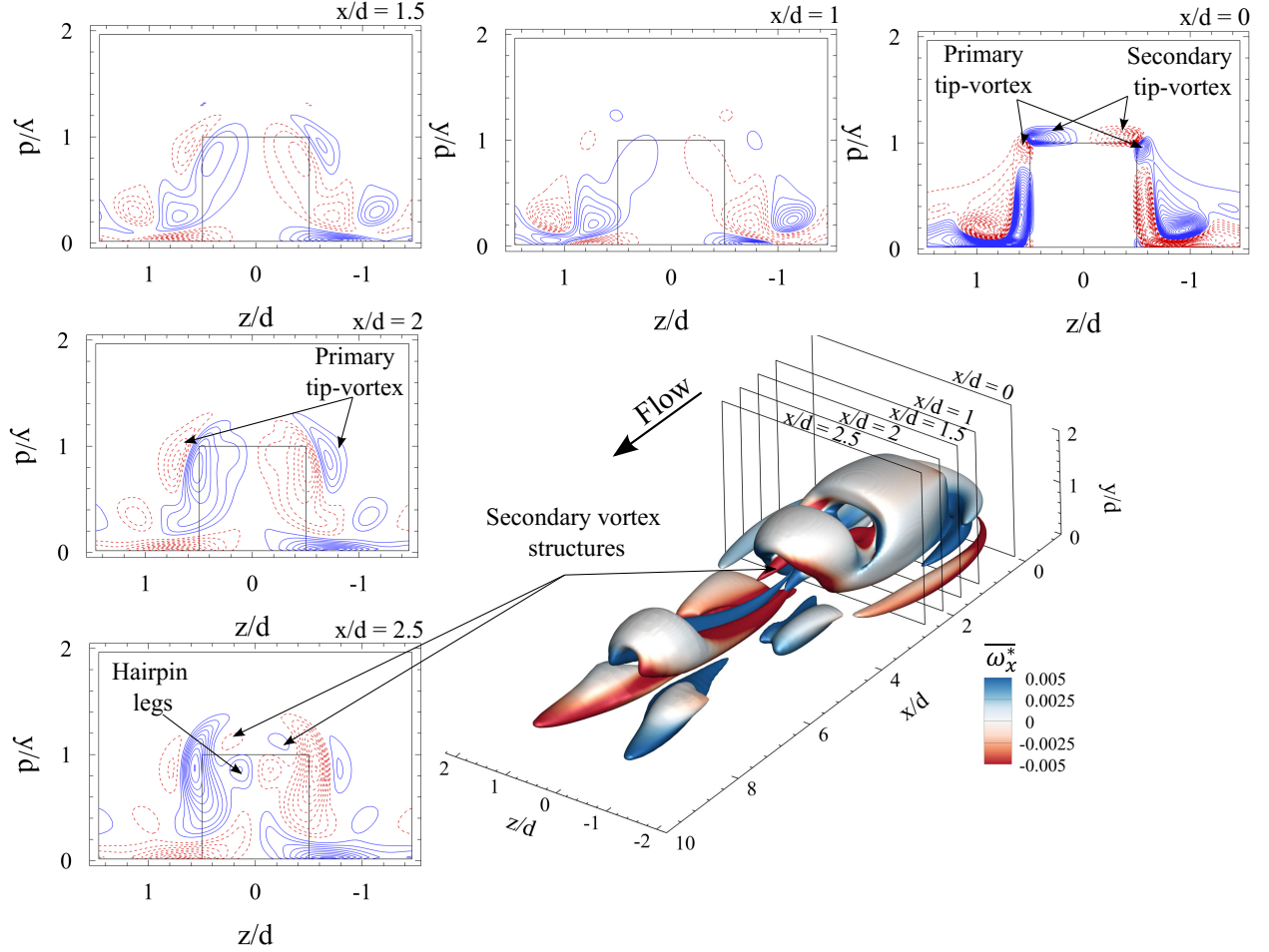


Figure 4.21: Instantaneous vortex structures identified using $Q^* = 6 \times 10^{-6}$ and overlaid with streamwise vorticity ($\overline{\omega}_x^*$), surrounded by the line contours of $\overline{\omega}_x^*$ (solid blue lines: positive values, dashed red lines: negative values) for $DR = 0.1$ prism at Reynolds number of 2.5×10^2 . The line contour cutoff levels for $\overline{\omega}_x^*$ are ± 0.12 and the contour interval is 0.001. Contours are shown at $x/d = 0, 1, 1.5, 2$ and 2.5 .

4.2 Summary

Flow over a wall-mounted finite prism with aspect-ratio 1 and varying depth-ratios (0.016 – 4) is numerically investigated at $Re = 5 \times 10^1 - 5 \times 10^2$ to characterize the implications of depth-ratio on flow dynamics. The minimum depth-ratio considered here accounts for the special case of a wall-mounted very thin prism (similar to a flat plate), which is used to establish the mechanism and wake evolution associated with the free-end effects and shear layer dynamics in small aspect-ratio prisms. These analyses and their related arguments are therefore expandable to other

cases (different depth-ratio and Re) that exhibit a similar wake classification. The wake analyses at a range of Reynolds numbers and depth-ratios suggest that threshold Re at which the wake experiences unsteady transition changes with increasing depth-ratio. Moreover, it is established that there is a unique asymmetric wake system formed behind wall-mounted prisms with sufficiently small depth-ratios resulting from alternating shear-layer peel-off on either side of the body.

The unsteady wake topology and dynamics, including symmetric and asymmetric wakes, are evaluated using the wake of the very thin prism as an example, which can be expanded to other cases with a similar wake classification. For the case of a thin prism ($DR = 0.016$) at $Re = 2.5 \times 10^2$, the wake was dominated by tilted hairpin-like structures that form an asymmetric wake system. This phenomenon was well suppressed, and wake symmetry restored, at a larger DR of 0.1. Further analysis revealed that threshold DR associated with the restoration of wake symmetry increases with Reynolds number. For example, the wake symmetry is restored by $DR = 0.3$ at $Re = 3 \times 10^2$, 1 at $Re = 4 \times 10^2$, and 2 at $Re = 5 \times 10^2$. This study identified and described a unique flow mechanism leading to this particular wake behavior using the results at $Re = 2.5 \times 10^2$. The alternating vortex shedding from either sides of the prism coincided closely with tilting of hairpin-like structures, and the formation of wake asymmetry. Moreover, it was determined that this alternating process is attributed to the out-of-phase detachment of shear layers on either side of the prism at a lower Strouhal number ($St_{sh}/2$). Moreover, it was identified that the wake features secondary streamwise structures that appear alternatively on either sides of the prism in downstream wake. The origin of secondary vortex structures was attributed to the alternate shedding of primary tip vortices. In case of asymmetric shedding, they resulted from an influx of vorticity from the shear-layer peel-off process, which fed into these structures. Increasing the depth-ratio to 0.1 lead to restoration of flow symmetry through symmetric shedding of the side surface shear layer. Secondary streamwise structures were also reported here, though they shed symmetrically and lost coherence fairly quickly downstream the prism.

Chapter 5

MEAN WAKE EVOLUTION BEHIND WALL-MOUNTED PRISMS[‡]

Past studies have primarily focused on identifying and characterizing flow structures around wall-mounted prisms, both instantaneous and time-averaged (mean). As discussed in Section 2.2, these investigations provide a detailed understanding of the evolution of mean wake topology with single-parameter dependencies. However, evolution of the mean wake as a multivariate function remains unexplored. Additionally, there is no consensus on the mean wake topology for small aspect-ratio prisms, as most studies emphasize the effects of aspect-ratio and boundary layer thickness (Derakhshandeh and Alam, 2019; Yauwenas et al., 2019). The role of downwash flow in shaping downstream wake topology is also unclear. While previous studies suggest that the tip vortex and its induced downwash flow significantly influence mean wake topology, particularly for small aspect-ratio prisms, these effects lack comprehensive analysis. Chapter 4 established that changes in depth-ratio strongly affect tip vortex strength, with increasing depth-ratio amplifying the downwash flow. This chapter addresses the gaps in understanding how changing depth-ratios (normalized length) affect the wake, extending the analysis from Chapter 4.

[‡]The content of this chapter has been published in *International Journal of Heat And Fluid Flow* under the citation (Goswami and Hemmati, 2023): “Goswami, S., & Hemmati, A. (2023). Mean wake evolution behind low aspect-ratio wall-mounted finite prisms. International Journal of Heat and Fluid Flow, 104, 109237”.

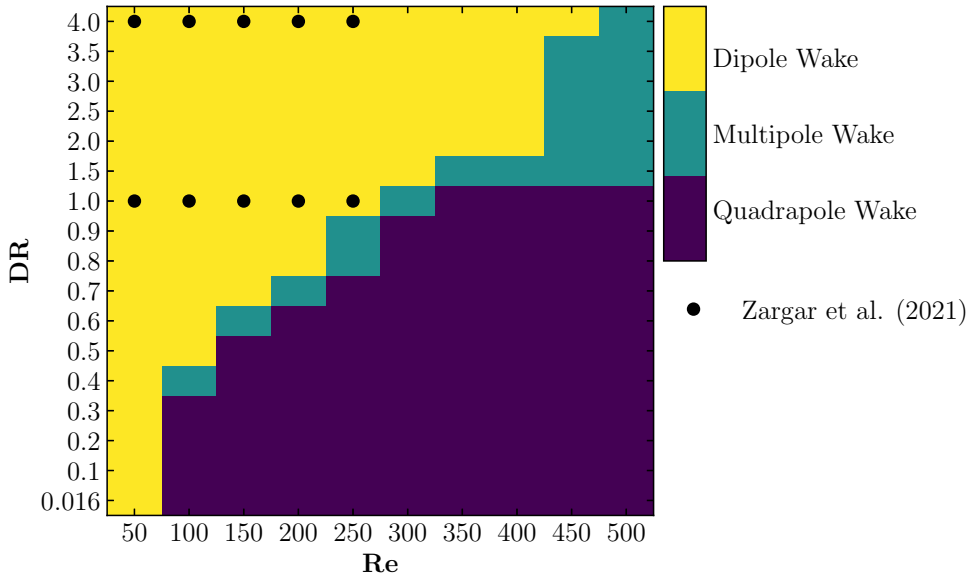


Figure 5.1: Classification of the mean wake topology in terms of Reynolds number and depth-ratio for prism with aspect-ratio of 1. Note: the vertical axis is non-linear, representing depth-ratios between 0.016–4.

Primary aim of this study is to ascertain the mechanism of the evolution of mean wake topology as a function of depth-ratio. The study focuses on prisms with $AR = 1$ and $DR = 0.016 – 4$ at $Re = 5 \times 10^1 – 5 \times 10^2$, doubling the Reynolds number range explored by Zargar et al. (2021b) and systematically increasing the depth-ratio. This chapter is structured such that the results and discussion are presented in Section 5.1, followed by a summary of the main findings in Section 5.2.

5.1 Results and Discussion

First, the mean wake topology is classified based on the presence of vortical structures in the flow. The main wake systems were Dipole, Multipole and Quadrupole-type wakes that were observed at a range of Reynolds numbers and depth-ratios, shown in Figure 5.1. This classification is based on the number of streamwise vortex pairs, i.e. tip and base vortices, formed in the downstream wake. For wall-mounted finite prisms, there are three main streamwise vortices observed in the wake, including the primary tip vortex (TV_1), secondary tip vortex (TV_2) and the base vortex or Upper

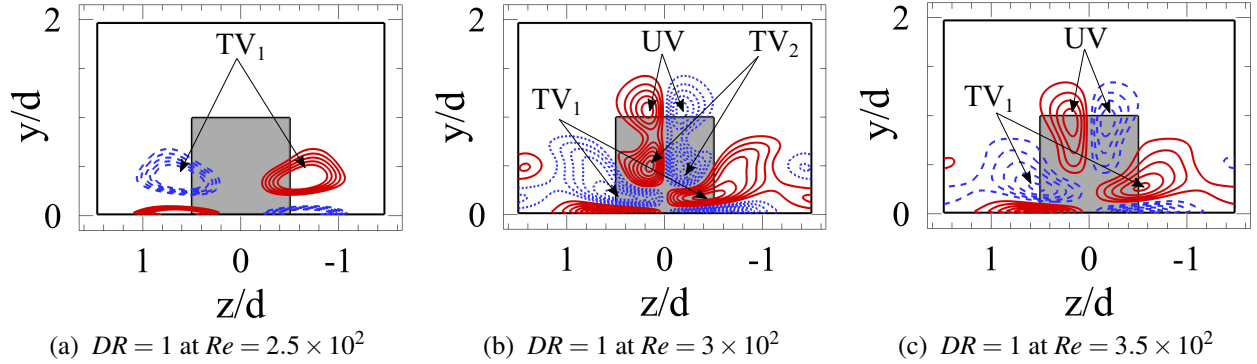


Figure 5.2: Line contours of $\bar{\omega}_x d / U_b$ (solid blue lines: positive values, dashed red lines: negative values) showing (a) Dipole-type, (b) Multipole, and (c) Quadrupole-type cross-sectional wake topology. All cases are for prism with Aspect-ratio of 1. Contours are shown at $x/d = 5$.

vortex (UV) (Wang and Zhou, 2009). Tip vortex (identified in Figure 5.2a) induces a downwash flow in downstream wake of the prism, while base (upper) vortex (identified in Figure 5.2c) induces an upwash flow. In the case of small aspect-ratio wall-mounted prisms, previous studies (da Silva et al., 2022) have referred to the base vortex pair as the “upper” vortex pair. Although the base vortex originates from the wall-body junction, due to the small aspect-ratio of the prism, these vortices transport near the prism free end downstream. Therefore, for consistency with the existing literature, these vortices (base vortex pair) are referred to as the “upper vortex pair”. Then, there are cases that exhibit a secondary tip vortex (TV_2) that is formed on the top surface of the prism with an opposite sign of rotation relative to the primary tip vortex (TV_1). The secondary tip vortex (TV_2) is associated with downwash flow as noted in Chapter 4. Line contour profiles of mean streamwise vorticity ($\bar{\omega}_x$) in Figures 5.2 further illustrates these identified mean wake topologies in cross-sectional profiles. Here the mean streamwise vorticity is normalized using prism width (d) and free-stream velocity (U_b) such that $\bar{\omega}_x^* = \bar{\omega}_x d / U_b$. Dipole-type wake in Figure 5.2a exhibits tip vortices that remain in the downstream wake, while Quadrupole-type wake (Figure 5.2c) involves both tip and upper vortices. Multipole-type wake in Figure 5.2b features an extra pair of vortices, referred to as secondary tip vortex (TV_2), that extend downstream. Multipole-type wake presents an evolutionary or Intermediate mean wake pattern between Quadrupole and Dipole wakes.

The results in Figure 5.1 indicate that the mean wake topology depends strongly on both Reynolds number and depth-ratio of the prism. For example, increasing Reynolds number from 2.5×10^2 to 3.5×10^2 results in the evolution of the mean wake topology from Dipole to Multipole to Quadrupole type wakes for $DR = 1$. The wake is dominated by a pair of tip vortex at Reynolds number of 5×10^1 , following which it evolves into Quadrupole-type wake at $Re \geq 1 \times 10^2$. At a particular Reynolds number, for example at $Re = 2.5 \times 10^2$, increasing depth-ratio results in evolution of mean wake topology from Quadrupole to Multipole to Dipole type wakes. As such, higher Reynolds number results in the enhancement of streamwise vortices, while increasing depth-ratio leads to suppression of streamwise vortices that results in mean wake evolution observed here. Previous investigations of Zargar et al. (2021b) and Rastan et al. (2021) have observed similar enhancement and suppression of streamwise vortices with increasing depth-ratio. Zargar et al. (2021b) showed that increasing depth-ratio led to enhancement of downwash flow resulting in a Dipole-type wake for large depth-ratio prisms, while Rastan et al. (2021) reported impairment of tip vortices with increasing depth-ratios. The contrary observations by Zargar et al. (2021b) and Rastan et al. (2021) stem from aspect-ratio effects in wall-mounted prisms. The numerical analysis of Rastan et al. (2021) looked at the influence of increasing depth-ratio on the wake of a large aspect-ratio (≈ 7) prism, while Zargar et al. (2021b) focused on prisms with aspect-ratio of ~ 1.2 . Yet no consensus exists in literature on the origin and role of enhancing/suppressing vortex structures in evolutionary wakes.

Figure 5.1 identifies that the threshold depth-ratio for evolution of mean wake topology increases with Reynolds number. It becomes clear that the wake is Quadrupole dominant in case of small depth-ratio prisms ($DR \leq 1$) and Dipole dominant in case of large depth-ratios ($DR > 1$). Increasing depth-ratio leads to the enhancement of downwash flow, resulting in the wake evolution from a simple to a more complex wake. Past studies have successfully identified the mean wake evolution with increasing prism aspect-ratio, although no such consensus exists in case of increasing depth-ratio at a range of Reynolds numbers. Moreover, the mechanism of the wake evolution evolution is not clear in the case of increasing depth-ratio. Thus, present study

aims to identify and characterize the evolution in mean wake topology and evaluate its mechanism as a function of depth-ratio and Reynolds number for the first time in literature.

Past studies on small aspect-ratio prisms ($AR \leq 3$) have explored the role of downwash flow (Tip vortex) in dictating the downstream wake topology (Sumner et al., 2004; Sumner and Heseltine, 2008). These studies have indicated three factors governing the downstream wake of small aspect-ratio wall-mounted prisms: (1) intensity of downwash flow, (2) the effect of upwash and downwash flow on spanwise momentum transfer, and (3) interactions between tip and upper vortex due to small aspect-ratio of the prism (Wang and Zhou, 2009; da Silva et al., 2022). Investigating these factors can provide further evidence on the wake dynamics and mechanism of mean wake evolution observed here. To this end, time-averaged (mean) wake topology is characterized as a function of changing Reynolds number and depth-ratio in the next section, followed by investigation of the intensity and influence of downwash flow on the wake structures, towards characterizing and identifying the mechanisms associated with wake evolution. Since a large number of cases are investigated over a broad parameter space, this chapter focuses on three cases for brevity, to identify and characterize the mean wake topology. These cases are $DR = 1$ at $Re = 2.5 \times 10^2, 3 \times 10^2$ and 3.5×10^2 , representing Dipole, Multipole and Quadrupole wake topology, respectively.

5.1.1 Time-averaged wake characteristics

Time-averaged vortical structures are shown in Figure 5.3 using the iso-surfaces of λ_2 overlaid by the contour of mean axial vorticity ($\bar{\omega}_x$). Top-right of each figure shows an overlapped slice featuring the mean wake topology in axial plane. Dipole-type wake structure is observed in Figure 5.3a, where two counter-rotating streamwise vortices emanating from the tip extend into the wake. These structures coincide with the Dipole-wake pattern shown in Figure 5.2a. Quadrupole wake topology (Figure 5.3c) shows both counter-rotating tip (TV_1) and upper vortices (UV) in the wake, similar to Figure 5.2c. Finally, the Multipole wake topology (Figure 5.3b) is reported, featuring a pair of secondary tip vortices (TV_2). TV_2 appears to have opposite-sign

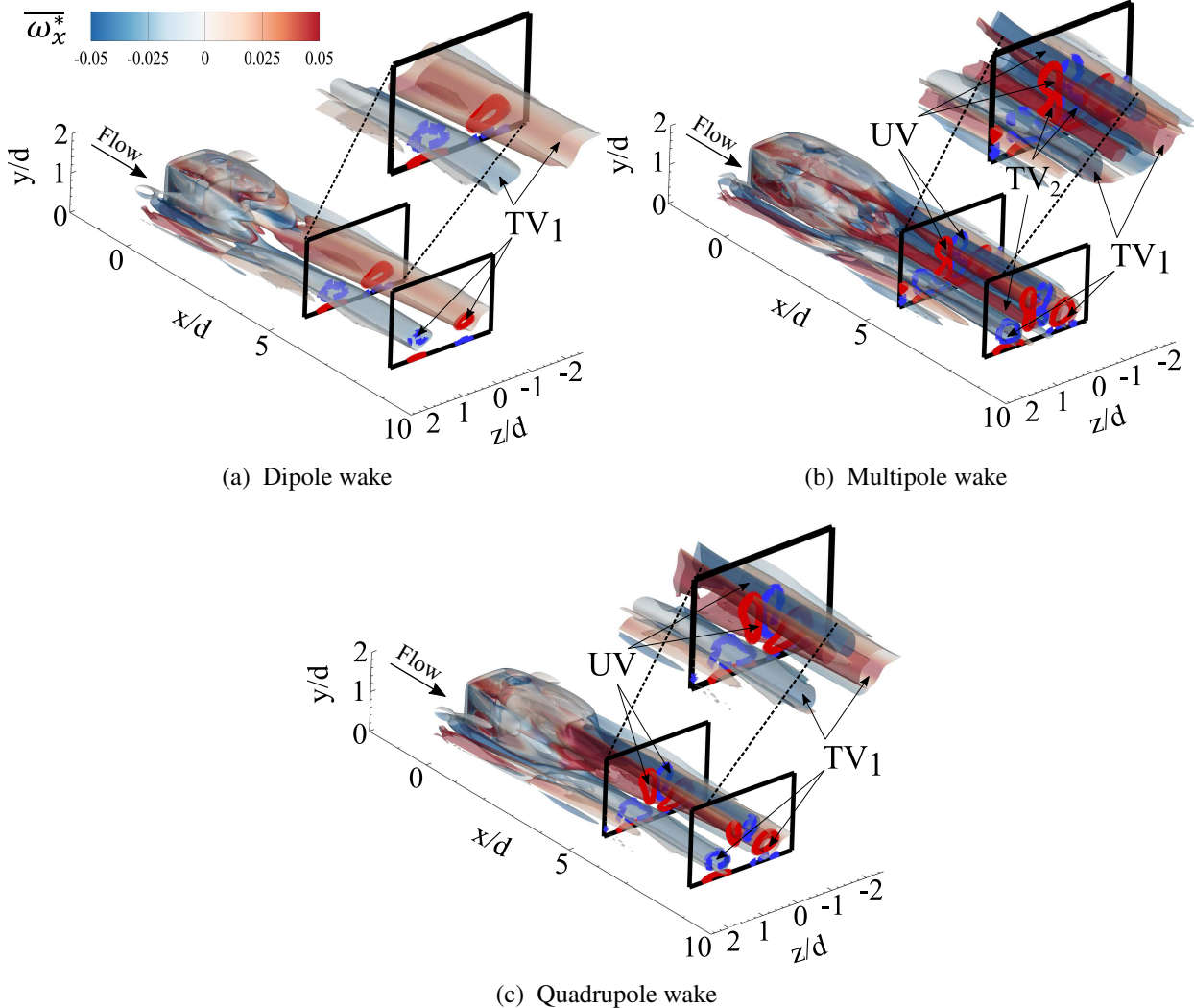


Figure 5.3: Time-averaged (mean) wake structures identified using $\lambda_2 = -0.0001$ colored with $\overline{\omega}_x d / U_b$. Shown are (a) $DR = 1$ at $Re = 2.5 \times 10^2$, (b) $DR = 1$ at $Re = 3 \times 10^2$, and (c) $DR = 1$ at $Re = 3.5 \times 10^2$. Line contours of $\overline{\omega}_x d / U_b$ are also drawn on the yz -planes at $x/d = 5$ and 8 , resembling the streamwise wake topology identified in Figure 5.2.

vorticity compared to TV_1 , consistent with Figure 5.2b. Figure 5.4 shows these topologies at different depth-ratios and Reynolds numbers. For clarification, Dipole wake is shown at depth-ratio of 2 at $Re = 3 \times 10^2$, Multipole wake at depth-ratio of 3 at $Re = 4.5 \times 10^2$, and Quadrupole wake pattern is presented at depth-ratio of 0.016 at $Re = 2.5 \times 10^2$. The consistencies between Figure 5.4 and Figure 5.3 suggest that the mean wake topology do not show solely the effect of changing depth-ratio or that of Reynolds number rather, these effects appear to be

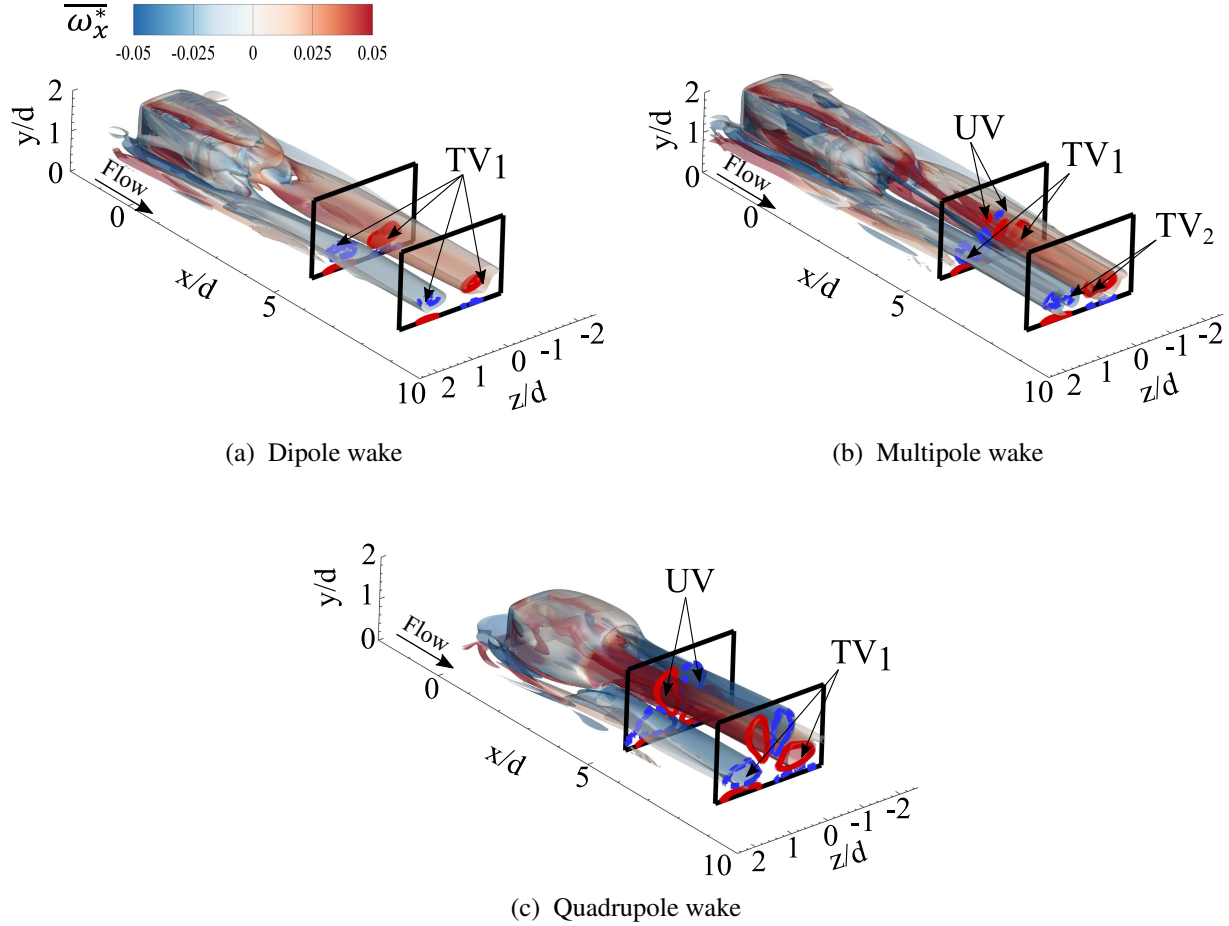


Figure 5.4: Time-averaged (mean) wake structures identified using $\lambda_2 = -0.0001$ colored with $\bar{\omega}_x d / U_b$. Shown are (a) $DR = 2$ at $Re = 3 \times 10^2$, (b) $DR = 3$ at $Re = 4.5 \times 10^2$, and (c) $DR = 0.016$ at $Re = 2.5 \times 10^2$. Line contours of $\bar{\omega}_x d / U_b$ are also drawn on the yz -planes at $x/d = 5$ and 8 , resembling the streamwise wake topology identified in Figure 5.2.

interconnected. These structures have been reported by Rastan et al. (2021) and Chapter 4, in which they emanate from the top surface of the prism leading edge and extend into the wake. Rastan et al. (2021) showed that secondary tip vortices vanish in the vicinity of the prism due to the large aspect-ratio and strong downwash flow. For small aspect-ratio prisms, however, they prevailed (Chapter 4). This hints at the influence of aspect-ratio in suppressing streamwise vortices in the wake.

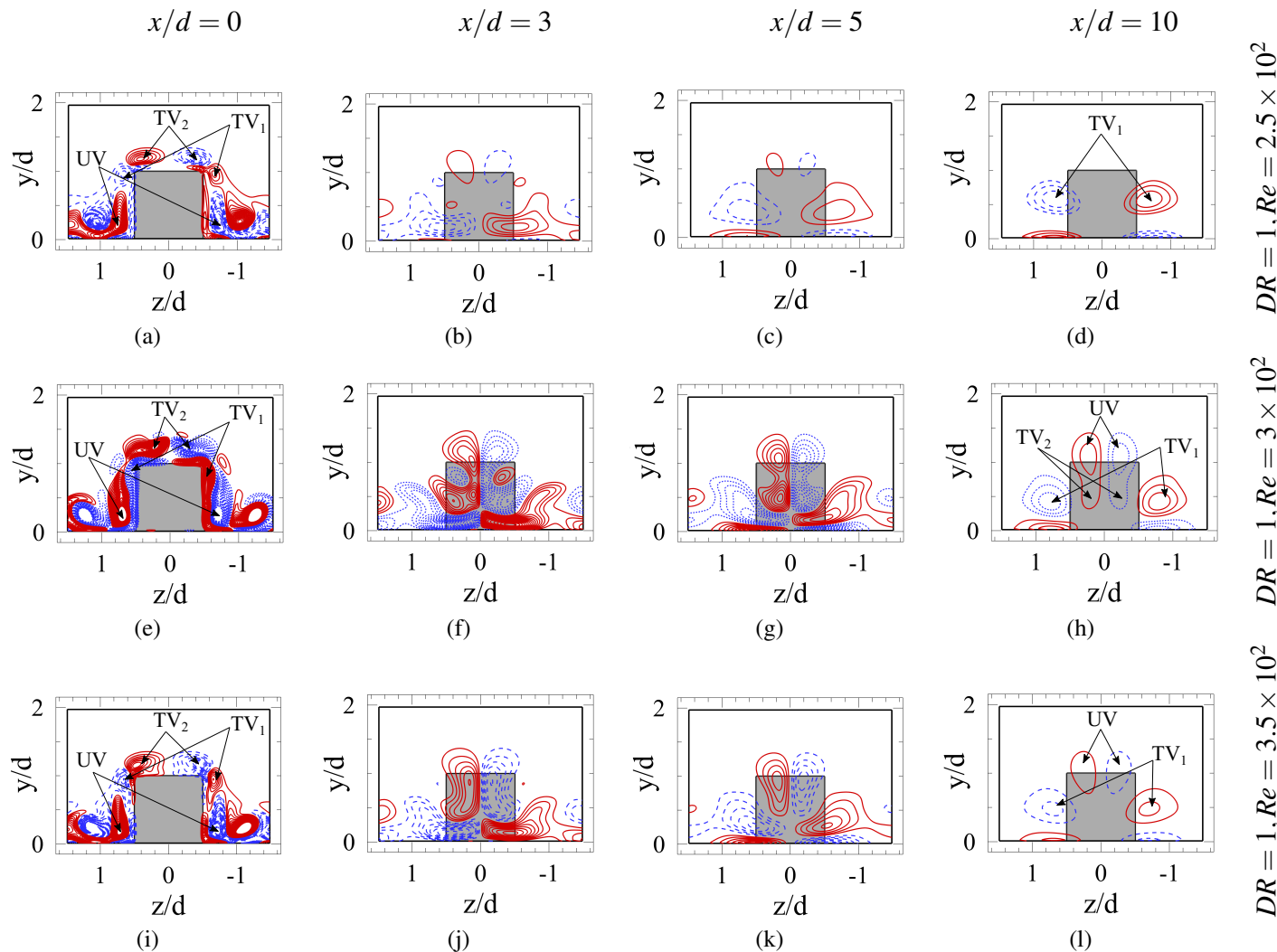


Figure 5.5: Line contours of $\bar{\omega}_x d / U_b$ (solid blue lines: positive values, dashed red lines: negative values) showing evolution of primary tip vortex (TV_1), secondary tip vortex (TV_2), and upper vortex (UV), in (a-d) Dipole-type ($DR = 1$ at $Re = 2.5 \times 10^2$), (e-h) Multipole ($DR = 1$ at $Re = 3 \times 10^2$), and (i-l) Quadrupole-type ($DR = 1$ at $Re = 3.5 \times 10^2$) wake topology. All cases are for prism with Aspect-ratio of 1.

The evolution of streamwise vortex structures are shown in Figure 5.5 using time-averaged streamwise vorticity ($\overline{\omega_x}$) contours at various axial locations in the wake for all wake topologies, including $x/d = 0, 3, 5$, and 10 . The abbreviations in Figure 5.5 refer to primary tip vortex (TV_1), secondary tip vortex (TV_2), and upper vortex (UV). Although these contours are analogous to flow visualizations in Figure 5.3, they quantify the wake strength and clarify vortex structure over the prism surfaces. For Dipole-type wake (Figures 5.5a–5.5d) the primary and secondary tip vortices are generated from the leading and side edges along the top surface of the prism, respectively. Further downstream, tip vortices transport closer to the ground due to the downwash flow while secondary tip vortices interact with the upper vortex. Secondary tip vortices diminish beyond $x/d = 3$ and vanish completely at $x/d = 10$. Thus, secondary tip vortices and upper vortex only appear in the near vicinity of the prism, while the primary tip vortex remains in the downstream wake and results in the formation of Dipole-type wake topology. Quadrupole wake (Figures 5.5i–5.5l) features streamwise vortices of nearly equal strength (in terms of circulation) at $x/d = 10$. In case of Multipole wake topology, the interaction of secondary tip vortex with upper vortex appears to prolong till $x/d = 10$, which results in a Multipole structure similar to one observed by Zhang et al. (2017).

Now, quantitative evaluation of the strength of the primary tip vortex (TV_1) and the upper vortex (UV) downstream the wake are presented in Figure 5.6. The strength of vortices are quantified in terms of circulation (Γ), which is the area integral of vorticity (Chapter 4 and Section 3.8) normalized by the free-stream velocity (U_b) and prism width (d). The strength of tip vortex initially reduces till $x/d = 2$. The weakening of vortex structures can be attributed to their interactions with the recirculation region behind the prism. In case of Quadrupole wake, a sharp increase in Γ is followed by a gradual drop till $x/d = 10$, while the change remains negligible for Dipole wake. Thus, it becomes clear that the primary tip vortex decays less rapidly and remains dominant in the downstream wake for all wake topologies. The upper vortex, however, decays rapidly for all wakes, as evident from the sharp drop in the strength of the upper vortex in Figure 5.6b.

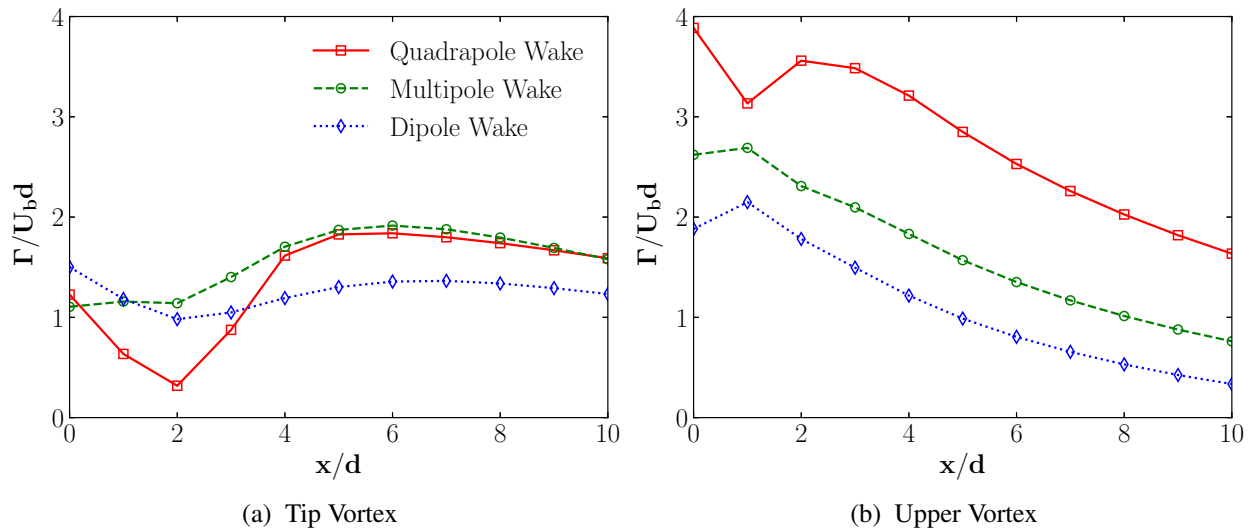


Figure 5.6: Variation in Circulation ($\bar{\Gamma}/U_b d$) of primary tip vortex (TV_1) and upper vortex (UV). Shown are Dipole ($DR = 1$ at $Re = 2.5 \times 10^2$), Multipole ($DR = 1$ at $Re = 3 \times 10^2$), and Quadrupole ($DR = 1$ at $Re = 3.5 \times 10^2$).

5.1.2 Effects of downwash and upwash flows

It is already established from the results in Chapter 4 that free-end vortices dictate the wake of wall-mounted prisms, which is why it becomes important to investigate their influence on changing wake topology. As such, contours of time-averaged normal velocity (\bar{v}) at $z/d = 0$ for different wake topologies are presented in Figure 5.7. Red and blue regions correspond to upwash and downwash flow, respectively. Upwash flow is evident at the leading edge for all cases, resulting from shear-layer separation at the leading edge of the prism. This further results in an upward curvature of streamlines, as noted by Zargar et al. (2021b). A region of downwash flow is apparent in front of the prism, which is related to the horseshoe vortex (Simpson, 2001). In case of Dipole-type wake, downwash flow dominated the wake close to the prism and further downstream. This is consistent with the observation from Figure 5.3. As the wake evolves from Dipole to Multipole, and further into Quadrupole-type, increasing intensity of upwash flow is apparent from Figures 5.7a, 5.7b, and 5.7c. The Multipole wake features the prolonged interaction of the tip and upper vortex in downstream wake.

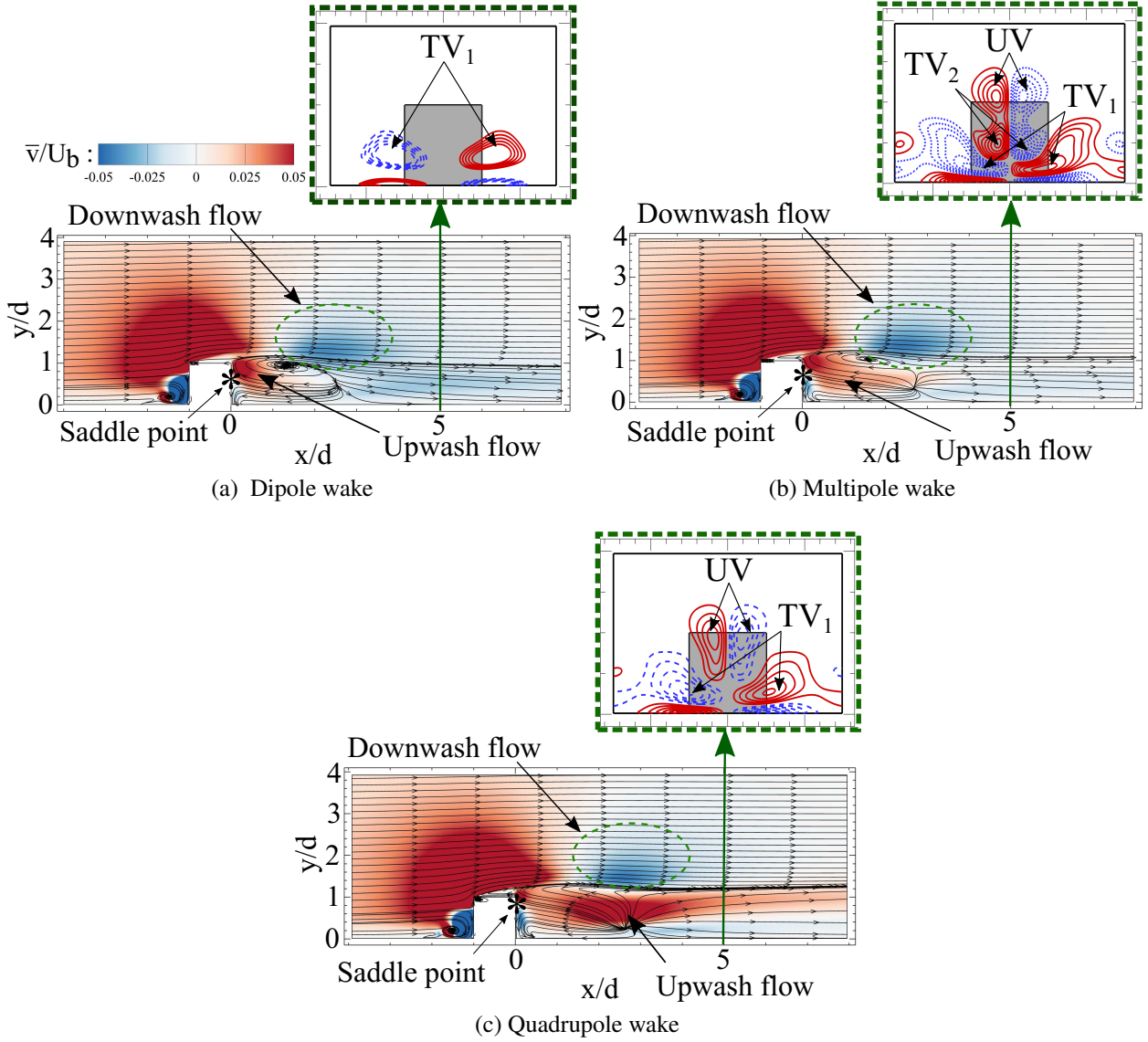


Figure 5.7: Contours of time-averaged normal velocity (\bar{v}/U_b) with wake topology identified using line contours of $\bar{\omega}_x d/U_b$ on top-right. Shown are (a) $DR = 1$ at $Re = 2.5 \times 10^2$, (b) $DR = 1$ at $Re = 3 \times 10^2$, and (c) $DR = 1$ at $Re = 3.5 \times 10^2$. Contours are shown at $z/d = 0$.

Quantitative investigation of the intensity of downwash flow is presented by looking at the trends of saddle point (\bar{Y}_s/d) in Figure 5.8. Saddle point indicates the balance between upwash and downwash flows (Wang and Zhou, 2009), and thus provides a quantitative measure to study the influence of downwash flow. Saddle points are marked by “*” in Figure 5.7. When upwash flow dominates, saddle point appears above the mid-plane of the prism ($\bar{Y}_s/d \geq 0.5$). It appears closer to the ground ($\bar{Y}_s/d < 0.5$) when downwash flow dominates. A correlation exists between the wake

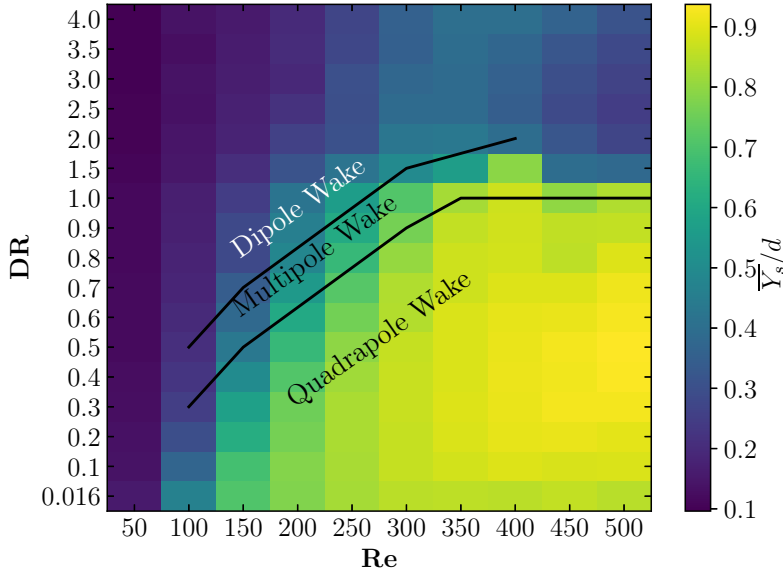


Figure 5.8: The location of saddle point (\bar{Y}_s/d) as a function of Re and DR for prisms with Aspect-ratio of 1. Note: the vertical axis is non-linear, representing depth-ratios between 0.016–4.

map and the location of saddle points, such that the Quadrupole-type wake appears at the region of dominant upwash flow. Dipole and Multipole type wakes are observed in cases that downwash flow dominates, while Multipole wake appears when the saddle point is closer to the mid-plane ($\bar{Y}_s/d \approx 0.5$). Figure 5.8 identifies, by inspection and based on the mean wake map in Figure 5.1, the boundary of evolution between various mean wake topologies. These results further hint at the role of downwash flow in describing the mean wake of small aspect-ratio prisms.

The effect of free-end on mean velocity for all cases is presented in Figure 5.9. For all wake topologies, mean axial velocity (\bar{u}) depends strongly on y because of the end-effects, such that \bar{u} is negative along most of the span of the prism ($y/d \leq 1$) for $x/d \leq 3$ (Figure 5.9a). Further, \bar{u} corresponds strongly with the size of reverse flow zone near the prism ($x/d \leq 3$). Increasing the intensity of upwash flow, as a result of evolution of mean wake to quadrupole wake, results in a larger recirculation region behind the prism (Wang et al., 2006; Zargar et al., 2021b). As such, Quadrupole wake results in larger recirculation zone compared to the Dipole-wake, which is attributed to a strong upper vortex (upwash flow) in case of Quadrupole-wake. This contributes to a significant reverse flow region. Further downstream, a prolonged velocity deficit is noted

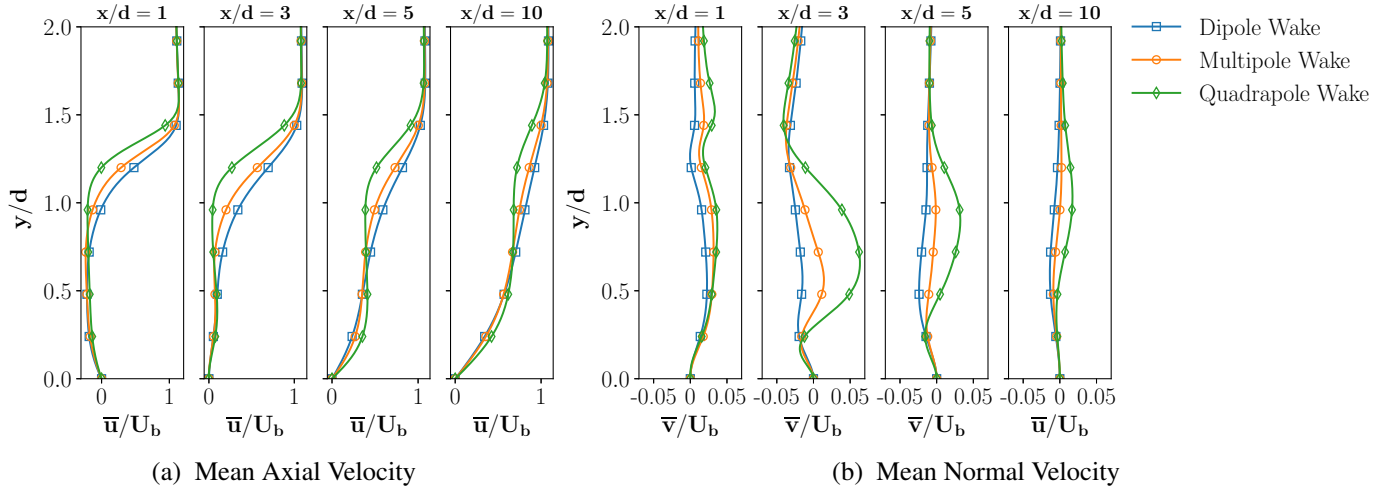


Figure 5.9: Spanwise variation of time-averaged (mean) axial (\bar{u}/U_b) and normal velocity (\bar{v}/U_b) for different wake topologies. Shown are Dipole ($DR = 1$ at $Re = 2.5 \times 10^2$), Multipole ($DR = 1$ at $Re = 3 \times 10^2$), and Quadrupole ($DR = 1$ at $Re = 3.5 \times 10^2$).

for Quadrupole and Multipole wakes, which correlates with a larger recirculation region due to significant upwash flow. The profiles of mean normal velocity (\bar{v}) exhibit a strong dependence on end-effects as seen in Figure 5.9b. Close to the prism at $x/d = 1$, due to a strong region of upwash flow in case of Multipole wake, \bar{v} is mostly negative in the span of the prism. In the region of $x/d \geq 3$, the influence of downwash flow becomes apparent, such that Dipole-wake results in smaller deficit of \bar{v} compared to Quadrupole-wake. In other words, the upwash flow enhancement results in larger deficit of \bar{v} in a Quadrupole-wake. The free-end downwash flow is pushed up by the upwash flow, which results in a shift in peak of \bar{v} closer to the prism tip. This is attributed to the wake evolution from Dipole to Quadrupole-type, in which case the upper vortex (upwash flow) enhances rapidly (Sumner et al., 2004; Wang et al., 2006).

Downwash and upwash flows have a significant effect on the shear-layer roll-up behind the prism, which further leads to the formation and convection of streamwise vortex structures downstream (Wang and Zhou, 2009). Formation and convection of these streamwise vortex structures is associated with streamwise momentum transport due to the second-order central moments or co-variance of velocity fluctuations, which are axial ($\bar{u}'\bar{u}'$) and shear stresses ($\bar{u}'\bar{v}'$) (Wang and Zhou, 2009). Since $\bar{u}'\bar{v}'$ accounts for stirring and mean momentum transport, it

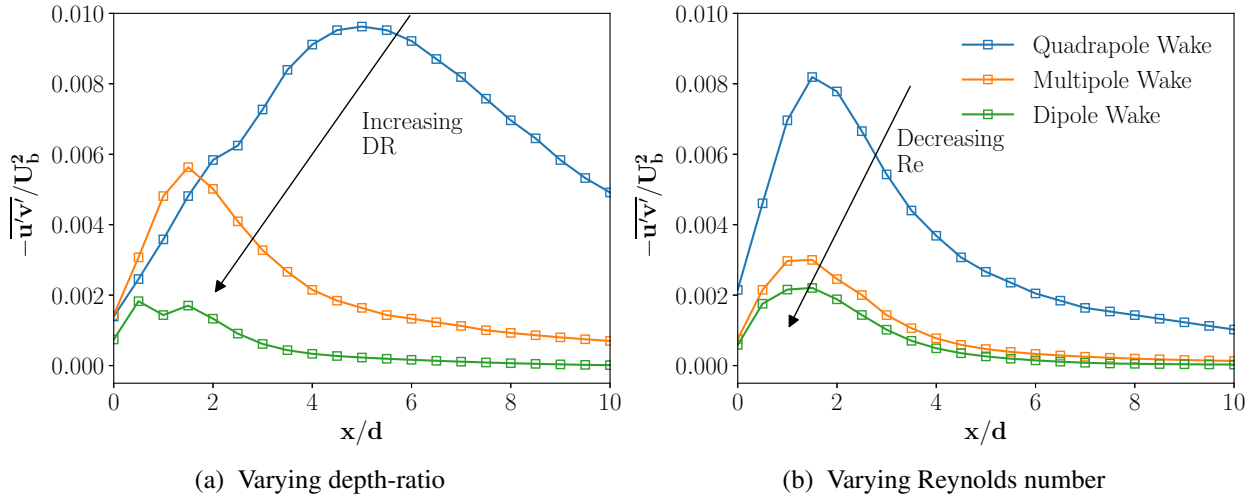


Figure 5.10: Streamwise variation of maximum shear stress ($-\bar{u}'v'$), normalized by free-stream velocity (U_b). Shown are Dipole ($DR = 1$ at $Re = 2.5 \times 10^2$), Multipole ($DR = 1$ at $Re = 3 \times 10^2$), and Quadrupole ($DR = 1$ at $Re = 3.5 \times 10^2$).

enables a deeper insight into the interactions of upper ($v' > 0$) and tip vortex ($v' < 0$) with the free-stream flow ($u' > 0$). Moreover, the co-variance of velocity fluctuations present a fundamental quantity to analyze the flow dynamics of shear-flows, such as that of wall-mounted prisms. Zdravkovich (2003) and Chapter 4 have shown that a stronger downwash flow leads to the elongation of the shear-layer and widening of the near-wake. Figure 5.10a shows the variation in magnitude of maximum shear stress ($\overline{u'v'}$) as the wake evolves with increasing depth-ratio. In case of a Quadrupole wake, due to intense upwash flow ($v' > 0$), the maximum value of $\overline{u'v'}$ occurs close to $x/d = 5$. Increasing the depth-ratio leads to a stronger tip vortex ($v' < 0$), causing a shift in the peak of maximum $\overline{u'v'}$ closer to the prism trailing edge. Further increasing depth-ratio leads to a Dipole wake with a stronger downwash flow, which significantly suppresses the streamwise momentum transfer ($\overline{u'v'}$). Suppression of $\overline{u'v'}$ remains consistent as the wake evolves with decreasing Reynolds number in Figure 5.10b.

Quantitative comparison of $\overline{u'u'}$ and $\overline{u'v'}$, at multiple axial locations for the Quadrupole, Multipole and Dipole-type topologies, is presented in Figure 5.11. Distribution of $\overline{u'u'}$ exhibits a stronger dependence on changing depth-ratio and Reynolds number, such that enhancing and decaying vortex structures are visible from the profiles (Figure 5.11a). A peak noted at

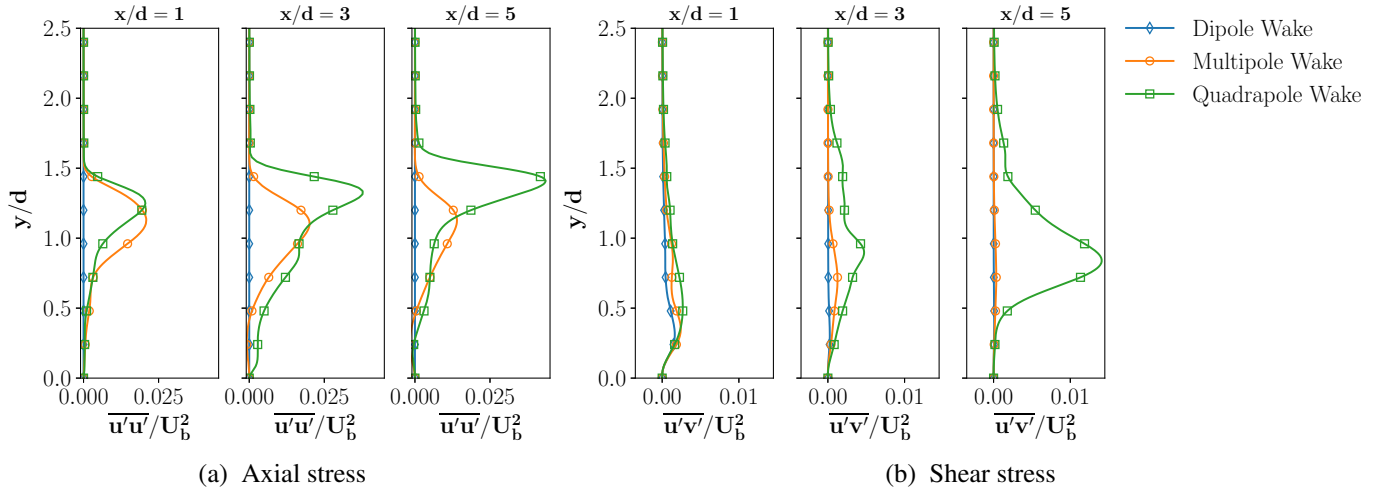


Figure 5.11: Streamwise variation of axial ($\overline{u'u'}$) shear stress ($\overline{u'v'}$) normalized by free-stream velocity (U_b). Shown are Dipole ($DR = 1$ at $Re = 2.5 \times 10^2$), Multipole ($DR = 1$ at $Re = 3 \times 10^2$), and Quadrupole ($DR = 1$ at $Re = 3.5 \times 10^2$) wakes.

$1 \leq y/d \leq 2$ is associated with the spread of tip vortex, a smaller peak is observed closer to the ground, which is associated with the upper-vortex. As the wake transforms from Quadrupole to Dipole topology, the upper-vortex appears to diminish, while tip vortex becomes stronger. At $x/d = 5$, the secondary peak deteriorates, hinting at deteriorating upper-vortex with increasing depth-ratio. Trends of $\overline{u'v'}$ in the downstream wake (Figure 5.11b) show that the magnitude of $\overline{u'v'}$ is largest for Quadrupole-type wake, as compared to Multipole and Dipole wake. This is mainly attributed to the significant influence of upwash flow ($v' > 0$) in Quadrupole-type wake. These results are consistent with previous observations in Figure 5.10a. At $x/d = 5$, the magnitude of $\overline{u'v'}$ for Multipole and Dipole-type wake diminish significantly. The suppression of $\overline{u'v'}$ is attributed to deteriorating upper-vortex ($v' > 0$), which significantly reduces the spanwise momentum transfer.

Figure 5.12 shows the quantitative comparison of $\overline{u'u'}$ and $\overline{u'v'}$, at multiple axial locations for the Dipole ($DR = 1$ at $Re = 400$), Multipole ($DR = 1.5$ at $Re = 4 \times 10^2$), and Quadrupole ($DR = 2$ at $Re = 4 \times 10^2$) wakes. In this case, the wake patterns evolve under changing depth-ratios at $Re = 4 \times 10^2$, as opposed to changing Reynolds numbers (in Figure 5.11). The trends remain consistent with that of Figure 5.11, which shows that this phenomenon remains invariant to flow or

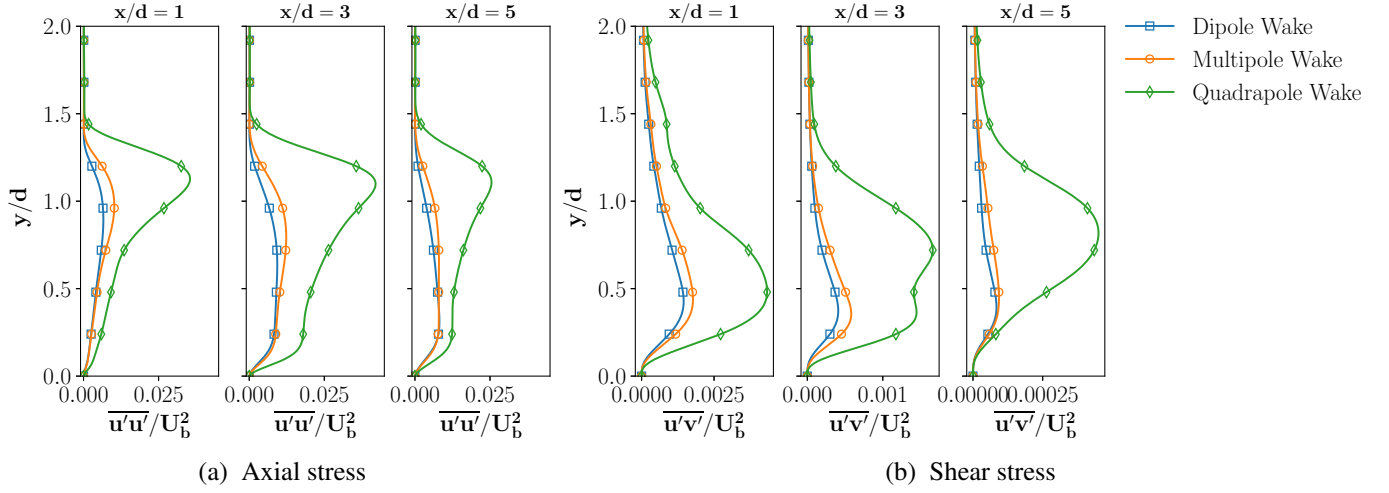


Figure 5.12: Streamwise variation of axial ($\overline{u'u'}$) shear stress ($\overline{u'v'}$) normalized by free-stream velocity (U_b). Shown are Dipole ($DR = 1$ at $Re = 4 \times 10^2$), Multipole ($DR = 1.5$ at $Re = 4 \times 10^2$), and Quadrupole ($DR = 2$ at $Re = 4 \times 10^2$) wakes.

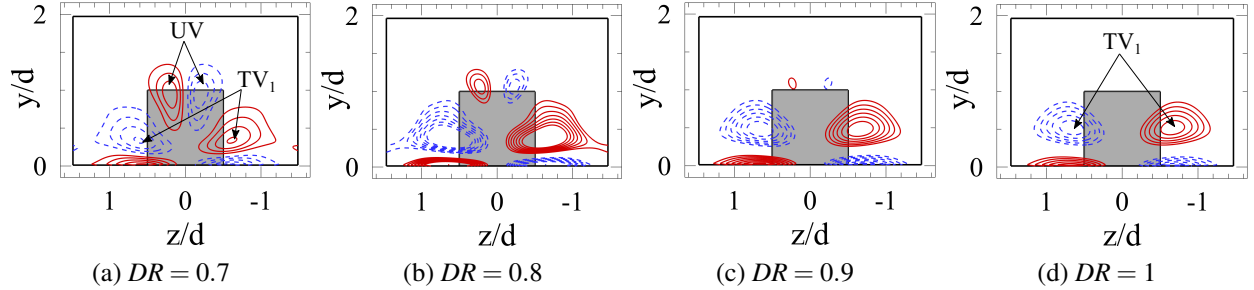


Figure 5.13: Line contours of $\overline{\omega_x}d/U_b$ (solid blue lines: positive values, dashed red lines: negative values) showing evolution from Quadrupole to Dipole wake, at $x/d = 5$, with increasing depth-ratio at Reynolds number of 2.5×10^2 .

geometrical parameters. Instead it only depends on the evolution of wake topology. As the wake evolves from Quadrupole to Dipole, the peak close to the ground diminishes, while that near the free-end becomes stronger. This correlates with the deterioration of upper vortex and strengthening of the tip vortex.

The effect of deteriorating upper-vortex on the mean wake evolution can be qualitatively observed in Figure 5.13. At a particular Reynolds number, for example 2.5×10^2 , the wake map in Figure 5.1 shows that mean wake changes from Quadrupole (at $DR = 0.7$) to Multipole wake (at $DR = 0.8 - 0.9$), followed by Dipole-type wake (at $DR = 1$). Line contours of $\overline{\omega_x}$ in

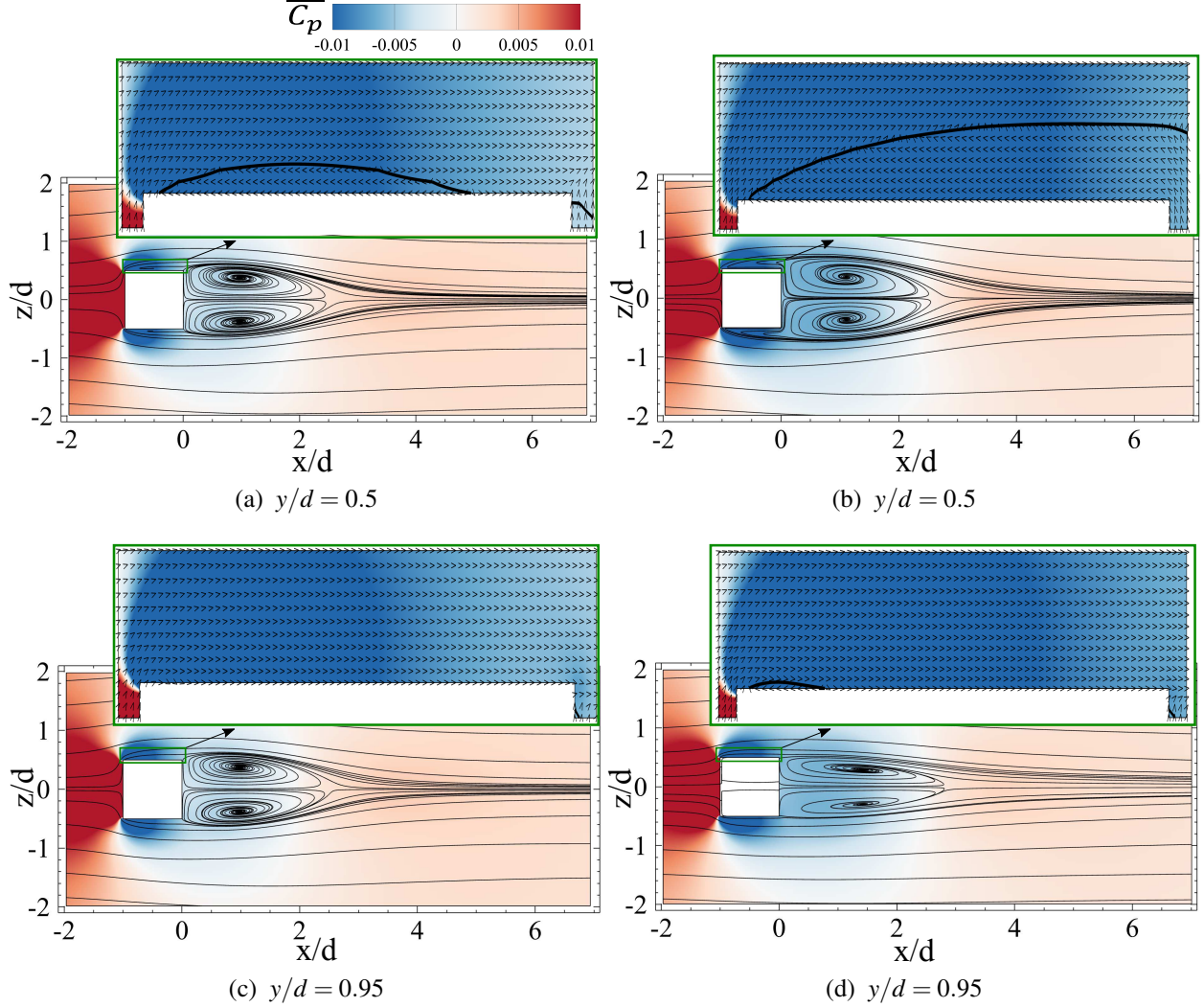


Figure 5.14: Time-averaged streamlines, overlaid by contours of \bar{C}_p , at spanwise plane of (a,b) $y/d = 0.5$ and (c, d) $y/d = 0.95$ for (a,c) Dipole and (b,d) Quadrupole-type wakes, along with mean velocity vectors in the top-right corner. Shown are (a,c) $DR = 1$ at $Re = 2.5 \times 10^2$, and (b,d) $DR = 1$ at $Re = 3.5 \times 10^2$.

Figure 5.13 show this variation in the cross-sectional plane at $x/d = 5$. The upper vortex deteriorates, leading to the evolution of mean wake topology from Quadrupole to Dipole-type with increasing depth-ratio (or decreasing Reynolds number). To scrutinize the mechanism of evolution this study needs to further evaluate the deterioration of upper vortex. Previous studies (Rastan et al., 2021) and results of Chapter 4 have reported that flow reattachment on the prism surfaces with increasing depth-ratio results in the suppression of streamwise vortex structures. Here, side shear-layer reattaches to the surface at $DR = 1$ at $Re = 2.5 \times 10^2$. Flow

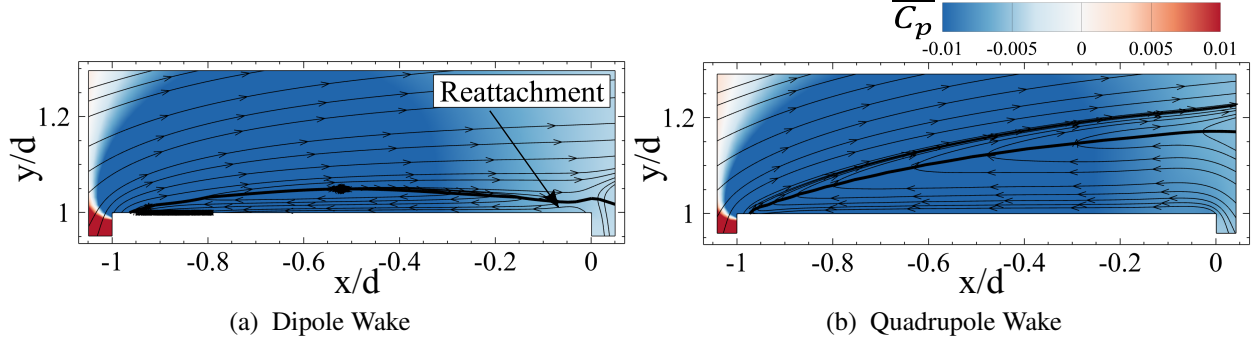


Figure 5.15: Time-averaged streamlines, overlaid by contours of $\overline{C_p}$ at normal plane of $z/d = 0$ for (a) Dipole and (b) Quadrupole-type wakes. The bold black line shows the mean velocity streamline of $\bar{u}/U_b = 0$. Shown are (a) $DR = 1$ at $Re = 2.5 \times 10^2$, and (b) $DR = 1$ at $Re = 3.5 \times 10^2$.

reattachment also plays an important role in the suppression of $\overline{u'v'}$ (Figures 5.10a and 5.11b) since the flow reattachment led to the suppression of velocity gradients downstream.

Figure 5.14 shows mean streamlines plots overlaid by contours of $\overline{C_p}$ at spanwise planes of $y/d = 0.5$ and 0.95 for Dipole ($DR = 1$ at $Re = 2.5 \times 10^2$) and Quadrupole ($DR = 1$ at $Re = 3.5 \times 10^2$) wakes. At $y/d = 0.5$, recirculation region behind the Dipole wake appears narrower compared to the Quadrupole wake. Moreover, the length of recirculation region for Quadrupole wake is larger compared to Dipole wake. The result is consistent with the concept that a predominant downwash flow suppresses the streamwise vortex dynamics in case of Dipole wake, thus reducing the length of reverse flow zone. Near the prism tip ($y/d = 0.95$), the influence of downwash flow is clearly noted such that the Quadrupole wake reverse flow region extends beyond $x/d = 3$, while it is limited to $x/d \approx 1.5$ for Dipole wake. The contours of $\overline{C_p}$ also note an adverse pressure gradient on the side edge for Dipole wake, which suggests a reattachment of flow on prism surfaces. In case of Quadrupole wake, while such adverse pressure gradient exists, there is a monotonic recovery of pressure behind the prism suggesting a partial or no reattachment of flow on sides of prism. The mean velocity vectors presented on the top-right corner of Figure 5.14 provides further evidence of flow reattachment. It become clear that reattachment of flow occurs near the prism trailing edge at $y/d = 0.5$ for the Dipole wake, while no reattachment is noted for the Quadrupole wake. At $y/d = 0.95$, both cases show a reattachment of flow near the prism leading edge, where tip vortices

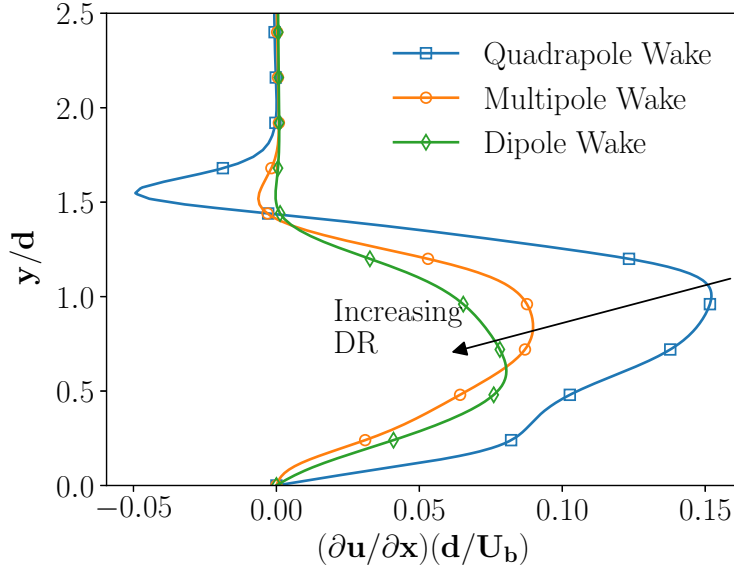


Figure 5.16: Streamwise axial velocity gradient ($\partial u / \partial x$) normalized by prism width (d) and free-stream velocity (U_b). Shown are Dipole ($DR = 1$ at $Re = 2.5 \times 10^2$), Multipole ($DR = 1$ at $Re = 3 \times 10^2$), and Quadrupole ($DR = 1$ at $Re = 3.5 \times 10^2$) wakes. Profiles are shown at $x/d = 5$.

emanate. This is further corroborated by a larger angle of flow curvature in case of Quadrupole wake, as opposed to a smaller angle for Dipole wake. Figure 5.15 shows the mean streamlines plots overlaid by contours of \bar{C}_p at normal plane of $z/d = 0$ for Dipole ($DR = 1$ at $Re = 2.5 \times 10^2$) and Quadrupole ($DR = 1$ at $Re = 3.5 \times 10^2$) wakes. The bold black line on the plot features the mean streamline of $\bar{u} = 0$, showing the mean recirculation region behind the prism. The observations remain consistent here, such that a flow reattachment is noted on the prism top surface in case of Dipole wake, while no reattachment is noted for Quadrupole wake. The monotonic recovery of pressure in case of Quadrupole wake is evident until $x/d \approx 2$, and $\bar{u} = 0$ extends into the wake suggesting no reattachment on the prism top surface.

Figure 5.16 further shows the suppression of velocity gradients for Multipole and Dipole-type wakes, while a larger velocity gradient is observed for the Quadrupole wake. Suppression of velocity gradient results from the reattachment of flow for Dipole wake, which further confirms the distortion of upper vortex as a result of the reattachment. It is evident from Figure 5.11a that a deficit in axial momentum ($\bar{u}'\bar{u}'$) is noted favoring the Quadrupole wake, as the wake evolves from Dipole to Quadrupole topology. This excess $\bar{u}'\bar{u}'$ is associated with the presence of two streamwise

vortex structures, tip and upper vortices, forming the Quadrupole wake. The shift in $\overline{u'u'}$ towards the prism tip is due to the influence of upwash flow ($v' > 0$). Thus, it becomes apparent that with increasing depth-ratio (or decreasing Re), a momentum deficit is induced due to the distortion of a streamwise vortex pair. This momentum deficit in turn results in the suppression of velocity gradients via an adverse pressure gradient behind the body. This leads to flow reattachment and wake evolution in the process.

5.2 Summary

The mean wake of a small aspect-ratio wall-mounted prism is evaluated at a range of depth-ratios (0.016 – 4) and Reynolds numbers ($5 \times 10^1 - 5 \times 10^2$), to identify and characterize the evolution of mean wake topology. The focus of this analysis is the mean wake evolution with increasing depth-ratio to ascertain the related mechanism. A wake map is presented first, which classified the mean wake topology as Dipole-type, Multipole and Quadrupole-type wakes at a range of Reynolds numbers and depth-ratios. This classification is based on the number of streamwise vortex pairs, which are the tip and upper-vortices, appearing in the downstream wake. A Multipole, intermediate wake pattern is observed as the evolutionary structure between Quadrupole and Dipole-type wakes. This classification indicated a strong multivariate influence on mean wake evolution such that the threshold depth-ratio changes with Reynolds number, while all prism studies had limited their geometrical study to variations of aspect-ratio.

To understand the mean wake evolution and its mechanism, three factors are investigated that govern the wake of small-aspect-ratio prisms: (1) strength of the downwash flow, (2) influence of upwash and downwash flow on the momentum transfer, and (3) interactions of tip and upper vortex in the symmetry plane. First, the role of downwash flow and tip vortex is established in dictating the downstream wake of small aspect-ratio prisms using quantitative comparison of the location of saddle points (\bar{Y}_s/d). Then, the influence of downwash and upwash flow on the formation and convection of streamwise vortex structures are observed in the wake. With increasing depth-

ratio, downwash flow intensifies, leading to suppression of the spanwise momentum transfer ($\overline{u'v'}$). Further, axial ($\overline{u'u'}$) and shear stress ($\overline{u'v'}$) trends characterize a deteriorating upper vortex with increasing depth-ratio, which is further confirmed through wake analysis. Interaction of tip and upper vortex in the symmetry plane is analyzed, which attributed the deterioration of upper vortex to the flow reattachment to the prism surfaces with increasing depth-ratio. A strong downwash flow leads to flow reattachment to the prism top and side surfaces with increasing depth-ratio. This results in the suppression of streamwise momentum transport by $\overline{u'v'}$ and velocity gradients under the dominant downwash flow ($v' < 0$). Thus, mean wake evolution between Quadrupole and Dipole-type occurs due to deterioration of the upper vortex with increasing depth-ratio.

Chapter 6

IMPACT OF DEPTH-RATIO ON SHEAR-LAYER DYNAMICS AND WAKE INTERACTIONS[‡]

The role of depth-ratio and multivariate interactions between the shear layer, wake structures, and prism surfaces have already been discussed at low Reynolds numbers ($5 \times 10^1 - 5 \times 10^2$). A detailed understanding of the flow dynamics around wall-mounted prisms were explored for this regime in Chapters 4 and 5. However, low Reynolds number flow dynamics may not fully capture the complexities at moderate or high Reynolds numbers, where the flow transitions to turbulence. At moderate and high Reynolds numbers, as discussed in Section 2.3, flow separates at the leading edge of the prism, forming a shear layer that rolls up into a train of small-scale vortices, leading to Kelvin-Helmholtz instabilities (KHI). These instabilities significantly influence the pressure distribution on the prism surfaces and contribute to the formation of downstream structures, such as hairpin-like vortices (Tenaud et al., 2016). Hairpin-like vortices, as large-scale coherent structures, play a critical role in momentum transfer and mixing processes. Thus, at

[‡]The content of this chapter has been published in *Physics of Fluids* under the citation (Goswami and Hemmati, 2024): “Goswami, S., & Hemmati, A. (2023). Impact of depth-ratio on shear-layer dynamics and wake interactions around wall-mounted prisms. *Physics of Fluids*, 36(11):115–149”.

moderate Reynolds numbers, wake dynamics are dictated by the interactions between KHI rollers and coherent structures. Studies on infinite-span rectangular prisms (outlined in Section 2.3) reveal that varying the depth-ratio affects the evolution and interactions of KHI rollers with large-scale flow dynamics. However, the impact of free-end effects and prism depth-ratio on these interactions for wall-mounted prisms remains unexplored.

This chapter investigates the formation and evolution of Kelvin-Helmholtz instability and its interactions with coherent wake structures, such as hairpin-like vortices, behind wall-mounted prisms. The focus is on prisms with $AR = 0.25 - 1.5$ and $DR = 1 - 4$ at $Re = 1 \times 10^3 - 2.5 \times 10^3$, using Large Eddy Simulations (LES) with the Dynamic Smagorinsky sub-grid scale model, as detailed in Chapter 3. Primary analysis emphasizes cases with $AR = 1$, $DR = 1$ and 4 at $Re = 2.5 \times 10^3$, representing a robust framework to examine complex wake behavior under extreme geometric parameters. This chapter is structured such that the results and discussion are presented in Section 6.1, followed by a summary of key findings in Section 6.2.

6.1 Results and Discussion

The wake visualization and analysis reveal the formation of distinct Kelvin-Helmholtz Instability rollers across the parameter space studied here. The KHI rollers emanate from the leading edge shear layer, characterized by their high-frequency signatures. These significantly impact the pressure distribution on the prism surfaces and contribute to forming downstream wake structures, such as the hairpin-like vortices. To better evaluate and characterize these wake features, this study focuses on two critical cases at the highest Reynolds number studied here, $Re = 2.5 \times 10^3$. The case of $AR = 1$, $DR = 1$ and 4 exhibit the most important wake features that are of interest in this study, across two extreme ends of our parameter space. While these cases may not exhibit wake complexities that belong to a unique parameter setting, they do feature wake systems that are observed similarly across all AR , DR and Re considered here. First, a qualitative illustration of

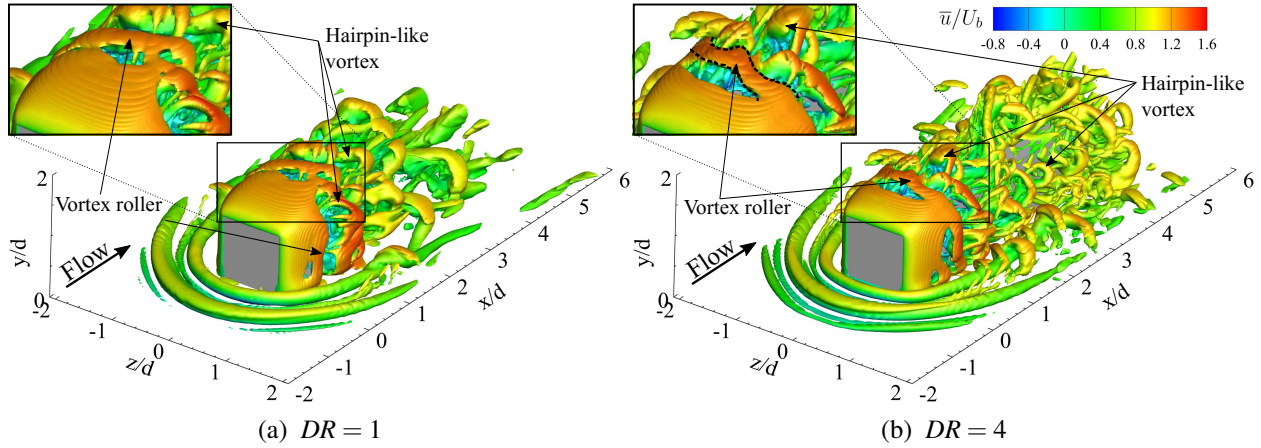


Figure 6.1: Instantaneous flow realizations identified using $Q^* = 10$ and overlaid with contours of streamwise velocity (u) for (a) $DR = 1$ and (b) $DR = 4$ at $Re = 2.5 \times 10^3$.

the flow is provided. To this end, the Kelvin-Helmholtz instability (KHI) and its interactions with the coherent flow structures, affecting various flow parameters, are analyzed

Instantaneous flow realizations using Q-criterion (Jeong and Hussain, 1995) overlaid with streamwise velocity (u) contours are presented in Figure 6.1 for $DR = 1$ and $DR = 4$ at $Re = 2.5 \times 10^3$. These plots also feature zoom-in inset focusing on the leading-edge shear-layer separation (top-left corner). The instantaneous wake exhibits a shear-layer separation at the leading edge, followed by a roll-up and shedding of hairpin-like vortices in the wake. Four major vortical structures are observed around the prism: horseshoe vortices in the front, leading-edge roll-up, spanwise and normal vortex rollers immediately following the roll-up, and hairpin vortex shedding. Flow over the top surface, separating from the leading edge, reattaches for the case of $DR = 4$, while it sheds directly into the wake for a shorter prism, $DR = 1$. The flow reattachment aligns with the dominant downwash phenomenon that was previously observed in Chapters 4 and 5 for prisms with increasing depth-ratio.

Figure 6.1 reveals a laminar separating flow profile for $x/d < 0.5$, characterized by a flat and continuous layer of spanwise vortical motion. The leading-edge shear layer undergoes distinct stages of growth, primary instability formation, and transition, ultimately leading to its breakdown (Chiarini and Quadrio, 2021), which triggers the emergence of Kelvin-Helmholtz

instability. These are manifested as finite spanwise rollers in the shear layer (Tenaud et al., 2016; Moore et al., 2019a), which resemble vortex tubes in the zoomed-in inset of Figure 6.1. KHI rollers exhibit high-frequency signatures that significantly impact the pressure distribution on the prism surfaces and contribute to downstream structures, for example hairpin-like vortices. Notably, these vortex tubes extend into the wake for $DR = 1$, while they appear on the prism surfaces for $DR = 4$. Similar vortex tubes are also observed on the side surfaces of both prisms. It is observed that KHI rollers are more pronounced for $DR = 4$, with more rollers and intense spanwise vortical motion. Moreover, KHI rollers exhibit modulations in the spanwise direction, resembling wave-like structures shown in Figure 6.1b. These modulations become more pronounced for $DR = 4$. The difference in streamwise velocity above and below the rollers intensifies these modulations, leading to the stretching and folding of rollers into hairpin-like vortices that shed downstream.

Previous studies have observed Kelvin-Helmholtz instabilities involving infinite-span, rectangular prisms (Tenaud et al., 2016; Moore et al., 2019a; Chiarini and Quadrio, 2021). In these investigations, KHI manifests in the form of long spanwise vortex tubes near the leading edge, initially exhibiting spanwise invariance but later developing spanwise modulation. The qualitative observations in the present study are consistent with the literature (Chiarini and Quadrio, 2021). There are limited studies on wall-mounted prisms, which have examined the occurrence of KHI. For example, (Rastan et al., 2021) documented the generation of Kelvin-Helmholtz-like vortices from the leading-edge shear-layer on side surfaces of a square prism with an aspect-ratio 7. They further elaborated on the impact of downwash flow in the wake, which leads to the suppression of vortices downstream. These observations were consistent with earlier experiments of Wang and Zhou (2009), where similar Kelvin-Helmholtz-like vortices were noted in the wake of a finite square prism. In both studies, co-rotating vortices resulting from KHI were observed in the wake, where flow interactions and a dominant downwash flow suppressed any impact of such instabilities on the flow. This dissertation presents the very first study to identify the presence of KHI rollers in the wake of a finite wall-mounted prism with a

small aspect-ratio and large depth-ratio. This study holds significant implications for understanding the flow dynamics around wall-mounted prisms, particularly the interactions between KHI and hairpin-like vortices, which is a precursor to the turbulence transition phenomenon.

Based on the present results, it is hypothesized that the presence of KHI rollers in the wake of a wall-mounted prism is influenced by the depth-ratio. At moderate Reynolds numbers, an increase in depth-ratio leads to an enhanced interaction between KHI and Kármán-like vortices, which in turn enhances vortex shedding in the wake. This is evident from the increased number of KHI rollers and the intense spanwise vortical motion observed for $DR = 4$ in Figure 6.1b. Further, these interactions are expected to significantly impact the pressure distribution on the prism surfaces, as well as the formation of downstream structures, such as hairpin-like vortices. In the following sections, a detailed analysis of KHI and its interactions with the coherent flow structures are provided, affecting various flow parameters, starting with mean and instantaneous flow characteristics, flow periodicity, and the frequency of KHI rollers.

6.1.1 Mean Flow Characteristics

Time-averaged (mean) velocity field around the prism is presented in Figure 6.2. Contours of mean axial velocity (\bar{u}/U_b) are overlaid with mean streamlines for $DR = 1$ and 4 at $z/d = 0$ and $y/d = 0.5$. Due to flow symmetry, resulting from the time-averaged quantities, only one side of the domain is shown at $y/d = 0.5$. The dotted streamlines identify regions of negative streamwise velocity. The flow separates at the leading edge for both prisms, and the separated shear layer extends into the wake region for $DR = 1$, while it attaches to the prism top and side surfaces with $DR = 4$. The shear-layer reattachment occurs at $\bar{x}_R/d \sim 2.12$ and $\bar{x}_R/d \sim 2.09$ on the top and side surfaces, respectively. These observations are consistent with previous literature on the increasing dominance of downwash flow with depth-ratio (Rastan et al., 2021). A secondary recirculation bubble is noted near the leading edge on the prism top surface, which is absent in the case of small depth-ratio prisms. This secondary recirculation bubble is characterized by a region of

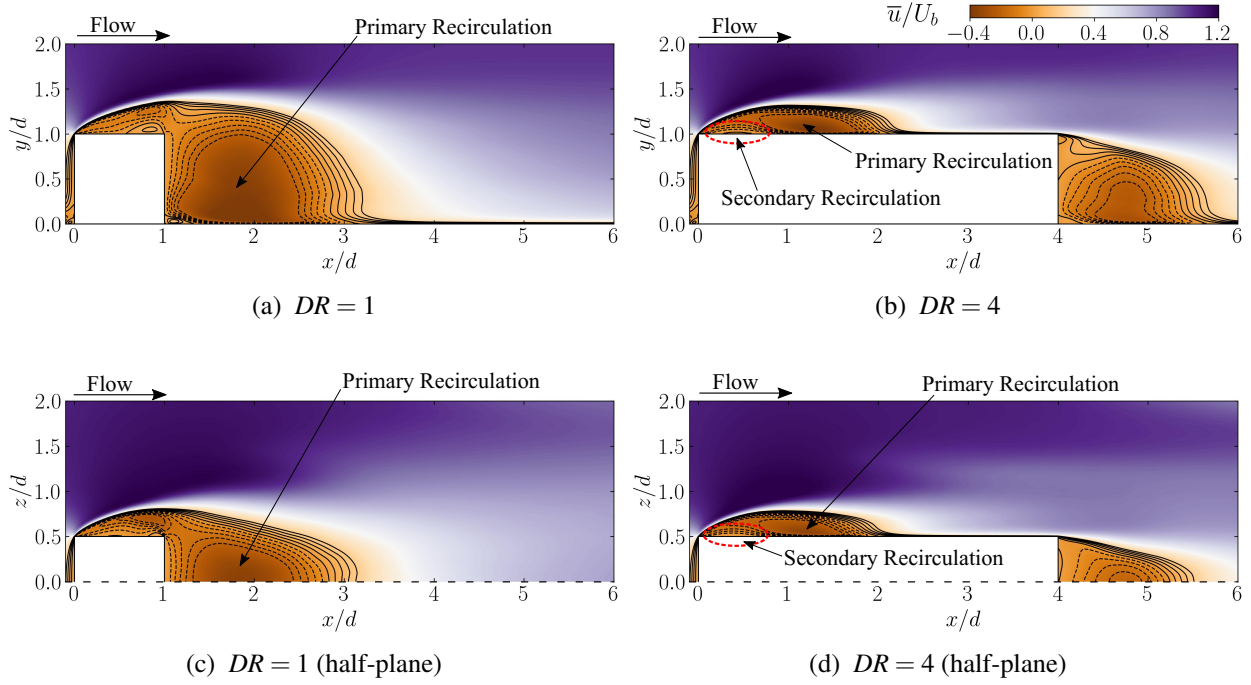


Figure 6.2: Contours of mean axial velocity (\bar{u}/U_b) overlaid with mean streamlines for (a,c) $DR = 1$ and (b,d) $DR = 4$ at (a,b) $z/d = 0$ and (c,d) $y/d = 0.5$. Dotted axis indicates the line of symmetry. Dotted streamlines show negative streamwise velocity regions.

negative streamwise velocity, as shown by the dotted streamlines in Figure 6.2. Furthermore, a secondary recirculation bubble appears for both short and long prisms on the side surfaces. Previous studies (Mashhadi et al., 2021; Rastan et al., 2021; Kumahor and Tachie, 2022) have established that a secondary recirculation bubble forms due to an adverse pressure gradient induced by the decelerating reverse flow near the leading edge. Moreover, the existence of secondary recirculation region is linked to shear-layer flapping motion and the formation of KHI rollers on the prism surfaces.

The shear-layer structure and behavior are investigated by examining the turbulence kinetic energy (k). Contours of k are presented in Figure 6.3 for $DR = 1$ and 4 at $z/d = 0$ and $y/d = 0.5$, where ‘ \times ’ marker shows the location of maximum turbulence kinetic energy. These contours reflect the shear-layer structure, with the maximum value of k occurring downstream of the prism leading-edge. In case of a short prism, an elevated region of k occurs downstream of the trailing edge, while similar elevated region of k is noticed over the top surface of a long prism. The high values of k

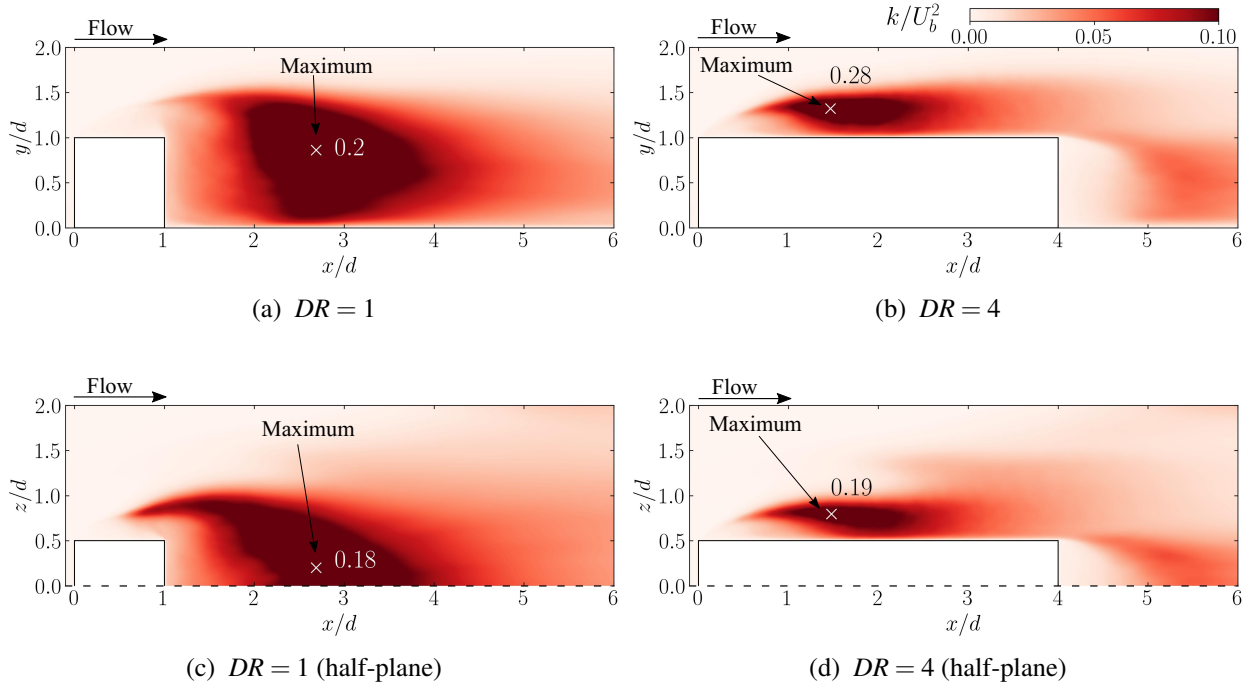


Figure 6.3: Contours of turbulence kinetic energy (k/U_b^2) for (a,c) $DR = 1$ and (b,d) $DR = 4$ at (a,b) $z/d = 0$ and (c,d) $y/d = 0.5$. Dotted axis indicates the line of symmetry. ‘ \times ’ marker shows the location of maximum turbulence kinetic energy.

are associated with the interactions between the wake and the shear layer, which make the flow highly incoherent. In other words, turbulent energy (k) is large inside the leading-edge shear-layer, which interacts with the wake later on and results in mixing. This leads to further enhancement of k in these regions. For $DR = 4$, the peak in k occurs close to the location of flow reattachment on the prism surfaces. Region of weaker k at the trailing edge is also noted. The latter region is attributed to the formation and interactions of vortices in the wake, while the former (near the flow reattachment) is attributed to the interactions of Kelvin-Helmholtz instability rollers with the wake.

The mean flow characteristics further elaborate on two important observations regarding the interactions of KHI rollers with coherent structures (wake). First, the presence of secondary recirculation bubbles on the prism surfaces is linked to the shear-layer flapping motion and the formation of KHI rollers (Cimarelli et al., 2018). The occurrence of shear-layer flapping motion is exclusive to the case of $DR = 4$, as it necessitates a surface for interaction (Ma et al., 2023). Second, the maximum turbulence kinetic energy is observed in regions where KHI rollers interact

with the wake. These observations are reinforced by the instantaneous flow realizations in Figure 6.1, which depicted the interaction of KHI rollers with the wake. Although the mechanism of interaction remains beyond the scope of this discussion, these findings examine the location and extent of interactions as a function of depth-ratio. Since the maximum value of k occurs in regions where the interactions take place, comparing the maximum values provides insights into the intensity of interactions. Maximum k for $DR = 4$ is approximately 40% larger than $DR = 1$ on either surface, suggesting a greater intensity of interactions in the case of a larger depth-ratio prism. Furthermore, the maximum value of k associated with the top surface shear-layer is approximately 11% and 48% larger, compared to the sides for $DR = 1$ and 4, respectively. This indicates that the top surface shear-layer dominates as the primary factor influencing downstream wake.

6.1.2 Flow periodicity and Instantaneous Flow Characteristics

Frequency of the KHI rollers is determined using premultiplied power spectral density of streamwise (E_u), normal (E_v), and spanwise velocity (E_w) for $DR = 1$ and $DR = 4$. Since KHI occurs closer to the leading edge of the prism, velocity signals were tracked at $(x/d, y/d, z/d) = (0.5, 1.3, 0)$. The rationale behind pre-multiplying the spectrum by the frequency is to facilitate the visualization of energy distribution across scales on a logarithmic plot. This transformation ensures that equal areas under the curve represent equal contributions to the total energy, providing a more intuitive representation of energy content at different scales. The spectra are computed using Welch's averaged modified periodogram method (Welch, 1967) for streamwise (E_u), normal (E_v), and spanwise (E_w) velocity fluctuations. The results are presented in Figure 6.4, where three dominant flow features are identified: (i) St_{sh} , associated with the shedding of hairpin-like vortices in the wake, (ii) St_{kh} , corresponding to the frequency of Kelvin-Helmholtz instability rollers, and (iii) $2St_{kh}$, associated with high-frequency harmonics. Further, a sub-harmonic frequency is noted in the case of spanwise (E_w) velocity fluctuations for

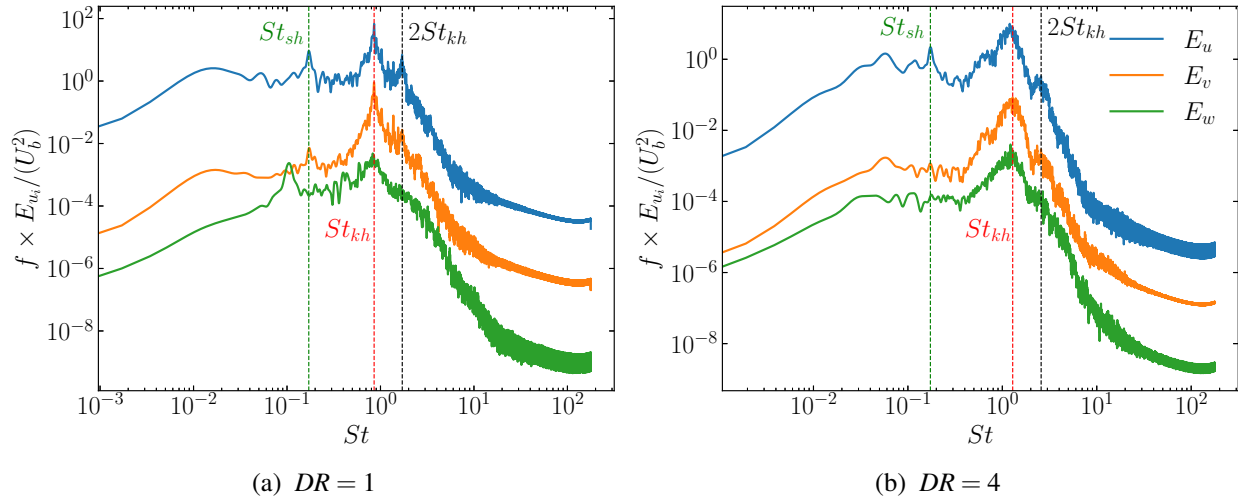


Figure 6.4: Premultiplied power spectral density of streamwise (E_u), Normal (E_v), and Span-wise velocity (E_w) fluctuations at $(x/d, y/d, z/d) = (0.5, 1.3, 0)$ for (a) $DR = 1$ and (b) $DR = 4$.

$DR = 1$, which vanishes at larger depth-ratios. This sub-harmonic frequency is associated with secondary vortex structures that appear alternatively on either side of the prism (see Chapter 4).

Hairpin-like vortices shed at $St_{sh} = 0.171$ and 0.173 for $DR = 1$ and 4 , respectively, agree well with Diaz-Daniel et al. (2017b). Frequency of KHI rollers (St_{kh}) are 0.855 and 1.29 for $DR = 1$ and 4 , respectively. The significantly higher KHI frequency for $DR = 4$ aligns with the stronger spanwise vortical motion observed in Figure 6.1. Similarly, higher frequency hairpin-like vortex of the for $DR = 4$ suggests a more complex wake structure. Lander et al. (2018) proposed a correlation for infinite-span square prisms that links the relative influence of KHI and large-scale shedding with Reynolds number (Re): $St_{kh}/St_{sh} = 0.18 \times Re^{0.6}$. In the present study, the ratio of frequencies for KHI-to-hairpin vortex (St_{kh}/St_{sh}) are ~ 5.0 and ~ 7.5 for $DR = 1$ and 4 , respectively. The criterion given by Lander et al. (2018) predicts a ratio of ~ 18 at the current Reynolds number. This significant discrepancy highlights that KHI is not only a function of Re , rather it is significantly influenced by free-end effects, such as downwash flow induced by wall-mounted prisms. Furthermore, increasing St_{kh}/St_{sh} with $DR = 4$ suggests a stronger interaction between KHI and hairpin shedding, consistent with the stronger spanwise vortical motion observed in Figure 6.1 as well as the observations in Figure 6.3.

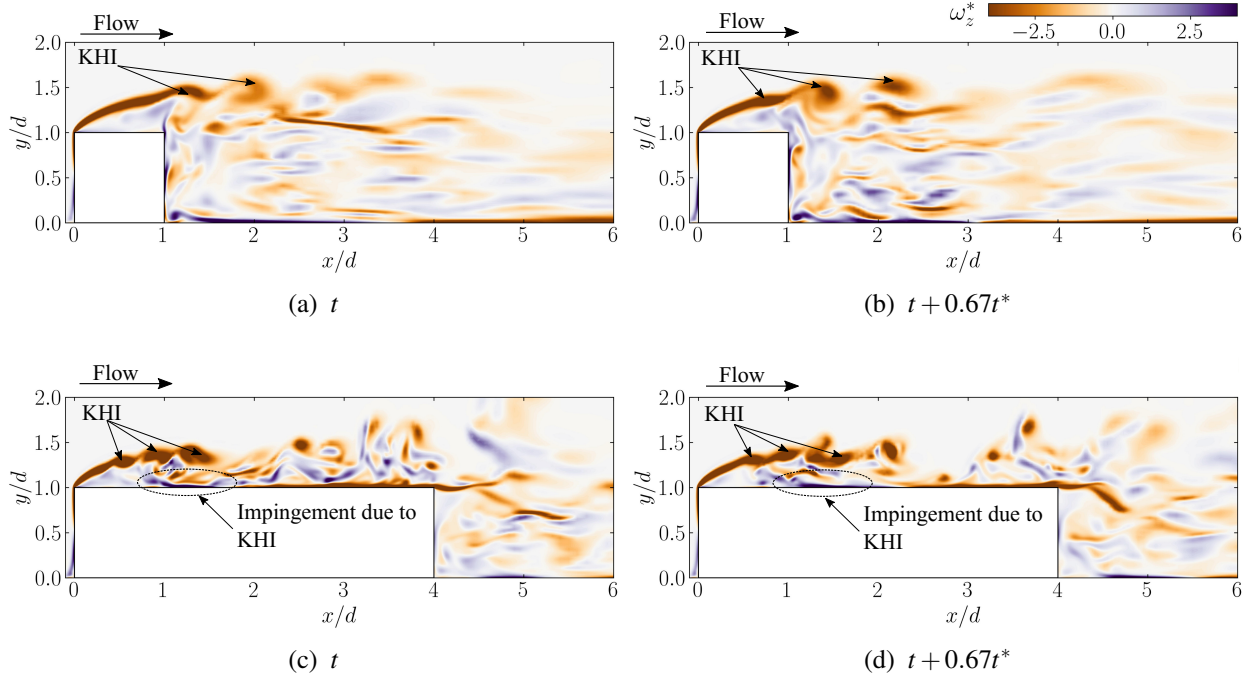


Figure 6.5: Instantaneous span-wise vorticity field for (a,b) $DR = 1$ and (c,d) $DR = 4$ at $z/d = 0$. The time increment, $t^* = d/U_b f_{kh}$, where f_{kh} is the frequency of KHI rollers.

Figure 6.5 shows contours of the instantaneous spanwise vorticity field at $z/d = 0$ for $DR = 1$ and 4. The time increment corresponds to the period of KHI rollers, $t^* = d/U_b f_{kh}$, where f_{kh} is the frequency of KHI rollers. For both cases, KHI roll-up and vortex pairing can be seen downstream of the leading edge. However, trajectory of the rollers is significantly different. For $DR = 1$, rollers are shed into the wake, while the rollers are shed towards the wall before shedding into the wake downstream for $DR = 4$. This mechanism is referred to as shear-layer flapping motion (Moore et al., 2019a), which is attributed to an oscillating reattachment point on the prism surfaces. The shear-layer flapping motion creates a complex interaction between KHI rollers and hairpin-like vortices in the wake, leading to a more complex wake structure for $DR = 4$. Furthermore, shear-layer flapping on the prism surface leads to an impingement of flow on the prism surfaces, which is absent in the case of $DR = 1$. This flow impingement creates a favorable pressure gradient and peak pressure fluctuation on the surface of the prism. This phenomenon is discussed later in this dissertation.

Flow dynamics behind wall-mounted prisms are significantly different from those of infinite-span prisms, which further contribute to a suppressed St_{kh}/St_{sh} , as noted earlier. The flow around wall-mounted prisms, as opposed to infinite-span prisms, are significantly influenced by three-dimensional effects, such as the presence tip and base vortices (Wang and Zhou, 2009). These three-dimensional effects are further influenced by the depth-ratio of the prism, leading to a more complex wake structure. For example, Chapter 4 noted enhancement of the dominant downwash flow with increasing depth-ratio, which suppressed the vortex shedding at low Reynolds numbers. Similar downwash flow was observed to suppress both tip and base vortices behind a large aspect-ratio prism at high Reynolds number (Rastan et al., 2021). The present study extends these observations to the interaction of KHI rollers with hairpin-like vortices in the wake.

Instantaneous axial velocity profiles (u/U_b) at $z/d = 0$ for $DR = 1$ and 4 are depicted in Figure 6.6. The profiles are segmented into two regions, A and B, based on the regions of shedding flow structures. Region B encompasses the primary vortex shedding region, while region A represents the area of reverse flow beneath the leading-edge shear-layer, indicated by dotted red lines tracing the shear-layer trajectory. A laminar profile is evident at the leading-edge in both cases. Downstream, velocity deficit increases in Region B due to interactions of KHI rollers with coherent flow structures. For $DR = 1$, the shear-layer directly sheds into the wake, as seen in the trajectory within Region B. Initially, a velocity deficit appears in Region A near the leading-edge ($x/d \leq 0.4$), mainly due to a secondary reverse flow region forming at the leading-edge. Overall, instantaneous velocity profiles on the top surface for the case of $DR = 1$ exhibit no apparent interactions since the shear-layer sheds directly into the wake. In contrast, for the prism with $DR = 4$, the shear-layer trajectory initially grows up to $x/d \sim 1.5$, after which it collapses towards the wall. In Region A, the velocity deficit is more pronounced, attributed to the presence of a secondary recirculation bubble. The deficit in Region A disappears at $x/d = 2$, coinciding with flow reattachment, followed by a velocity influx in Region A at $2 \leq x/d \leq 2.5$, primarily due to flow impingement on the top surface of the prism. This impingement creates a

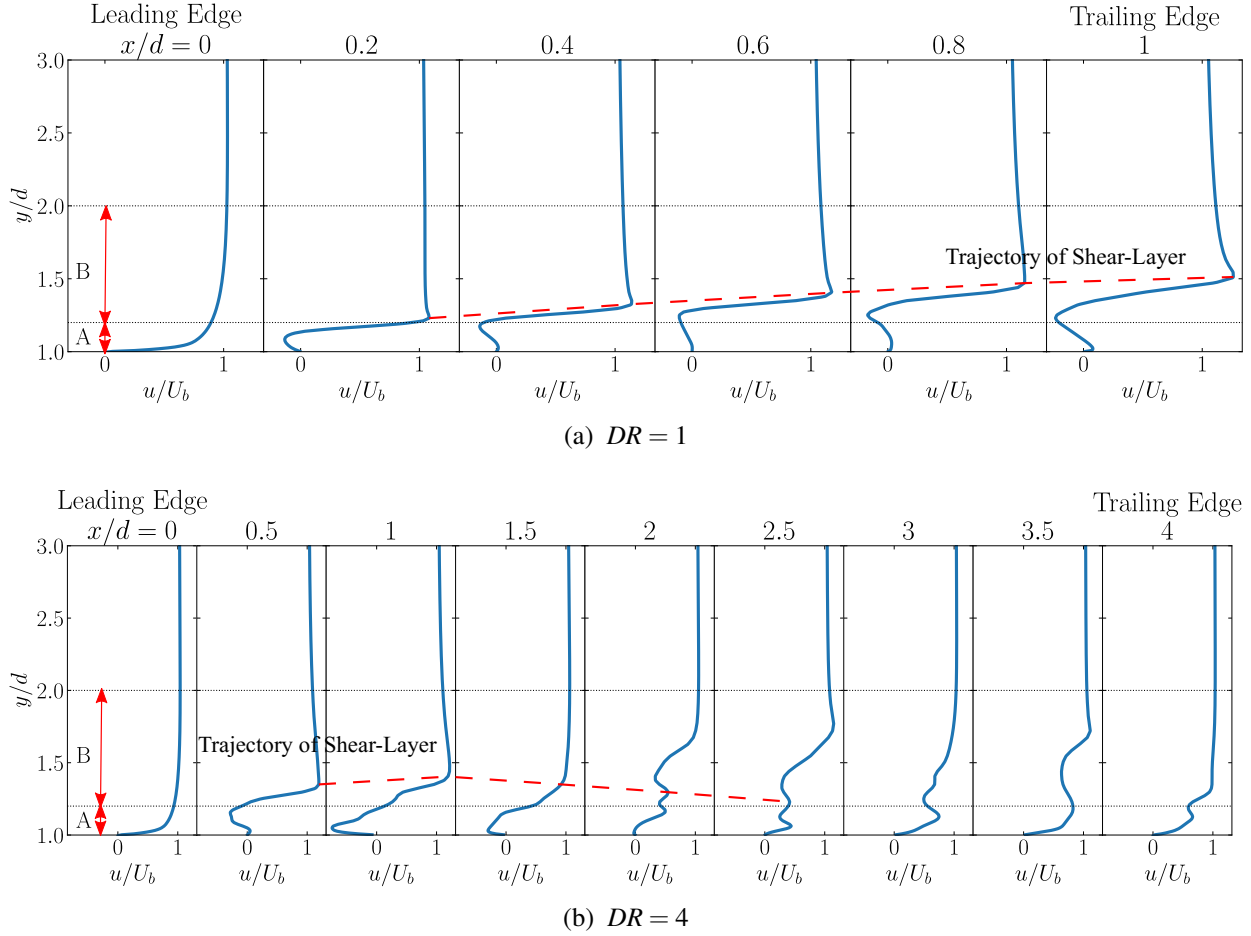


Figure 6.6: Instantaneous axial velocity profiles (u/U_b) at $z/d = 0$ for (a) $DR = 1$ and (b) $DR = 4$. Dotted red lines show the trajectory of shear-layer.

favorable pressure gradient and a peak in pressure fluctuation on the prism surface, which is explained in detail later. In Region B, a velocity deficit initiates at $x/d = 2$ and persists as the flow progresses downstream, with intermittent variations that are indicative of oscillating KHI rollers.

The interactions between these KHI rollers and the wake are further analyzed using the trends of axial pressure gradients ($\partial p/\partial x$) at $z/d = 0$ for $DR = 1$ and 4, as depicted in Figure 6.7. This method of quantifying large-scale interactions in an unsteady separating flow follows the approach of (Obabko and Cassel, 2002) and (Verma et al., 2023). For the prism with $DR = 1$, considerable axial pressure gradients are observed at the leading-edge, indicating a significant deficit. Downstream of the leading-edge, a recovering trend is observed where the negative peak in $\partial p/\partial x$ decreases and shifts towards the free-stream flow. Finally, at the trailing edge, a sharp

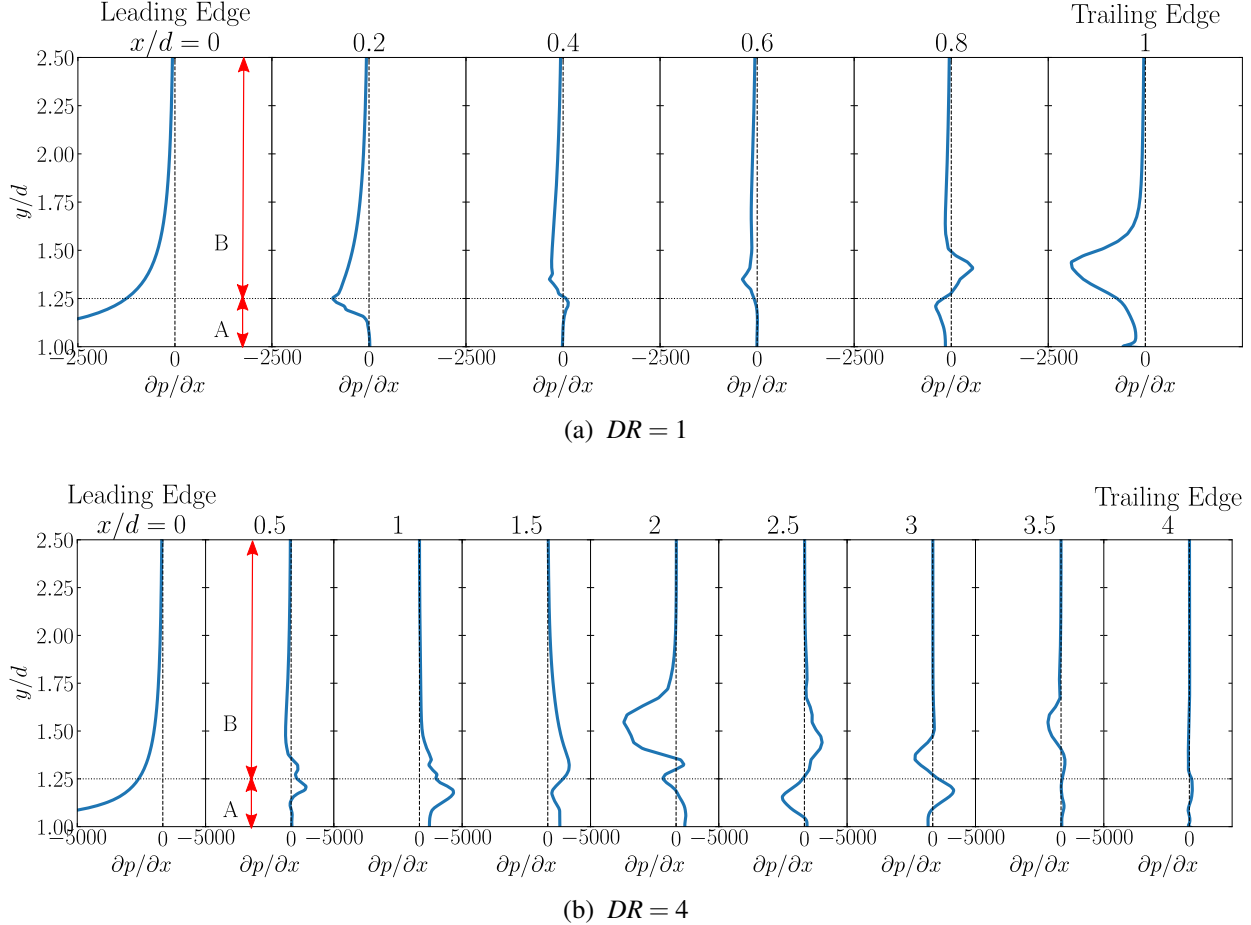


Figure 6.7: Axial pressure gradient profiles ($\partial p / \partial x$) at $z/d = 0$ for (a) $DR = 1$ and (b) $DR = 4$.

deficit is noted, attributed to trailing edge flow separation and reverse flow due to upwash effects (see Chapter 5). In the case of $DR = 4$, a positive axial pressure gradient in Region A explains the reverse flow region at $0 \leq x/d \leq 1.5$, followed by a sharp change in the axial pressure gradient at $x/d = 2.5$, where flow reattaches to the body. This change is attributed to flow impingement on the top surface, creating a favorable pressure gradient and a peak in pressure fluctuation on the prism surface. In Region B, a negative axial pressure gradient is noted near this location, which is attributed to interactions of KHI rollers with coherent flow structures (Obabko and Cassel, 2002). These findings illustrate that interactions between KHI rollers and coherent flow structures result in a sudden spike in pressure gradients near the flow reattachment region, dividing the primary recirculation region into co-rotating vortices. Additionally, the formation of a locally adverse pressure gradient induced by these interactions at $x/d = 2.5$ in region A are attributed to the flow

impingement on the prism top surface, where the shear-layer flapping motion forces newly formed vortices into the prisms surfaces.

6.1.3 Wall Pressure Distribution

Pressure distribution on the prism surfaces is a key indicator of wake characteristics (Rastan et al., 2021). Mean coefficient of pressure (\bar{C}_p) and root-mean-square of pressure fluctuations (p'_{rms}) were computed on the top and side surfaces for cases of depth-ratios 1 and 4 at $Re = 2.5 \times 10^3$. The results are presented in Figure 6.8. The coefficient of pressure is defined as

$$C_p = (p - p_\infty) / (0.5 \rho U_b^2),$$

where p and p_∞ are the local and free-stream pressures, respectively, and ρ is the fluid density. Root-mean-square of pressure fluctuations is defined as

$$p'_{rms} = \sqrt{\overline{p'p'}},$$

where p' is the pressure fluctuation. Furthermore, downstream distance from the leading edge is normalized by the prism length (l) for consistent comparison. The results reveal a distinct pressure distribution on the top surfaces with C_p and p'_{rms} exhibiting significant differences between the two depth-ratios.

Figure 6.8a compares \bar{C}_p on the prism top and side surfaces at $z/d = 0$ and $y/d = 0.5$. After the leading edge, there is a sudden decrease in \bar{C}_p due to flow separation. This leads to pressure recovery downstream for $DR = 4$ but not for $DR = 1$. The recovery extends towards maximum \bar{C}_p at $x/l \approx 0.53$, indicating flow reattachment on the top surface. The overshoot of \bar{C}_p for $DR = 4$ suggests favorable pressure distribution after reattachment. However, for $DR = 1$, pressure recovery is absent, maintaining low \bar{C}_p along the top surface, due to direct shedding of the leading-edge shear layer into the wake. Additionally, increased turbulence causes pressure overshoot in $DR = 4$, evident from strong vortical motions in the wake. The side surface exhibits

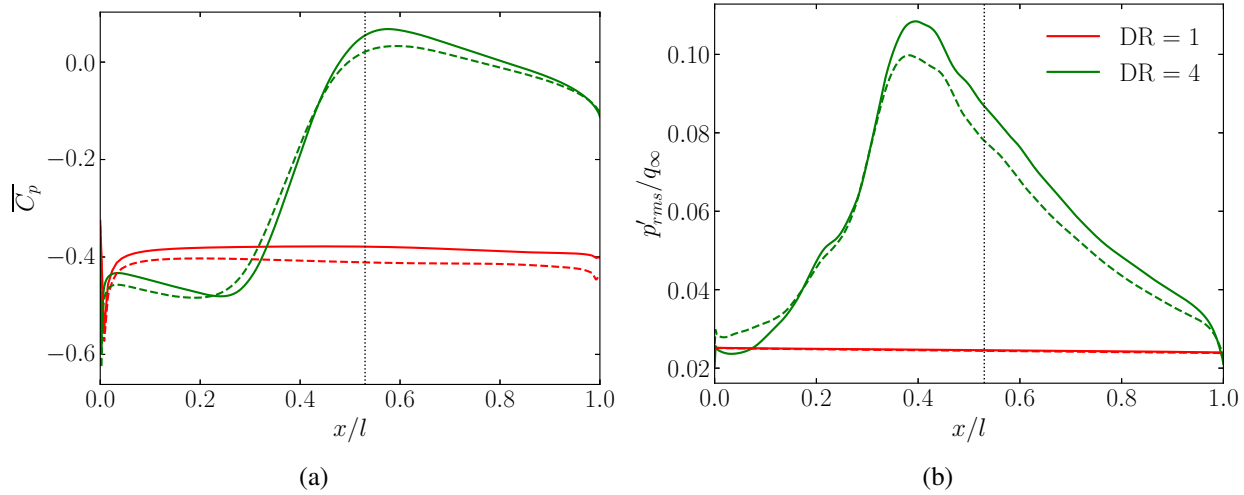


Figure 6.8: Distribution of (a) coefficient of pressure (\bar{C}_p) and (b) root-mean-square of pressure fluctuations (p'_{rms}) on the prism top ($z/d = 0$) and side ($y/d = 0.5$) surfaces with depth-ratio of $DR = 1$ and $DR = 4$ at $Re = 2.5 \times 10^3$. Solid line represents top surface and dashed line represents side surface of the prism. Dotted line shows the mean reattachment point (\bar{x}_R) on $DR = 4$ prism.

a similar pressure distribution for both depth-ratios, with slight reductions for $DR = 4$, indicating dominance of the top surface shear layer in downstream flow dynamics.

The root-mean-square of pressure fluctuations (p'_{rms}) is presented in Figure 6.8b. Maximum p'_{rms} for $DR = 4$ occurs at the rear part of the recirculation bubble. Previously, (Farabee and Casarella, 1984) attributed the maximum p'_{rms} behind a backward-facing step to the separated flow impingement on the surfaces. Based on the results in Figure 6.8b, the maximum value of p'_{rms} occurs slightly upstream ($x/l \approx 0.4$) of the mean reattachment point. As shown in Figure 6.3, the maximum value of turbulence kinetic energy (k) occurs at $x/l \approx 0.4$, which is associated with the interactions of KHI with the coherent wake structures in this region. Also KHI rollers are shed towards the wall before shedding into the wake downstream as shown in Figure 6.5. This mechanism is called shear-layer flapping (Moore et al., 2019a), which is attributed to an oscillating reattachment point on the prism surfaces. Based on these observations, the maximum value of p'_{rms} coincides with the interactions of the KHI rollers with the wake. The result of these interactions is the impingement of flow on the prism surfaces. Following this impingement, a favorable pressure

gradient is created (Figure 6.7b) at $x/d = 2$, which elevates the flow momentum in this region and enhances the vortex shedding resulting in a more complex wake (shown in Figure 6.1).

The trend of p'_{rms} trends for $DR = 1$ indicate a more stable flow on the top surface, resulting in a lower p'_{rms} compared to $DR = 4$. This can be attributed to the lack of reattachment on the prism surfaces, resulting from vortices that do not impinge on the walls. The trends of p'_{rms} on the side surface are consistent with the trends on top, although they are slightly suppressed, indicating that the top surface shear layer dominates the flow dynamics downstream. The results in Figure 6.8 highlight the importance of depth-ratio in shaping the pressure distribution on prism surfaces.

6.1.4 Origins of fluctuating wall pressure

Pressure fluctuations (p') in incompressible flow can be expressed in terms of velocity fluctuations (u' , v' , and w') through the Poisson equation (Pope, 2001). This equation couples fluctuating velocity from the numerical simulations with wall pressure fluctuations. By rearranging the governing equations, the fluctuating pressure is determined as follows:

$$\nabla^2 p' = -\rho \left(2 \overline{\frac{\partial u_i}{\partial x_j}} \frac{\partial u'_j}{\partial x_i} + \frac{\partial^2}{\partial x_i \partial x_j} (u'_i u'_j - \overline{u'_i u'_j}) \right)$$

Here, ∇^2 represents the Laplacian operator, $\overline{u_i}$ denotes the mean flow velocity, and u'_i indicates the fluctuating velocity components. The first term signifies the turbulence-mean-shear interaction (TMI), accounting for the rapid changes in mean flow induced by the fluctuating flow. The second term represents turbulence-turbulence interaction (TTI), which corresponds to the nonlinear behavior of turbulent structures. These two terms are considered the primary sources of pressure fluctuations in the flow (Hemmati et al., 2019).

The root-mean-square of turbulence-mean-shear interaction and turbulence-turbulence interaction are presented in Figures 6.9 and 6.10, respectively, for $DR = 1$ and 4 at $z/d = 0$ and $y/d = 0.5$. Figure 6.9 reveals heightened TMI near the leading edge of both prisms, where separated shear-layers are created. The vorticity associated with these shear-layers alter the mean

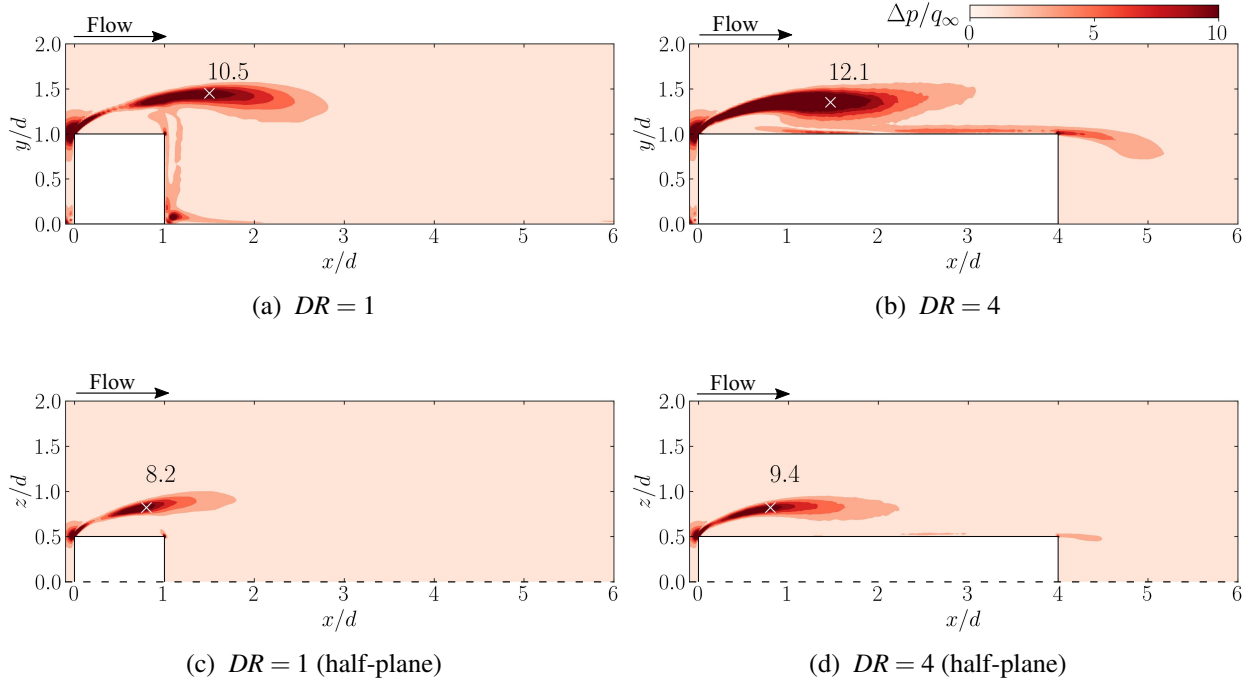


Figure 6.9: Contours of root-mean-square of turbulence-mean-shear interaction (TMI) for (a,c) $DR = 1$ and (b,d) $DR = 4$ at (a,b) $z/d = 0$ and (c,d) $y/d = 0.5$. Dotted axis indicates the line of symmetry. ‘ \times ’ marks the location of maximum TMI.

flow in this region, explaining the extensive TMI at the leading edge. For $DR = 4$, heightened TMI is also noted near the trailing edge, showcasing separating shear-layer at trailing-edge that interact with the downstream wake. In order to quantify the intensity of TMI, maximum TMI values are compared on the top and side surfaces. The maximum TMI for $DR = 4$ is $\approx 15\%$ larger than that of $DR = 1$ on either surface, suggesting a greater intensity of interactions in the case of a larger depth-ratio prism. Further, the maximum TMI on the top surface is $\approx 28\%$ and $\approx 30\%$ larger than on the side surface for $DR = 1$ and 4, respectively. This indicates that the top surface shear-layer is the primary source of pressure fluctuations.

Contours of TTI are presented in Figure 6.10. While TMI is concentrated near the leading and trailing edges, TTI is more distributed throughout the flow field. This is likely due to the velocity fluctuations produced by the mean flow alterations (TMI) gradually affecting the surrounding flow field. While TMI points towards the origins of mean flow modulation, TTI highlights the interactions between turbulent structures (Lowson, 1965; George et al., 1984). As such, the

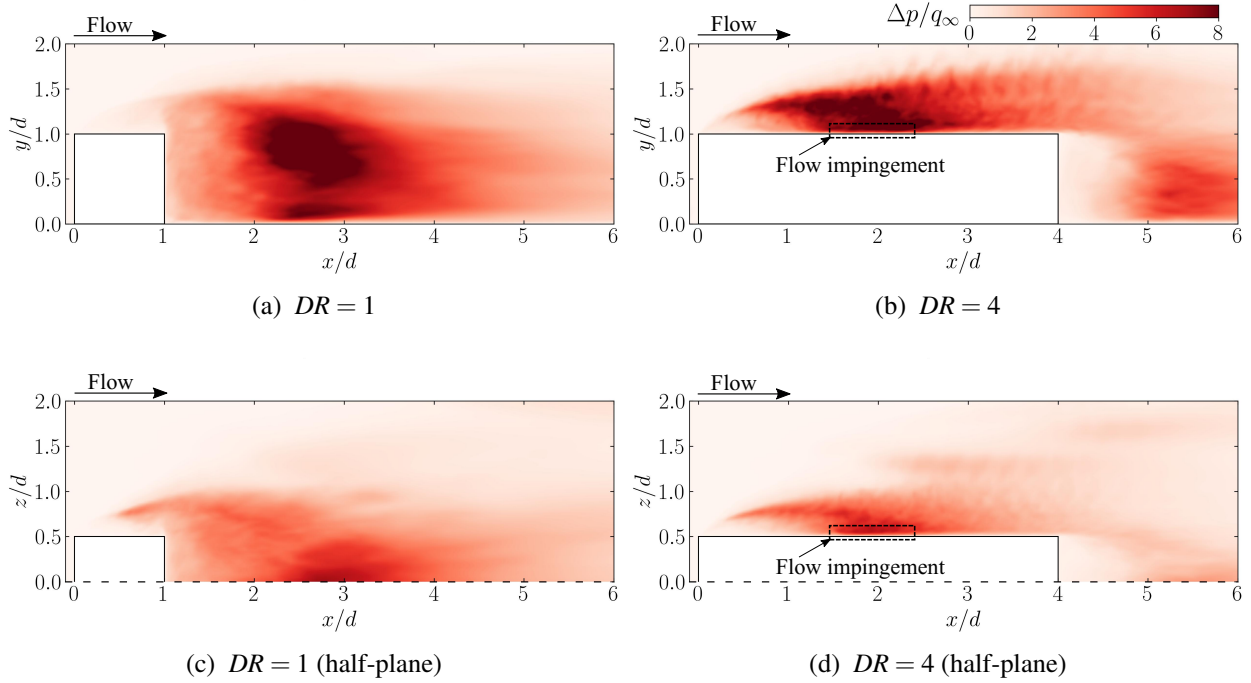


Figure 6.10: Contours of root-mean-square of turbulence-turbulence interaction for (a,c) $DR = 1$ and (b,d) $DR = 4$ at (a,b) $z/d = 0$ and (c,d) $y/d = 0.5$. Dotted axis indicates the line of symmetry.

results in Figure 6.10 scrutinize the interactions between KHI and coherent structures in the wake, formed due to modulations of mean flow and pressure fluctuations at the leading edge. For $DR = 1$, TTI is elevated downstream of the trailing edge on both top and side surfaces, where the leading-edge shear-layer sheds and interacts with the wake. Similarly, TTI for $DR = 4$ is elevated downstream of the leading edge, over the prism top and side surfaces, where KHI rollers interact with coherent wake structures. Further, flow impingement on the prism surfaces is noted, leading to a peak in TTI. These results provide evidence for two important observations: (i) flow modifications are led by the top surface leading-edge shear-layer, and (ii) interactions between KHI and coherent structures produce a more complex wake in case of $DR = 4$.

Finally, since the leading-edge shear layer is the primary source of pressure fluctuations, the cross-spectral density of pressure fluctuations (p') is computed to identify the co-dominant frequencies downstream of the leading edge. This sheds light on the influence of KHI rollers on coherent structures in the wake, downstream of the leading-edge. The cross-spectral density ($E_{p_i p_j}$) of pressure fluctuations is presented in Figure 6.11 for $DR = 1$ and 4. Cross-spectral

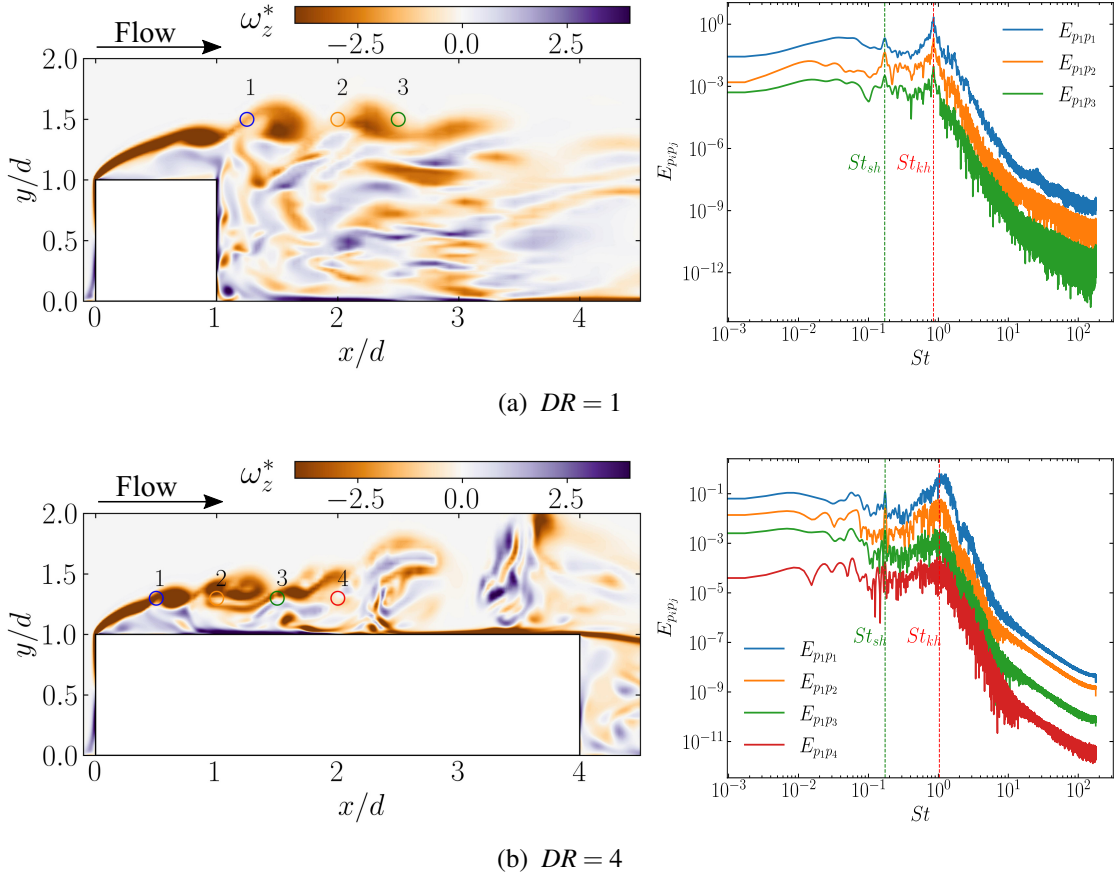


Figure 6.11: Cross spectral density of pressure fluctuations (p') for (a) $DR = 1$ and (b) $DR = 4$, at locations marked in the contour of ω_z^* on left.

density measures the correlation between Fourier components of two signals, p_i and p_j . $E_{p_i p_j}$ is used to determine the influence of one signal in relation to the other. $E_{p_i p_j}$ is computed at locations marked in the contour of ω_z^* on the left-hand side, in relation to signal p_1 recorded near the leading edge of both prisms. The results reveal that the dominant frequency of pressure fluctuations is consistent with the frequency of Kelvin-Helmholtz instability rollers (St_{kh}) identified in Section 6.1.2. At location 1 of both prisms, the dominant frequency of St_{kh} indicates that the flow dynamics are primarily driven by Kelvin-Helmholtz instability. For $DR = 1$, the influence of St_{kh} reduces gradually till location 3, where the influence of St_{sh} becomes dominant. Thus for $DR = 1$, mixing and interactions of KHI with the wake suppresses these rollers and the wake itself. However, the influence of St_{kh} remains dominant further downstream of the leading edge for $DR = 4$, suggesting the dominance of high-frequency structures in the wake. These

high-frequency structures enhance the flow momentum over the prism surfaces and lead to a more complex wake, further highlighting the importance of depth-ratio in shaping the flow dynamics around prisms.

Our observations and insights are not limited to the specific cases of $DR = 1$ and 4 at $Re = 2.5 \times 10^3$. The results presented in this study are consistent across the broad parameter space considered, i.e., varying aspect-ratios ($0.25 - 1.5$), depth-ratio ($1 - 4$) and Reynolds numbers ($1 \times 10^3 - 2.5 \times 10^3$). Based on previous investigations in Chapter 4 and 5, the wake topology of wall-mounted prisms is a function of both Reynolds numbers and the prism geometry. For example, Chapter 4 established that secondary vortex structures, and subsequent wake asymmetry, develop at sufficiently small depth-ratios with increasing Reynolds numbers. The same is true for the mean wake evolution behind small aspect-ratio wall-mounted prisms as presented in Chapter 5.

While scope of the present study is to analyze the formation and evolution of Kelvin-Helmholtz instability rollers and their interactions with coherent wake structures, the results are consistent across the broader parameter space. Instantaneous flow illustrations in Figure 6.12 depict these across different AR , DR and Re . Iso-surfaces of $Q^* = 10$ overlaid with contours of streamwise velocity (u) are shown for prisms with $DR = 2$ and 4 at $Re = 1 \times 10^3$, and $DR = 1.5$ and 3.5 at $Re = 1.5 \times 10^3$. The results are consistent with the observations for $DR = 1$ and 4 at $Re = 2.5 \times 10^3$. At sufficiently small depth-ratios ($DR = 1, 1.5, 2$), the leading-edge shear layer extends into the wake, resulting in a more stable flow and suppressed Kelvin-Helmholtz instability (KHI) rollers. This behavior is consistent across these depth-ratios, with $DR = 1.5$ and 2 presenting similar features compared to $DR = 1$ due to the persistent extension of the shear layer into the wake. Contrarily, the shear layer collapses towards the wall for larger depth-ratios ($DR = 3.5, 4$), leading to shear-layer flapping motions and increased interactions with the wake. These depth-ratios exhibit similar dynamics with collapse of the shear layer (near the wall) becoming more prominent at higher depth-ratios ($DR = 3.5, 4$), causing increased flow unsteadiness. These interactions enhance the flow momentum over the prism surfaces and lead to a more complex wake structure. Further, the influence of Reynolds numbers is evident in Figure 6.12 such that the flow is much more stable

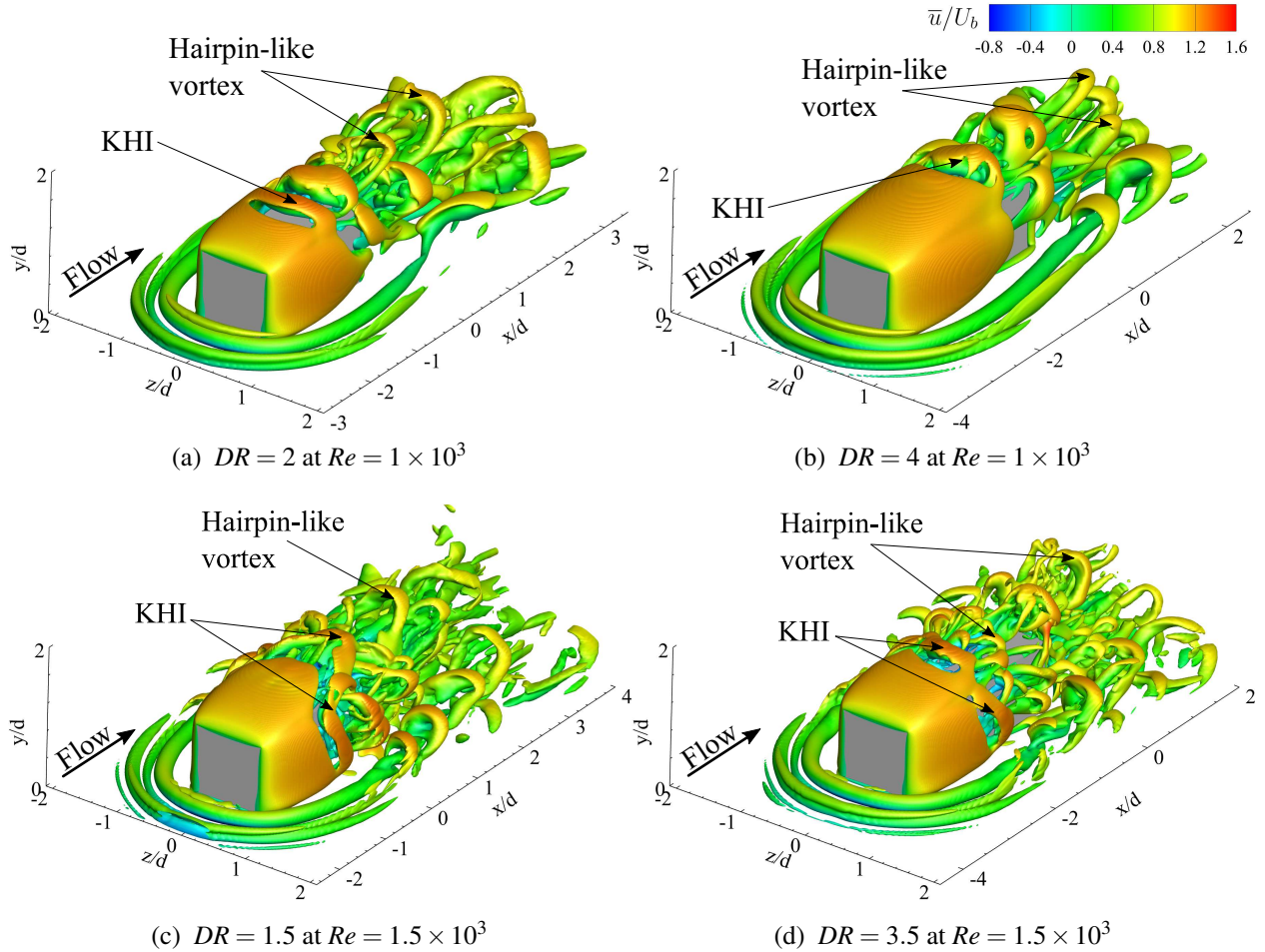


Figure 6.12: Instantaneous flow realizations identified using $Q^* = 10$ and overlaid with contours of streamwise velocity (u) at (a) $DR = 2$ and (b) 4 at $Re = 1 \times 10^3$; and (c) $DR = 1.5$ and (d) 3.5 at $Re = 1.5 \times 10^3$.

and laminar at $Re = 1 \times 10^3$ while it becomes irregular at $Re = 1.5 \times 10^3$. In our analysis, results underscore the importance of depth-ratio in shaping the flow dynamics around prisms, with larger depth-ratios leading to a more complex wake structure.

6.2 Summary

This chapter focuses on examining the formation and evolution of Kelvin-Helmholtz Instability and their interactions with the coherent wake structures, i.e., hairpin-like vortices. Additionally, this study underscores the impact of depth-ratio on surface pressure distribution and the origins of

pressure fluctuations in the wake of wall-mounted prisms. While results were presented for the case of $AR = 1$, $DR = 1$ and 4 at $Re = 2.5 \times 10^3$, they were consistent across the broader parameter space. The results revealed the formation of distinct KHI rollers originating from the leading edge shear layer, characterized by their high-frequency signatures. Increasing depth-ratio enhances the vortex shedding, especially the high-frequency KHI rollers in the wake. This aligned with stronger spanwise vortical motions at larger depth-ratios.

Shear-layer flapping motion is observed for the larger depth-ratio prisms, leading to an oscillating reattachment point on the prism surfaces. Shear-layer flapping motion avails the flow impingement on the prism surfaces by driving vortices formed post leading-edge separation onto the prism surfaces. Such shear-layer flapping remains absent for the shorter prisms. Moreover, shear-layer flapping motion avails a complex interaction between KHI rollers and hairpin-like vortices in the wake. This leads to a more complex wake structures at larger depth-ratios. Specifically, shear-layer flapping and flow impingement on the prism surfaces elevate the flow momentum, which in turn enhances vortex shedding and leads to a more complex wake.

Interactions between KHI rollers and coherent wake structures are quantified using the turbulence-mean-shear interaction and turbulence-turbulence interaction terms of the Poisson's equation. The results indicate that the top surface shear layer is the primary source of pressure fluctuations, with the interactions between KHI and coherent wake structures contributing to pressure fluctuations. Enhanced pressure fluctuations further motivates velocity fluctuations, resulting in the elevated momentum and complex wake topology. Finally, cross-spectral density of pressure fluctuations highlight the influence of KHI rollers in the wake downstream of the leading edge. Dominant frequency of pressure fluctuations is consistent with the frequency of KHI rollers, indicating that flow dynamics are primarily driven by Kelvin-Helmholtz instability. These findings underscore the importance of depth-ratio in shaping the flow dynamics around the prism, with the depth-ratio of 4 leading to a more complex wake structure.

Chapter 7

INFLUENCE OF DEPTH-RATIO ON TURBULENCE TRANSITION[‡]

Increasing depth-ratio enhances downwash flow, which suppresses wake unsteadiness, as described in Section 2.2. Conversely, increasing aspect-ratio amplifies upwash flow, contributing to wake irregularity (Saha, 2013). This indicates that wake unsteadiness in wall-mounted prisms can be intensified by either increasing their aspect-ratio and/or reducing their depth-ratio. The resulting heightened wake irregularity suggests a connection between abrupt geometric changes and the transition to turbulence, which forms the focus of this chapter on investigating how wake irregularity evolves with the flow transitions into a higher Reynolds number regime. Specifically, this chapter evaluates the potential for enhanced momentum transport with increasing depth-ratio as a precursor to wake transition. The hypothesis centers on the idea that an unsteady shear layer may intensify interactions between leading-edge shear-layer instabilities and prism surfaces. These enhanced interactions could elevate flow momentum and play a critical role in the transition process. The study examines prisms with $AR = 0.25 - 1.5$ and $DR = 1 - 4$ at $Re = 1 \times 10^3 - 5 \times 10^3$, employing Large Eddy Simulations (LES) with the Dynamic

[‡]The content of this chapter has been accepted for publication in *Journal of Fluid Mechanics* under the citation: “Goswami, S., & Hemmati, A. (2024). Influence of depth-ratio on turbulence transition in the wake of wall-mounted prisms. *Journal of Fluid Mechanics*”.

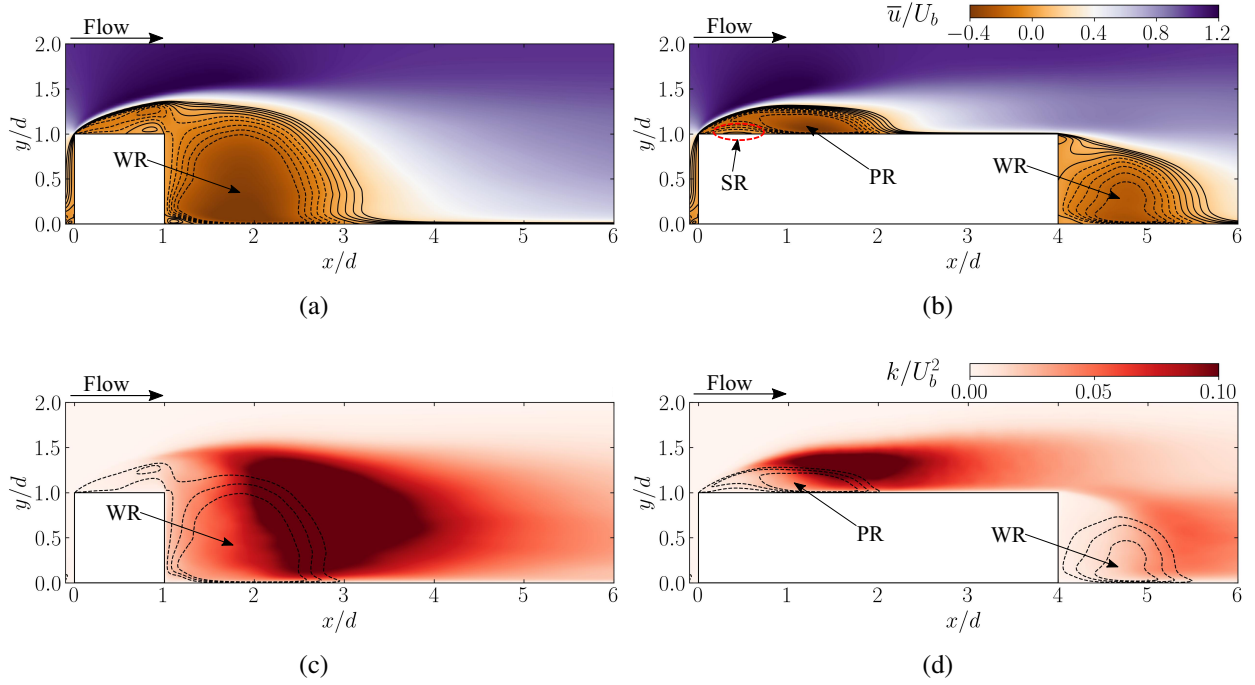


Figure 7.1: (a,b) Mean streamwise velocity (\bar{u}) and (c,d) turbulent kinetic energy (k) contours overlaid with mean velocity streamlines at $z/d = 0$ for (a, c) $DR = 1$ and (b, d) $DR = 4$ prisms.

Smagorinsky sub-grid scale model, as detailed in Chapter 3. The key findings are presented in Section 7.1 and summarized in Section 7.2.

7.1 Results and Discussion

Main features of the mean flow are first reported. As shown in Figures 7.1a and 7.1b, streamlines highlight the presence of flow separation at the leading edge, which in case of $DR = 1$ prolongs into the wake and reattaches at $x/d \approx 2.12$ for $DR = 4$. Reattachment length is quantified by tracing the time-averaged wall shear stress across the top surface of $DR = 4$ prism. A large scale recirculation region is present on the top surface of $DR = 4$, hereby referred to as the primary recirculation (PR) region. A second recirculation bubble is present below the PR region, noted as the secondary recirculation (SR) zone. Indeed, the reverse flow induced in the near-wall region of the PR forms a boundary-layer moving upstream, resulting in the formation of SR. Following the trailing-edge separation of the flow, a tertiary recirculation region is formed, referred to as the

wake recirculation (WR) region. For a short prism, the absence of PR and SR is attributed to a lack of flow reattachment on the prism surfaces. As such, only WR is noted due to shedding of the leading-edge shear-layer directly into the wake. Contours of turbulence kinetic energy ($k = \frac{1}{2}\bar{u'_i u'_i}$) are presented in Figures 7.1c and 7.1d. Initially, both prisms highlight an almost laminar state of the leading-edge shear-layer. Instabilities associated with the leading-edge shear-layer amplify the intensity of fluctuating velocities, initiating the transition-to-turbulence (Wang and Zhou, 2009). These regions of intense fluctuations result in high turbulence intensity (u'_i) and thus maximizing k . For the larger prisms, maximum k occurs on the prism top surface, while the shorter prisms experience it in the wake. The region of maximum k occurs in the primary vortex shedding region.

Qualitative illustrations of instantaneous vortex structures for $DR = 1$ and 4 are presented in Figure 7.2. Following the leading-edge separation, shear-layer undergoes distinct stages of growth and primary instability formation (Moore et al., 2019a). This triggers the formation of Kelvin-Helmholtz instability (KHI) of the shear-layer for both prisms, as evident by the finite spanwise vortex rollers forming near the leading edge. Such rollers are delayed and less frequent for $DR = 1$, and their formation occur over a larger distance compared to $DR = 4$. This is evident from the distribution of maximum turbulent kinetic energy (k_{\max}) along the mid-span ($z/d = 0$) of both prisms at $Re = 2.5 \times 10^3$ in Figure 7.3. Previous studies (Moore et al., 2019b) have used similar methods to identify the location of vortex roll-up behind sharp-edged bluff bodies. Figure 7.3 shows that the roll-up phenomenon, that is the location of maximum turbulent kinetic energy, is delayed for $DR = 1$ compared to $DR = 4$. In case of $DR = 4$, the roll-up occurs close to $x/d \approx 2$, while it occurs at $x/d \approx 3$ for $DR = 1$. These rollers become more prominent with increasing depth-ratio. Thus there is evidence of a strong dependence on depth-ratio for the generation of these instabilities. Evidence of the flow periodicity and frequency signatures is provided in Section 7.1.2. Figures 7.2c and 7.2d presents the lateral view of the instantaneous vortex structures for $DR = 1$ and 4 prisms. In case of $DR = 1$, amplified quasi-periodic perturbations resulting from an unsteady shear-layer are less frequent and delayed, whereas they are more pronounced for $DR = 4$, and they occur more frequently, especially in the wake region

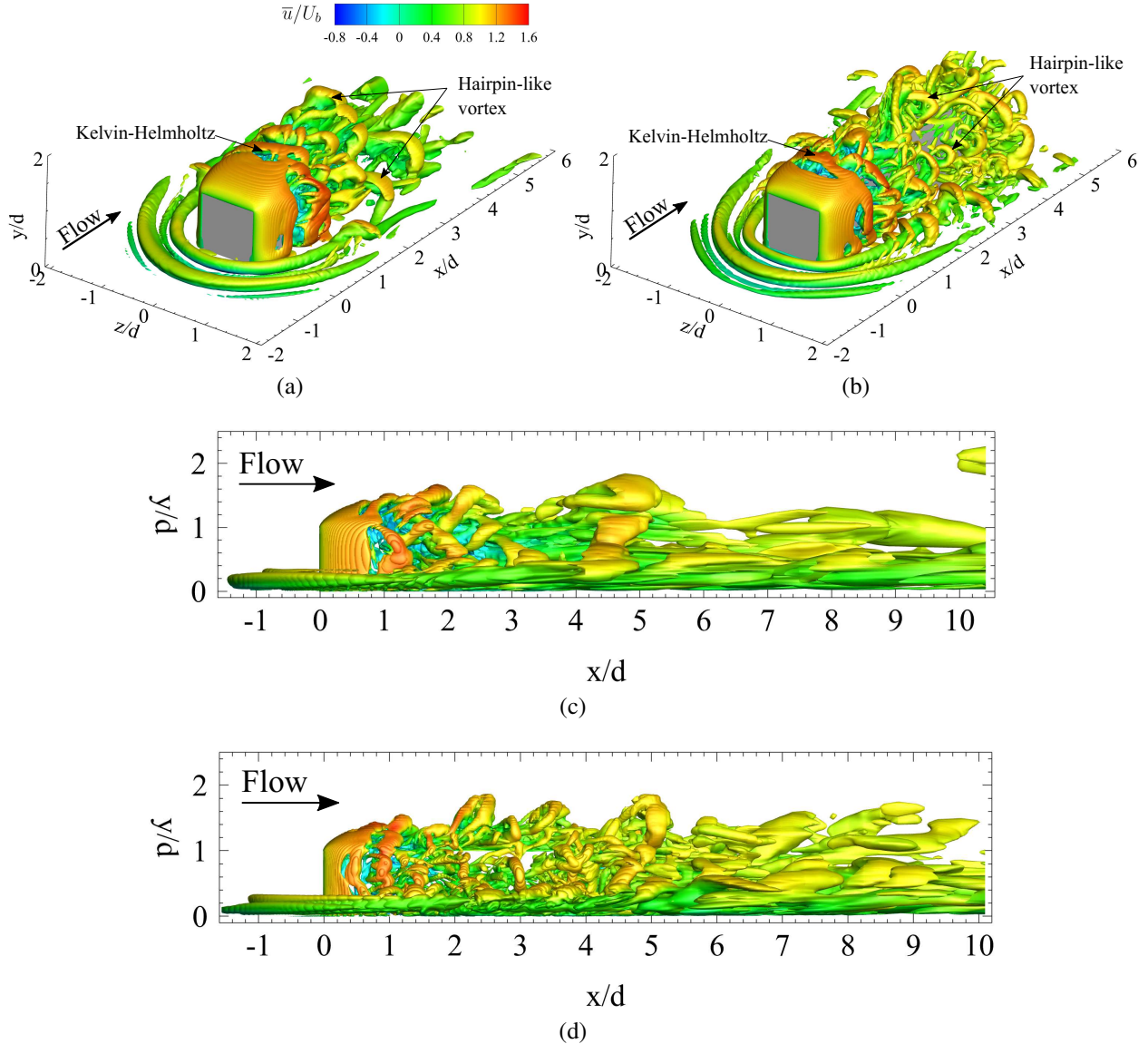


Figure 7.2: Instantaneous vortex structures overlaid with axial velocity (u) contours for (a) $DR = 1$ and (b) $DR = 4$ prisms identified using Q -criterion ($Q^* = 1$). Lateral view of the instantaneous vortex structures for (c) $DR = 1$ and (d) $DR = 4$ prisms.

($1 \leq x/d \leq 6$). As such, it becomes apparent that large-scale vortex shedding is more pronounced for $DR = 4$ compared to $DR = 1$. Following the leading-edge shear-layer separation and instability development, flapping-like motion (Cimarelli et al., 2018) leads to perturbations in the shear-layer which amplify and propagate downstream, ultimately interacting with and influencing large-scale vortex shedding. Further evidence of shear-layer flapping is presented in Section 7.1.1 and discussion on interactions is presented in Section 7.1.3.

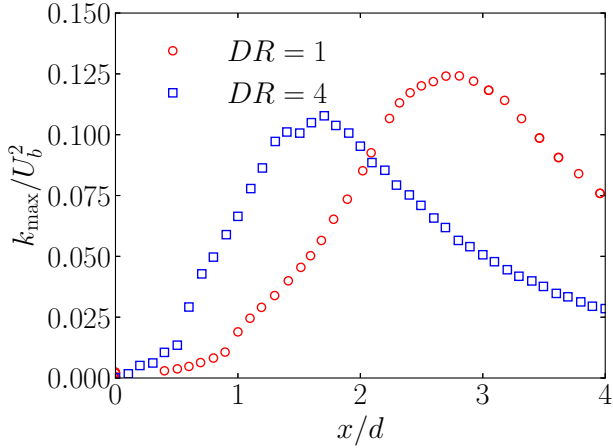


Figure 7.3: Distribution of maximum turbulent kinetic energy (k_{\max}) along the mid-span ($z/d = 0$) of both prisms at $Re = 2.5 \times 10^3$.

Figure 7.4 present contours of span-wise vorticity (ω_z^*) for both prisms, superimposed with instantaneous streamlines and the isopleth of $\bar{u} = 0$ at $z/d = 0$. Formation of KHI rollers from the leading-edge shear-layer is evident for both depth-ratios. As presented in the zoomed-in sub-figure, an early initiation of KHI rollers is noted near the leading-edge for $DR = 4$ compared to $DR = 1$, where the instability appears in the wake at $x/d \geq 1$. The onset of KHI rollers is quantified by streamwise position of the first appearance of spanwise vortices, which is at $x/d \approx 0.4$ and 1 for $DR = 4$ and 1, respectively. This indicates that depth-ratio significantly influences the onset of KHI rollers in the wake of wall-mounted prism. Furthermore, the leading edge shear-layer sheds directly into the wake for the case of $DR = 1$, while the flow reattaches on surfaces of the larger prism. The larger prism shows a prominent span-wise vortex shedding with hairpin-like vortices appearing over the prism surfaces. However vortex shedding is suppressed by interactions between the separating shear-layer and the wake in WR for shorter prism. These observations along with the formation of KHI rollers and their interaction with surfaces of the prism are a precursor to the transition-to-turbulence in the wake of wall-mounted prisms.

Previous studies have noted that the wake dynamics are significantly influenced by the depth-ratio and aspect-ratio of the prism, as well as the flow Reynolds number (Wang et al., 2006; Rastan et al., 2021; Zargar et al., 2022b). Rastan et al. (2021) showed that increasing depth-ratio

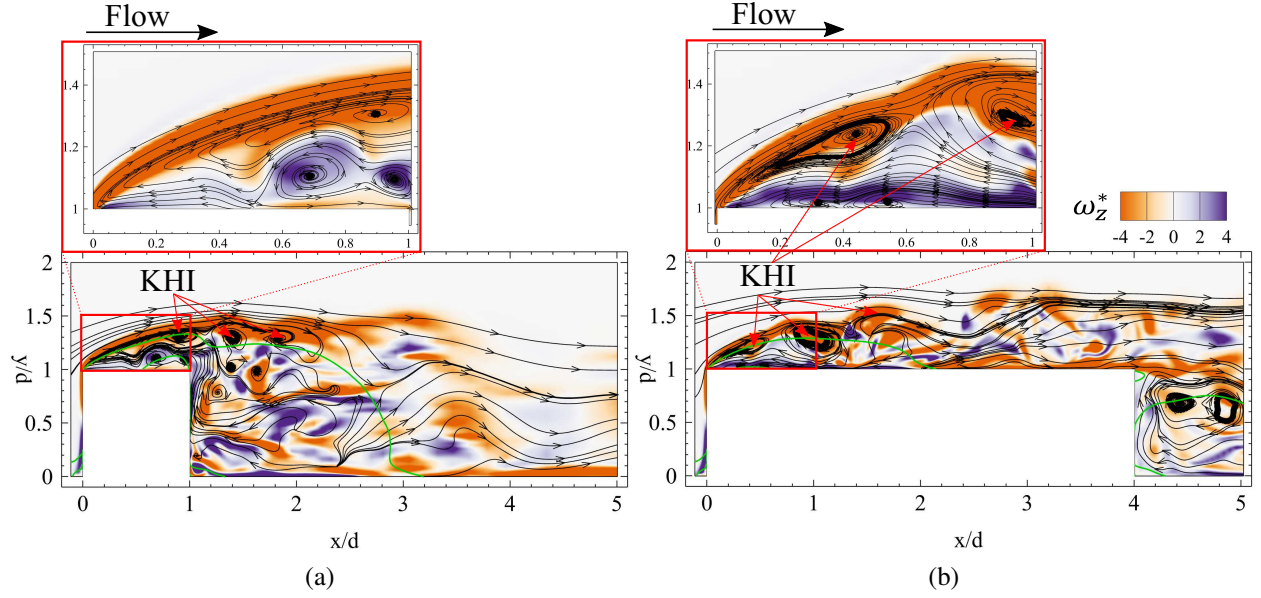


Figure 7.4: Contours of span-wise vorticity, ω_z^* , for (a) $DR = 1$ and (b) $DR = 4$, superimposed with instantaneous streamlines and the isopleth of $\bar{u} = 0$ (bold, green line) at $z/d = 0$.

for a large AR prism resulted in decreased vortex shedding due to diminished interactions between the separating shear-layer and the wake. This effect correlates with strengthening of the downwash flow. These results are consistent with the wake observed behind low aspect-ratio prisms with changing depth-ratio, where increasing depth-ratio resulted in suppressed wake unsteadiness for $Re \leq 5 \times 10^2$ (Chapter 4). Further, Zargar et al. (2022b) demonstrated that increasing the Reynolds number beyond 7.5×10^2 for a long prism ($DR = 5$) resulted in an irregular unsteady wake, resembling a transitional state. In summary, previous studies have indicated that increasing the depth-ratio (DR) suppresses wake irregularity (Chapter 4) while for a long prism the wake evolves into an irregular unsteady wake with increasing Reynolds number (Zargar et al., 2022b). This observation underscores the complexity of the flow dynamics around wall-mounted prisms and suggests that multiple factors influence the interaction between the shear layer and wake structures which results in wake transitions, such as the flow Reynolds number and prism geometry parameters. The present study portrays a novel perspective where the flow irregularity is enhanced with depth-ratio. Current study focuses on the role of Reynolds number in the transition phenomenon, while investigating the influence of depth-ratio on the wake

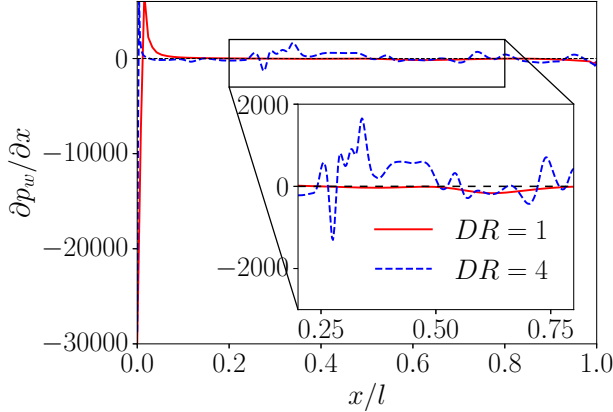


Figure 7.5: Axial wall-pressure gradient ($\partial p_w / \partial x$) along the mid-span ($z/d = 0$) of both prisms at $Re = 2.5 \times 10^3$.

dynamics. At moderate Reynolds numbers, the unsteadiness of the shear-layer (Moore et al., 2019a) is stronger, which interact with the prism surfaces and elevate the flow momentum in this region due to large depth-ratio. This further enhances the interactions between KHI and the wake coherent structures, leading to the wake transition. Evidence of this mechanism is discussed further in this article by first presenting the unsteady shear-layer motion, followed by the wake frequency signatures, and enhanced interactions using the Poisson equation. Finally, the triadic interactions are quantified using bi-spectral mode decomposition (BMD) to further understand the transition phenomenon. Here, the interactions between KHI and the large-scale vortex shedding are analyzed.

7.1.1 Unsteady Shear-Layer Motion

Axial wall-pressure gradient along the mid-span ($z/d = 0$), of both prisms at $Re = 2.5 \times 10^3$, are investigated in Figure 7.5. The rapid increase in pressure gradient near the leading-edge is attributed to streamwise flow compression due to an abrupt flow separation at the leading edge (Obabko and Cassel, 2002). This yields a favorable pressure gradient, indicated by an overshoot of $\partial p_w / \partial x$ towards a positive value. Then, the pressure gradient recovers for $DR = 1$ due to the absence of flow reattachment and shedding of the shear-layer into the wake. For $DR = 4$, pressure gradient remains elevated due to the reattachment of the shear-layer on the

prism surfaces. The elevated pressure-gradients feature oscillatory motion, which results in flow compression and expansion (Obabko and Cassel, 2002). This leads to an unsteady shear-layer characterized by flapping-like motion. Similar oscillatory shear-layer motions are observed in infinite-span prisms (Kiya and Sasaki, 1983; Cimarelli et al., 2018) as well as in 2D forward-backward-facing steps (Fang and Tachie, 2019). The unstable shear-layer motion is associated with the formation of large-scale structures in the wake and their interactions, which are responsible for the momentum transport and mixing processes (More et al., 2015; Moore et al., 2019a).

Unsteady motion of the shear-layer is quantitatively analyzed using the wall shear-stress ($\tau_w = \mu \partial u / \partial y$) along the top surface of the long prism, as depicted in Figure 7.6. Temporal variations between the mean reattachment point are recognized by the border between the reverse flow ($\tau_w < 0$) and forward flow ($\tau_w > 0$) regions. Previous studies (Lander et al., 2018) suggest two main mechanisms that control the flow unsteadiness around sharp edged prisms: vorticity-roll-up and shear-layer flapping. For long prisms, the shear-layer roll-up near the leading-edge intermittently forces the newly formed vortices towards the prism surfaces, resulting in a flapping motion (Moore et al., 2019a). This induces oscillations of the primary recirculation bubble (PR) between $x/d \approx 1.2$ and ≈ 2.1 . As presented in Figure 7.6, mean reattachment point at $z/d = 0$ for the large depth-ratio prism follows an oscillatory pattern. Further, SR also appears to oscillate, albeit in the opposite direction. With time, SR moves further upstream, while PR moves downstream. This behavior may be linked to the mechanism of shear-layer flapping, though it remains out of scope for this study, which only focuses on the transition phenomenon.

7.1.2 Flow Periodicity

The flow periodicity is investigated by using the pre-multiplied power spectral density of the streamwise (E_u), normal (E_v) and spanwise (E_w) velocity fluctuations near the leading-edge at $(0.5, 1.3, 0)$ in Figure 7.7. Multiple peaks are noted in the power spectrum of both cases, with the one at St_{kh} appearing to be dominant. This frequency is associated with KHI of the leading-edge

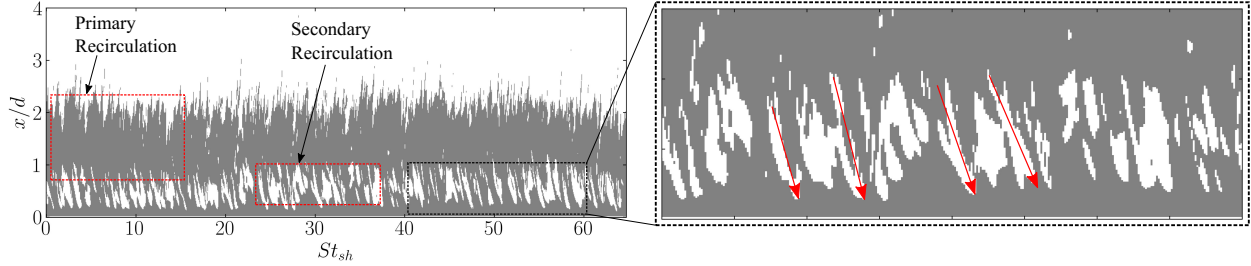


Figure 7.6: Space-time plot of the instantaneous wall shear-stress (τ_w) along the top surface of the prism with $DR = 4$ at $z/d = 0$. $\tau_w > 0$ (White) represents the region of forward flow, while $\tau_w < 0$ (Gray) represents the region of reverse flow.

shear-layer. Moreover a harmonic of KHI is observed at $2St_{kh}$. Another frequency centered at St_{sh} is also observed, mainly attributed to the Kármán-like vortex shedding. At $DR = 1$, St_{sh} and St_{kh} are 0.170 and 0.855, respectively, while $St_{sh} = 0.173$ and $St_{kh} = 1.290$ at $DR = 4$. With increasing depth-ratio from 1 to 4, a meager increase in St_{sh} is noted, while St_{kh} and $2St_{kh}$ are significantly enhanced. In other words, the depth-ratio enhances KHI of the leading-edge shear-layer, and further explains the strong span-wise vortex shedding (observed in Figure 7.2b). Additionally, as noted in Figure 7.2a, the formation of KHI rollers for $DR = 1$ occurs over a larger distance compared to $DR = 4$. This delay in onset of KHI rollers is reflected in Figure 7.7, where St_{kh} for $DR = 1$ is lower compared to $DR = 4$. This further suggests that structures associated with St_{kh} for $DR = 1$ are larger and slow-growing compared to $DR = 4$. Finally, a sub-harmonic spanwise frequency is noted, which is attributed to alternate shedding of the secondary vortex structures in the wake (Chapter 4).

Motion of the unsteady shear-layer is correlated with the vortex-pairing mechanism in sharp-edged prisms (Ma et al., 2023). Following the flow separation at the leading-edge, both the shear-layer rolls-up and newly formed vortices are intermittently forced towards the prism surfaces and convect downstream (flapping mechanism). These vortices pair with other ones in the wake, growing into large-scale structures, such as hairpin-like vortices (vortex-pairing mechanism). Large scale vortex shedding away from the leading edge is associated with large scale momentum transport. The vortex-pairing and interactions of KHI with large-scale vortices

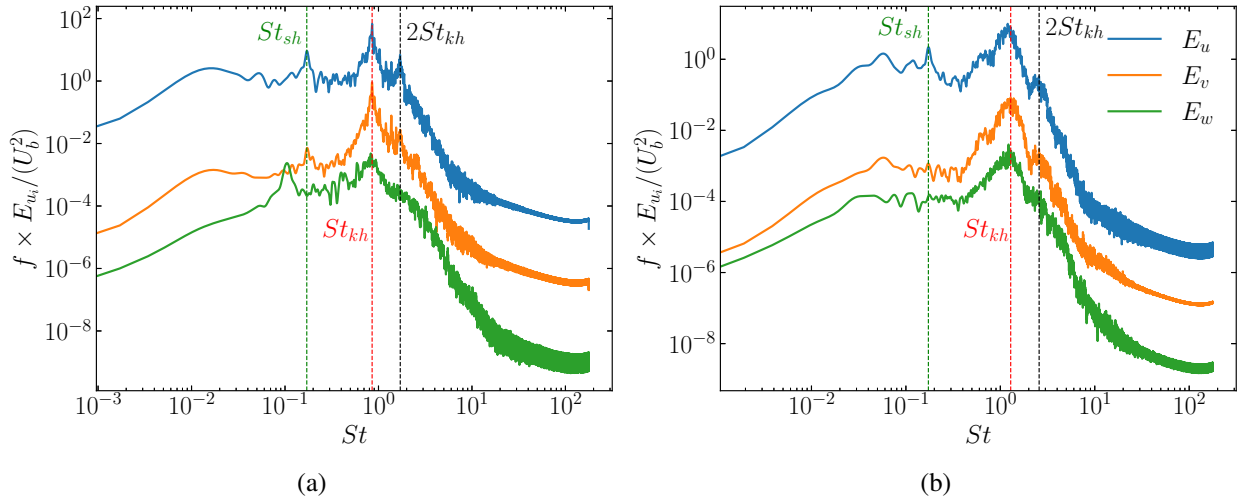


Figure 7.7: Pre-multiplied power spectral density of streamwise (E_u), normal (E_v) and spanwise (E_w) velocity fluctuations near the leading-edge at $(0.5, 1.3, 0)$ for (a) $DR = 1$ and (b) $DR = 4$.

are quantified using the correlation: $St_{kh}/St_{sh} = 0.18Re^{0.6}$ (Lander et al., 2018). Since these interactions are a function of Reynolds number, empirically this ratio should be $St_{kh}/St_{sh} = 18$ for $Re = 2.5 \times 10^3$ (Lander et al., 2018). For example, this ratio is $St_{kh}/St_{sh} = 26.5$ for flow around a 2D square prism at $Re = 2 \times 10^3$ (Brun et al., 2008). In our cases, results in Figure 7.7 indicate that this ratio is ~ 5.0 and ~ 7.5 for $DR = 1$ and 4 , respectively. This suggests that interactions between KHI and large-scale structures depend on depth-ratio, and they are suppressed compared to infinite span and 2D prisms (Brun et al., 2008; Kumahor and Tachie, 2022), potentially due to the three-dimensional effects in the wake.

7.1.3 Leading-edge Shear-layer Interactions

Interactions between KHI and large-scale vortex shedding can be further quantified by analyzing the Poisson equation:

$$\nabla^2 p = -\rho \left(2 \frac{\overline{\partial u_i}}{\partial x_j} \frac{\partial u'_j}{\partial x_i} + \frac{\partial^2}{\partial x_i \partial x_j} (u'_i u'_j - \overline{u'_i u'_j}) \right).$$

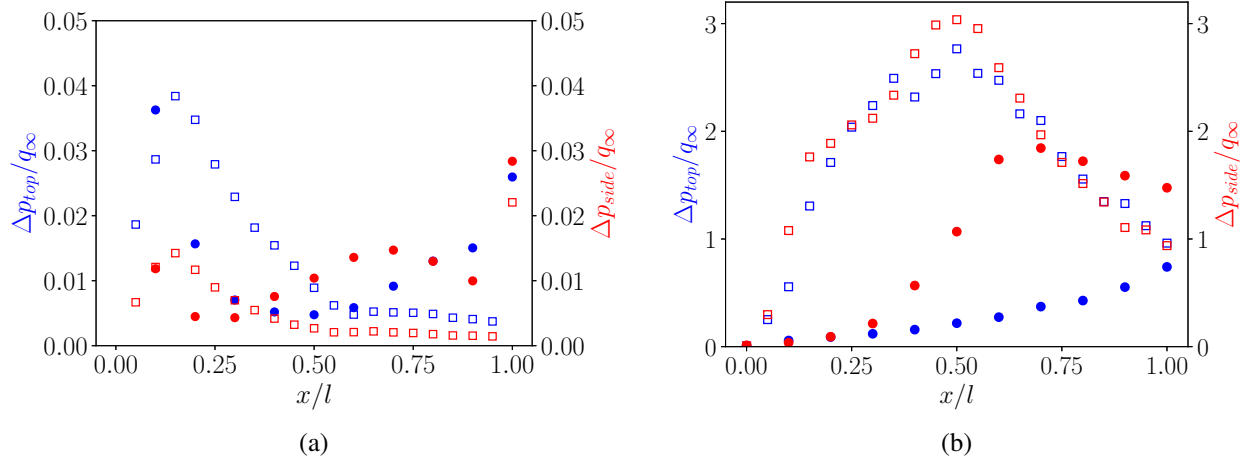


Figure 7.8: Profiles of maximum values of root-mean-squared (a) turbulence-mean-shear interaction (TMI_{max}) and (b) turbulence-turbulence interaction (TTI_{max}) terms of the Poisson's equation for $DR = 1$ and 4 prisms at $z/d = 0$ (Blue) and $y/d = 0.5$ (red). The axial distances are normalized using prism length (l). \circ represents $DR = 1$; \square represents $DR = 4$.

Here, the right-hand side can be decomposed into two terms: turbulence-mean-shear interaction (TMI) and turbulence-turbulence interaction (TTI). TMI accounts for the rapid changes in mean flow due to fluctuating fields, while TTI is associated with non-linear interactions of turbulent structures. These two terms are considered the primary sources of pressure fluctuations in the flow (Ma et al., 2023). Figure 7.8 presents the profiles of maximum values of TMI and TTI terms of the Poisson equation for $DR = 1$ and 4 at $z/d = 0$ (Blue) and $y/d = 0.5$ (red). Figure 7.8a reveals heightened TMI closer to the leading edge, where separated shear-layers are created for both prisms. Following the abrupt shear-layer separation at the leading-edge, vorticity associated with the shear-layer alter the mean flow in this region, resulting in enhanced momentum. This explains the high values of TMI near the leading-edge. Initially, TMI_{max} for both prisms remains large, though it subsides quickly for $DR = 1$. Due to a lack of flow reattachment in $DR = 1$, TMI_{max} for top shear-layer reduces till $x/l \approx 0.5$, followed by a gradual increase due flow interactions with the upwash flow at the trailing edge (Chapter 5). TMI for $DR = 4$ remains large in $0.1 \leq x/l \leq 0.3$, indicating a region of elevated mean-flow modulations by KHI. For both cases, TMI_{max} on side surfaces is significantly suppressed compared to the top, indicating that the top surface shear-layer plays a dominant role in driving the downstream flow. Finally, TMI points to the origins of mean

flow modulations, which are associated with the shear-layer flapping-like motion. Thus, enhanced TMI near the leading-edge for $DR = 4$ identify the location that shear-layer flapping-like motion is most pronounced.

The TTI term, presented in Figure 7.8b, highlights the interactions between different flow structures (Ma et al., 2023). While TMI is concentrated near the leading-edge, TTI is more distributed across the top and side surfaces of both prisms. The distribution is likely due to the enhanced flow momentum (velocity fluctuations) produced by the mean flow alterations that gradually affect the surrounding flow field. For $DR = 1$, TTI_{max} is elevated closer to the trailing-edge, which is attributed to direct shedding of the leading-edge shear-layer into the wake. This enhances the interactions and vortex mixing in the wake region (WR) (Chapter 5). For $DR = 4$, elevated TTI_{max} occurs close to location of the flow reattachment on the prism surfaces ($\bar{x}_R/l \approx 0.53$). This region is associated with the breakdown of KHI rollers into hairpin-like vortices, which are then convected downstream. The interactions between KHI rollers and large-scale vortex shedding are most pronounced in this region, leading to an increased turbulence intensity and mixing (previously shown in Figure 7.1d). These processes enhance the flow momentum due to an influx of energy by the mean flow modulation (TMI). As such, increased momentum results in the enhancement of vortex shedding and wake transition. These interactions are driven by the flow geometry, since such a mechanism is absent for the short prism, where TTI_{max} steadily rises up to the trailing-edge. Finally, TTI_{max} are comparable for the top and side surface shear-layers for both prisms, which indicates an invariance of energy production and dissipation on top and side surfaces.

Triadic interactions form the basis of the energy transfer mechanism in the wake transition phenomenon (Craik, 1971). Frequency triad, described by the interactions between two flow structures at frequencies St_i and St_j , results in a third frequency of St_{i+j} such that $St_i \pm St_j \pm St_{i+j} = 0$. These interactions are quantified using bi-spectral mode decomposition (BMD) analysis, proposed by Schmidt (2020). Figure 7.9 shows the magnitude of mode bi-spectrum for $DR = 4$ in the sum and difference regions. Their interactions with large-scale

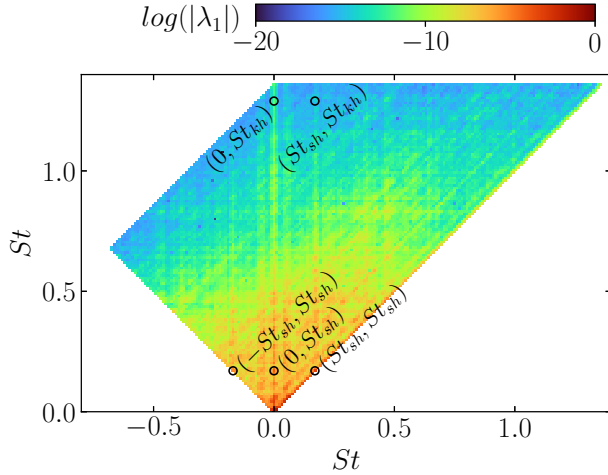


Figure 7.9: Magnitude mode bi-spectrum for $DR = 4$, using $N_{fft} = 2^{10}$, in the sum and difference regions.

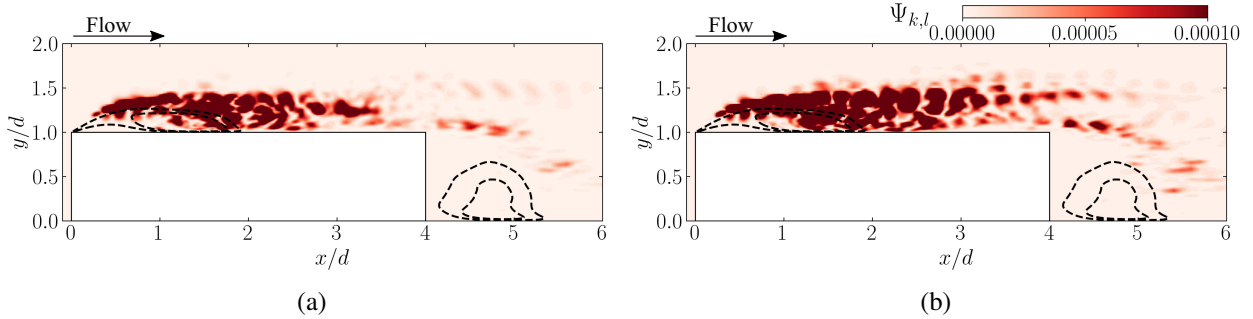


Figure 7.10: BMD interaction map for $DR = 4$ prism, showing the interactions between (a) Kelvin-Helmholtz instability and mean flow and (b) Kelvin-Helmholtz instability and large-scale vortex shedding.

vortex shedding frequency (St_{sh}) are noted in Figure 7.9 along with the sum interaction of St_{kh} with St_{sh} , and the fundamental mode of St_{sh} . The intensity of the spectrum is large of the large-scale frequencies (St_{sh}), while it reduces significantly for St_{kh} . Further, the sum interaction of St_{sh} corresponds to the global maximum of mode bi-spectrum, consistent with the separated flow in Schmidt (2020).

Interactions of KHI with the mean flow and large-scale vortex shedding are presented through a BMD interaction map in Figure 7.10. This map quantifies the average local bi-correlation between

three frequencies, St_i , St_j and St_{i+j} , involved in the triad. The interactions are defined as

$$\Psi_{k,l} = |\phi_{k+l} \circ \phi_{k \circ l}|,$$

where ϕ_{k+l} represents the resultant mode of triadic interaction and $\phi_{k \circ l}$ represents the influence of input modes. For more information regarding the formulation, the readers are referred to Schmidt (2020). For both cases, the interactions are most pronounced near the leading-edge and through-out the upper surface of the prism up to $x/d \approx 2$, where the flow reattaches to the surface. Interactions of KHI with the mean flow is dominant outside the PR, with the maximum value occurring at $x/d \approx 0.8$. This is consistent with the location of maximum TMI in Figure 7.8a. This interaction is associated with the mean-flow modulation by KHI due to shear-layer flapping-like motion. A slightly elevated interaction at the trailing edge also corresponds to the trailing-edge shear-layer interacting with the flow downstream. Interactions of KHI with large-scale vortex shedding are distributed across the prism surface. Near the center of PR, these interactions enhance due to the flow impingement on prism surfaces as a result of unsteady shear-layer. This region of elevated interactions is consistent with the region of maximum TTI in Figure 7.8b. These results confirm that flow modulations at the leading-edge, due to KHI, are convected downstream and interact with large-scale vortex shedding, enhancing the flow momentum. Due to the interactions and vortex breakdown, the flow momentum reduces further till the trailing-edge. While not showed here for $DR = 1$, such interactions remain absent, underscoring the influence of depth-ratio in the wake transition phenomenon. These results provide a novel understanding of the interactions between KHI and large-scale vortex shedding in the wake of wall-mounted prisms.

7.1.4 Observations across the parameter space

Observations and insights from the specific cases of $DR = 1$ and 4 at $Re = 2.5 \times 10^3$ are expandable across the broad parameter space considered in this study, *i.e* varying aspect-ratio (0.25 – 1.5), depth-ratio (1 – 4), and Reynolds numbers (1×10^3 – 5×10^3). For example, consider the cases

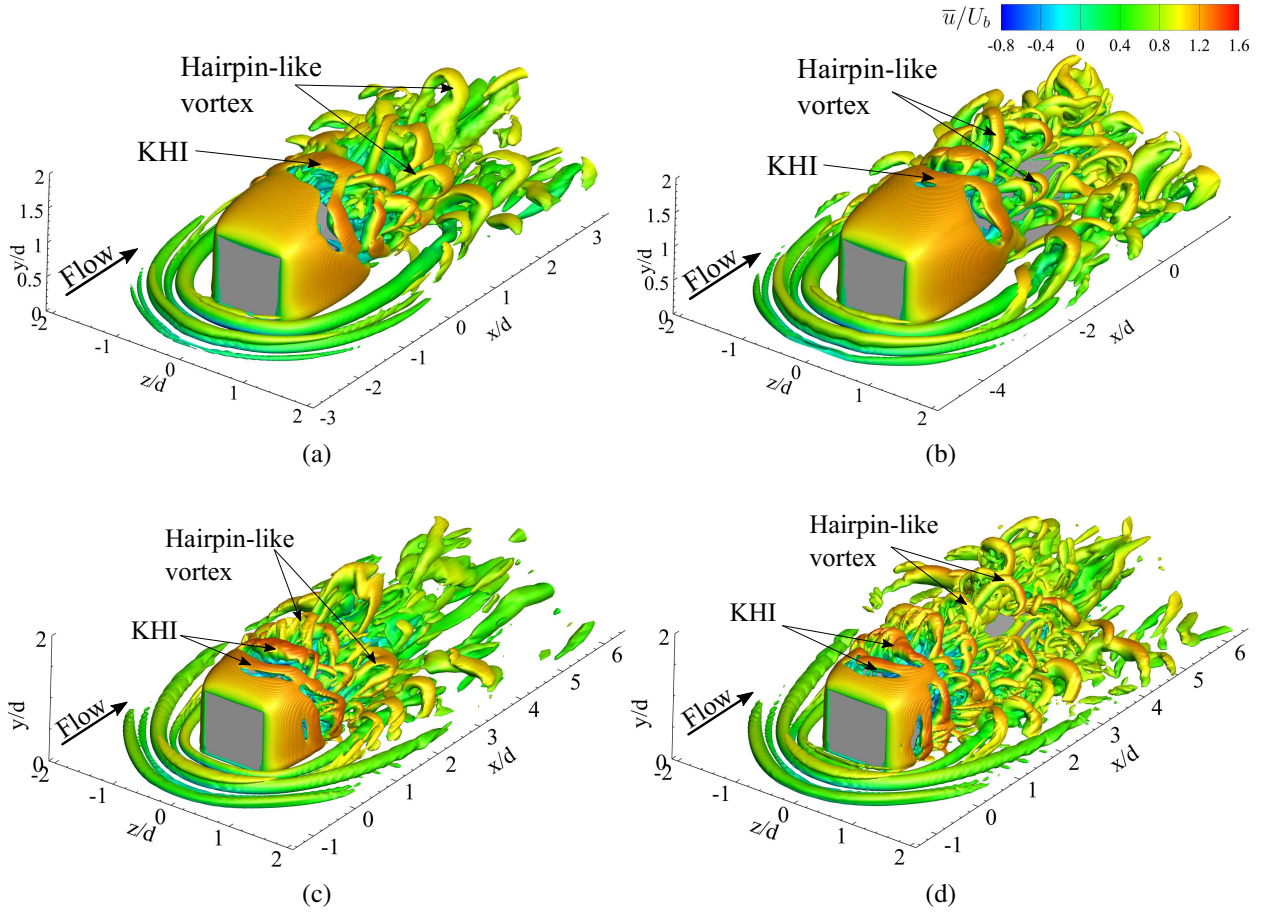


Figure 7.11: Instantaneous vortex structures overlaid with axial velocity (u) contours for (a, c) $DR = 1.5$ and (b, d) 3.5 at (a, b) $Re = 1.5 \times 10^3$, (c, d) $Re = 4 \times 10^3$ identified using Q -criterion ($Q^* = 1$).

of $DR = 1.5$ and 3.5 at $Re = 1.5 \times 10^3$ and 4×10^3 in Figure 7.11. These instantaneous vortex structures reveal that for a short depth-ratio prism ($DR = 1.5$), the leading-edge shear-layer extends and sheds directly into the wake. The influence of Reynolds number becomes apparent, where the unsteady wake is classified into regular unsteady wake, consistent with the observations of Zargar et al. (2022b). In contrast, larger depth-ratio prism ($DR = 3.5$) exhibits the shear-layer reattachment to the prism surfaces, leading to an unsteady shear-layer motion and enhanced interactions with large-scale vortex shedding. This results in the formation of large-scale vortex rollers and hairpin-like vortices in the wake, consistent with previous observations from the case of $DR = 4$ at $Re = 2.5 \times 10^3$.

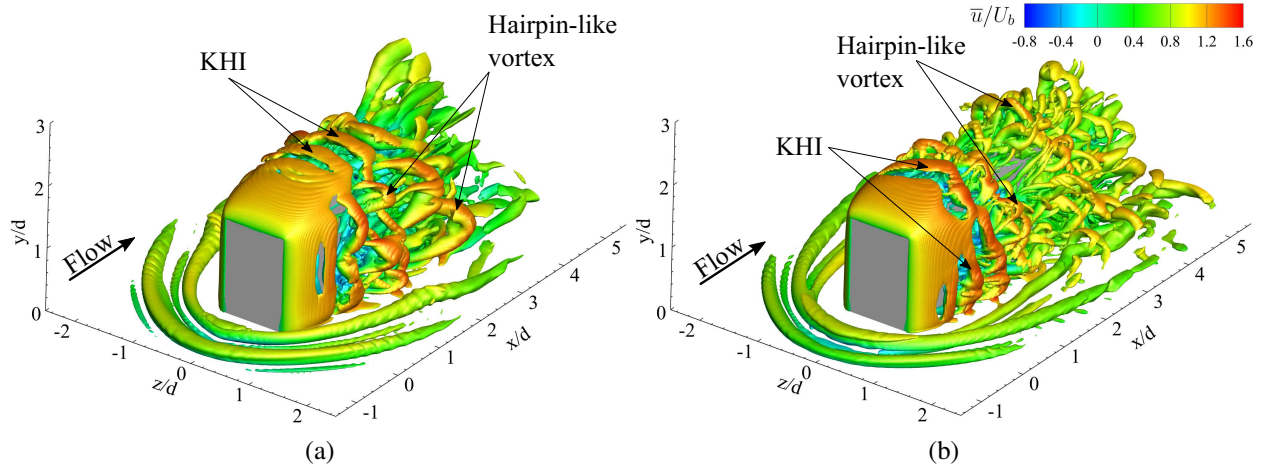


Figure 7.12: Instantaneous vortex structures overlaid with axial velocity (u) contours for prisms with $AR = 1.5$ and (a) $DR = 1.5$ and (b) 3.5 at $Re = 2.5 \times 10^3$ identified using Q -criterion ($Q^* = 1$).

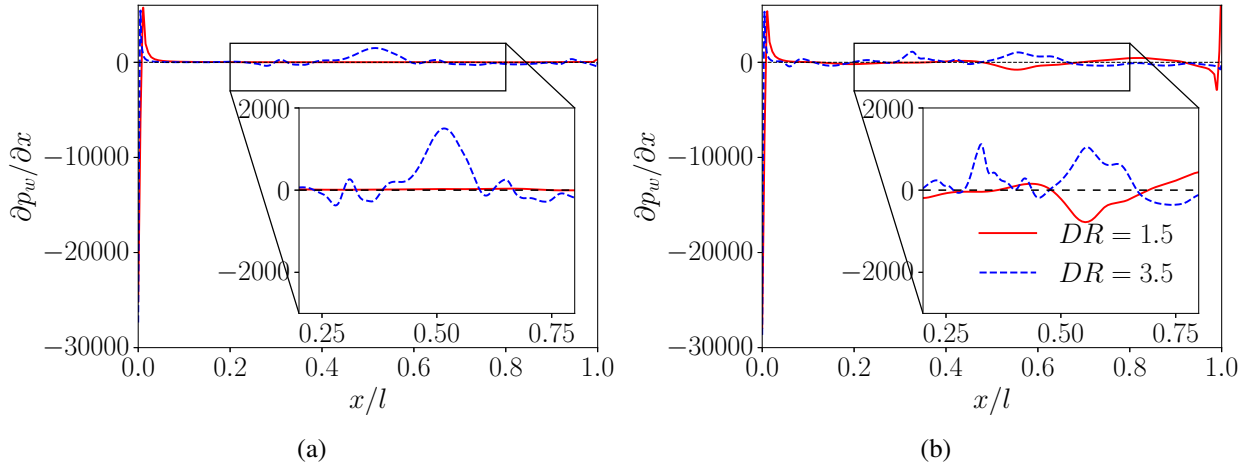


Figure 7.13: Axial wall-pressure gradient along the mid-span ($z/d = 0$) of prisms with (a) $AR = 1.5$ at $Re = 2.5 \times 10^3$, and (b) $AR = 1$ at $Re = 4 \times 10^3$.

Next, consider the cases of prisms with $AR = 1.5$ and $DR = 1.5$ and 3.5 at $Re = 2.5 \times 10^3$ in Figure 7.12. The results are consistent with the observations from $AR = 1$, where the interactions of KHI with large-scale vortex shedding is more pronounced for larger depth-ratio. This results in a more complex wake topology downstream of the leading-edge, as opposed to $DR = 1.5$, where shedding of the shear-layer into the wake suppresses the interactions resulting in a more stable flow. Influence of prism aspect-ratio is further evident in Figure 7.12, where the flow unsteadiness enhances with aspect-ratio, consistent with observations of Saha (2013). Finally, the unsteady

shear-layer is quantitatively observed by axial wall-pressure gradients plotted along the prism mid-span ($z/d = 0$) in Figure 7.13. Here, the cases of $DR = 1.5$ and 3.5 at $AR = 1.5$ at $Re = 2.5 \times 10^3$ and $AR = 1$ at $Re = 4 \times 10^3$ are presented. Rapid overshoot of pressure gradient near the leading-edge, suggesting an abrupt flow separation, is consistent in all cases. The trends of $\partial p_w / \partial x$ for $DR = 1.5$ remain steady at $Re = 2.5 \times 10^3$, while small oscillations are noted at $Re = 4 \times 10^3$. Although Reynolds number effects are not the primary focus of this study, the oscillations in $\partial p_w / \partial x$ at higher Reynolds numbers can be linked to unsteady wake dynamics. Notably, for larger depth-ratio prism ($DR = 3.5$), the oscillatory behavior of the pressure gradient becomes evident and more pronounced across both aspect-ratios and Reynolds numbers. Oscillations enhance with depth-ratio and they are associated with shear-layer flapping-like phenomenon, which is pronounced for these cases (see Figure 7.11, 7.12). Previous Chapters, 4 and 5, have established that unsteady and mean wake topology of wall-mounted prisms are functions of both Reynolds number and body geometry. Our results expand this argument to turbulence transition, where the interactions between KHI and large-scale vortex shedding are enhanced with increasing depth-ratio. These interactions are driven by the unsteady shear-layer motion, which is most pronounced for large depth-ratio prisms. These interactions enhance the flow momentum over the prism surfaces, resulting in a more complex wake structure and ultimately leading to turbulence transition.

7.2 Summary

This chapter focused on the wake transition phenomenon at Reynolds number of 2.5×10^3 for prisms with aspect-ratio of 1 and depth-ratios of 1 and 4. Results were consistent for the entire parameter space studied in this dissertation ($AR = 0.25 - 1.5$, $DR = 1 - 4$, and $Re = 1 \times 10^3 - 5 \times 10^3$). The wake unsteadiness is enhanced with increasing depth-ratio. Kelvin-Helmholtz instability is noted for all cases, forming finite spanwise vortex rollers. However, the intensity and frequency of the rollers are more pronounced for longer prisms

($DR \geq 3$), while for short prisms they are delayed and less frequent. Additionally, the formation of KHI for short prisms takes place over a larger distance compared to longer prisms. Enhanced wake unsteadiness is attributed to interactions between Kelvin-Helmholtz instability and large-scale vortex shedding, induced by an unsteady shear-layer flapping-like motion in the wake of large depth-ratio prisms. Evidence of unsteady shear-layer is provided by analyzing the space-time wall shear-stress contours, showing an oscillating recirculating region. Interactions between Kelvin-Helmholtz instability and large-scale vortex shedding are quantified using the Poisson equation and bi-spectral decomposition. Turbulence-mean-shear interaction term of Poisson's equation is elevated near the leading-edge, while turbulence-turbulence interaction term is distributed across the prism surfaces. Elevated TMI near the leading-edge points to the mean flow manipulations due to unsteady shear-layer, while enhanced TTI on the prism surfaces indicates interactions between Kelvin-Helmholtz instability and large-scale vortex shedding. Elevated TMI shows that the leading-edge flow manipulations provide energy, which is then transferred to the large-scale vortex shedding, enhancing the flow momentum. Increased momentum in the wake enhances vortex shedding, which is a precursor to turbulence transition. Finally, bi-spectral mode decomposition analysis provides evidence of the interactions between Kelvin-Helmholtz instability and large-scale vortex shedding, further confirming the transition process. This study underscores the role of depth-ratio in the transition-to-turbulence phenomenon at moderate Reynolds numbers, as defined in Section 1.1 and provides novel insights into the interaction mechanisms of Kelvin-Helmholtz instability and large-scale vortex shedding in the wake of wall-mounted prisms.

Chapter 8

DESTABILIZATION OF LEADING-EDGE SHEAR-LAYER[‡]

The impact of depth ratio on flow irregularity and vortex shedding characteristics of wall-mounted prisms was partially addressed in Chapter 7. This chapter focuses on mechanisms that drive the destabilization of the leading-edge shear layer, emphasizing flow topology and the onset of KHI. These instabilities enhance flow irregularity and modulate spanwise vortex structures. As discussed in Section 2.2, leading-edge shear-layer separation and reattachment are defining features of the flow around wall-mounted long prisms. This flow combines small-scale turbulent motions near the leading edge with large-scale vortex shedding, resulting in nonlinear interactions that amplify wake irregularity (discussed in Chapter 7) and significantly influence surface pressure distribution (confirmed in Chapter 6). The precise dynamics of these interacting processes and their influence on flow topology are explained in this chapter. This chapter expands on previous sections by investigating the destabilization mechanisms of the leading-edge shear layer in the wake of wall-mounted long prisms. The primary focus is on the onset of Kelvin-Helmholtz instability, which

[‡]The contents of this chapter are under review by *Journal of Fluid Mechanics* under the citation: “Goswami, S., & Hemmati, A. (2025). Destabilization of leading-edge shear-layer in the wake of wall-mounted long prisms. *Journal of Fluid Mechanics*”.

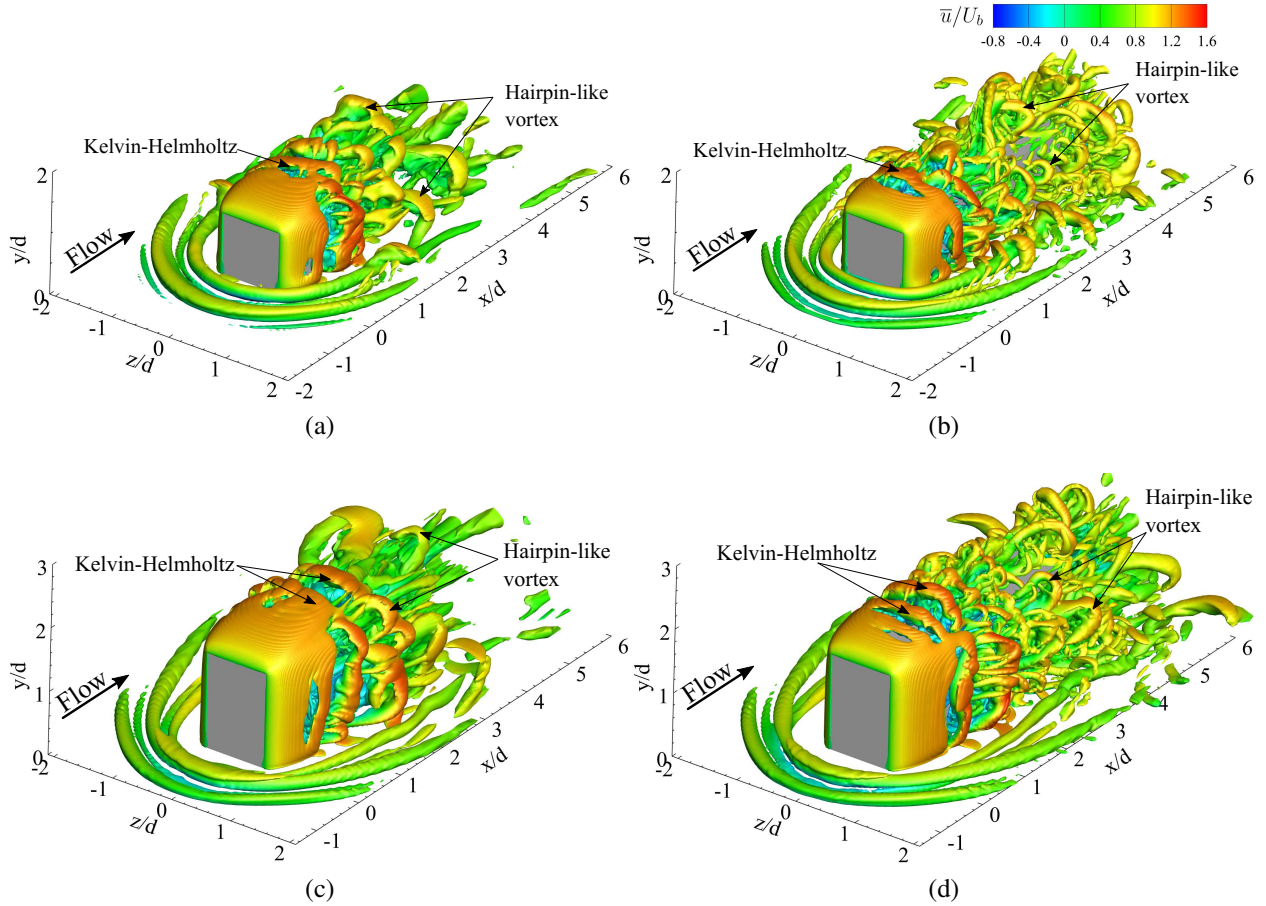


Figure 8.1: Instantaneous vortex structures overlaid with axial velocity (u) contours for (a, c) $DR = 1$ and (b, d) $DR = 4$ prisms with (a, b) $AR = 1$ and (c, d) $AR = 1.5$ at Reynolds number of 2.5×10^3 , identified using Q -criterion ($Q^* = 1$).

intensifies flow irregularity and modulates spanwise vortex structures. Here, prisms with $AR = 0.25 - 1.5$ and $DR = 1 - 4$ are specifically examined at $Re = 2.5 \times 10^3$, 5×10^3 , and 1×10^4 .

8.1 Results and Discussion

First, the main features of the instantaneous wake around wall-mounted prisms are analyzed. Figure 8.1 displays the instantaneous three-dimensional vortex structures for prisms with $DR = 1$ and 4 and $AR = 1$ and 1.5, at a $Re = 2.5 \times 10^3$. Sharp leading edge of the prism fixes the boundary layer detachment point, leading to the formation of a leading-edge shear layer. This shear layer undergoes distinct stages of growth and onset of primary instabilities (Moore et al.,

2019a). A Kelvin-Helmholtz instability first develops, resulting in the formation of finite spanwise vortex rollers near the leading edge, as shown in Figure 8.1. A secondary instability associated with KHI then destabilizes these spanwise rollers, resulting in the formation of hairpin-like vortices downstream. For both aspect-ratios, the long prism ($DR = 4$) exhibits prominent spanwise vortex shedding and formation of hairpin-like vortices over the prism surfaces. Contrarily, leading-edge shear layer sheds directly into the wake for the short prism ($DR = 1$), triggering secondary instabilities described in Chapter 4, which suppress vortex shedding. This suppression is evident in Figure 8.1, where the long prism ($DR = 4$) shows more prominent spanwise vortex shedding compared to the short prism ($DR = 1$). In this chapter, the term “*long prism*” refers to $DR = 4$ and “*short prism*” refers to $DR = 1$.

Figure 8.2 illustrates instantaneous vortex structures for prisms with $DR = 1$ and 4 at $Re = 5 \times 10^3$ and 1×10^4 . Results indicate that vortex shedding becomes more pronounced at higher Reynolds numbers, with the long prism displaying notably stronger spanwise vortex shedding compared to the short prism. Additionally, vortex shedding is more irregular at higher Reynolds numbers than $Re = 2.5 \times 10^3$ (see Figure 8.1). These observations in Figure 8.2 confirm the impact of prism depth-ratio on flow irregularity and vortex shedding characteristics at elevated Reynolds numbers. Onset of Kelvin-Helmholtz instability is observed near the leading edges of both prisms, resulting in the formation of spanwise KHI rollers. At higher Reynolds numbers, these KHI rollers form closer to the leading edge. However, downstream formation of hairpin-like vortices and the overall spanwise vortex shedding pattern remain consistent with those at $Re = 2.5 \times 10^3$.

While previous studies have scrutinized the vortex shedding mechanism for infinite-span rectangular prisms (Cimarelli et al., 2018; Zhang et al., 2023), there are no studies that focus on quantitative investigation of the onset of KHI instabilities and subsequent enhancement of the wake irregularity for finite-span prisms. Moreover, previous studies have discussed the evolution of leading-edge vortex rollers for infinite-span rectangular prisms. However, there has been limited attention given to destabilization of the leading-edge shear-layer. Since the wake of finite wall-mounted prisms is impacted by various end-effects (Wang and Zhou, 2009), the source of

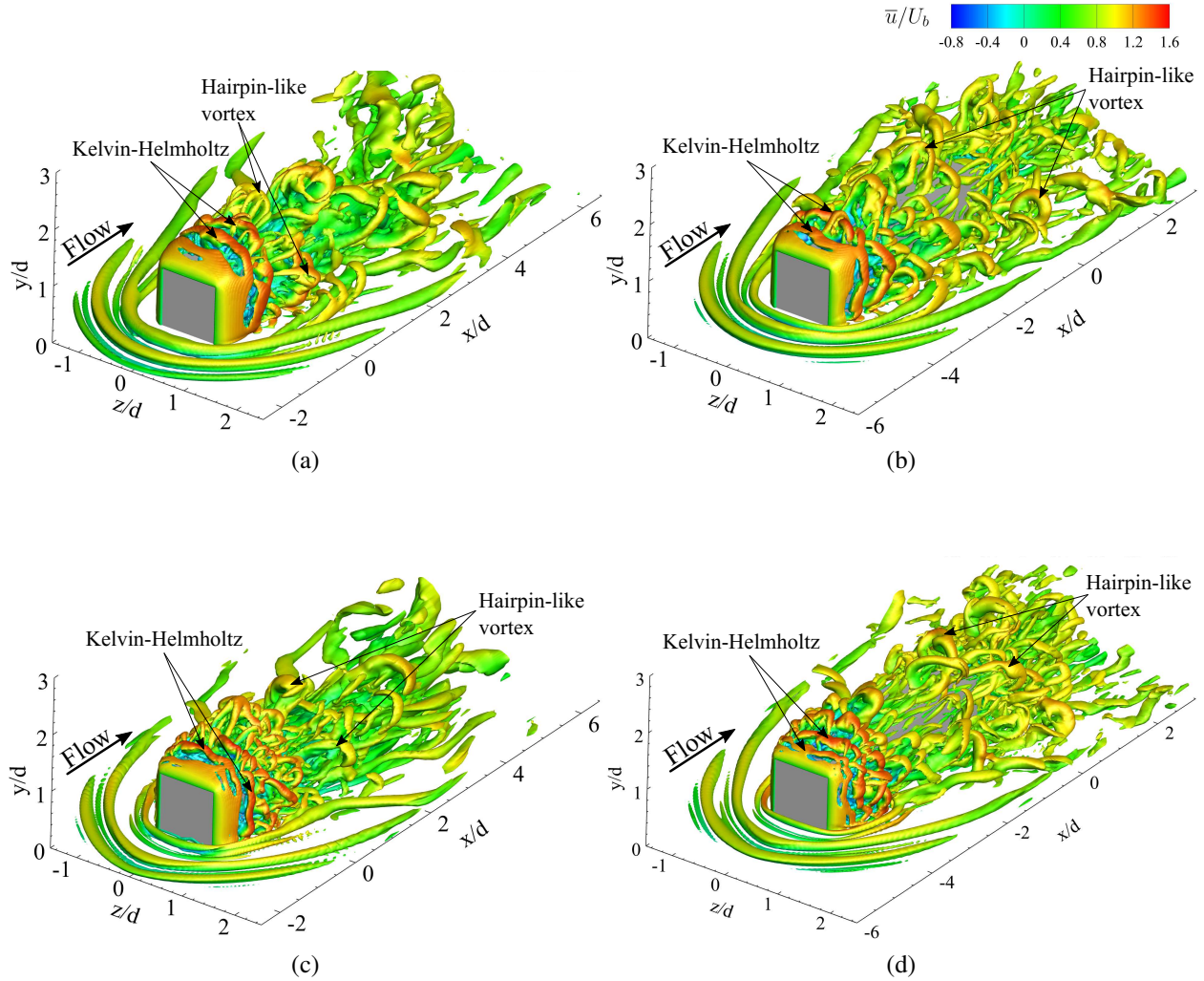


Figure 8.2: Instantaneous vortex structures overlaid with axial velocity (u) contours for (a, c) $DR = 1$ and (b, d) $DR = 4$ prisms at (a, b) $Re = 5 \times 10^3$ and (c, d) $Re = 1 \times 10^4$, identified using Q -criterion ($Q^* = 1$).

unsteadiness in the leading-edge shear-layer remains unclear. Moreover, Zargar et al. (2022b) examined the transitional mechanism and early wake developments behind long prisms ($DR \geq 3$), suggesting that hairpin-like vortices form after the initial shear-layer roll-up. Preliminary results in this dissertation, however, show that a destabilization mechanism deforms the spanwise roller following the initial shear-layer roll-up, which subsequently form hairpin-like structures. Thus, this work aims to address this knowledge gap by investigating the mechanism of destabilization in the leading-edge shear-layer at increasing depth-ratio.

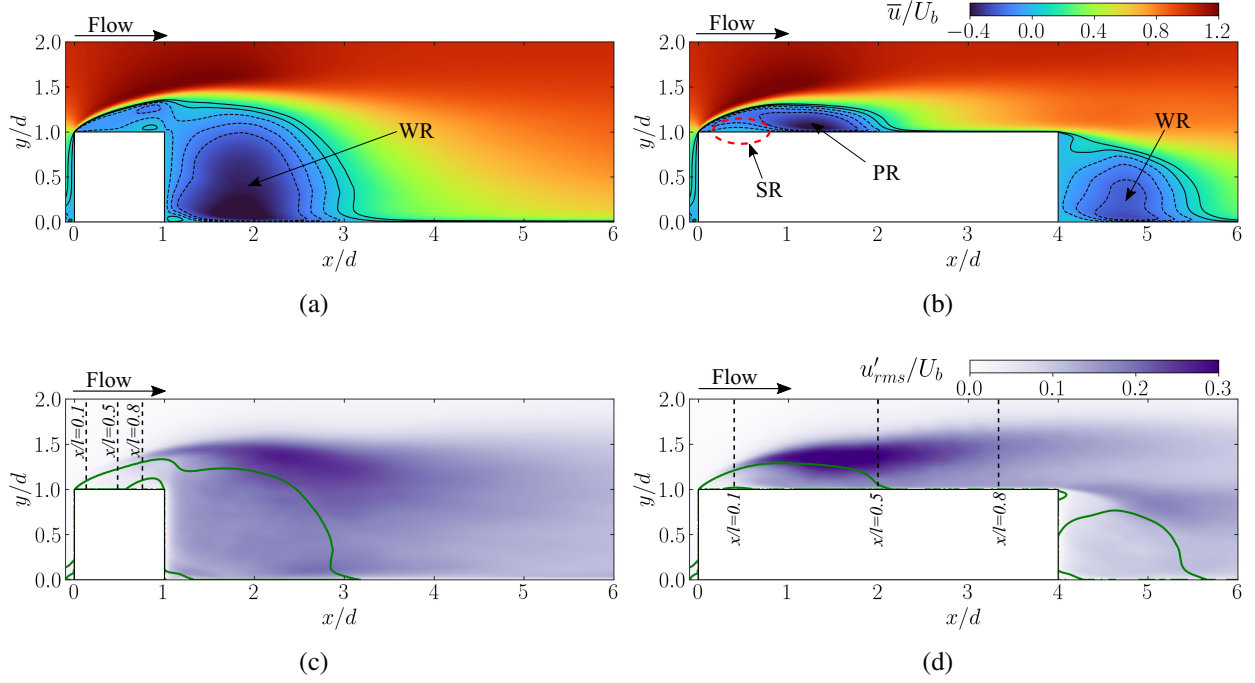


Figure 8.3: (a,b) Mean streamwise velocity (\bar{u}) contours overlaid with mean velocity streamlines; and (c,d) contours of root-mean-squared streamwise fluctuations (u'_{rms}) overlaid with streamline of $\bar{u} = 0$. Contours presented for (a,c) $DR = 1$ and (b,d) $DR = 4$ prisms at $Re = 2.5 \times 10^3$ at spanwise plane of $z/d = 0$.

8.1.1 Mean flow characteristics

Main features of the mean flow topology are discussed in this section to provide a comprehensive understanding of the flow characteristics around wall-mounted prisms. Figures 8.3a and 8.3b present mean streamwise velocity (\bar{u}) contours overlaid with mean velocity streamlines for both prisms, highlighting flow separation at the leading edge. For the short prism, the leading-edge shear layer extends into the wake, forming a wake recirculation (WR) region. For $DR = 4$, the shear layer reattaches to the top surface of the prism at $x/d \approx 2.12$, creating a primary recirculation (PR) region on the top surface. Additionally, a secondary recirculation (SR) region forms below the PR region, due to the reverse flow induced by the near-wall region of the PR, resulting in an upstream-moving boundary layer. For the short prism, PR and SR regions are absent due to a lack of flow reattachment on the prism surfaces. Figures 8.3c and 8.3d show contours of root-mean-squared streamwise fluctuations (u'_{rms}) overlaid with the $\bar{u} = 0$ streamline

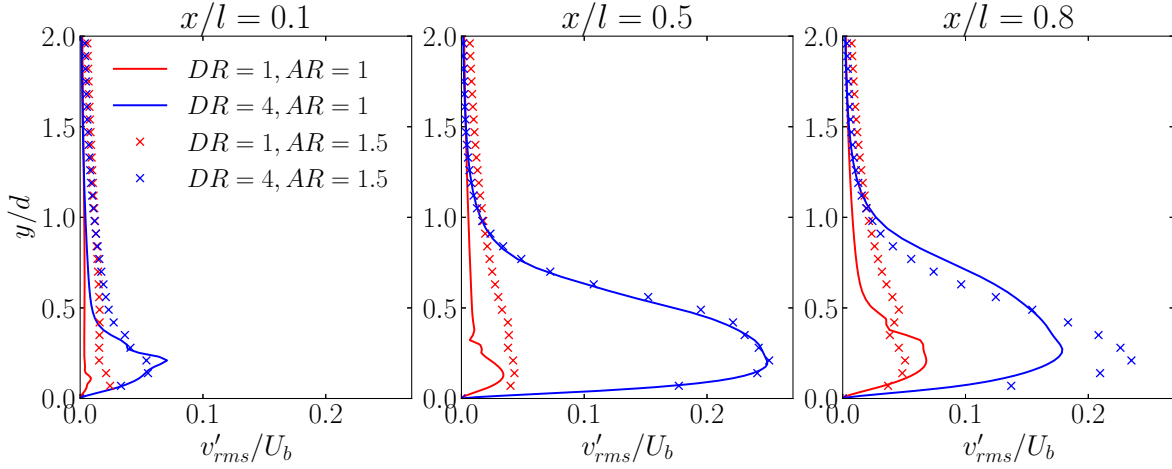


Figure 8.4: Profiles of root-mean-squared of the normal velocity fluctuations (v'_{rms}) at different streamwise locations shown in Figures 8.3c and 8.3d for (red) $DR = 1$ and (blue) $DR = 4$ prisms at $Re = 2.5 \times 10^3$. Solid lines show profiles for $AR = 1$ prisms, while the \times markers indicate the profiles for $AR = 1.5$ prisms.

(in green) for both prisms. These figures indicate that the initial leading-edge shear layer exhibits laminar characteristics. However, velocity fluctuations intensify with the onset of Kelvin-Helmholtz Instability (KHI) vortex rollers and their subsequent interactions (Chapter 7), marking the transition to turbulence (already discussed in Chapter 7). Regions of intense fluctuations show high turbulence intensity (u'_i) and maximum turbulence kinetic energy ($u'_i u'_i$). For $DR = 1$, u'_{rms} intensifies near the WR region and then gradually declines downstream. For $DR = 4$, u'_{rms} amplification is more pronounced near the PR region with another peak near the WR region, coinciding with trailing-edge flow separation.

Figure 8.4 shows profiles of the root-mean-squared normal velocity fluctuations (v'_{rms}) at different streamwise locations immediately downstream of the leading edge for both prisms (shown in Figures 8.3c and 8.3d), comparing the profiles for aspect-ratios $AR = 1$ and 1.5. Streamwise locations are normalized by the prism length (l) to facilitate comparison between prisms of different depth-ratios. This comparison reveals that wake oscillation intensity is significantly higher for $DR = 4$ than $DR = 1$. Additionally, wake oscillation intensity reaches a peak at $x/l = 0.5$ for $DR = 4$, corresponding to the location of leading-edge shear-layer reattachment. This confirms that the wake strength is influenced by the prism depth-ratio, as flow

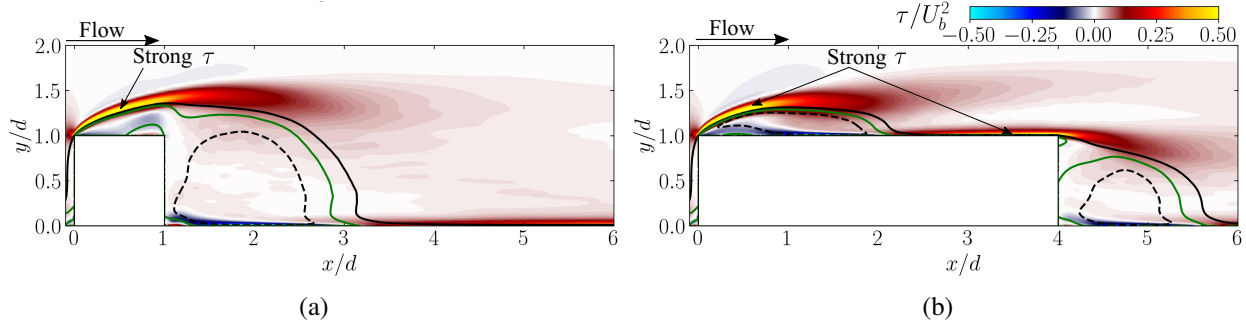


Figure 8.5: Mean shear (τ) at leading-edge of (a) $DR = 1$ and (b) $DR = 4$ prisms with $AR = 1$ at $Re = 2.5 \times 10^3$. Contours are overlaid with streamline of $\bar{u} = 0$ (green) and critical streamlines (black).

separation and reattachment vary across surfaces. Long prism shows stronger velocity fluctuations (v'_{rms}) compared to the short prism, further highlighting the role of depth-ratio in enhancing wake irregularity. Similar conclusions are apparent from comparisons of prisms with $AR = 1.5$, where the longer prism ($DR = 4$) displayed a stronger wake compared to $DR = 1$.

Figure 8.5 presents contours of the mean shear stress, defined as $\tau = \mu \frac{\partial \bar{u}}{\partial y}$. Results highlight strong τ at the leading edge of both prisms, while intensity of τ rises with increasing depth-ratio, leading to a greater overall shear stress. Additionally, a region of intense mean shear flow is observed near the trailing edge for the longer prism ($DR = 4$), where the leading-edge shear layer reattaches and separates again. The stronger mean shear stress associated with the higher depth-ratio prism significantly influences the inception and development of hairpin-like vortices. For example, Zhang et al. (2023) demonstrated that hairpin vortex formation is driven by the background mean shear flow with regions of high shear stress forming the vortex head in high-momentum zones, while low-momentum regions form vortex legs.

8.1.2 Onset of Kelvin-Helmholtz Instability

The onset of Kelvin-Helmholtz instability vortex roll-up was shown in Chapter 6 to depend on the prism depth-ratio. For $DR = 1$, vortex tubes extend into the downstream wake region, whereas, they appear over the prism surfaces for $DR = 4$. Similar vortex tubes are observed along side

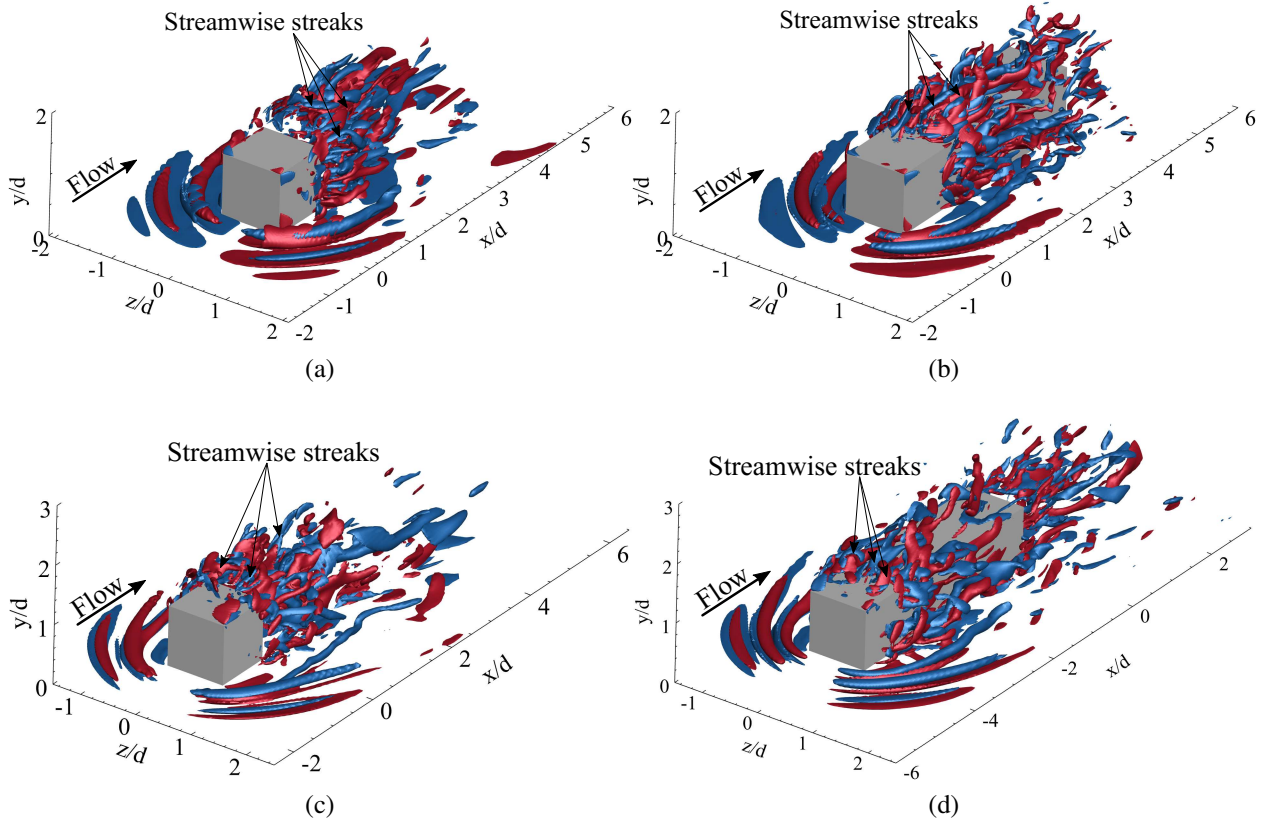


Figure 8.6: Iso-surfaces of streamwise vorticity, $\omega_x^* = \pm 5$, at (a,b) $Re = 2.5 \times 10^3$ and (c,d) $Re = 1 \times 10^4$ for (a,c) $DR = 1$ and (b,d) $DR = 4$ prisms.

surfaces of both prisms. Following this, streamwise vortex tubes undergo modulation in the spanwise direction, locations of which align with the local maxima of mean shear stress (Figure 8.5). Under the influence of strong mean shear flow, modulated vortex tubes are stretched and roll-up into hairpin-like vortices, arranged in a staggered formation, which are shed downstream. Figure 8.6 illustrates the pattern adopted by the streamwise vorticity (ω_x), highlighting the flow motion and development of streamwise vortices, which induce flow entrainment due to high- and low-speed streaks (Jimenez, 1983). At high Reynolds numbers, similar high- and low-speed streaks appear (see Figures 8.6c and 8.6d). Flow entrainment is particularly evident near the leading edge of the long prism with streamwise vortices extending into the wake region. Contrarily, streamwise vortices emerge well into the wake for $DR = 1$.

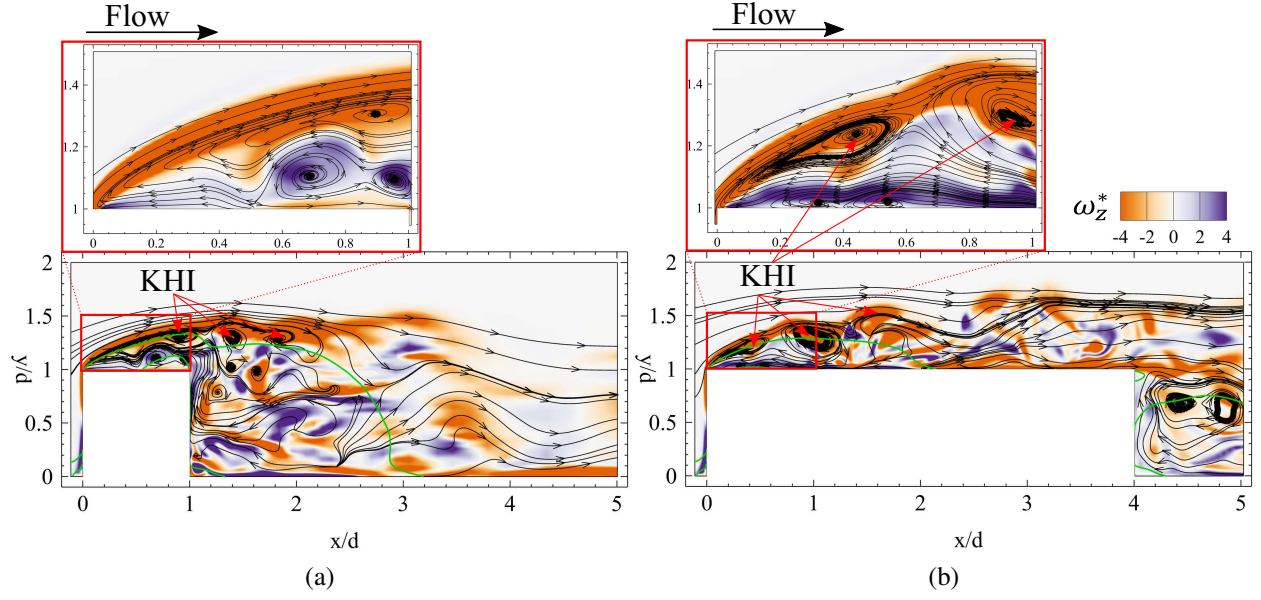


Figure 8.7: Contours of span-wise vorticity, ω_z^* , for (a) $DR = 1$ and (b) $DR = 4$ at Reynolds number of 2.5×10^3 , superimposed with instantaneous streamlines and the isopleth of $\bar{u} = 0$ (bold, green line) at $z/d = 0$.

These observations suggest that flow entrainment is more pronounced near the leading edge for the long prism compared to the short prism.

Instantaneous vortex shedding is closely examined near the leading edge of both prisms, in Figure 8.7, which includes contours of spanwise vorticity (ω_z^*) overlaid with instantaneous streamlines and $\bar{u} = 0$ isopleth at $z/d = 0$. In both cases, the generation of Kelvin-Helmholtz-like vortices from the leading edge is notable. A zoomed-in sub-figure near the leading edge in Figure 8.7 reveals an earlier initiation of Kelvin-Helmholtz instability for $DR = 4$ compared to $DR = 1$, where the instability appears further downstream at $x/d \geq 1$. For the former, streamlines show flow entrainment near the prism top surface, characterized by a region of positive ω_z^* and an upstream trajectory. This entrainment is less pronounced for $DR = 1$. For $DR = 4$, flow entrainment from the primary recirculation bubble impinges on the top surface, leading to the formation of two boundary layers: one moving upstream and the other downstream (Cimarelli et al., 2018). Downstream flow structures predominantly align in the streamwise direction, as shown in Figure 8.6b. Conversely, upstream-moving structures form a strong region of positive

ω_z^* (see Figure 8.7), corresponding to spanwise-aligned flow structures reminiscent of vortex tubes aligned in the spanwise direction. This region of positive ω_z^* may be the source of undulations forming on the vortex tubes near the leading edge. Further investigation is presented later in this chapter.

Onset of Kelvin-Helmholtz instability and subsequent formation of hairpin-like vortices are further analyzed by tracking the downstream trajectory of maximum turbulent kinetic energy (k_{\max}) along the prisms mid-span ($z/d = 0$). Based on the dynamics described in prior studies (Moore et al., 2019a,b), turbulent kinetic energy is expected to increase in amplitude as fluctuations grow downstream of the leading edge. This implies that the trajectory of k_{\max} could align with the path of the leading-edge shear layer and the subsequent vortex shedding. Figure 8.8 shows the downstream trajectory of k_{\max} for both prisms. At $Re = 2.5 \times 10^3$, k_{\max} grows rapidly for both prisms, starting near zero at the leading edge, where flow separation occurs. For $DR = 1$ at $Re = 2.5 \times 10^3$, k_{\max} reaches a maximum in the wake at $x/d \approx 2.8$, after which it saturates and drops. Increasing Reynolds number shifts this saturation point upstream, closer to the prism trailing edge. At higher Reynolds numbers, a secondary peak in k_{\max} appears in the wake, primarily due to the wake interactions (see Figure 8.3c), resulting in increased momentum transport. Similar upstream shifts in the onset of Kelvin-Helmholtz instability at higher Reynolds number have been observed in previous studies, notably by Moore et al. (2019a) and Cimarelli et al. (2024).

For the long prism, a similar trend is observed, where k_{\max} rapidly increasing from near zero at the leading edge towards a maxima close to the shear-layer reattachment location on the top surface. Shift in the peak of k_{\max} is more pronounced for the long prism than the short prism, indicating a more intense growth of turbulence intensities. Following the flow reattachment, k_{\max} decreases moving downstream. Near the leading edge, k_{\max} is significantly higher for long prism compared to the short prism, indicating greater turbulence intensity, consistent with the results in Figures 8.3c and 8.3d. Saturation point of k_{\max} has been linked in previous studies (Moore et al., 2019a) to the onset of Kelvin-Helmholtz instability. This implies that the onset of Kelvin-Helmholtz instability shifts upstream with increasing Reynolds numbers for wall-mounted prisms.

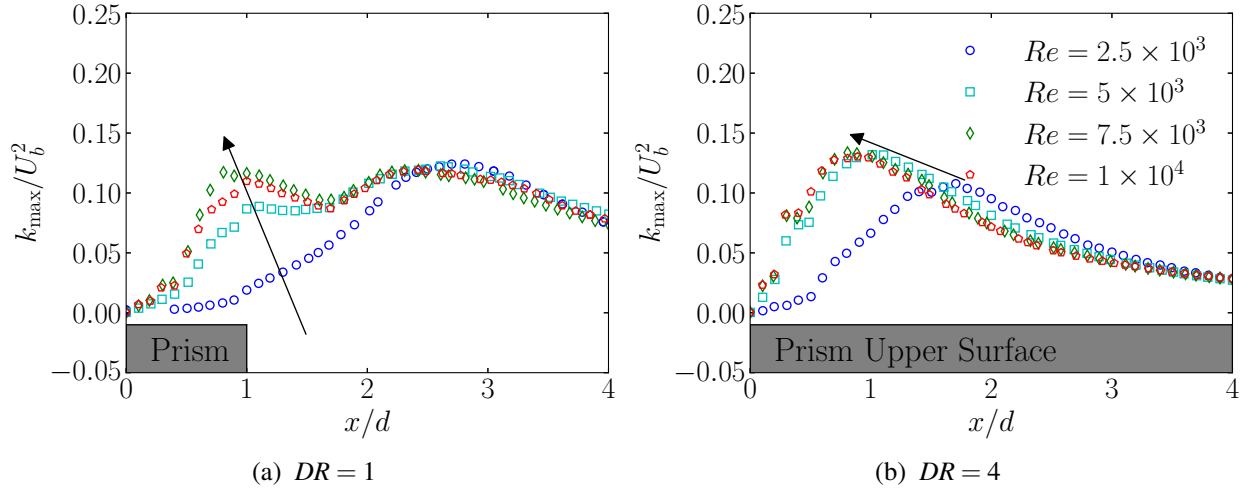


Figure 8.8: Downstream trajectory of maximum turbulence kinetic energy (k_{\max}) along the prism mid-span ($z/d = 0$) for (a) $DR = 1$ and (b) $DR = 4$ prisms. Leading-edge of the prisms (shown in grey) is located at $x/d = 0$.

At higher Reynolds numbers, a self-similarity trend is observed in k_{\max} for both prisms, which is more pronounced for the long prism with trends of k_{\max} converging at $Re = 5 \times 10^3$. Although this trend is not observed for the short prism within the current range of Reynolds numbers, it is reasonable to hypothesize that extending Re beyond 1×10^4 could yield a similar effect, based on analogous behaviors observed in comparable geometries at higher Reynolds numbers (Moore et al., 2019a,b). Self-similarity of k_{\max} at higher Reynolds numbers suggests a Reynolds number invariant behavior, indicating that turbulence intensities are primarily influenced by depth-ratio (prism geometry) at high Re .

Vorticity in the flow is generated under the influence of non-uniform pressure gradient along the prism length, while turbulent kinetic energy is generated by fluctuations in the presence of a mean velocity gradient (Pope, 2001). Integrated turbulent kinetic energy downstream of the leading edge reflects the cumulative amount at any given location, which can be used to quantitatively track the growth of turbulence intensity (Moore et al., 2019a). Figure 8.9 presents the integrated turbulent kinetic energy along the prism mid-span ($z/d = 0$) for both prisms, which shows its rise downstream of the leading edge for both cases. This indicates a substantial turbulence production. Growth rate of turbulent kinetic energy is more pronounced along the long

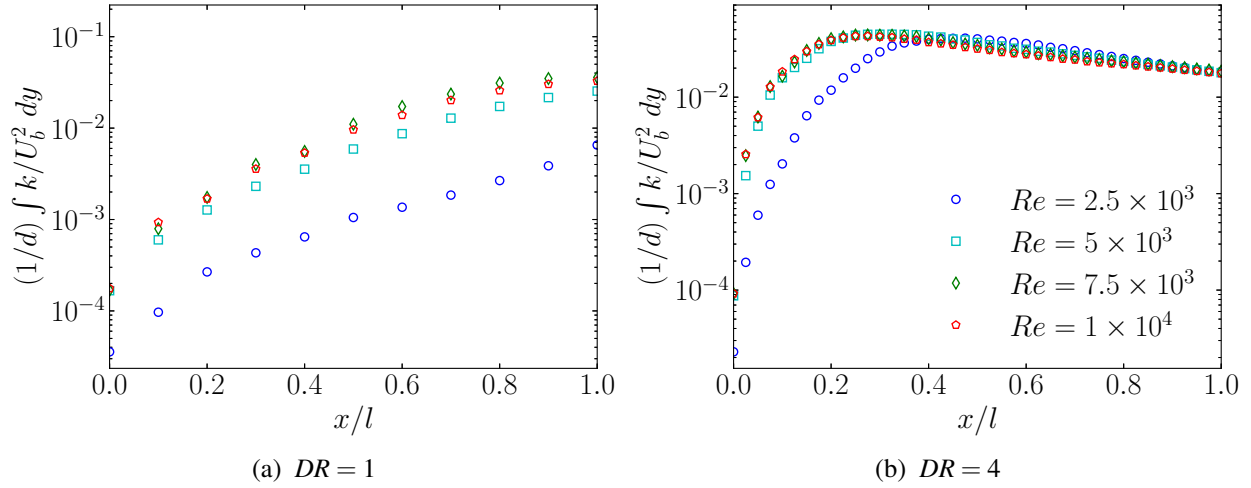


Figure 8.9: Integrated turbulence kinetic energy along the prism mid-span ($z/d =$) for (a) $DR = 1$ and (b) $DR = 4$ prisms. Axial length is normalized by the prism length (l).

prism compared to the short prism, suggesting pronounced flow irregularity. Increased unsteadiness near the leading edges is attributed to flow reattachment on surfaces of the long prism, leading to a rise in turbulence intensity (Figure 8.8b). These results quantitatively indicate that turbulence intensity is significantly higher for the long prism than short prism, highlighting that depth-ratio strongly influences the overall flow unsteadiness.

8.1.3 Flow processes with typical frequencies

Inherent instabilities in the flow give rise to distinct frequencies associated with specific physical flow phenomena. This section investigates flow periodicity and analyzes the flow processes corresponding to these frequencies. Figure 8.10 presents the pre-multiplied power spectral density of streamwise (E_u) velocity fluctuations near the leading edge at $(0.5, 1.3, 0)$ for both prisms. The results show that two dominant frequencies characterize the flow, corresponding to large-scale vortex shedding and Kelvin-Helmholtz instability. Large-scale vortex shedding frequency occurs at $St_{sh} \approx 0.17$ for both prisms, while frequencies of Kelvin-Helmholtz instability are $St_{kh} \approx 0.855$ and 1.290 for $DR = 1$ and 4 , respectively. Similar observations are made at higher Reynolds numbers, where frequencies of large-scale vortex shedding remain

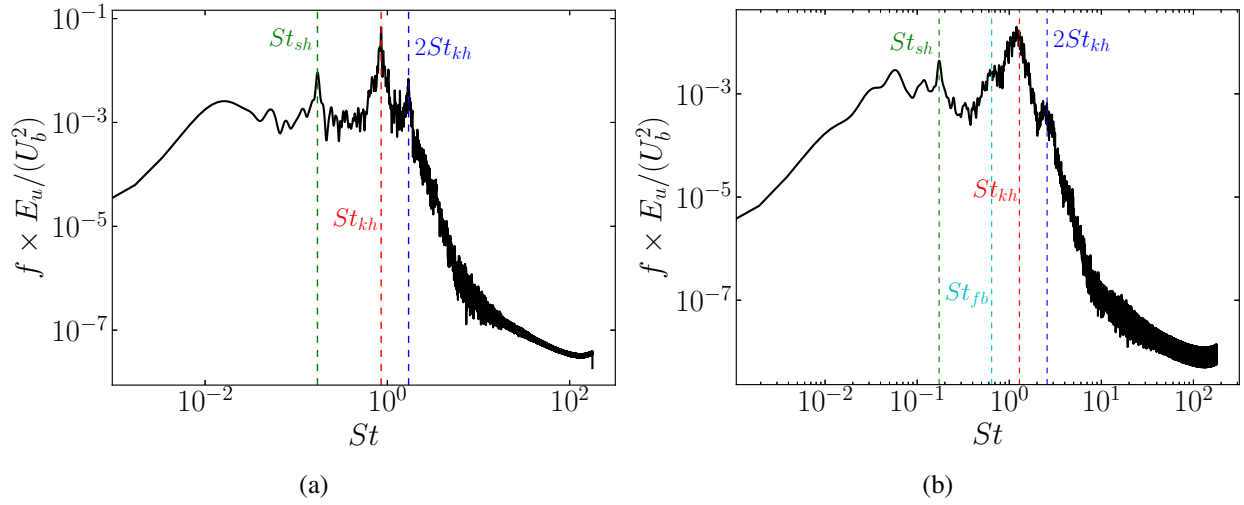


Figure 8.10: Pre-multiplied power spectral density of streamwise (E_u) velocity fluctuations near the leading-edge at $(0.5, 1.3, 0)$ for (a) $DR = 1$ and (b) $DR = 4$.

constant for both prisms, while frequency associated with KHI increases. For larger depth-ratios, frequency of KHI rises, indicating a stronger influence of KHI downstream of the leading edge as was described in Chapter 7. A tertiary frequency, noted at $St_{fb} \approx 0.59$ for the long prism at $Re = 2.5 \times 10^3$, is attributed to the feedback frequency from the secondary recirculation region to the primary recirculation region. Similar fractional harmonics (St_{fb}), corresponding to the feedback of impinging leading-edge shear layer, were observed previously for suspended prisms (Zhang et al., 2023). However, such feedback frequencies have not been reported in the literature for wall-mounted prisms. Therefore, flow mechanisms related to this frequency are further explored here on.

Topological structures corresponding to large-scale vortex shedding and KHI frequencies are next analyzed using Dynamic Mode Decomposition (DMD). Figure 8.11 presents contours of the real part of DMD modes for the streamwise component, corresponding to the shear layer and KHI for short and long prisms at $Re = 2.5 \times 10^3$. Figures 8.11a and 8.11c show structures associated with the large-scale vortex shedding frequency, displaying alternating streamwise structures arranged in a regular pattern. These structures originate near the location of shear-layer reattachment for $DR = 4$ and in the wake for $DR = 1$. Since large-scale vortex shedding mainly

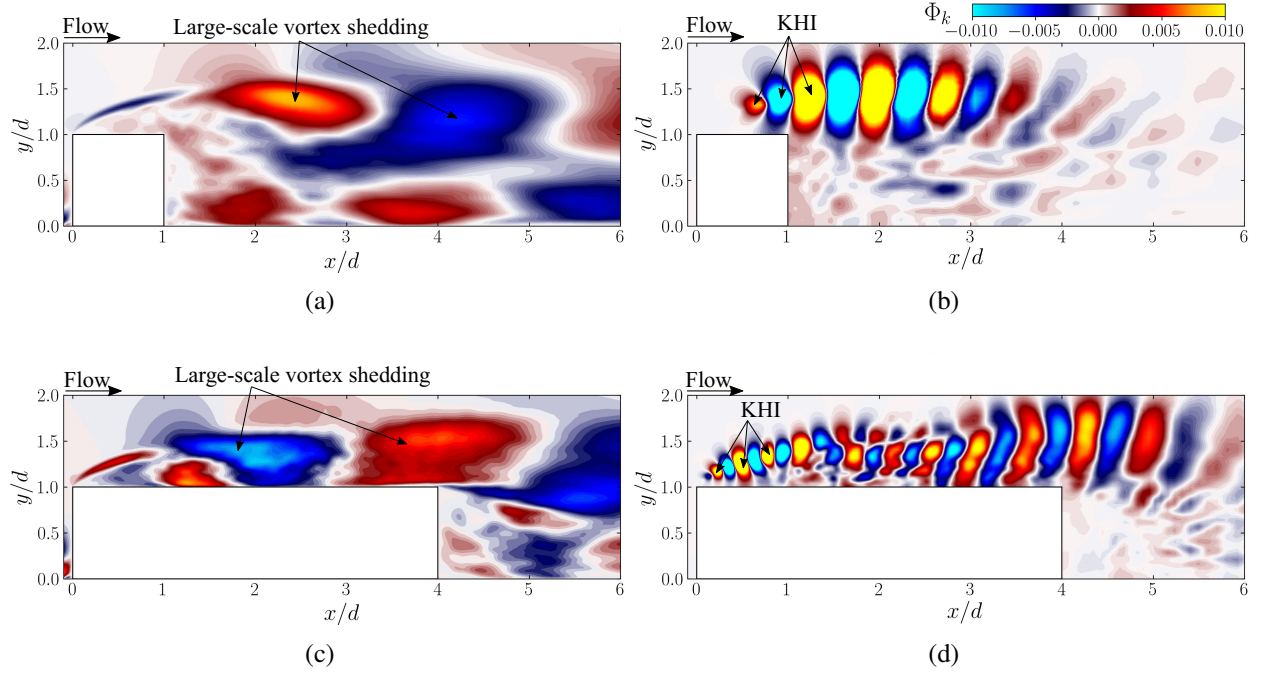


Figure 8.11: Contours of the real part of DMD mode for streamwise component, corresponding to (a,c) shear-layer and (b,d) Kelvin-Helmholtz instability for (a,b) $DR = 1$ and (c,d) $DR = 4$ prism at $Re = 2.5 \times 10^3$.

consists of hairpin-like vortices that shed from the breakdown of the leading-edge shear layer (Zhang et al., 2023), structures in Figures 8.11a and 8.11c correspond to the onset of hairpin-like vortex shedding in the wake. These structures are more pronounced for the long rather than short prisms, indicating a more substantial growth of large-scale vortex shedding for the former.

Figures 8.11b and 8.11d show structures associated with the KHI frequency. These structures feature spanwise vortex tubes aligned in the streamwise direction, shedding from the leading-edge shear layer. In both cases, structures initiate near the leading edge, with the onset of KHI occurring closer to the leading edge for the long prism than for the short prism, consistent with Figure 8.7. For the short prism, KHI structures decay rapidly into the wake and vanish downstream. In contrast, KHI structures persist further downstream and interact with the wake for the long prism. This interaction region is visible in Figure 8.11d for the long prism, where KHI structures engage with the primary recirculation bubble and large-scale vortex shedding. Following this

interaction, KHI structures destabilize and evolve into hairpin-like vortices that shed into the wake. Similar interactions were quantified in Chapter 6, where KHI structures were shown to interact with large-scale vortex shedding.

8.1.4 Mechanism of destabilization of leading-edge shear-layer

Before discussing the mechanism of leading-edge shear layer destabilization, it is helpful to briefly review the main characteristics of separating and reattaching flow over wall-mounted prisms with varying depth-ratios. For a cube ($DR = 1$), the flow is characterized by a shear layer that separates at the leading edge and extends into the wake, as shown in Figure 8.3a. In this case, downstream WR exhibits increased turbulence intensity and large-scale vortex shedding. For a long prism, the flow separates at the leading edge and reattaches on the prism top surface, forming a PR, as illustrated in Figure 8.3b, which features large unsteady fluctuations and spanwise vortex shedding. Shear layer reattachment also generates a SR region beneath the PR, characterized by reverse flow and an upstream-moving boundary layer. Destabilization of the leading-edge shear layer occurs in the PR, leading to the formation of hairpin-like vortices that shed into the wake. Immediately downstream of the leading-edge separation, flow instabilities lead to the formation of spanwise structures, as shown in Figure 8.1b. Interactions between spanwise structures and the strong shear flow (Figure 8.5b) results in a spanwise modulation of vortex structures. This modulation stretches structures in the streamwise direction, forming hairpin-like and streamwise vortices, as observed in Figure 8.6b. Two branches of turbulent structures emerge: one moves downstream as detached fluctuations into the wake, while the other impinges on the wall, moving upstream toward the leading edge and forming the secondary recirculation region.

Destabilization mechanism in long prisms lead to increased flow irregularity and modulation of spanwise vortex structures. Results for the long prism are only considered to retain the focus in this study. The main analysis is performed along the two critical streamlines identified in Figure 8.5b. First critical streamline represents the recirculating flow region formed by the shear-layer reattachment and it will be referred to as the “*recirculating region*”. Looking along

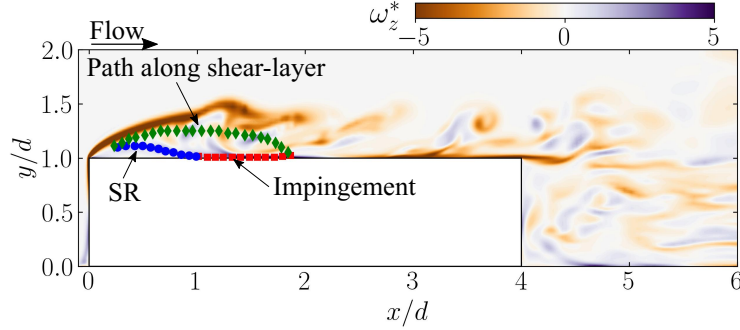


Figure 8.12: Contours of spanwise vorticity (ω_z^*) overlapped with critical streamline representing Recirculating region, at $Re = 2.5 \times 10^3$ for $DR = 4$ prism.

the curvilinear coordinate length (γ), defined by the mean velocity streamline ($\gamma = \int d\gamma$ where $d\gamma = \sqrt{dx^2 + dy^2 + dz^2}$), this path (γ) enables studying flow in PR and SR regions, and interactions between the leading-edge shear layer and the SR region. The second critical streamline, referred to as the “*path following free shear-layer*”, enables analysis of the flow along the free shear-layer and its development towards the free flow.

Path following recirculation region

The critical streamline that represent the recirculating region is shown in Figure 8.12, overlaid with contours of spanwise vorticity (ω_z^*). For easier understanding of the flow dynamics, this recirculating region is divided into three sub-regions: (1) the area between shear-layer separation and reattachment (highlighted in green); (2) the impinging flow region and the branch of flow moving upstream (in red); and (3) secondary recirculation (SR) region below the primary recirculation (PR) region (in blue). Figure 8.13 shows trends of pressure and root-mean-squared velocity fluctuations (u'_{rms} , v'_{rms} , w'_{rms}) along the recirculating region depicted in Figure 8.12. Following flow separation at the leading edge, mean pressure decreases until it reaches the primary vortex core in the PR region at $\gamma' \approx 0.3$. Pressure then rises downstream, peaking at the shear-layer reattachment location ($\gamma' \approx 0.5$) on the prism top surface. This increase in pressure indicates a significant adverse pressure gradient, contributing to the formation of the PR. Beyond this point, pressure drops along the impingement region, moving upstream into the reverse

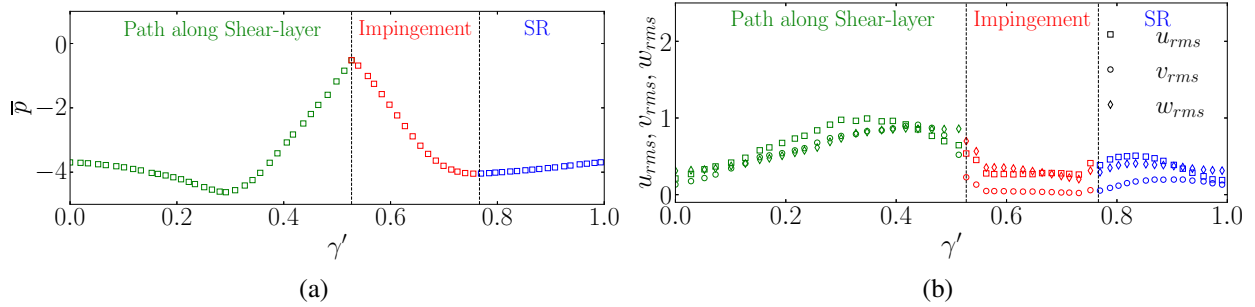


Figure 8.13: Trends of (a) pressure and (b) root-mean-squared velocity fluctuations (u'_{rms} , v'_{rms} , w'_{rms}) along the recirculating region for $DR = 4$ prism at $Re = 2.5 \times 10^3$. γ' represents the normalized curvilinear coordinate length.

boundary layer. Subsequently, mean pressure exhibits a favorable gradient, nearing the free-stream pressure as the flow enters the SR. Here, pressure shows another adverse gradient as it moving back towards the leading edge.

Figure 8.13b shows trends of the root-mean-squared velocity fluctuations (u'_{rms} , v'_{rms} , w'_{rms}). Along the leading-edge shear layer (green symbols), velocity fluctuations increase due to the amplification of instabilities and transition to turbulence (discussed in Chapter 6). Streamwise velocity fluctuations are most prominent here, reaching their maximum near the primary vortex core. Spanwise and normal fluctuations display similar intensities, with slightly larger spanwise fluctuations near the primary vortex core. Following this, normal and streamwise velocity fluctuations drop sharply until flow reattachment at $\gamma' \approx 0.5$, while spanwise fluctuations continue to increase. This results in maximized spanwise fluctuations near the shear-layer reattachment, suggesting the presence of intense spanwise vortex structures in this area. This is evident by the presence of spanwise KHI rollers in Figure 8.1b. In the impingement and reverse boundary layer regions (red symbols), overall velocity fluctuations drop sharply. Along the impingement region ($0.55 \leq \gamma' \leq 0.75$), normal velocity fluctuations become negligible, while streamwise and spanwise fluctuations remain steady. This indicates the formation of intense streamwise and spanwise structures, and the presence of spanwise sweeping of flow structures at impingement. Finally, normal velocity fluctuations increase in the SR (blue symbols), while streamwise and spanwise fluctuations rise sharply until reaching a local maximum near the secondary vortex core.

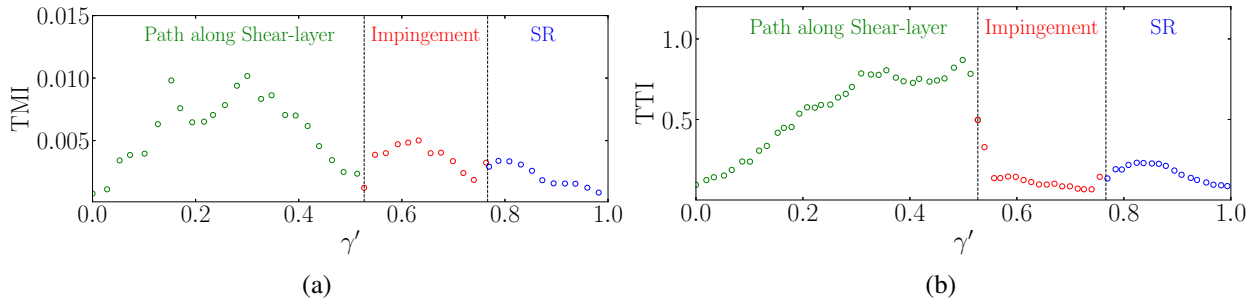


Figure 8.14: Trends of (a) turbulence-mean-shear interaction (TMI) and (b) turbulence-turbulence interaction (TTI) along the recirculating region. γ' represents the normalized curvilinear coordinate length.

Beyond this point, streamwise fluctuations decrease rapidly, while spanwise and normal fluctuations remain steady, closing the loop of the secondary recirculation region.

Pressure fluctuations (p') are influenced by velocity fluctuations (u' , v' , and w') in incompressible flows (Pope, 2001). Poisson's equation links fluctuating velocities with pressure fluctuations. Two terms of Poisson equation, turbulence-mean-shear interaction (TMI) and turbulence-turbulence interaction (TTI), are used to quantify the interactions between the mean flow and turbulence, as well as among turbulent structures, which is essential for analyzing flow irregularity and destabilizing mechanisms in the leading-edge shear layer. A Similar approach was employed in Chapters 6 and 7 to analyze the flow dynamics and interactions in the wake.

Figure 8.14 illustrates the trends of TMI and TTI along the recirculating region. Along the leading-edge shear layer, TMI in Figure 8.14a shows two prominent peaks of equal magnitude, corresponding to the onset of KHI and the primary vortex core, respectively. Since TMI represents the energy influx through mean flow modulation, the first peak at the onset of KHI indicates that energy is injected into the flow by mean flow modulation due to the instability (shown in Chapter 7). The second peak at the primary vortex core signifies that energy is injected into the flow by amplified streamwise and normal velocity fluctuations (evident from Figure 8.13b). Vorticity associated with the shear-layer alters the mean flow in this region, resulting in enhanced momentum transport that was already discussed in Chapter 7. Beyond this, TMI decreases towards the shear layer reattachment point, suggesting energy dissipation through

flow reattachment (Mansour et al., 1988). Similar trends were noted previously in Chapter 7. In the impingement region, TMI exhibits another peak, mainly due to spanwise sweeping of flow structures and heightened spanwise velocity fluctuations (Kumahor and Tachie, 2023). Moving upstream into the SR, TMI shows a local maximum near the secondary vortex core, then decreases toward the leading edge, hinting at the mean flow modulation by the secondary vortex core and consequent energy influx into the flow. The TTI, shown in Figure 8.14b, increases steadily along the leading-edge shear layer, indicating strong interactions of leading-edge shear-layer with downstream turbulent fluctuations. A peak near the primary vortex core suggests that these interactions are most intense downstream of the core. TTI then rises again until the reattachment location, where it sharply drops in the impingement region (symbols in red). This sharp drop, due to the upstream-moving reverse boundary layer, reflects reduced fluctuations along the reverse boundary layer (evident from Figure 8.13b). Finally, TTI rises again near the secondary vortex core into the SR region, indicating that turbulence-turbulence interactions contribute energy to the leading-edge shear layer through mean flow modulation near the secondary vortex core, consistent with TMI trends (see Figure 8.14a).

To analyze energy transfer along the recirculating region, Figure 8.15 presents trends of turbulence kinetic energy production (P_k), dissipation (ε_k) and convection (C_k) along this region. Turbulence kinetic energy production (Pope, 2001) is defined as

$$P_k = -(\overline{u'_i u'_j} - 2\overline{v_\tau S_{ij}}) \frac{\partial \overline{u_i}}{\partial x_j},$$

dissipation is defined as

$$\varepsilon_k = 2\overline{\tau_{ij}^{SGS} S_{ij}} + 2\overline{v_\tau S_{ij} S_{ij}}$$

and convection is defined as

$$C_k = \frac{1}{2}\overline{u_i} \frac{\partial \overline{u'_i u'_i}}{\partial x_i}.$$

As anticipated, P_k rises along the leading-edge shear layer, reaching a maximum at the point of peak streamwise velocity fluctuations (see Figure 8.13b). Following this peak, P_k experiences a

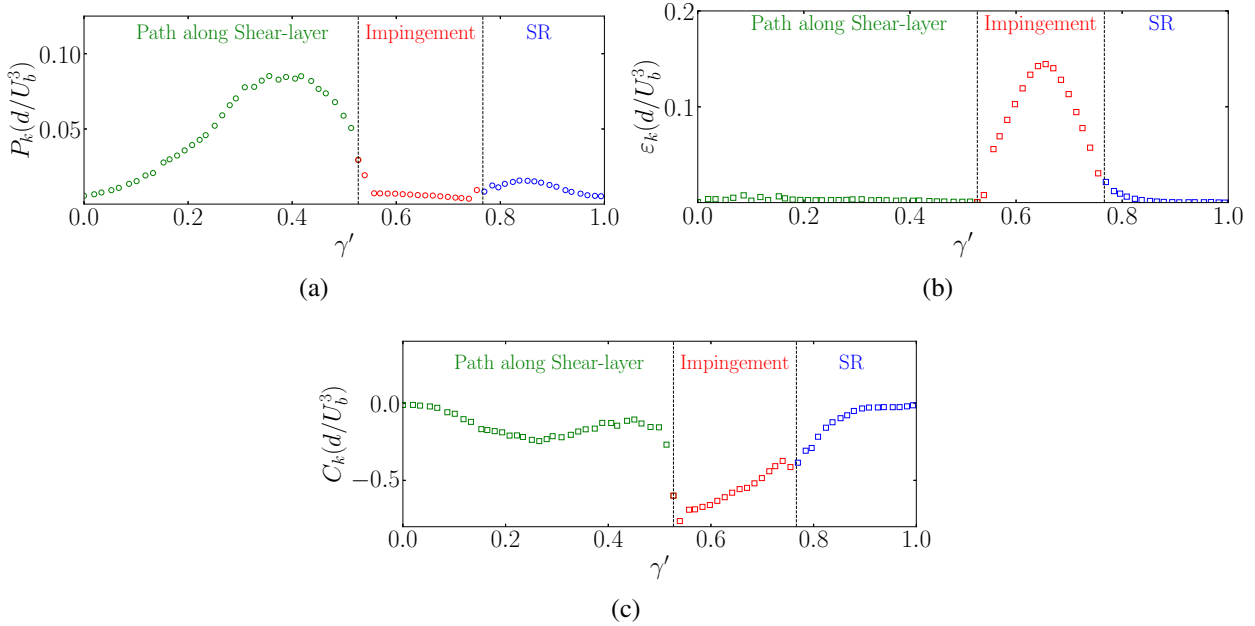


Figure 8.15: Trends of (a) turbulence kinetic energy production (P_k), (b) turbulent dissipation (ε_k) and (c) convection (C_k) along the recirculating region. γ' represents the normalized curvilinear coordinate length. Quantities are normalized by the free-stream velocity and prism width.

sharp drop and then exhibits steady production along the impingement region, consistent with expected trends from velocity fluctuations and mean shear stress. In the impingement region, mean shear stress ($\frac{\partial \bar{u}}{\partial y}$) decreases while streamwise and spanwise velocity fluctuations remain relatively constant, resulting in lower P_k . Further, profiles of ε_k suggests that energy is dissipated through flow impingement and the reverse boundary layer. Chiarini and Quadrio (2021) made similar observations, where large values of dissipation occurs in the core of PR. Intuitively, amplified dissipation in the reverse boundary layer confirms the larger degree of universality for the dissipative phenomena near a wall (Mansour et al., 1988). A peak of P_k is observed in SR, which is consistent with the amplified turbulence-turbulence interactions and velocity fluctuations. This indicates that energy is produced within SR. The convection profile (C_k) along SR shows a steady increase, suggesting that energy is transported upstream. Given the adverse pressure gradient and amplified convection in SR, turbulent fluctuations are able to reach the leading-edge shear-layer, thus completing the cycle.

Figure 8.16a shows the pre-multiplied power spectral density of streamwise velocity fluctuations (E_u) along the SR, in the detached reverse flow region at $(0.5d, 1.05d, 0)$. Figure 8.16a indicates a distinct frequency corresponding to the feedback frequency (St_{fb}) observed earlier. Higher frequency peak is evident at St_{kh} and sub-harmonics of St_{fb} are noted, however, the peak in premultiplied frequency spectrum at $St_{fb} \approx 0.59$ is most prominent. The probability density function of the mean streamwise velocity along the SR region (Figure 8.16b) reveals strong upstream advection characterized by a negative mean streamwise velocity. This finding further supports the upstream convection of energy by flow structures at the feedback frequency along the SR region. The long negative tail of the probability density function suggests rare but strong reverse flow events in this region, which are associated with the upstream transfer of energy generated in the SR. Since St_{fb} is much lower than the frequency of KHI, flow structures in the SR tend to cluster and amplify, as evidenced by the high probability of near-zero mean streamwise velocity. These clusters then move upstream toward the leading edge, contributing to the destabilization of the leading-edge shear layer. A vortex reconnection phenomenon is also anticipated (Cimarelli et al., 2018), where streamwise vortices stretch in the spanwise direction due to the feedback effect. This is consistent with the stronger spanwise velocity fluctuations along the SR (Figure 8.13b), and the lower streamwise fluctuations. Finally, Figure 8.17a shows contours of streamwise velocity fluctuations (u'), revealing feedback effects near the SR. Here, a region of negative streamwise velocity fluctuations is evident in the SR. The DMD mode corresponding to St_{fb} is presented in Figure 8.17b, illustrating streamwise vortices that signal feedback from the SR into the leading-edge shear layer.

Streamline following free shear-layer

The critical streamline representing the path following free shear-layer is shown in Figure 8.18. Similar to the recirculating region, path following free shear-layer is divided into three sub-regions: (1) the area following the leading-edge shear layer up to the flow reattachment on the prism surface (highlighted in green), (2) the flow along the attached boundary layer (in red) and

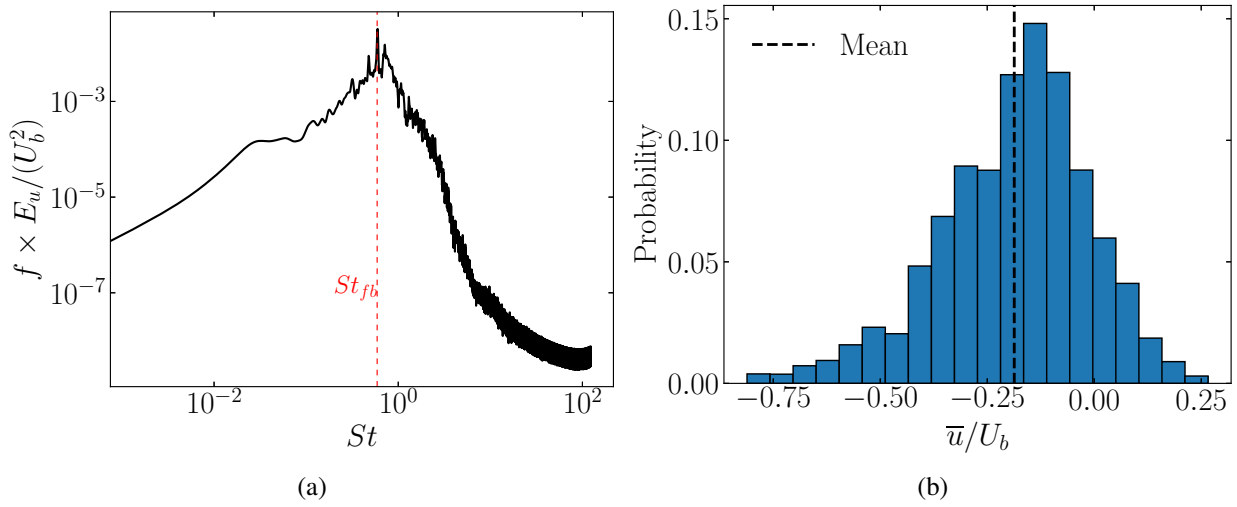


Figure 8.16: (a) Pre-multiplied power spectral density of streamwise velocity fluctuations (E_u) in SR, at $(x, y, z) = (0.5d, 1.05d, 0)$, and (b) probability density function of mean streamwise velocity (\bar{u}) along the secondary recirculation region.

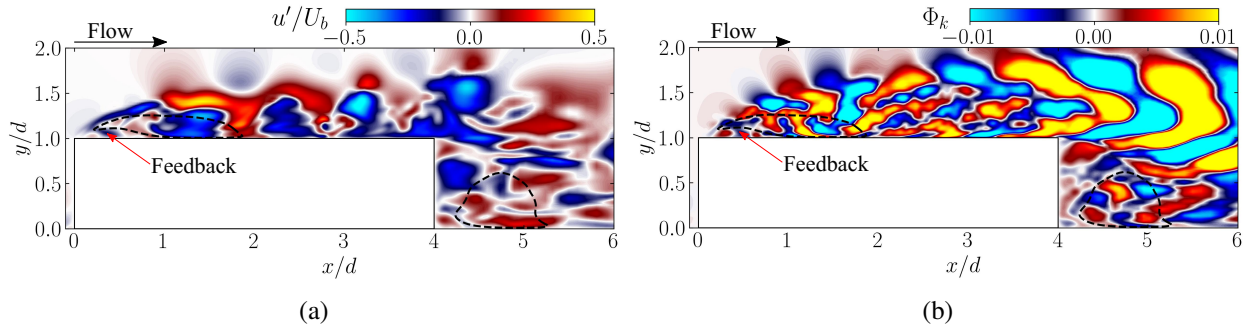


Figure 8.17: (a) Streamwise velocity fluctuation (u') showing feedback near SR region; and (b) Contours of the real part of DMD mode for streamwise component corresponding to feedback frequency (St_{fb}), for $DR = 4$ prism at $Re = 2.5 \times 10^3$.

(3) flow development in the wake of $DR = 4$. Similar to the recirculating region, analyzing the path following free shear-layer provides insights into the first branch of turbulent flow structures emerging from the leading-edge shear layer and moving downstream into the wake.

Evolution of pressure and root-mean-squared velocity fluctuations ($u'_{rms}, v'_{rms}, w'_{rms}$) along the path following free shear-layer are shown in Figure 8.19. Mean pressure along the shear-layer path (shown in green) aligns with the corresponding section in the recirculating region. Initially, pressure decreases up to the location of the primary vortex core, then increases due to the adverse

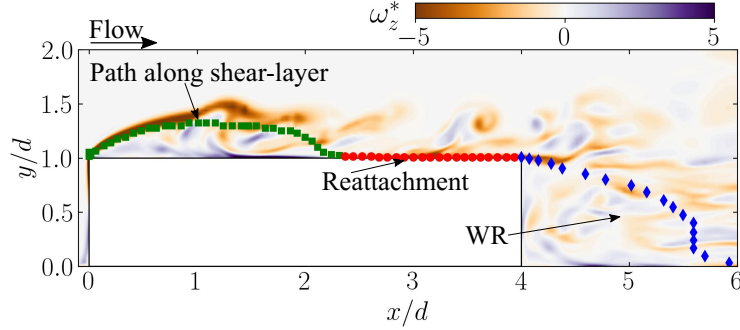


Figure 8.18: Contours of spanwise vorticity (ω_z^*) overlapped with critical streamline representing the path following free shear-layer, at $Re = 2.5 \times 10^3$ for $DR = 4$ prism.

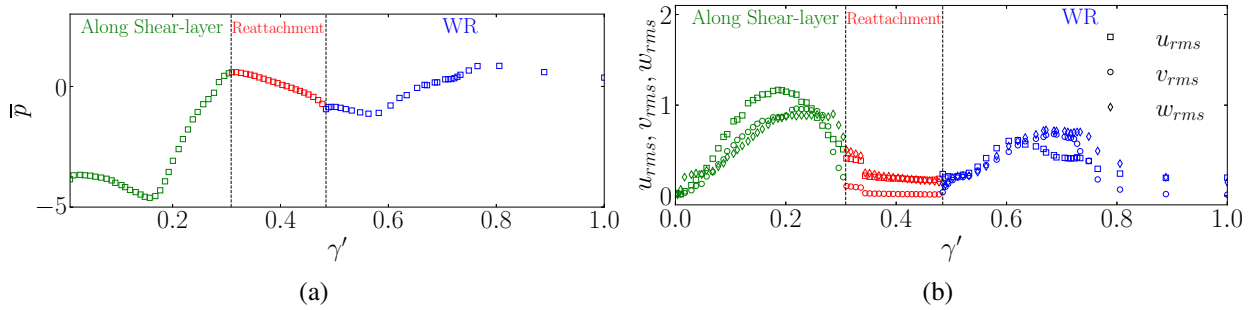


Figure 8.19: Trends of (a) pressure and (b) root-mean-squared velocity fluctuations (u'_{rms} , v'_{rms} , w'_{rms}) along the path following free shear-layer for $DR = 4$ prism at $Re = 2.5 \times 10^3$. γ' represents the normalized curvilinear coordinate length.

pressure gradient until shear-layer reattachment on the prism surface. This adverse gradient is sustained in the attached boundary-layer region (shown in red), followed by a slight reduction due to a favorable pressure gradient extending to the trailing edge. This favorable gradient continues into the WR (blue), where it reaches a local minimum before returning to its free stream value downstream. Turbulence intensities in Figure 8.19b increase along the leading-edge shear layer, following trends observed in the recirculating region. Instabilities amplify in this region, leading to shear-layer roll-up and the formation of spanwise vortex structures. Near the reattachment point, turbulence intensities drop sharply until normal velocity fluctuations become negligible in the attached boundary layer. As the boundary layer develops downstream and detaches at the trailing edge, turbulence intensities increase. In WR, turbulence fluctuations grow further due to mixing and interactions between spanwise and normal flow structures in the recirculating flow.

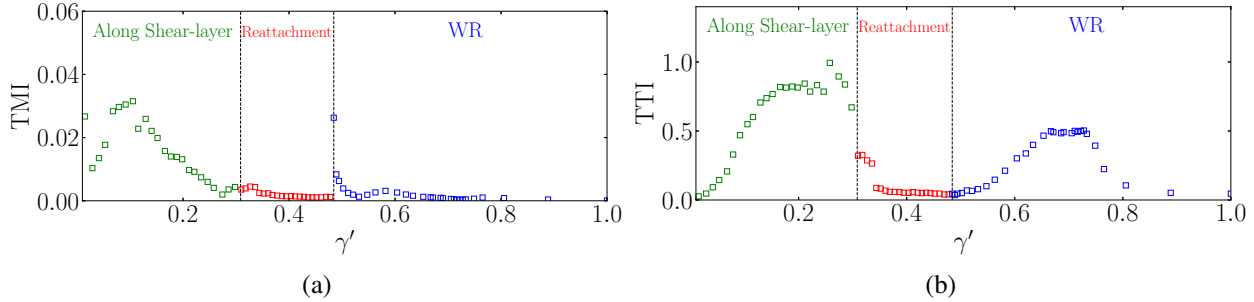


Figure 8.20: Trends of (a) turbulence-mean-shear interaction (TMI) and (b) turbulence-turbulence interaction (TTI) along the path following free shear-layer. γ' represents the normalized curvilinear coordinate length.

To further examine mean flow modulation and turbulent flow interactions, TMI and TTI along the path following free shear-layer are shown in Figure 8.20. As anticipated, TMI increases to its maximum near the secondary vortex core. Since the SR convects energy upstream into the leading-edge shear layer, mean flow modulation occurs closer to the leading edge, as indicated by the TMI peak. Following this peak, TMI drops sharply as the flow reattaches to the prism surface. Due to the negligible velocity fluctuations in the attached boundary-layer region (shown in red), mean flow modulation is also minimal until the flow separates again at the trailing edge. A local maximum is observed right at the trailing-edge separation point, decreasing significantly into the WR and downstream. WR is primarily characterized by spanwise and normal flow variations (Kumahor and Tachie, 2023), which is evident from the profiles in Figure 8.19b. Thus, mean flow modulation is minimal here, as turbulence intensities are largely driven by the mixing of spanwise and normal flow structures (Chiarini and Quadrio, 2021). As expected, TTI (in Figure 8.20b) rises along the shear layer, reaching its peak, and then decreasing again upon flow reattachment to the prism surface. Turbulent interactions are minimal along the attached boundary layer and increase again in the WR. Due to the mixing and interaction of flow structures along WR, turbulence-turbulence interactions intensify, promoting the growth of turbulence intensities in this area.

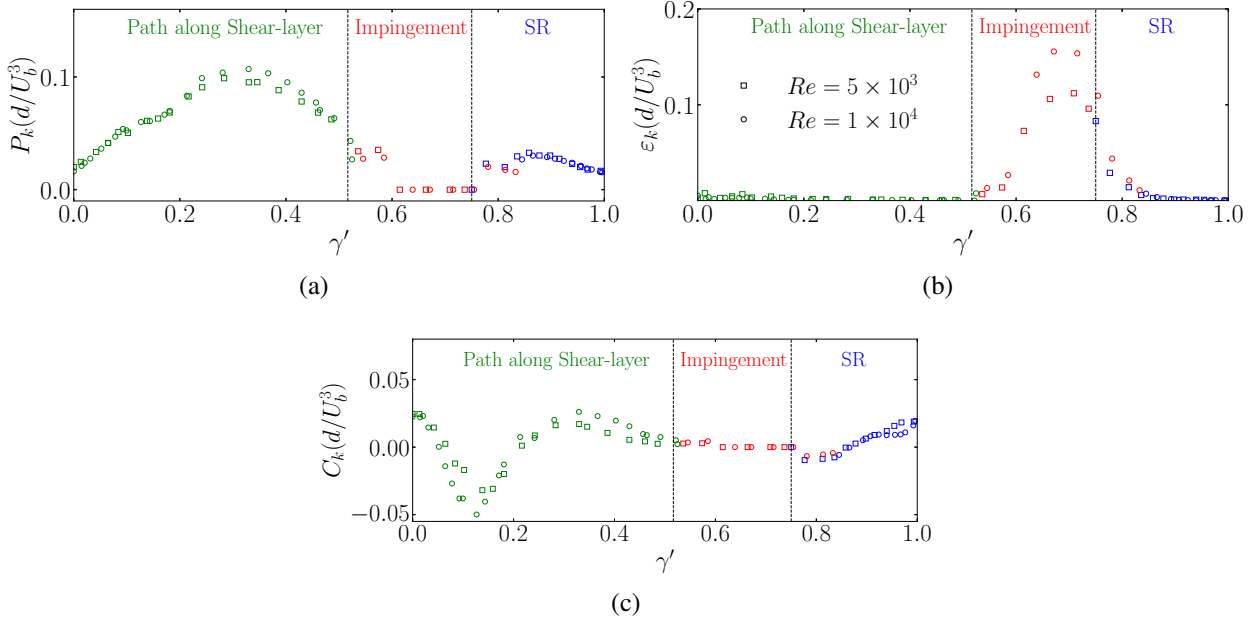


Figure 8.21: Trends of (a) turbulence kinetic energy production (P_k), (b) turbulent dissipation (ε_k) and (c) convection (C_k) along the recirculating region for (\square) $Re = 5 \times 10^3$ and (\circ) 1×10^4 . γ' represents the normalized curvilinear coordinate length. P_k and C_k are normalized by the free-stream velocity and prism width.

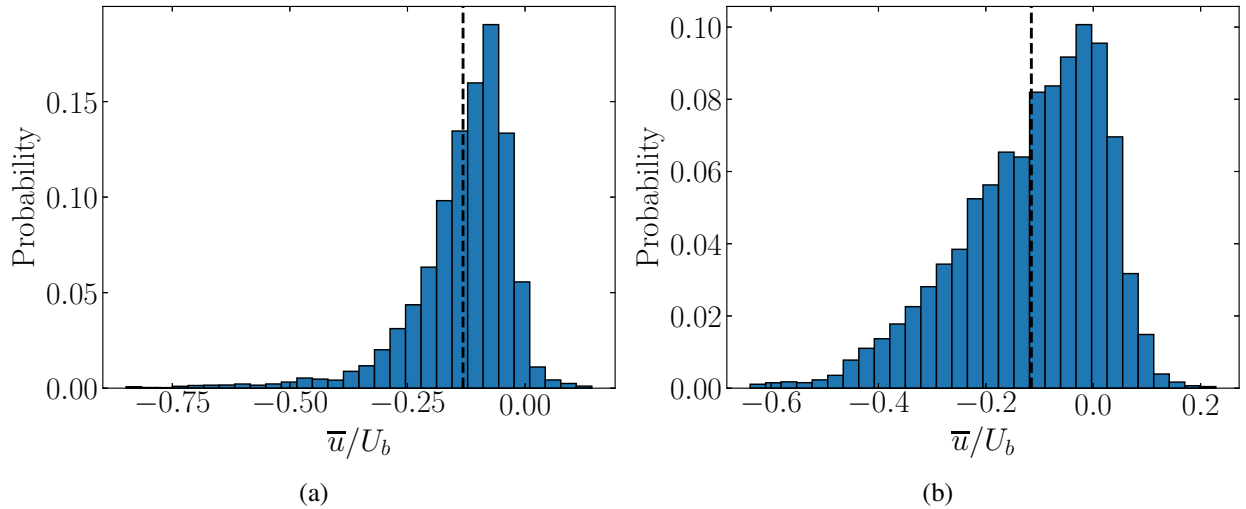


Figure 8.22: Probability density function of mean streamwise velocity (\bar{u}) along the secondary recirculation region for (a) $Re = 5 \times 10^3$ and (b) 1×10^4 . Dashed line represents the mean streamwise velocity.

8.1.5 High Reynolds number flow

Destabilization mechanism described above persists at higher Reynolds numbers, which is apparent from the results at $Re = 5 \times 10^3$ and $Re = 1 \times 10^4$. Figure 8.21 shows the trends of P_k and C_k along the recirculating region at $Re = 5 \times 10^3$ and $Re = 1 \times 10^4$, which align with those observed at $Re = 2.5 \times 10^3$. Specifically, P_k is most pronounced along the leading-edge shear layer and sharply decreases after the shear-layer reattachment, where energy dissipates (evident from Figure 8.21b) and turbulence intensities drop notably in the impingement region. Additionally, P_k exhibits a secondary peak near the location of the secondary vortex core, signifying energy production by the secondary recirculation region. The energy convection trends match the production patterns, showing that energy is carried upstream by flow structures. The probability density function of mean streamwise velocity (\bar{u}) in the SR for $Re = 5 \times 10^3$ and $Re = 1 \times 10^4$ is presented in Figure 8.22. These trends are consistent with those observed at $Re = 2.5 \times 10^3$, indicating rare yet intense upstream convection events of flow structures. Such events amplify energy within the SR region and are expected to cluster and propagate upstream toward the leading edge, contributing to destabilization of the leading-edge shear layer.

8.2 Summary

Destabilization mechanism of leading-edge shear-layer and the onset of Kelvin-Helmholtz instability were evaluated at high Reynolds numbers ($Re = 2.5 \times 10^3$, 5×10^3 , and 1×10^4) for the cases of $AR = 0.25 - 1.5$ and $DR = 1 - 4$. Wake unsteadiness enhanced with increasing depth-ratio, and KHI was noted for all cases, forming finite spanwise vortex rollers. Moreover, depth-ratio influenced the intensity of mean-shear experienced by the downstream flow, significantly impacting the inception and evolution of hairpin-like vortices in the wake. The onset of KHI closer to the leading-edge for long prisms ($DR \geq 3$) resulted in the shear-layer roll-up and spanwise elongated vortex structures appearing on the prisms surfaces. At higher Reynolds numbers, the onset of KHI shifted upstream and closer to the leading-edge, maximizing

turbulence kinetic energy and the accumulation of energy, leading to enhanced flow irregularity for long prisms. Furthermore, destabilization of the leading-edge shear-layer was investigated quantitatively by focusing on the recirculating region and the path following free shear-layer. The results highlighted the crucial role of secondary recirculation regions in modulating flow structures and facilitated upstream convection of energy, which in turn destabilized the leading-edge shear-layer. Flow structures in SR were clustered due to vortex reconnection, and thus amplified. A feedback mechanism was noted, where the clustered and energized structures moved upstream towards the leading-edge, transferring energy into the leading-edge shear-layer and resulting in its destabilization. Turbulence kinetic energy production and convection distributions revealed that the destabilization process was closely related to energy production in both primary and secondary recirculation zones. Here, energy was produced by the secondary recirculation and convected upstream, driving further instability. Probability density functions revealed the presence of rare and intense upstream convection events, which amplified turbulence and facilitated the destabilization process, regardless of Reynolds number. Thus, this study quantified the impact of secondary vortex interactions, feedback mechanism, and vortex reconnection phenomena in enhancing turbulence intensities, which ultimately led to the shear-layer destabilization and flow separation.

Chapter 9

CONCLUSIONS

This dissertation identified and characterized the mechanisms that govern flow transitions and vortex interactions around wall-mounted prisms. In this study, a total of 310 three-dimensional, high-fidelity numerical simulations were conducted to investigate the wake dynamics and vortex interactions. These simulations were performed using OpenFOAM CFD toolbox. Simulations varied across a range of depth-ratios, aspect-ratios and Reynolds numbers, providing a comprehensive dataset to analyze and understand the wake dynamics of wall-mounted bluff bodies. The main objective of this study was to advance the community's understanding of wake evolution and dynamics using numerical simulations of wakes. Specifically, the focus was on the influence of depth-ratio (*DR*) on vortex dynamics and wake interactions in finite prisms. The dissertation addressed four key research areas: (A) Classification of wake topology as a multivariate function of depth-ratio and Reynolds number; (B) Characterization of interactions between secondary vortex structures and leading-edge shear-layer roll-up; (C) Investigation of the role of depth-ratio in interactions between Kelvin-Helmholtz instability (KHI) and hairpin-like vortices; and (D) Identification of the mechanism of destabilization of the leading-edge shear-layer at moderate Reynolds numbers.

Wake analyses across a range of Reynolds numbers and depth-ratios revealed that the threshold Reynolds number for unsteady wake transition increased with larger depth-ratios. For

small depth-ratio prisms ($DR = 0.016$ and 0.1), the wake exhibited unsteady behavior. At $DR = 0.016$, the wake featured asymmetrically arranged hairpin-like vortex shedding, whereas for $DR = 0.1$, the hairpin-like structures became symmetrically organized, indicating that flow symmetry was restored with increasing depth-ratio. The mean wake features an arch-type structure forming due to shear-layer roll-up behind the prism. A clear evolution was observed in the wake characteristics. Symmetric to asymmetric transitions occurred with increasing Reynolds number. Wake topology was classified into three regimes with wake evolutions governed by both depth-ratio and Reynolds number: steady, asymmetric, and symmetric. For $DR \geq 0.3$, the wake was steady, with a dominant downwash flow replacing the previously strong upwash flow observed in smaller depth-ratio prisms. For prisms with $DR \geq 0.3$, the flow separated at the prism leading edge, followed by shear-layer reattachment along the side and top surfaces, producing a steady wake. Large depth-ratio prisms exhibited intensified downwash flow near the trailing edge, entraining the flow into the wake. At low Reynolds numbers, unsteady wake evolution was driven by the amplified downwash flow as depth-ratio increased, emphasizing the multivariate dependence of wake topology on depth-ratio and Reynolds number.

A unique asymmetric wake pattern emerged at lower depth-ratios starting at Reynolds number of 2.5×10^2 . This pattern evolved into a symmetric wake with increasing depth-ratio. The asymmetric wake developed due to alternate shear-layer peel-off from either side of the prism, driven by the out-of-phase shedding of tip vortices at a lower Strouhal number ($St_{sh}/2$). This shedding interacted with the detaching side shear layers, resulting in a momentum imbalance, where the side that exhibited a stronger shear-layer (larger circulation) tilted the separating hairpin vortex on that side. A phase difference of π was observed, indicating alternate tip-vortex shedding. In turn, it generated secondary vortex structures fueled by excess vorticity from detaching side shear layers. With increasing depth-ratio, simultaneous shedding of tip vortices restored the symmetric wake pattern. Dynamic Mode Decomposition (DMD) analysis identified two key frequencies including, dominant frequency associated with the shedding of hairpin-like structures and the sub-harmonic frequency ($St_{sh}/2$) responsible for distorting heads of the

hairpin-like vortices. Results showed that secondary vortex structures and wake asymmetry primarily developed at small depth-ratios with increasing Reynolds number. At higher Reynolds numbers and depth-ratios, interaction of shed structures with detaching shear layers resulted in near-wake incoherence and the presence of multiple sub-harmonic and harmonic frequencies. Further, stronger interactions between secondary vortex structures and separating shear layers caused a more disorganized distribution of downstream wake structures.

This study also examined the influence of depth-ratio on interactions between KHI and large-scale vortex shedding at moderate Reynolds numbers ($1 \times 10^3 - 2.5 \times 10^3$). The findings revealed the presence of distinct KHI rollers originating from the leading-edge shear layer, intensity and frequency of which increased for higher depth-ratios. Increasing depth-ratio amplified vortex shedding, particularly the high-frequency KHI rollers in the wake. Larger depth-ratio prisms ($DR \geq 3$) exhibited pronounced interactions between KHI rollers and coherent wake structures, resulting in a more intricate wake system. This was evidenced by an increased number of KHI rollers and intense spanwise vortical motion. For larger depth-ratio prisms, a flapping motion of the shear-layer led to an oscillating reattachment point on the prism surfaces. The top-surface shear layer was quantified to be the primary source of pressure fluctuations, driven by interactions between KHI rollers and coherent wake structures. Enhanced pressure fluctuations amplified velocity fluctuations, further increasing the momentum transport and contributing to a more complex wake topology.

This study further investigated the mechanism of turbulence transition for increasing depth-ratio. The role of depth-ratio in amplifying wake irregularity was highlighted, which facilitated the onset of turbulence. Increasing depth-ratio resulted in significantly higher turbulence kinetic energy, with an increase of $\approx 90\%$ near the leading edge. Heightened turbulence kinetic energy was accompanied by the emergence of irregular, unsteady vortex shedding. The unsteady shear layer exhibited flapping-like motion, driven by interactions between KHI and large-scale vortex shedding. These interactions enhanced the momentum transport, resulting in increased turbulence intensity and mixing, which accelerated the wake transition

process. For prisms with larger depth-ratios, KHI-induced vortices interacted more frequently with large-scale wake structures, intensifying flow fluctuations and producing irregular wake patterns. These intensified interactions modified the frequency and coherence of vortex shedding, revealing a complex coupling mechanism with KHI-driven instabilities amplifying interactions between the shear layer and large-scale wake dynamics. This mechanism was identified as a key driver of the transition to turbulence, marking a shift from regular to irregular wake behaviors.

Mechanisms of the leading-edge shear layer destabilization and the onset of KHI were evaluated for high Reynolds numbers ($2.5 \times 10^3 - 1 \times 10^4$). The results revealed key changes in the behavior of long prisms at higher Reynolds numbers, where the onset of KHI occurred closer to the leading edge of the prism, particularly for prisms with $DR \geq 3$. This shift resulted in maximization of turbulence kinetic energy and an increase in flow irregularity, as the accumulation of energy intensified. Distributions of turbulence kinetic energy production and convection indicated that the destabilization process was closely linked to energy production in both primary and secondary recirculation regions. Destabilization of the leading-edge shear layer was primarily driven by the upstream convection of energy from the secondary recirculation region. In this region, flow structures were clustered due to a vortex reconnection phenomenon, which amplified the flow energy. The energy was then transferred to the leading-edge shear layer through a feedback mechanism, triggering its destabilization, which further drove wake instability.

Chapter 10

FUTURE WORK

The key findings from this thesis have provided substantial insight into the wake dynamics of wall-mounted prisms across a range of Reynolds numbers and geometrical parameters. Through Direct Numerical Simulations (DNS) and Large Eddy Simulations (LES), this research has uncovered the multivariate interactions between depth-ratio, Reynolds number, and flow structures like Kelvin-Helmholtz instabilities and hairpin-like vortices. Notably, the investigation has shown the critical role of depth-ratio in determining the wake dynamics behind wall-mounted prisms. However, while this research has deepened understanding of wake behavior under specific conditions, notable gaps remain. For instance, the precise influence of other geometrical parameters, such as variations in the free-end shape and surface roughness, were not fully explored. Similarly, the wake dynamics at high Reynolds numbers, which are relevant to many practical applications, have yet to be investigated in detail. Moreover, the role of wall effects, secondary flows, and instabilities beyond the range studied here may provide additional insights into the wake formation mechanisms.

This chapter outlines several potential avenues for future research, aiming to address these gaps and expand upon the findings presented in this thesis. These suggestions are intended to guide future investigations into the wake dynamics of wall-mounted prisms, with the goal of enhancing

our understanding of the flow physics and improving the predictive capabilities of wake models. The avenues for future work are as follows:

1. **Higher Reynolds Number Investigations:** While this thesis focused on Reynolds numbers up to 1×10^4 , future work could extend the analysis to higher Reynolds numbers, especially in the turbulent regime (e.g., $Re > 1 \times 10^4$). This could provide insight into more complex turbulent wake patterns and the role of depth-ratio in fully developed turbulence.
2. **Investigation of Free-End Effects:** The free-end flow effects on wake dynamics were briefly touched on in this thesis, but a more detailed investigation of free-end vortices at higher Reynolds numbers would shed light on the role of end conditions and finite geometry on flow behavior. This could include investigating the variations in free-end surface geometry and boundary-layer characteristics.
3. **Unsteady Flow and Active Control:** Future studies could focus on actively controlling the unsteady wake patterns, such as using oscillating control surfaces or surface actuators, to mitigate the wake irregularity and enhance aerodynamic performance. This is particularly relevant for engineering applications like drag reduction and noise control in bluff body designs. Previous work by (Rastan et al., 2019) has demonstrated the effectiveness of active flow control in reducing wake-induced drag and noise.
4. **Data-Driven Modeling and Machine Learning:** Leveraging machine learning and data-driven approaches could be an effective way to model and predict wake transitions, especially for complex interactions between Kelvin-Helmholtz instability and large-scale vortex shedding. Data-driven reduced-order models could help in developing efficient predictive tools for flow dynamics in real-time applications. Further, employing novel methods such as Fourier-Averaged Navier-Stokes (FANS) (Freeman et al., 2024) or deep learning-based flow prediction (Ling et al., 2016) could provide valuable insights into the wake dynamics of wall-mounted prisms.

Bibliography

- Adrian, R. J. (2007). Hairpin vortex organization in wall turbulence. *Physics of Fluids*, 19(4):041301.
- Akhtar, I., Nayfeh, A. H., and Ribbens, C. J. (2009). On the stability and extension of reduced-order galerkin models in incompressible flows. *Theoretical and Computational Fluid Dynamics*, 23(3):213–237.
- Awasthi, M., Devenport, W. J., Glegg, S. A., and Forest, J. B. (2014). Pressure fluctuations produced by forward steps immersed in a turbulent boundary layer. *Journal of Fluid Mechanics*, 756:384–421.
- Bai, H. and Alam, M. M. (2018). Dependence of square cylinder wake on reynolds number. *Physics of Fluids*, 30(1).
- Balachandar, R. (1990). *Characteristics of separated flows including cavitation effects*. PhD thesis, Concordia University.
- Barkley, D. and Henderson, R. D. (1996). Three-dimensional floquet stability analysis of the wake of a circular cylinder. *Journal of Fluid Mechanics*, 322:215–241.
- Baskaran, A. and Kashef, A. (1996). Investigation of air flow around buildings using computational fluid dynamics techniques. *Engineering Structures*, 18(11):861–875.
- Behera, S. and Saha, A. K. (2019). Characteristics of the flow past a wall-mounted finite-length square cylinder at low reynolds number with varying boundary layer thickness. *Journal of Fluids Engineering*, 141(6):061204.
- Berger, E., Scholz, D., and Schumm, M. (1990). Coherent vortex structures in the wake of a sphere and a circular disk at rest and under forced vibrations. *Journal of Fluids and Structures*, 4(3):231–257.
- Blasius, H. (1950). *The boundary layers in fluids with little friction*. Number 1256. National Advisory Committee for Aeronautics.
- Bloor, M. S. (1964). The transition to turbulence in the wake of a circular cylinder. *Journal of Fluid Mechanics*, 19(2):290–304.
- Boersma, B. J., Brethouwer, G., and Nieuwstadt, F. T. (1998). A numerical investigation on the effect of the inflow conditions on the self-similar region of a round jet. *Physics of fluids*, 10(4):899–909.

- Bourgeois, J., Sattari, P., and Martinuzzi, R. (2011). Alternating half-loop shedding in the turbulent wake of a finite surface-mounted square cylinder with a thin boundary layer. *Physics of Fluids*, 23(9):095101.
- Bradshaw, P. and Wong, F. (1972). The reattachment and relaxation of a turbulent shear layer. *Journal of Fluid Mechanics*, 52(1):113–135.
- Brun, C., Aubrun, S., Goossens, T., and Ravier, P. (2008). Coherent structures and their frequency signature in the separated shear layer on the sides of a square cylinder. *Flow, turbulence and combustion*, 81:97–114.
- Cannon, S., Champagne, F., and Glezer, A. (1993). Observations of large-scale structures in wakes behind axisymmetric bodies. *Experiments in Fluids*, 14(6):447–450.
- Cantwell, B. and Coles, D. (1983). An experimental study of entrainment and transport in the turbulent near wake of a circular cylinder. *Journal of fluid mechanics*, 136:321–374.
- Castillo, L. and Johansson, T. G. (2002). The effects of the upstream conditions on a low reynolds number turbulent boundary layer with zero pressure gradient. *Journal of Turbulence*, 3(1):031.
- Castro, I. and Robins, A. (1977). The flow around a surface-mounted cube in uniform and turbulent streams. *Journal of fluid Mechanics*, 79(2):307–335.
- Celik, I., Klein, M., and Janicka, J. (2009). Assessment measures for engineering les applications.
- Chan, L., Skvortsov, A., and Ooi, A. (2022). Flow over a confined mounted fence at low and moderate reynolds number: A numerical study. *International Journal of Heat and Fluid Flow*, 96:109001.
- Chiarini, A. and Quadrio, M. (2021). The turbulent flow over the barc rectangular cylinder: a dns study. *Flow, Turbulence and Combustion*, 107:875–899.
- Choi, H., Lee, J., and Park, H. (2014). Aerodynamics of heavy vehicles. *Annual Review of Fluid Mechanics*, 46:441–468.
- Cimarelli, A., Corsini, R., and Stalio, E. (2024). Reynolds number effects in separating and reattaching flows with passive scalar transport. *Journal of Fluid Mechanics*, 984:A20.
- Cimarelli, A., Leonforte, A., and Angeli, D. (2018). On the structure of the self-sustaining cycle in separating and reattaching flows. *Journal of Fluid Mechanics*, 857:907–936.
- Corten, G. P. (2001). Flow separation on wind turbine blades. *University of Utrecht*.
- Craik, A. D. (1971). Non-linear resonant instability in boundary layers. *Journal of Fluid Mechanics*, 50(2):393–413.
- da Silva, B. L., Chakravarty, R., Sumner, D., and Bergstrom, D. J. (2020). Aerodynamic forces and three-dimensional flow structures in the mean wake of a surface-mounted finite-height square prism. *International Journal of Heat and Fluid Flow*, 83:108569.

- da Silva, B. L., Sumner, D., and Bergstrom, D. J. (2022). Mean and dynamic aspects of the wakes of a surface-mounted cube and block. *Journal of Fluids Engineering*, 144(1).
- da Silva, B. L., Sumner, D., and Bergstrom, D. J. (2024). On the flow dynamics around a surface-mounted cube and boundary layer effects. *Journal of Fluid Mechanics*, 991:A17.
- Derakhshandeh, J. and Alam, M. M. (2019). A review of bluff body wakes. *Ocean Engineering*, 182:475–488.
- Diaz-Daniel, C., Laizet, S., and Vassilicos, J. (2017a). Direct numerical simulations of a wall-attached cube immersed in laminar and turbulent boundary layers. *International Journal of Heat and Fluid Flow*, 68:269 – 280.
- Diaz-Daniel, C., Laizet, S., and Vassilicos, J. C. (2017b). Direct numerical simulations of a wall-attached cube immersed in laminar and turbulent boundary layers. *International Journal of Heat and Fluid Flow*, 68:269–280.
- Dimaczek, G., Tropea, C., and Wang, A.-B. (1989). Turbulent flow over two-dimensional, surface-mounted obstacles: plane and axisymmetric geometries. In *Advances in Turbulence 2*, pages 114–121. Springer.
- Dominy, R. (1992). Aerodynamics of grand prix cars. *Proceedings of the Institution of Mechanical Engineers, Part D: Journal of Automobile Engineering*, 206(4):267–274.
- Duong, D. V., Van Nguyen, L., Van Nguyen, D., Dinh, T. C., Zuhal, L. R., and Ngo, L. I. (2024). Direct numerical simulation of 45° oblique flow past surface-mounted square cylinder. *Journal of Fluid Mechanics*, 992:A12.
- Durst, F. and Wang, A.-B. (1989). Experimental and numerical investigations of the axisymmetric, turbulent pipe flow over a wall-mounted thin obstacle. In *7th Symposium on Turbulent Shear Flows, Volume 1*, volume 1, pages 10–4.
- Dutta, P., Saha, S. K., Nandi, N., and Pal, N. (2016). Numerical study on flow separation in 90° pipe bend under high reynolds number by k- ϵ modelling. *Engineering Science and Technology, an International Journal*, 19(2):904–910.
- El Hassan, M., Bourgeois, J., and Martinuzzi, R. (2015). Boundary layer effect on the vortex shedding of wall-mounted rectangular cylinder. *Experiments in Fluids*, 56(2):1–19.
- Fage, A. and Johansen, F. (1927). On the flow of air behind an inclined flat plate of infinite span. *Proceedings of the Royal Society of London. Series A, Containing Papers of a Mathematical and Physical Character*, 116(773):170–197.
- Fang, X. and Tachie, M. F. (2019). Flows over surface-mounted bluff bodies with different spanwise widths submerged in a deep turbulent boundary layer. *Journal of Fluid Mechanics*, 877:717–758.
- Farabee, T. and Casarella, M. (1984). Effects of surface irregularity on turbulent boundary layer wall pressure fluctuations. *Journal of Vibration, Acoustics, Stress, and Reliability in Design*.

- Farhadi, M. and Rahnama, M. (2006). Large eddy simulation of separated flow over a wall-mounted cube.
- Ferziger, J. H., Perić, M., and Street, R. L. (2002). *Computational methods for fluid dynamics*, volume 3. Springer.
- Freeman, B. R., Martinuzzi, R. J., and Hemmati, A. (2024). Momentum analysis of complex time-periodic flows. *Journal of Fluid Mechanics*, 979:A50.
- George, W. K., Beuther, P. D., and Arndt, R. E. (1984). Pressure spectra in turbulent free shear flows. *Journal of Fluid Mechanics*, 148:155–191.
- Godoy-Diana, R., Marais, C., Aider, J.-L., and Wesfreid, J. E. (2009). A model for the symmetry breaking of the reverse bénard–von kármán vortex street produced by a flapping foil. *Journal of Fluid Mechanics*, 622:23–32.
- Goswami, S. and Hemmati, A. (2020). Response of turbulent pipeflow to multiple square bar roughness elements at high reynolds number. *Physics of Fluids*, 32(7):075110.
- Goswami, S. and Hemmati, A. (2021a). Evolution of turbulent pipe flow recovery over a square bar roughness element at a range of reynolds numbers. *Physics of Fluids*, 33(3):035113.
- Goswami, S. and Hemmati, A. (2021b). Response of viscoelastic turbulent pipeflow past square bar roughness: The effect on mean flow. *Computation*, 9(8):85.
- Goswami, S. and Hemmati, A. (2022). Mechanisms of wake asymmetry and secondary structures behind low aspect-ratio wall-mounted prisms. *Journal of Fluid Mechanics*, 950:A31.
- Goswami, S. and Hemmati, A. (2023). Mean wake evolution behind low aspect-ratio wall-mounted finite prisms. *International Journal of Heat and Fluid Flow*, page 109237.
- Goswami, S. and Hemmati, A. (2024). Impact of depth-ratio on shear-layer dynamics and wake interactions around wall-mounted prisms. *Physics of Fluids*, 36(11):115–149.
- Gursul, I., Cleaver, D., and Wang, Z. (2014). Control of low reynolds number flows by means of fluid–structure interactions. *Progress in Aerospace Sciences*, 64:17–55.
- Hassan, S., Molla, M. M., Nag, P., Akhter, N., and Khan, A. (2022). Unsteady rans simulation of wind flow around a building shape obstacle. In *Building Simulation*, volume 15, pages 291–312. Springer.
- Hemati, M., Deem, E., Williams, M., Rowley, C. W., and Cattafesta, L. N. (2016). Improving separation control with noise-robust variants of dynamic mode decomposition. In *54th AIAA Aerospace Sciences Meeting*, page 1103.
- Hemati, M. S., Rowley, C. W., Deem, E. A., and Cattafesta, L. N. (2017). De-biasing the dynamic mode decomposition for applied koopman spectral analysis of noisy datasets. *Theoretical and Computational Fluid Dynamics*, 31(4):349–368.

- Hemmati, A., Wood, D. H., and Martinuzzi, R. J. (2015). Direct numerical simulation of the wake of a normal thin flat plate: infinite vs. finite width. In *Ninth International Symposium on Turbulence and Shear Flow Phenomena*. Begel House Inc.
- Hemmati, A., Wood, D. H., and Martinuzzi, R. J. (2016). Effect of side-edge vortices and secondary induced flow on the wake of normal thin flat plates. *International Journal of Heat and Fluid Flow*, 61:197–212.
- Hemmati, A., Wood, D. H., and Martinuzzi, R. J. (2017). Evolution of vortex formation in the wake of thin flat plates with different aspect-ratios. In *Progress in Turbulence VII*, pages 227–232. Springer.
- Hemmati, A., Wood, D. H., and Martinuzzi, R. J. (2018a). On simulating the flow past a normal thin flat plate. *Journal of Wind Engineering and Industrial Aerodynamics*, 174:170–187.
- Hemmati, A., Wood, D. H., and Martinuzzi, R. J. (2018b). On simulating the flow past a normal thin flat plate. *Journal of Wind Engineering and Industrial Aerodynamics*, 174:170–187.
- Hemmati, A., Wood, D. H., and Martinuzzi, R. J. (2019). Wake dynamics and surface pressure variations on two-dimensional normal flat plates. *AIP Advances*, 9(4).
- Holzmann, T. (2016). Mathematics, numerics, derivations and openfoam®. *Loeben, Germany: Holzmann CFD*.
- Hosseini, Z., Bourgeois, J., and Martinuzzi, R. (2013). Large-scale structures in dipole and quadrupole wakes of a wall-mounted finite rectangular cylinder. *Experiments in fluids*, 54(9):1–16.
- Hucho, W. and Sovran, G. (1993). Aerodynamics of road vehicles. *Annual review of fluid mechanics*, 25(1):485–537.
- Hunt, J., Wray, A., and Moin, P. (1988). Eddies, stream, and convergence zones in turbulent flows. *Studying Turbulence Using Numerical Simulation Databases-II*, 193.
- Hunt, J. C., Abell, C. J., Peterka, J. A., and Woo, H. (1978). Kinematical studies of the flows around free or surface-mounted obstacles; applying topology to flow visualization. *Journal of Fluid Mechanics*, 86(1):179–200.
- Hussain, A. F. (1983). Coherent structures—reality and myth. *The Physics of fluids*, 26(10):2816–2850.
- Hussain, A. F. (1986). Coherent structures and turbulence. *Journal of Fluid Mechanics*, 173:303–356.
- Hussein, H. J. and Martinuzzi, R. (1996). Energy balance for turbulent flow around a surface mounted cube placed in a channel. *Physics of Fluids*, 8(3):764–780.
- Hwang, J.-Y. and Yang, K.-S. (2004). Numerical study of vortical structures around a wall-mounted cubic obstacle in channel flow. *Physics of Fluids*, 16(7):2382–2394.

- Jasak, H. (1996). Error analysis and estimation for the finite volume method with applications to fluid flows.
- Jeong, J. and Hussain, F. (1995). On the identification of a vortex. *Journal of fluid mechanics*, 285:69–94.
- Jia, Y., Punithakumar, K., Noga, M., and Hemmati, A. (2021). Blood flow manipulation in the aorta with coarctation and arch narrowing for pediatric subjects. *Journal of Applied Mechanics*, 88(2):021001.
- Jiang, G. and Yoshie, R. (2020). Side ratio effects on flow and pollutant dispersion around an isolated high-rise building in a turbulent boundary layer. *Building and Environment*, 180:107078.
- Jimenez, J. (1983). A spanwise structure in the plane shear layer. *Journal of Fluid Mechanics*, 132:319–336.
- Johnson, D. A. and King, L. (1985). A mathematically simple turbulence closure model for attached and separated turbulent boundary layers. *AIAA journal*, 23(11):1684–1692.
- Joubert, E., Harms, T., and Venter, G. (2015). Computational simulation of the turbulent flow around a surface mounted rectangular prism. *Journal of Wind Engineering and Industrial Aerodynamics*, 142:173–187.
- Jovic, S. and Driver, D. (1995). Reynolds number effect on the skin friction in separated flows behind a backward-facing step. *Experiments in Fluids*, 18(6):464–467.
- Katz, J. (2006). Aerodynamics of race cars. *Annu. Rev. Fluid Mech.*, 38:27–63.
- Kawamura, F., Seki, Y., Iwamoto, K., and Kawamura, H. (2007). Dns of heat transfer in turbulent and transitional channel flow obstructed by rectangular prisms. *International journal of heat and fluid flow*, 28(6):1291–1301.
- Khalid, M. S. U., Wang, J., Akhtar, I., Dong, H., and Liu, M. (2020). Modal decompositions of the kinematics of crevalle jack and the fluid–caudal fin interaction. *Bioinspiration & Biomimetics*, 16(1):016018.
- Khan, M. H., Khan, H. H., Sharma, A., and Agrawal, A. (2020a). Laminar vortex shedding in the wake of a cube. *Journal of Fluids Engineering*, 142(11):111301.
- Khan, M. H., Sharma, A., and Agrawal, A. (2020b). Simulation of flow around a cube at moderate reynolds numbers using the lattice boltzmann method. *Journal of Fluids Engineering*, 142(1):011301.
- Kiewat, M. (2019). *Streaming Modal Decomposition Approaches for Vehicle Aerodynamics*. PhD thesis, Technische Universität München.
- Kim, J., Kline, S., and Johnston, J. (1980). Investigation of a reattaching turbulent shear layer: flow over a backward-facing step.

- Kim, T., Kato, S., and Murakami, S. (2001). Indoor cooling/heating load analysis based on coupled simulation of convection, radiation and hvac control. *Building and Environment*, 36(7):901–908.
- Kindree, M. G., Shahroodi, M., and Martinuzzi, R. J. (2018). Low-frequency dynamics in the turbulent wake of cantilevered square and circular cylinders protruding a thin laminar boundary layer. *Experiments in Fluids*, 59(12):1–26.
- Kiya, M. and Sasaki, K. (1983). Structure of a turbulent separation bubble. *Journal of Fluid Mechanics*, 137:83–113.
- Krajnović, S. and Davidson, L. (2005). Flow around a simplified car, part 1: large eddy simulation.
- Kumahor, S. and Tachie, M. F. (2022). Turbulent flow around rectangular cylinders with different streamwise aspect ratios. *Journal of Fluids Engineering*, 144(5):051304.
- Kumahor, S. and Tachie, M. F. (2023). Effects of streamwise aspect ratio on the spatio-temporal characteristics of flow around rectangular cylinders. *International Journal of Heat and Fluid Flow*, 101:109133.
- Lander, D., Moore, D., Letchford, C., and Amitay, M. (2018). Scaling of square-prism shear layers. *Journal of Fluid Mechanics*, 849:1096–1119.
- Launder, B. E. and Spalding, D. B. (1983). The numerical computation of turbulent flows. In *Numerical prediction of flow, heat transfer, turbulence and combustion*, pages 96–116. Elsevier.
- Li, Y., Zhang, J., Dong, G., and Abdullah, N. S. (2020). Small-scale reconstruction in three-dimensional kolmogorov flows using four-dimensional variational data assimilation. *Journal of Fluid Mechanics*, 885:A9.
- Lighthill, M. J. (1963). Introduction boundary layer theory. *Laminar boundary layers*.
- Lilly, D. K. (1992). A proposed modification of the germano subgrid-scale closure method. *Physics of Fluids A: Fluid Dynamics*, 4(3):633–635.
- Lin, J., Howard, F., and Selby, G. (1991). Exploratory study of vortex-generating devices for turbulent flow separation control. In *29th aerospace sciences meeting*, page 42.
- Ling, J., Kurzawski, A., and Templeton, J. (2016). Reynolds averaged turbulence modelling using deep neural networks with embedded invariance. *Journal of Fluid Mechanics*, 807:155–166.
- Lowson, M. (1965). *Pressure fluctuations in turbulent boundary layers*, volume 3156. National Aeronautics and Space Administration.
- Lyn, D., Einav, S., Rodi, W., and Park, J.-H. (1995). A laser-doppler velocimetry study of ensemble-averaged characteristics of the turbulent near wake of a square cylinder. *Journal of Fluid Mechanics*, 304:285–319.
- Ma, C.-H., Awasthi, M., Moreau, D., and Doolan, C. (2023). Aeroacoustics of turbulent flow over a forward-backward facing step. *Journal of Sound and Vibration*, 563:117840.

- Mansour, N. N., Kim, J., and Moin, P. (1988). Reynolds-stress and dissipation-rate budgets in a turbulent channel flow. *Journal of Fluid Mechanics*, 194:15–44.
- Marshall, D. and Stanton, T. E. (1931). On the eddy system in the wake of flat circular plates in three dimensional flow. *Proceedings of the Royal Society of London. Series A, Containing Papers of a Mathematical and Physical Character*, 130(813):295–301.
- Martinuzzi, R. and AbuOmar, M. (2003). Study of the flow around surface-mounted pyramids. *Experiments in fluids*, 34(3):379–389.
- Martinuzzi, R. and Tropea, C. (1993). The flow around surface-mounted, prismatic obstacles placed in a fully developed channel flow (data bank contribution).
- Martinuzzi, R. J. (2008). Dual vortex structure shedding from low aspect ratio, surface-mounted pyramids. *Journal of Turbulence*, (9):N28.
- Martinuzzi, R. J. and Havel, B. (2000). Turbulent flow around two interfering surface-mounted cubic obstacles in tandem arrangement. *J. Fluids Eng.*, 122(1):24–31.
- Mashhadi, A., Sohankar, A., and Alam, M. M. (2021). Flow over rectangular cylinder: Effects of cylinder aspect ratio and reynolds number. *International Journal of Mechanical Sciences*, 195:106264.
- McClean, J. and Sumner, D. (2014). An experimental investigation of aspect ratio and incidence angle effects for the flow around surface-mounted finite-height square prisms. *Journal of Fluids Engineering*, 136(8).
- Mendez, M. A., Iapiro, A., Noack, B. R., and Brunton, S. L. (2023). *Data-driven fluid mechanics: combining first principles and machine learning*. Cambridge University Press.
- Meng, Q., An, H., Cheng, L., and Kimiae, M. (2021). Wake transitions behind a cube at low and moderate reynolds numbers. *Journal of Fluid Mechanics*, 919.
- Menter, F. R., Kuntz, M., and Langtry, R. (2003). Ten years of industrial experience with the sst turbulence model. *Turbulence, heat and mass transfer*, 4(1):625–632.
- Miau, J.-J., Wu, S.-J., Hu, C.-C., and Chou, J.-H. (2004). Low-frequency modulations associated with vortex shedding from flow over bluff body. *AIAA journal*, 42(7):1388–1397.
- Mittal, R. and Balachandar, S. (1995). Generation of streamwise vortical structures in bluff body wakes. *Physical review letters*, 75(7):1300.
- Moin, P. and Mahesh, K. (1998). Direct numerical simulation: a tool in turbulence research. *Annual review of fluid mechanics*, 30(1):539–578.
- Mollicone, J.-P., Battista, F., Gualtieri, P., and Casciola, C. M. (2017). Effect of geometry and reynolds number on the turbulent separated flow behind a bulge in a channel. *Journal of Fluid Mechanics*, 823:100–133.

- Moore, D., Letchford, C., and Amitay, M. (2019a). Energetic scales in a bluff body shear layer. *Journal of Fluid Mechanics*, 875:543–575.
- Moore, D., Letchford, C., and Amitay, M. (2019b). Transitional shear layers on rectangular sections. In *Proceedings of the XV Conference of the Italian Association for Wind Engineering: IN-VENTO 2018* 25, pages 519–533. Springer.
- More, B. S., Dutta, S., Chauhan, M. K., and Gandhi, B. K. (2015). Experimental investigation of flow field behind two tandem square cylinders with oscillating upstream cylinder. *Experimental thermal and fluid science*, 68:339–358.
- Moreau, R. J. (2013). *Magnetohydrodynamics*, volume 3. Springer Science & Business Media.
- Morton, C., Martinuzzi, R. J., Kindree, M., Shahroodi, M., and Saeedi, M. (2018). Wake dynamics of a cantilevered circular cylinder of aspect ratio 4. *International Journal of Heat and Fluid Flow*, 72:109–122.
- Najjar, F. and Balachandar, S. (1998). Low-frequency unsteadiness in the wake of a normal flat plate. *Journal of Fluid Mechanics*, 370:101–147.
- Najjar, F. M. and Vanka, S. (1995). Effects of intrinsic three-dimensionality on the drag characteristics of a normal flat plate. *Physics of fluids*, 7(10):2516–2518.
- Narasimhamurthy, V. D. and Andersson, H. I. (2009). Numerical simulation of the turbulent wake behind a normal flat plate. *International Journal of Heat and Fluid Flow*, 30(6):1037–1043.
- Norberg, C. (2001). Flow around a circular cylinder: aspects of fluctuating lift. *Journal of fluids and structures*, 15(3-4):459–469.
- Obabko, A. and Cassel, K. (2002). Navier–stokes solutions of unsteady separation induced by a vortex. *Journal of Fluid Mechanics*, 465:99–130.
- Okajima, A. (1982). Strouhal numbers of rectangular cylinders. *Journal of Fluid mechanics*, 123:379–398.
- Okamoto, S. and Sunabashiri, Y. (1992). Vortex shedding from a circular cylinder of finite length placed on a ground plane.
- Park, C.-W. and Lee, S.-J. (2000). Free end effects on the near wake flow structure behind a finite circular cylinder. *Journal of Wind Engineering and Industrial Aerodynamics*, 88(2-3):231–246.
- Park, Y. G., Yoon, H. S., and Ha, M. Y. (2013). Numerical study on the laminar fluid flow characteristics around a rectangular cylinder with different width to height ratios. *Progress in Computational Fluid Dynamics, an International Journal*, 13(3-4):244–262.
- Paterson, D. and Apelt, C. (1989). Simulation of wind flow around three-dimensional buildings. *Building and Environment*, 24(1):39–50.
- Perry, A. E. and Fairlie, B. (1975). Critical points in flow patterns. In *Advances in geophysics*, volume 18, pages 299–315. Elsevier.

- Pope, S. B. (2001). Turbulent flows.
- Porteous, R., Moreau, D. J., and Doolan, C. J. (2014). A review of flow-induced noise from finite wall-mounted cylinders. *Journal of Fluids and Structures*, 51:240–254.
- Ranjan, P. and Dewan, A. (2016). Effect of side ratio on fluid flow and heat transfer from rectangular cylinders using the pans method. *International Journal of Heat and Fluid Flow*, 61:309–322.
- Rastan, M., Shahbazi, H., Sohankar, A., Alam, M. M., and Zhou, Y. (2021). The wake of a wall-mounted rectangular cylinder: Cross-sectional aspect ratio effect. *Journal of Wind Engineering and Industrial Aerodynamics*, 213:104615.
- Rastan, M., Sohankar, A., and Alam, M. M. (2017). Low-reynolds-number flow around a wall-mounted square cylinder: Flow structures and onset of vortex shedding. *Physics of Fluids*, 29(10):103601.
- Rastan, M., Sohankar, A., Doolan, C., Moreau, D., Shirani, E., and Alam, M. M. (2019). Controlled flow over a finite square cylinder using suction and blowing. *International Journal of Mechanical Sciences*, 156:410–434.
- Ravindran, S. (1999). Active control of flow separation over an airfoil.
- Reif, B. P. and Durbin, P. (2011). *Statistical theory and modeling for turbulent flows*. John Wiley & Sons.
- Ren, X., Su, H., Yu, H.-H., and Yan, Z. (2022). Wall-modeled large eddy simulation and detached eddy simulation of wall-mounted separated flow via openfoam. *Aerospace*, 9(12):759.
- Roache, P. J. (1982). Scaling of high-reynolds-number weakly separated channel flows. In *Numerical and Physical Aspects of Aerodynamic Flows*, pages 87–98. Springer.
- Robertson, E., Choudhury, V., Bhushan, S., and Walters, D. K. (2015). Validation of openfoam numerical methods and turbulence models for incompressible bluff body flows. *Computers & Fluids*, 123:122–145.
- Robichaux, J., Balachandar, S., and Vanka, S. (1999). Three-dimensional floquet instability of the wake of square cylinder. *Physics of Fluids*, 11(3):560–578.
- Rodi, W. (1997). Comparison of les and rans calculations of the flow around bluff bodies. *Journal of wind engineering and industrial aerodynamics*, 69:55–75.
- Roshko, A. (1961). Experiments on the flow past a circular cylinder at very high reynolds number. *Journal of fluid mechanics*, 10(3):345–356.
- Roshko, A. (1993). Perspectives on bluff body aerodynamics. *Journal of Wind Engineering and Industrial Aerodynamics*, 49(1-3):79–100.
- Rowley, C. W., Mezić, I., Bagheri, S., Schlatter, P., and Henningson, D. S. (2009). Spectral analysis of nonlinear flows. *Journal of fluid mechanics*, 641:115–127.

- Saathoff, P. J. and Melbourne, W. H. (1997). Effects of free-stream turbulence on surface pressure fluctuations in a separation bubble. *Journal of Fluid Mechanics*, 337:1–24.
- Saeedi, M., LePoudre, P. P., and Wang, B.-C. (2014). Direct numerical simulation of turbulent wake behind a surface-mounted square cylinder. *Journal of Fluids and Structures*, 51:20–39.
- Saeedi, M. and Wang, B.-C. (2015). Large-eddy simulation of turbulent flow over an array of wall-mounted cubic obstacles. In *Direct and Large-Eddy Simulation IX*, pages 451–457. Springer.
- Saha, A. K. (2004). Three-dimensional numerical simulations of the transition of flow past a cube. *Physics of Fluids*, 16(5):1630–1646.
- Saha, A. K. (2013). Unsteady flow past a finite square cylinder mounted on a wall at low reynolds number. *Computers & Fluids*, 88:599–615.
- Saha, A. K., Muralidhar, K., and Biswas, G. (2000). Vortex structures and kinetic energy budget in two-dimensional flow past a square cylinder. *Computers & fluids*, 29(6):669–694.
- Sakamoto, H. and Arie, M. (1983). Vortex shedding from a rectangular prism and a circular cylinder placed vertically in a turbulent boundary layer. *Journal of Fluid Mechanics*, 126:147–165.
- Sattari, P., Bourgeois, J., and Martinuzzi, R. (2012). On the vortex dynamics in the wake of a finite surface-mounted square cylinder. *Experiments in Fluids*, 52:1149–1167.
- Scarano, F. and Poelma, C. (2009). Three-dimensional vorticity patterns of cylinder wakes. *Experiments in fluids*, 47:69–83.
- Scarano, F. and Riethmuller, M. L. (2000). Advances in iterative multigrid piv image processing. *Experiments in fluids*, 29(Suppl 1):S051–S060.
- Schlichting, H. and Gersten, K. (2016). *Boundary-layer theory*. Springer.
- Schmid, P. J. (2010). Dynamic mode decomposition of numerical and experimental data. *Journal of fluid mechanics*, 656:5–28.
- Schmidt, O. T. (2020). Bispectral mode decomposition of nonlinear flows. *Nonlinear dynamics*, 102(4):2479–2501.
- Schofield, W. and Logan, E. (1990). Turbulent shear flow over surface mounted obstacles.
- Shah, M. S., Joshi, J. B., Kalsi, A. S., Prasad, C., and Shukla, D. S. (2012). Analysis of flow through an orifice meter: Cfd simulation. *Chemical engineering science*, 71:300–309.
- Simpson, R. L. (1989). Turbulent boundary-layer separation. *Annual Review of Fluid Mechanics*, 21(1):205–232.
- Simpson, R. L. (2001). Junction flows. *Annual Review of Fluid Mechanics*, 33(1):415–443.
- Singh, S. and Mittal, S. (2005). Flow past a cylinder: shear layer instability and drag crisis. *International journal for numerical methods in fluids*, 47(1):75–98.

- Slessor, M., Bond, C., and Dimotakis, P. (1998). Turbulent shear-layer mixing at high reynolds numbers: effects of inflow conditions. *Journal of Fluid Mechanics*, 376:115–138.
- Smits, A., Ding, L., and Van Buren, T. (2019a). Flow over a square bar roughness. In *Proc. Turbulence and Shear Flow Phenomena*, volume 11.
- Smits, A., Ding, L., and Van Buren, T. (2019b). Flow over a square bar roughness. In *Proceedings of Turbulence and Shear Flow Phenomena*, volume 11.
- Smits, A. J., Young, S., and Bradshaw, P. (1979). The effect of short regions of high surface curvature on turbulent boundary layers. *Journal of fluid mechanics*, 94(2):209–242.
- Sohankar, A. (2008). Large eddy simulation of flow past rectangular-section cylinders: Side ratio effects. *Journal of wind engineering and industrial aerodynamics*, 96(5):640–655.
- Sohankar, A., Norberg, C., and Davidson, L. (1998). Low-reynolds-number flow around a square cylinder at incidence: study of blockage, onset of vortex shedding and outlet boundary condition. *International journal for numerical methods in fluids*, 26(1):39–56.
- Sousa, J., García-Sánchez, C., and Gorlé, C. (2018). Improving urban flow predictions through data assimilation. *Building and Environment*, 132:282–290.
- Sumner, D. and Heseltine, J. (2008). Tip vortex structure for a circular cylinder with a free end. *Journal of Wind Engineering and Industrial Aerodynamics*, 96(6-7):1185–1196.
- Sumner, D., Heseltine, J., and Dansereau, O. (2004). Wake structure of a finite circular cylinder of small aspect ratio. *Experiments in Fluids*, 37:720–730.
- Sumner, D., Rostamy, N., Bergstrom, D., and Bugg, J. (2017). Influence of aspect ratio on the mean flow field of a surface-mounted finite-height square prism. *International Journal of Heat and Fluid Flow*, 65:1–20.
- Swanson, R. C. and Langer, S. (2016). Comparison of naca 0012 laminar flow solutions: structured and unstructured grid methods. Technical report.
- Tabor, G. R. and Baba-Ahmadi, M. (2010). Inlet conditions for large eddy simulation: A review. *Computers & Fluids*, 39(4):553–567.
- Taira, K., Hemati, M. S., Brunton, S. L., Sun, Y., Duraisamy, K., Bagheri, S., Dawson, S. T., and Yeh, C.-A. (2020). Modal analysis of fluid flows: Applications and outlook. *AIAA journal*, 58(3):998–1022.
- Taneda, S. (1952). An experimental study on the structure of the vortex street behind a circular cylinder of finite length. *Reports of the Research Institute for Applied Mechanics*, 1:131–144.
- Tenaud, C., Podvin, B., Fraigneau, Y., and Daru, V. (2016). On wall pressure fluctuations and their coupling with vortex dynamics in a separated–reattached turbulent flow over a blunt flat plate. *International Journal of Heat and Fluid Flow*, 61:730–748.

- Tiwari, S. S., Bale, S., Patwardhan, A. W., Nandakumar, K., and Joshi, J. B. (2019). Insights into the physics of dominating frequency modes for flow past a stationary sphere: Direct numerical simulations. *Physics of Fluids*, 31(4):045108.
- Tominaga, Y. (2015). Flow around a high-rise building using steady and unsteady rans cfd: Effect of large-scale fluctuations on the velocity statistics. *Journal of Wind Engineering and Industrial Aerodynamics*, 142:93–103.
- Uffinger, T., Ali, I., and Becker, S. (2013). Experimental and numerical investigations of the flow around three different wall-mounted cylinder geometries of finite length. *Journal of Wind Engineering and Industrial Aerodynamics*, 119:13–27.
- Verma, S. and Hemmati, A. (2020). Performance of overset mesh in modeling the wake of sharp-edge bodies. *Computation*, 8(3):66.
- Verma, S. and Hemmati, A. (2021). Evolution of wake structures behind oscillating hydrofoils with combined heaving and pitching motion. *Journal of Fluid Mechanics*, 927.
- Verma, S., Khalid, M. S. U., and Hemmati, A. (2023). On the association of kinematics, spanwise instability and growth of secondary vortex structures in the wake of oscillating foils. *Proceedings of the Royal Society A*, 479(2276):20230353.
- Von Karman, T. (1911). Über den mechanismus des widerstandes, den ein bewegter körper in einer flüssigkeit erfährt. *Nachrichten von der Gesellschaft der Wissenschaften zu Göttingen, Mathematisch-Physikalische Klasse*, 1911:509–517.
- Von Kármán, T. (1963). *Aerodynamics*, volume 9. McGraw-Hill New York.
- Wang, F. and Lam, K. M. (2019a). Geometry effects on mean wake topology and large-scale coherent structures of wall-mounted prisms. *Physics of Fluids*, 31(12).
- Wang, F. and Lam, K. M. (2019b). Geometry effects on mean wake topology and large-scale coherent structures of wall-mounted prisms. *Physics of Fluids*, 31(12):125109.
- Wang, H. and Zhou, Y. (2009). The finite-length square cylinder near wake. *Journal of Fluid Mechanics*, 638:453–490.
- Wang, H., Zhou, Y., Chan, C., and Lam, K. S. (2006). Effect of initial conditions on interaction between a boundary layer and a wall-mounted finite-length-cylinder wake. *Physics of Fluids*, 18(6):065106.
- Wang, X., Hao, Z., Zhang, J.-X., and Tan, S. (2014). Flow around two tandem square cylinders near a plane wall. *Experiments in Fluids*, 55(10):1818.
- Wei, T. and Smith, C. (1986). Secondary vortices in the wake of circular cylinders. *Journal of Fluid Mechanics*, 169:513–533.
- Welch, P. (1967). The use of fast fourier transform for the estimation of power spectra: a method based on time averaging over short, modified periodograms. *IEEE Transactions on audio and electroacoustics*, 15(2):70–73.

- Weller, H. G., Tabor, G., Jasak, H., and Fureby, C. (1998). A tensorial approach to computational continuum mechanics using object-oriented techniques. *Computers in physics*, 12(6):620–631.
- Wilcox, D. C. et al. (1998). *Turbulence modeling for CFD*, volume 2. DCW industries La Canada, CA.
- Williamson, C. (1996). Vortex dynamics in the cylinder wake.
- Williamson, C. (1988). The existence of two stages in the transition to three-dimensionality of a cylinder wake. *The Physics of fluids*, 31(11):3165–3168.
- Williamson, C. (1996). Three-dimensional wake transition. *Journal of Fluid Mechanics*, 328:345–407.
- Wu, S., MIAU, J.-J., Hu, C., and Chou, J. (2005). On low-frequency modulations and three-dimensionality in vortex shedding behind a normal plate. *Journal of Fluid Mechanics*, 526:117–146.
- Yakhot, A., Liu, H., and Nikitin, N. (2006). Turbulent flow around a wall-mounted cube: A direct numerical simulation. *International journal of heat and fluid flow*, 27(6):994–1009.
- Yamagata, T., Ito, A., Sato, Y., and Fujisawa, N. (2014). Experimental and numerical studies on mass transfer characteristics behind an orifice in a circular pipe for application to pipe-wall thinning. *Experimental thermal and fluid science*, 52:239–247.
- Yauwenas, Y., Porteous, R., Moreau, D. J., and Doolan, C. J. (2019). The effect of aspect ratio on the wake structure of finite wall-mounted square cylinders. *Journal of Fluid Mechanics*, 875:929–960.
- Yin, G., Andersen, M., and Ong, M. C. (2020). Numerical simulations of flow around two tandem wall-mounted structures at high reynolds numbers. *Applied Ocean Research*, 99:102124.
- Ying, X., Xu, F., and Zhang, Z. (2012). Numerical simulation and visualization of flow around rectangular bluff bodies. In *The Seventh International Colloquium on Bluff Body Aerodynamics and Applications (BBA7) Shanghai, China*, pages 272–281.
- Zagarola, M. V. and Smits, A. J. (1998). Mean-flow scaling of turbulent pipe flow. *Journal of Fluid Mechanics*, 373:33–79.
- Zargar, A., Goswami, S., and Hemmati, A. (2022a). On the wake of a large depth ratio wall-mounted prism at a normal incident angle. *Journal of Wind Engineering and Industrial Aerodynamics*, 230:105168.
- Zargar, A., Gungor, A., Tarokh, A., and Hemmati, A. (2021a). Coherent structures in the wake of a long wall-mounted rectangular prism at large incident angles. *Physical Review Fluids*, 6(3):034603.
- Zargar, A., Tarokh, A., and Hemmati, A. (2021b). The steady wake of a wall-mounted rectangular prism with a large-depth-ratio at low reynolds numbers. *Energies*, 14(12):3579.

- Zargar, A., Tarokh, A., and Hemmati, A. (2022b). The unsteady wake transition behind a wall-mounted large-depth-ratio prism. *Journal of Fluid Mechanics*, 952:A12.
- Zdravkovich, M. (2003). Flow around circular cylinders vol 2: Applications, oxford university press, oxford.
- Zdravkovich, M. M. (1997). *Flow around circular cylinders: Volume 2: Applications*, volume 2. Oxford university press.
- Zhang, D., Cheng, L., An, H., and Zhao, M. (2017). Direct numerical simulation of flow around a surface-mounted finite square cylinder at low reynolds numbers. *Physics of Fluids*, 29(4):045101.
- Zhang, Z., Kareem, A., Xu, F., and Jiang, H. (2023). Global instability and mode selection in flow fields around rectangular prisms. *Journal of Fluid Mechanics*, 955:A19.
- Zheng, H., Xie, F., Zheng, Y., Ji, T., and Zhu, Z. (2019). Propulsion performance of a two-dimensional flapping airfoil with wake map and dynamic mode decomposition analysis. *Physical Review E*, 99(6):063109.
- Zhong, H., Chen, S., and Lee, C. (2011). Experimental study of freely falling thin disks: Transition from planar zigzag to spiral. *Physics of Fluids*, 23(1).
- Zhou, Y., Zhang, H., and Yiu, M. (2002). The turbulent wake of two side-by-side circular cylinders. *Journal of Fluid Mechanics*, 458:303–332.